

Structural and Catalytic Studies of Copper-based Materials for the Direct Electrochemical Reduction of CO₂ – Investigations from Fundamental to Technological Current Densities

vorgelegt von

M. Sc.

Tim Frederik Möller

an der Fakultät II – Mathematik und Naturwissenschaften

der Technischen Universität Berlin

zur Erlangung des akademischen Grades

Doktor der Naturwissenschaften

Dr. rer. Nat.

genehmigte Dissertation

Promotionsausschuss

Vorsitzender Prof. Dr. Thomas Friedrich

Gutachter Prof. Dr. Peter Strasser

Gutachterin Prof. Dr. Mehtap Özaslan (Technische Universität Braunschweig)

Tag der wissenschaftlichen Aussprache: 29. Januar. 2021

Berlin 2021

Danksagung

An dieser Stelle möchte ich Allen danken, die zum erfolgreichen Zustandekommen dieser Arbeit beigetragen haben.

Spezieller Dank gilt meiner Freundin Stella, meinen Eltern Thomas und Sabine, meinem Bruder Janis und meiner Schwägerin Sumin. Ohne eure vielfältige, liebevolle und stetige Unterstützung in allen Lebenslagen wäre diese Arbeit für mich nicht möglich gewesen. Auch der Familie Kalantzis möchte ich für ihre Unterstützung danken, die weit über den sonntäglichen Brunch hinausgeht. Natürlich möchte ich auch all meinen Freunden danken, die trotz unterschiedlich ausgeprägter Aversion gegenüber der Chemie immer ein offenes Ohr für meine fachlichen Monologe hatten.

Besonderer Dank gilt meinem Betreuer Prof. Dr. Peter Strasser, der mir die wissenschaftliche Auseinandersetzung mit dem Thema der Elektrokatalyse schon im Rahmen der Masterarbeit ermöglichte und mich seitdem fachlich fördert und fordert. Ich bedanke mich für die Möglichkeit meine Promotion in deinem Arbeitskreis durchführen zu dürfen und für die vielfältigen, wie auch tiefgreifenden Einblicke in die Katalysatorforschung. Die unterschiedlichen Aufgaben von technischer, fachlicher und organisatorischer Natur haben mir über die Jahre viel Spaß gemacht und mir geholfen ein besserer Wissenschaftler zu werden. Ich möchte mich ebenfalls bei Prof. Dr. Mehtap Özasan für die Übernahme des Zweitgutachtens meiner Promotion bedanken, wie auch bei Prof. Dr. Thomas Friedrich für die Übernahme des Prüfungsvorsitzes.

Aus dem Arbeitskreis Strasser gilt mein besonderer Dank meinen ehemaligen fachlichen Betreuern Dr. Ana Sofia Varela Gasque, Dr. Zarko Jovanov und Dr. Cheonghee Kim, die mir mit ihrer freundlichen, kompetenten Art stets zu helfen wussten. Ebenfalls meinen langjährigen Kollegen des CO₂RR-Teams Dr. Wen Ju, Dr. Xingli Wang und Dr. Jorge Ferreira de Araújo gilt mein Dank. Die regen Diskussionen haben mir immer Spaß gemacht und viel zu meinem wissenschaftlichen und technischen Verständnis beigetragen. Auch Trung Ngo Thanh, Clara Hartling und Yuhang Duan möchte ich danken für ihre Unterstützung meiner Arbeit im Rahmen ihrer Masterarbeit, Arbeit als studentischer Hilfskraft und Forschungspraktika. Auch allen hier nicht namentlich erwähnten Mitgliedern des Arbeitskreises von Prof. Peter Strasser möchte ich für ein angenehmes, kollegiales Arbeitsumfeld danken.

Zudem möchte ich mich auch bei den Mitarbeitern der feinmechanischen Werkstatt, unserem Glasbläser Carsten Hirschfeld, Astrid Müller-Klauke und Benjamin Paul für ihr hervorragende Zusammenarbeit und vielfältige Hilfe bedanken.

Zusammenfassung

Der Anteil der erneuerbaren Energien an der weltweiten Stromerzeugung ist über die letzten Jahrzehnte stetig gestiegen und soll in naher Zukunft eine vollständige Umstellung auf eine kohlenstoffneutrale Energieversorgung ermöglichen. Diese Abkehr von fossilen Energieträgern stellt enorme Herausforderungen an die Entwicklung hoch-effizienter und skalierbarer Stromspeichertechnologien, die dem globalen Ausmaß dieser Umstellung gerecht werden müssen. Hierbei ist die elektrokatalytische Umwandlung von CO_2 in reduzierte Kohlenstoffverbindungen ein vielversprechender Ansatz, der sowohl eine nachhaltige, einstufige Produktion von Grundchemikalien, wie auch von flüssigen Brennstoffen mit einer hohen Energiedichte ermöglicht. Die Produktion dieser ökonomisch bedeutsamen Verbindungen erfordert, bis auf wenige Ausnahmen, die Verwendung von Kupfer als kathodisches Katalysatormaterial für die elektrokatalytische CO_2 Reduktionsreaktion (CO_2RR). Trotz des großen wirtschaftlichen Potentials der CO_2RR verhindern eine unzureichende Kontrolle über die katalytische Selektivität und mangelhaftes Verständnis der entscheidenden Materialeigenschaften eine großtechnische Nutzung der Reaktion. Im Rahmen dieser Arbeit sollen die zugrundeliegenden Struktur-Selektivitäts-Beziehungen erforscht werden, um somit ein besseres Verständnis der Reaktion zu erzielen und hierdurch zur zukünftigen Entwicklung der Technologie beizutragen.

Zu diesem Zweck werden in dieser Arbeit die Synthese, sowie die physikochemische und elektrokatalytische Untersuchung verschiedener kationischer Cu Verbindungen vorgestellt. Zunächst werden Zusammenhänge zwischen der Art der Anionen (N^{3-} , S^{2-} , O^{2-}) und der katalytischen Selektivität während elektrochemischer Untersuchungen bei niedrigen Stromdichten abgeleitet. Hierbei ermöglichte die Variationen der Anionen Art in Kupferverbindung die Bildung von selektiven Katalysatoren zur Herstellung von CH_4 , HCOO^- und C_2H_4 . Eine morphologische und kompositionelle Analyse der untersuchten Katalysatoren zeigte den Vorgang von komplexen Strukturübergängen, die durch die kathodischen Potentiale der elektrochemischen CO_2RR ausgelöst wurden. Dabei zeigte sich, dass die kathodischen Reaktionsbedingungen nicht immer zur Bildung eines vollständig metallischen Zustands führten und, dass ein Teil der untersuchten kationischen Cu Verbindungen einen gewissen Grad an Widerstandsfähigkeit gegen diesen Reduktionsprozess aufwiesen. Zusätzlich konnte gezeigt werden, dass die so gebildeten Cu Strukturen über einen hohen Anteil an Fehlstellen und unterkoordinierten Stellen verfügten.

Auf der Grundlage der katalytischen Untersuchungen bei niedrigen Stromdichten wurden nanokubische Cu_2O -Partikel als Modellkatalysator ausgewählt, um die CO_2RR bei hohen Stromdichten in einem Flusszellen-Elektrolyseur zu untersuchen. Es konnte gezeigt werden, dass die katalytische Selektivität von Messungen bei niedrigen Strömen zwar qualitativ mit der Selektivität bei deutlich höheren Strömen übereinstimmen kann, sich jedoch die absoluten Werte stark unterscheiden. Zusätzlich konnten Degradationspfade beobachtet werden, die ausschließlich bei Langzeitmessungen

unter hohen Stromdichten auftraten und auf eine Notwendigkeit dieser Messungen zur umfassenden Katalysatorcharakterisierung hinwiesen. Schließlich wurde gezeigt, dass die Struktur der Gasdiffusionselektroden und die Reaktionsumgebung entscheidende Elemente eines Systems für effiziente CO₂RR bei hohen Strömen sind und dass diese einen starken Einfluss auf die katalytische Selektivität der Reaktion haben.

Die vorliegende Arbeit bietet mit ihren Ergebnissen ein besseres Verständnis der selektivitätsbestimmenden Faktoren für die elektrochemische CO₂RR auf Kupferkatalysatoren. Dabei geben die vorgestellten Studien sowohl Einblicke in Prozesse auf einer fundamentalen Ebene als auch zu Systemen von technologischer Relevanz. Zusammenfassend bieten die gewonnenen Erkenntnisse einen Leitfaden für zukünftige Forschungsansätze und helfen somit bei der Entwicklung effizienterer CO₂RR-Elektrolyseure.

Abstract

Renewable energies have steadily increased their share of global power generation in recent years and are hoped to enable a carbon-neutral energy supply within the next decades. This far-reaching development away from fossil energy carriers poses as an enormous task for the development of efficient power-storage technologies that can cope with the global scale of the requirements. Here, the electrocatalytic conversion of CO₂ to reduced carbon compounds has been emerging as a promising approach that allows the sustainable production of commodity chemicals and liquid fuels of high energy density. This special quality is limited, with few exceptions, to the use of copper as cathode catalyst during the electrocatalytic CO₂ reduction reaction (CO₂RR). Despite the great potential and versatility of the CO₂RR, missing understanding and control over the catalytic properties of copper has led to issues of reaction selectivity and has largely inhibited its technological realization. This work sets out to investigate structure-selectivity relations for the electrochemical CO₂RR catalysed by Cu-based materials.

For this purpose, this thesis presents the synthesis and the physicochemical characterization, as well as the electrocatalytic testing of various cationic Cu compounds for the CO₂RR. Initially, correlations between anion identity, e.g. N³⁻, O²⁻, S²⁻, and catalytic selectivity are deduced for a regime of low current density. Here, selective catalysts for production of either CH₄, C₂H₄, or HCOO⁻ were obtained by identity variations of the anion contained in nanosized cationic Cu compounds. Morphological and compositional analysis of the investigated catalysts revealed complex structural transitions caused by the cathodic potentials during the electrochemical CO₂RR. In this, the cathodic conditions are shown to not always cause the formation of a completely metallic state and that the cationic compounds can be, to a certain degree, resilient to the reduction. Furthermore, an inherent connection between the abundant presence of undercoordinated Cu sites and the reductive restructuring of cationic Cu compounds during CO₂RR is proposed.

Based on the initial catalytic investigations at low reaction rates, nanocubic Cu₂O particles are chosen as a model catalyst to study the CO₂RR at high reaction rates in a Flow-Cell electrolyzer. It is deduced that the results derived from measurements at low currents can be qualitatively in line with the performance at much higher technological currents, but that the detailed metrics and temporal changes in catalytic properties can deviate considerably. Finally, the electrode structure and reaction environment are shown to be crucial elements for an efficient CO₂RR electrolyzer at high currents and that variations show a strong influence on the catalytic selectivity.

The present work offers a better understanding of selectivity determining metrics for the electrocatalytic CO₂RR. The introduced studies provide insight from a fundamental level towards technological relevant findings. In summary, the gained knowledge offers a guideline for future work and aids in the development of more efficient CO₂RR electrolyzers.

Table of contents

Danksagung	I
Zusammenfassung.....	III
Abstract.....	V
1 Introduction	1
1.1 Environmental and economic scope of electrocatalysis	1
1.2 The electrocatalytic CO ₂ reduction reaction.....	4
1.2.1 Mechanistic insights for Cu-catalyzed CO ₂ RR.....	6
1.2.2 Research on Cu-based catalysts for the CO ₂ RR	7
1.2.3 Influence of the reaction environment on the Cu-catalyzed CO ₂ RR	8
1.2.4 Cu-catalyzed CO ₂ RR at high current densities	9
1.3 Motivation, goal, and outline of this thesis	11
2 Theoretical and scientific background	15
2.1 General considerations of electrochemistry	15
2.1.1 The electrochemical double layer	15
2.1.2 Thermodynamics of electrochemistry.....	17
2.1.3 Kinetics of electrochemistry	21
2.1.4 Efficiency of electrochemical reactions.....	25
2.2 Correlation of bond strength and catalytic reaction rates – The Sabatier principle	29
3 Experimental section.....	31
3.1 Synthesis of nanosized cationic Cu catalysts	32
3.1.1 Preparation of cubic Cu ₂ O nanoparticles	32
3.1.2 Supporting procedure of cubic Cu ₂ O nanoparticles	32
3.1.3 Preparation of Cu ₃ N nanoparticles.....	32
3.1.4 Preparation of CuS nanoparticles.....	33
3.1.5 Preparation of CeO _x /Cu ₂ O nanoparticles	33
3.2 Electrochemical characterization	34
3.2.1 Electrode preparation.....	34
3.2.2 Testing procedure in an H-Cell setup	35
3.2.3 Testing procedure in a Flow-Cell setup	37
3.2.4 Equations used as part of electrochemical characterization	38
3.3 Physicochemical characterization.....	40

3.3.1	Powder and grazing incidence x-ray diffraction (PXRD and GI-XRD)	40
3.3.2	X-ray absorption spectroscopy (XAS)	40
3.3.3	X-ray photoelectron spectroscopy (XPS)	41
3.3.4	Scanning and transmission electron microscopy (SEM and TEM)	41
3.3.5	Inductively coupled plasma optical emission spectroscopy (ICP-OES)	41
3.3.6	Thermogravimetric analysis and differential scanning calorimetry (TGA-DSC)	42
3.4	Product quantification	43
3.4.1	Gas phase analysis	43
3.4.2	Liquid phase analysis	43
4	Low-Current H-Cell investigations of copper-based catalyst systems	45
4.1	Electrocatalytic CO ₂ reduction on CuO _x nanocubes: tracking the evolution of chemical state, geometric structure, and catalytic selectivity using <i>operando</i> spectroscopy	47
4.1.1	Introduction	48
4.1.2	Results and discussion	48
4.1.3	Conclusions	59
4.2	Preparation and catalytic selectivity of Cu ₃ N particles for the electrochemical CO ₂ RR	61
4.2.1	Introduction	61
4.2.2	Results and discussion	61
4.2.3	Conclusions	66
4.3	Catalytic selectivity and phase changes of CuS particles during CO ₂ RR prepared by anion exchange of Cu ₂ O structures	69
4.3.1	Introduction	69
4.3.2	Results and discussion	69
4.3.3	Conclusions	75
4.4	Introduction of CeO _x to Cu ₂ O nanocubes: a bimetallic CuO _x /CeO _x system for the electrocatalytic CO ₂ RR	77
4.4.1	Introduction	77
4.4.2	Results and discussion	77
4.4.3	Conclusions	83
5	High-Current Flow-Cell investigations of copper-based catalyst systems	85
5.1	Correlation of membrane conductivity, acid-base equilibria, and electrolyte stability during prolonged CO ₂ electrolysis in aqueous solutions of KHCO ₃	87
5.1.1	Introduction	87
5.1.2	Results and discussion	87
5.1.3	Conclusions	91
5.2	High-rate CO ₂ RR on carbon-supported and unsupported cubic Cu ₂ O nanoparticles	93

5.2.1	Introduction	94
5.2.2	Results and discussion	94
5.2.3	Conclusions	98
5.3	Influence of concentration gradients and electrode structure on the electrocatalytic CO ₂ RR selectivity during high rate electrolysis in pH buffering media	99
5.3.1	Introduction	100
5.3.2	Results and discussion	100
5.3.3	Conclusions	113
6	Summary and perspective	115
6.1	Summary of results from H-Cell investigations	116
6.2	Summary of results from Flow-Cell investigations	119
6.3	Perspective	121
7	References	123
	Appendix	133
A 1	Supplementary information to CO ₂ RR in an H-Cell	133
A 2	Supplementary information to CO ₂ RR in a Flow-Cell	147
	List of figures	159
	List of tables	165
	List of chemicals	167
	List of abbreviations	169
	List of publications	171

1 Introduction

1.1 Environmental and economic scope of electrocatalysis

The contribution of the anthropogenic emission of greenhouse gases, such as CO₂, N₂O and CH₄, to global warming has received increasing political, scientific, and public attention in recent decades. In the 5th assessment report of the intergovernmental panel on climate change (IPCC) of the United Nations a high probability of a direct relationship between anthropogenic emissions of greenhouse gases and global warming has been strongly suggested. Such emissions are largely driven by global population and economic growth since the pre-industrial era and they have caused an unprecedented increase in atmospheric concentrations of the respective greenhouse gases for thousands of years. This change in atmospheric composition affects the earth's energy balance by increased adsorption of infrared radiation causing the global increase in temperature over the last century. Such a change in the earth's energy balance has been suggested to strongly influence the global weather, increasing the probability and magnitude of extreme phenomena as heat waves, floods, and droughts. The direct and indirect effects of global warming are suspected to impact far-reaching aspects of everyday life, such as health, water, food, infrastructure, economy, and security. Accordingly, global warming has been deemed a topic that threatens people's prosperity and basic needs for living. ^[1, 2]

The fundamental problem of the global population and economic growth is that the large associated energetic demand is being covered by fossil fuels. Historically, fossil energy carriers allowed a fast industrial and technological development, which enabled the economic and population growth in the first place. Initially coal and later oil and gas were and still are the most important energy precursors that make the prosperity of modern societies possible. ^[3] While there is a lot of debate on the global amount of technologically accessible reserves of fossil fuels, there is no doubt about their inherent connection to the release of greenhouse gases upon energetic exploitation. In particular the emission of CO₂ during combustion reactions is a central issue of using fossil energy carriers, see Figure 1.1. ^[4] To regulate the atmospheric concentration of CO₂ and therefore hamper global warming, the Paris Agreement was resolved in 2015. It puts targets of limitation on the CO₂ emissions, politically acknowledging the global importance of the subject. However, to cause a considerable reduction of the CO₂ emissions and meet the targets of the Paris Agreement the change to non-fossil sources of energy is crucial. Such alternative sources are well known in form of nuclear and renewable energy. From an exclusive consideration of the CO₂ emissions of nuclear energy, it may appear to be a suitable substitute for fossil fuels, but the not negligible issues of operational safety and the long-term storage of hazardous radioactive waste strongly speak against a sustainable use of the technology. ^[5] Consequentially, there is widespread agreement that the expansion of renewable energies plays a central role in the efforts to stop climate change. ^[6]

The global carbon cycle

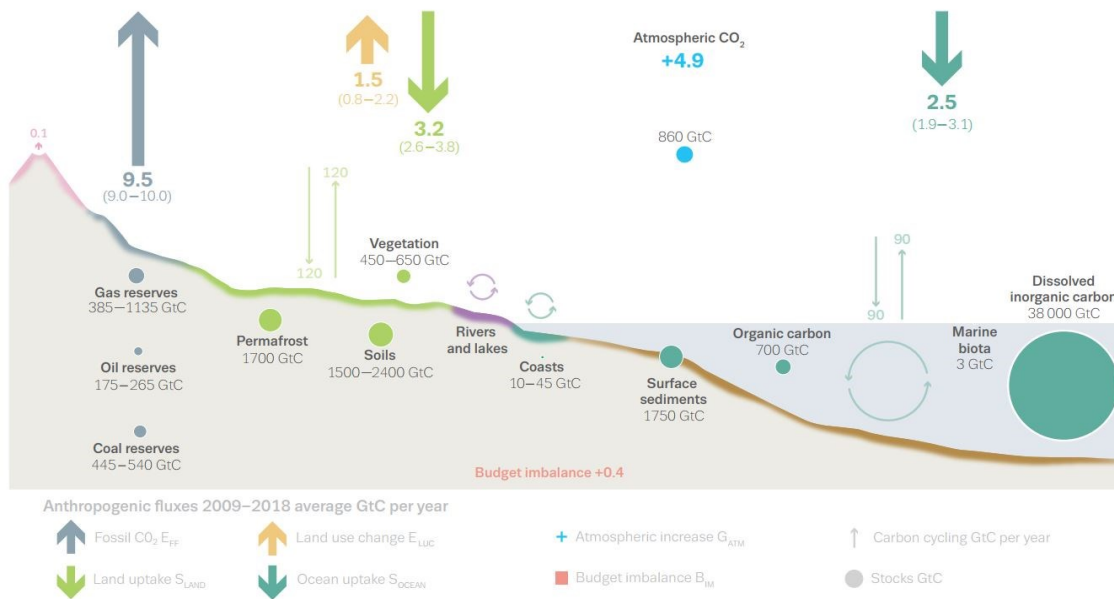


Figure 1.1 Illustration of the overall perturbation of the global carbon cycle caused by anthropogenic activities, averaged globally for the decade 2009–2018. The figure was reproduced from P. Friedlingstein et al., *Earth System Science Data* **2019**, *11*, 1783–1838 (reference ^[4]).

The sources of renewable energies can be divided into five different main groups: Geothermal, hydro, biomass, solar, and wind. A comprehensive supply of energy, which is primarily based on renewable sources presents new challenges for the power grids. Those challenges of using renewable energies arise from the strong dependence of the available power on geographic location, for geothermal and hydro, and time of day or season, for solar and wind. In contrast to the constant and comparably well-controllable power output provided by fossil energy sources, the intermittent nature of solar and wind energy requires the availability of dependable and efficient energy storage systems of suitable capacity to balance power demand and supply. Such a development of storage technologies deals with a variety of different methods based on thermal, mechanical, and chemical means of temporary storage of electrical energy. Currently, the most established technology for large scale storage of electrical energy is provided by pumped storage hydropower. However, while this technology can provide a local solution for the storage of large amounts of electrical energy, its viability depends strongly on geographical conditions, which complicates a considerable expansion. Here, electrochemistry can make a major contribution to a future energy storage solution, as it offers technologies both for short-term, medium-scale energy storage in the form of batteries and for long-term, large-scale energy storage in the form of water electrolysis. ^[7–9]

While the energy sector is commonly one of the main contributors to the emission of CO₂, other economic sectors as transportation, industry, and housing cause also a considerable share. In those sectors, electrical power represents only a small energy source and the greatest demand is met by fossil

energy carriers.^[10] In order to influence these sectors through electrical energy from renewable sources and thus reduce CO₂ emissions, a sector coupling in the form of electrification must first be created.^[11] Such electrification of the private transportation sector is currently being initiated by the implementation of Li ion batteries as the mobile energy storage unit and is supported in Germany by policy makers through financial incentives.^[12] While batteries might be a suitable solution for electrification of the private transportation, the low volumetric and gravimetric energy density of current battery technology makes a similar application for heavy duty transportation, aviation, trucks, and ships unlikely. For those cases, electrolysis offers the possibility of storing electrical energy in a much denser form than batteries, i.e. in small chemical molecules. Water electrolysis in combination with a hydrogen fuel cell poses as an attractive option to use hydrogen as an energy dense intermediate storage molecule for electrical energy. This way, a significant higher range can be achieved in respect to a battery powered system at comparable weight and dimensions.^[8]

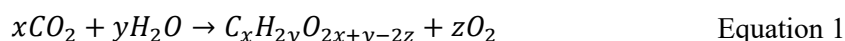
Recently, also other molecules as N₂ and CO₂ have been investigated as reactants during electrolysis. While the electrolytic reduction of N₂ (NRR) and CO₂ (CO₂RR) are still at a state of fundamental research, they promise a sustainable production of fuels and additionally offer an alternative, non-fossil source of commodity chemicals, such as ammonia and ethylene.^[13, 14] One of the attractive aspects of CO₂RR is that an industrial waste product is used as the material precursor for producing value-added chemicals and carbon-based fuels, thus enabling circular processes. While the electrocatalytic CO₂RR is currently lacking in efficiency to meet commercial and economic requirements, it shows the potential to profoundly contribute to a future chemical industry based on sustainable resources being powered by renewable energies.^[15]

In summary, electrolysis can provide the necessary scale and reaction diversity to enable a deeper coupling of the economic sectors such as energy, transportation, and industry. Thus, it is very likely that electrolysis is one technology among others that will shape a future sustainable economy with low greenhouse gas emissions and largely powered by renewable energy.

1.2 The electrocatalytic CO₂ reduction reaction

First reports on the possibility to electrochemically reduce CO₂ date back to the 19th century and primarily involved mercury-based cathodes, which showed production of formate.^[16-19] Despite those early reports, it took some time until further scientific interest in the electrochemical CO₂ reduction reaction (CO₂RR) arose. In the 1980s to 1990s Yoshio Hori and co-workers pioneered the field and performed comprehensive and profound investigations that have significantly contributed to the current understanding of the reaction.^[20-26] Nevertheless, it took roughly another 25 years before the electrocatalytic CO₂RR became the highly investigated reaction of today. This growth in scientific and political interest in the electrocatalytic CO₂RR is largely motivated by the general agreement on building a sustainable economy that is poor in anthropogenic CO₂ emissions and independent from fossil resources. For this objective, the CO₂RR offers a perspective that allows the further utilization of the highly advantageous properties of carbon-based chemicals and fuels without the considerable drawbacks connected to the exploitation of fossil sources. In this context, the idea of recycling CO₂ by its electrochemical conversion into useful compounds is poised to help for future conservation of natural resources by enabling a circular economy.^[15, 27-33]

Formally, the research on electrocatalytic CO₂RR deals with electrochemical reactions that reduce the oxidation state of carbon from its most oxidized form. Here, usually water acts as proton source and is the most common reaction partner during CO₂RR, making the oxygen evolution reaction (OER) the natural counter reaction on the anode. The combination of aqueous CO₂RR with the OER can be generalized according to Equation 1.



The electrocatalytic CO₂RR is a complex reaction that shows a variety of possible products. Although this circumstance represents the great attractiveness of the reaction, it is also one of the major problems. Parallel mechanistic reaction pathways lead to issues of the catalytic CO₂RR selectivity, which is symbolized by the detection of 16 different products on a Cu electrode.^[34] Furthermore, the thermodynamic equilibrium potentials of CO₂RR products are close to the equilibrium potential of water reduction, causing the hydrogen evolution reaction (HER) to be an ever-present side reaction. Additionally, sluggish kinetics, and unfavorable binding-strength of vital reaction intermediates lead to large overpotentials of around 1 V. Finally, Cu often shows a complex temporal evolution of its catalytic selectivity, which favors the HER over time and causes issues of reaction stability. Consequentially, the research on Cu-based CO₂RR faces many challenges and aims to improve activity, selectivity, and stability in order to design efficient systems for CO₂RR.^[14, 35]

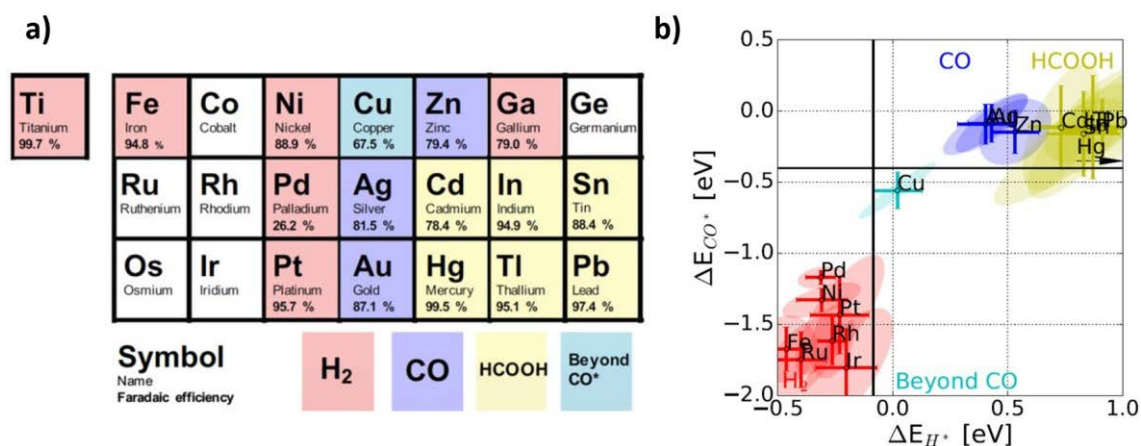


Figure 1.2 (a) Classification of electrode materials according to the major product generated during CO₂RR in 0.1 M KHCO₃. (b) Binding energies for CO* and H* on various electrode materials. Reproduced with permission from *ChemPhysChem* **2017**, 18, 3266-3273 (reference [36]). Copyright 2017 Wiley-VCH Verlag GmbH & Co. KGaA, Weinheim.

In the early studies by Hori and co-workers, the product spectrum was shown to be highly dependent on the type of metal used as electrode material.^[25, 26] Here, the different materials can be grouped according to the main products formed during electrocatalytic CO₂RR: Either 2e⁻ products, such as CO, HCOO⁻, and H₂, or >2e⁻ products, such as hydrocarbons and oxygenates, see Figure 1.2(a). While each group of the 2e⁻ reduction products shows multiple representatives, it is apparent that Cu is the only metal that enables a further reduction and allows the considerable production of hydrocarbons and oxygenates. Later computational work used density functional theory (DFT) calculations to determine binding energies of reactive intermediates on the surface of various metals to explain the origin of the experimentally observed selectivity. Here, too, Cu held a special position and was the only metal with an intermediate binding strength of *H and *CO, see Figure 1.2 (b). It is generally believed that this intermediate binding strength is the origin of the unique ability for the production of hydrocarbons and oxygenates on Cu, which follows the idea of the Sabatier principle for existence of an optimal binding strength of reactants.^[36-38]

Based on this special property of Cu to enable the production of industrial relevant and economically valuable compounds from a beyond 2e⁻ reduction of CO₂, much research has been focused on achieving better control over the catalytic selectivity. Complementary studies were conducted to advance mechanistic insights through experimental and computational work, the special design of nanostructured Cu-based catalysts, and adjustment of reaction environment through careful engineered conditions and geometries of electrochemical cells.^[14] The following sections give an overview over the scientific development in the field of electrocatalytic CO₂RR on Cu catalysts.

1.2.1 Mechanistic insights for Cu-catalyzed CO₂RR

A lot of experimental and computational work has been conducted over the recent years to understand the reaction mechanism during electrochemical CO₂RR on Cu. While some conclusions are generally agreed upon, there is still much debate on the exact reaction pathways.

In the early experimental work by Hori and coworkers it was shown that CO is not only a product, but also a central intermediate of the CO₂RR.^[20, 21, 24] Here, two different binding modes to Cu surfaces were suggested to occur during the early steps of CO₂RR, one being a carbon-down binding of CO₂ that leads to CO formation, while the other is an oxygen-down binding that results in the production of HCOO⁻.^[39] While the HCOO⁻ formation was shown to be an electrochemical dead end and represents a compound, which cannot be further reduced, the formation of CO is believed to be one of the major intermediates during CO₂RR and an important branching point.

Later theoretical work agreed with the early results of Hori and proposed subsequent concerted proton-electron transfer (CPET) reactions during CO₂RR.^[40, 41] Here, the initial reduction steps were suggested to show either a carbon-down orientation of CO₂, denoted as *COOH, or an oxygen-down orientation, denoted as *OCHO. Those two parallel pathways were suggested to lead to the production of CO through the *COOH intermediate, or HCOO⁻ through the *OCHO intermediate. The highly controversial nature of the topic is reflected by other work reporting subsequent proton-electron transfer (SPET) reactions and an initial formation of a radical anion during activation of CO₂, which is protonated in a subsequent step. After the formation of surface-bound *CO, the reaction was suggested to split into two parallel pathways, where one leads towards C₂₊ products, e.g. C₂H₄ and EtOH, and the other towards C₁ compounds, as CH₄ and MeOH. In this context, the different dimerization steps of either two *CO molecules at moderate potentials or a *CO and a *CHO adsorbate at higher overpotential, were reported to be rate-limiting in the formation of C₂₊ products.^[42-48] As this dimerization step is believed to be decoupled from a proton transfer and to be either a purely chemical process or to just involves the transfer of an electron, the production of C₂₊ compounds does not show a dependence on proton concentration. In contrast, the rate-limiting pathway leading to C₁ species is believed to proceed through CPET reactions, thus, depends on proton concentration. The difference in rate-limiting reaction steps was also shown experimentally by a CO₂RR study involving Cu single crystals. Here, the Cu crystals displayed a favored production of C₂H₄ at low proton concentration, whereas CH₄ was preferred at high proton concentration.^[42, 49]

Furthermore, the orientation of the exposed crystal facet has been shown experimentally and theoretically to affect the selectivity of Cu during electrochemical CO₂RR. In this context, Hori and coworkers tested a range of Cu single crystals for CO₂RR and observed a preferred production of C₂H₄ on a Cu(100) facet, whereas a Cu(111) facet showed higher selectivity for CH₄. Further tests on higher index planes, e.g. (210), (310), (211), (311) etc., showed the potential for additional enhancement of

oxygenate and C_2H_4 selectivity.^[50] Later, computational work revealed a stabilization of the $*OCCO$ dimer on a Cu (100) facet due to the favorable formation energy on the squared surface arrangement of Cu atoms.^[42, 46, 51, 52]

1.2.2 Research on Cu-based catalysts for the CO_2RR

Initial Cu-based CO_2RR research largely involved the use of mechanically or electrochemically polished polycrystalline Cu foils as planar electrodes. Inspired by results from Hori and coworkers on the pronounced facet dependency of the product spectrum in CO_2RR , research groups started to investigate (nano-)structured Cu electrodes and shaped Cu nanoparticles to alter the catalytic properties and improve selectivity and activity.^[50]

For Cu foils, physical, thermal, and electrochemical treatments were conducted to vary the material morphology and composition. An early study on electrochemically roughened Cu foils showed an increased selectivity for C_{2+} products and suppression of CH_4 , which raised much scientific attention due to the often high CH_4 to C_2H_4 FE-ratios obtained on polycrystalline Cu foils. The authors attributed the effect to an abundance of undercoordinated sites and referred to previous results on high index facets of Cu single crystals.^[53] Soon after, Kanan and coworkers reported a high catalytic activity of thermally oxidized Cu foils, which were reduced electrochemically prior to CO_2RR and are often referred to as oxide derived Cu foils (OD-Cu).^[54] They showed a strong suppression of the competing HER and high activity for the CO_2RR already at overpotentials as low as $-0.4 V_{RHE}$. The authors suggested that the detailed surface structure of the electrochemically reduced films was the origin of the reported special performance. Later experiments involved the thermal programmed desorption (TPD) of CO and suggested an abundant presence of strong binding sites on OD-Cu foils in comparison to untreated Cu foils.^[55] The authors correlated the surface population of those strong binding sites to the special catalytic properties of OD-Cu during the CO_2RR . Interestingly, the improved selectivity for the CO_2RR due to a prior oxidative treatment was shown to be not exclusive for Cu and has also been shown to impact Ag and Au catalysts in production of CO.^[56-58]

Later, oxidative plasma treatments of Cu foils were reported to largely improve the C_{2+} selectivity and suggested that the concept of OD-catalysts could be extended beyond thermal treatments.^[59] The authors reported a sustained presence of Cu(I) species after the CO_2RR in contradiction to the thermodynamic driving force of the highly reductive potentials to form metallic Cu. This observation started a vivid scientific discussion on the origin of the catalytic properties of OD-Cu. Here, the sustained presence of cationic Cu species, oxides and subsurface oxygen have all been suggested to cause a more favorable binding of reactants and thereby improve C_{2+} selectivity.^[60-64] In a contrary view, other studies reported on the complete reduction of OD-Cu to metallic Cu and that the high C_{2+} selectivity originates in the generally higher electrode surface, which results from the successive oxidation and reduction treatments.^[65-71] An electrode of high surface area was suggested to cause a

local alkalization and a correlated suppression of CH_4 , which in turn leads to a higher C_{2+} selectivity. Such effects of an impaired mass transport within a mesostructured Cu layer were also suggested to be selectivity determining for electrodes of various thicknesses and porosity.^[72, 73] In contrast to the ill-defined morphology of OD-Cu electrodes, the cycling of the electric potential in aqueous solutions of Cu salts in presence of chloride allowed the production of highly defined, cubic Cu_2O structures in the dimension of roughly 100 nm.^[74, 75] Those systems were reported to be selective towards the production of C_2H_4 , which was correlated to an abundance of (100) facets. While such structures were electrochemically deposited on Cu electrodes, they represent an intersection of continuous, foil-derived electrodes and nanoparticles.

Purely nanoparticle-based CO_2RR research has also seen a progressive increase in scientific attention. This is largely motivated by the high degree of morphological control enabled by solution-based chemical procedures and the great versatility in possible fabrication methods of catalyst powders. In here, spherical Cu nanoparticles were reported to display a pronounced size-effect for CO_2RR and showed a decreased hydrocarbon selectivity as well as an increased HER and CO production, when their diameter was successively decreased from 15 to 2 nm. The effect was correlated to an disadvantageous surface arrangement of the Cu atoms for CO_2RR , when the particle size was decreased below 5 nm.^[76] In addition, studies on shaped Cu nanoparticles of below 100 nm showed a pronounced morphological effect for spherical and cubic Cu particles on the observed catalytic selectivity for the CO_2RR . In this context, a favored formation of C_{2+} products on the cubic structures was reported, which is in accordance with previous studies on Cu(100) single crystals. Furthermore, a pronounced size-effect of the cubic Cu particles was suggested, which was proposed to originate in a beneficial ratio of {110} to {100} facets for an edge-length of around 40 nm. In addition, the morphological instability of nanostructured systems was shown to be a general issue during CO_2RR and that major restructuring occurs over relatively short periods of time at potentials that are relevant for C_{2+} product formation.^[77-79]

1.2.3 Influence of the reaction environment on the Cu-catalyzed CO_2RR

Hori and coworkers were the first to report that the CO_2RR selectivity on Cu electrodes is sensitively dependent on the employed reaction media.^[20] They showed an increased production C_{2+} compounds from CO_2RR , when the electrolysis was conducted in a dilute solution of KHCO_3 or solutions of KCl , K_2SO_4 , and KClO_4 . In contrast, the use of higher concentrated KHCO_3 or K_2HPO_4 solutions led to an increased catalytic selectivity for CH_4 .^[80] The effect was rationalized by a local alkalization, which describes a rise in pH near the surface of the electrode. This originates in the interplay of the pH buffering properties of the employed electrolyte and cathodic generation of OH^- during HER and CO_2RR .

Since the pioneering work from Hori on the local alkalization during CO₂RR, much scientific effort was put forth to understand the nature of the impact and magnitude of the local increase in pH for Cu electrodes during electrolysis. Here, a considerable increase of the near electrode surface pH was calculated during CO₂RR in commonly used KHCO₃ electrolyte on planar Cu electrodes based on acid-base equilibria.^[81] In more recent studies, the process of surface alkalization was directly observed in-situ by means of surface-enhanced infrared and Raman spectroscopy, which showed a drastic increase of pH at already moderate cathodic potentials.^[68, 82, 83] The mechanistic origin of the observed shift in catalytic selectivity of Cu during CO₂RR correlated to the local alkalization was explained by differences in the pathways for the production of C₂₊ and C₁ compounds and the resulting distinct pH sensibilities. Generally, the C₂₊ products were suggested to show a pH independent rate limiting step, whereas the rate limiting step for CH₄ involves a proton transfer. Therefore, the production of C₂₊ compounds was suggested to be favored in more alkaline conditions.^[49, 69, 84, 85]

Furthermore, the identity of the alkali metal cations in HCO₃⁻ electrolytes of constant concentration has been reported to influence the CO₂RR selectivity. Here, the FE ratio between C₂H₄ and CH₄ was suggested to increase with increasing cation size and followed the first main group of the periodic table from Li⁺ to Cs⁺.^[86, 87] This observation was rationalized by buffering effects of the cations and according changes in local pH, changes in the outer Helmholtz plane potential by specific adsorption, the stabilization of reactive intermediates, and an increase in interfacial electrical fields.^[88-91] Also, the identity of halide anions have been reported to influence the CO₂RR selectivity and activity. While the presence of halides also led to a considerable morphological restructuring of Cu, it has been suggested that the most prominent effect on the catalytic performance originates from a specific adsorption of the halides. Here, in particular the addition of I⁻ was reported to increase the catalytic activity of Cu during CO₂RR.^[92-95]

1.2.4 Cu-catalyzed CO₂RR at high current densities

Much of CO₂RR research has been conducted in setups that involve quiescent liquid electrolytes that show only minor convection through the gaseous introduction of CO₂ directly to the electrolyte in a certain proximity to the electrode. In such setups, often referred to as H-Cells, the CO₂RR rate is limited by the solubility of CO₂ and a non-convective transport throughout the electrolyte. This constraint in the reactant transport leads to limiting currents for CO₂RR in a range of 10-50 mA cm⁻², which is depending on the detailed setup. In order to approach technologically relevant production rates, currents that clearly exceed 100 mA cm⁻² are required in order to meet the industrial targets of productivity. Here, the CO₂RR research has moved towards the use of gas diffusion electrodes (GDE) and Flow-Cell electrolyzers. Here, the gaseous feed of CO₂ is directly introduced to the porous structure of the GDE allowing a faster reactant transport and higher accessible conversion rates.

Kenis and coworkers pioneered the field of high rate CO₂RR with the use of micro fluid reactors and showed that many of the insights derived from experiments at low currents can be transferred to a regime of much higher currents under employment of Flow-Cell electrolyzers.^[96-99] Here, the spatial separation of the CO₂ feed and the electrolyte by a central positioning of the GDE enabled the use of alkaline electrolytes, which was previously not possible due to the instability of CO₂ in an environment of high pH.

Sargent and coworkers reported a record FE of 70 % for C₂H₄ in highly alkaline conditions of up to 10 M KOH, which they attributed to a combination of a suppressed HER and a kinetically favored CO₂RR due to the high OH⁻ concentration.^[100] They also suggested that the flooding of the catalytic Cu layer with electrolyte can be prevented by a structural design of the GDE and control over its hydrophobicity. This flooding of the catalytic layer and the crystallization of salt within its porous structure are believed to be the most common physical degradation processes, which can impede the supply of CO₂ directed towards the catalytically active sites and can lead to diminishing CO₂RR rates.^[101] Due to the advantageous properties of an alkaline environment for CO₂RR, many studies focused on high-pH systems and employed KOH as a common electrolyte. In accordance with previous results on OD-Cu electrodes for the low current regime, rough Cu surfaces that were prepared by successive oxidation and reduction were shown to enable a high C₂₊ selectivity of 60 to 80 % FE.^[102, 103]

Additionally, shaped Cu nanoparticles were also employed as catalysts in Flow-Cell electrolyzers and the catalytic CO₂RR selectivity was shown to be highly sensitive to the detailed morphology of the particles. In this, spherical and cubic nanoparticles in KOH electrolytes of various concentrations were shown to be strongly influenced by the OH⁻ concentration, which dictated the catalytic selectivity during CO₂RR. Here, the production of CH₄ was generally suppressed, but the selectivity for C₂H₄ and HCOO⁻ was highly sensitive to the OH⁻ concentration.^[104] Interestingly, the use of octahedral Cu nanoparticles was reported to allow a high catalytic selectivity for CH₄ production during CO₂RR in 1 M KOH in accordance with previous work on Cu (111) single crystals. This observation suggests that structural properties of the catalyst are still important to steer the reaction selectivity and are not completely dominated by extremely alkaline conditions during electrolysis.^[105]

Due to the high currents and the underlying cathodic production of OH⁻ during CO₂RR and HER, it is generally assumed that alkalization is very pronounced in Flow-Cell electrolyzers and occurs in many different electrolytes. The associated concentration gradients of CO₂ and OH⁻ near the surface of the electrode are suggested to considerably contribute to the observed catalytic selectivity and can even lead to a complete depletion of CO₂.^[106-110]

1.3 Motivation, goal, and outline of this thesis

Since the pioneering work from Hori and coworkers, who largely established the scientific foundation of today's research in the field of Cu-based electrocatalytic CO₂RR, much work has been put forth to understand and control the determining factors of activity, selectivity, and stability. Especially the selective conversion of CO₂ to multi-carbon products, as ethylene and ethanol, has seen raising interest from academia and industry due to their high economic value and potential use in a circular economy. On this matter, cationic Cu compounds have been repeatedly described as promising catalysts, but a clear understanding of the origin and control over their special performance is still missing. Furthermore, the overwhelming majority of studies investigated the CO₂RR at very low currents far from any technological application, which raises the question to what degree the obtained knowledge can be transferred to industrial electrolyzers that operate at much larger currents.

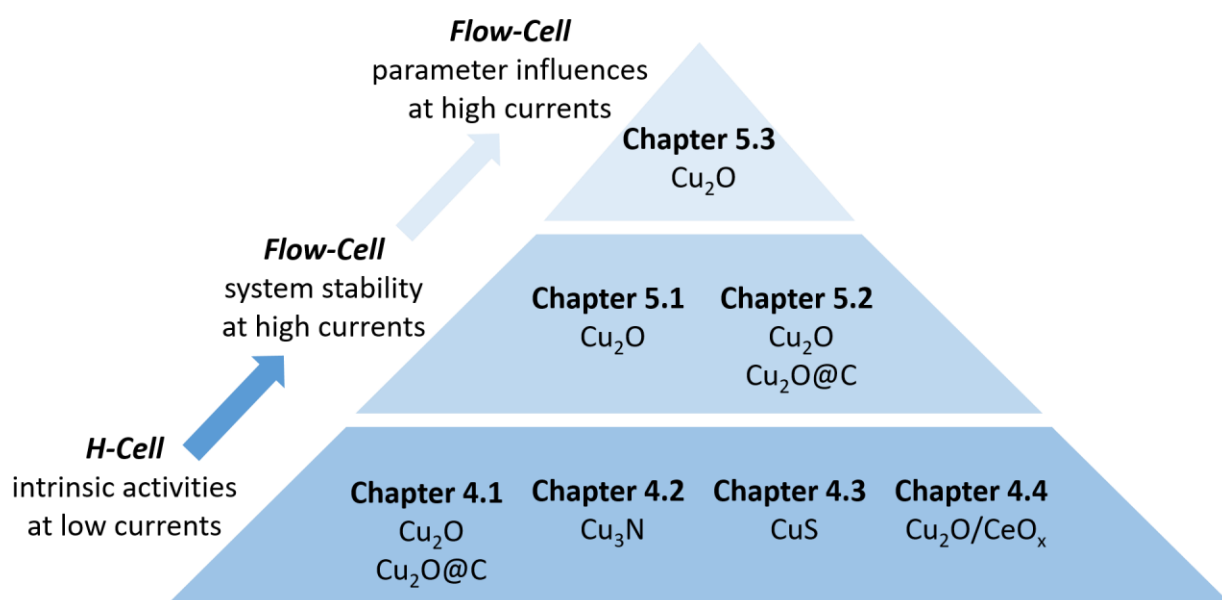


Figure 1.3 Schematic outline of the present work with reference to the different investigated materials and systems within each chapter.

The present work aims at extending the insight in Cu-based CO₂RR derived from cationic Cu compounds by combination of fundamental investigations at low currents and technologically relevant tests at high currents. The electrocatalytic tests are complemented by ex situ, in situ and operando characterization techniques to determine morphological and compositional changes of the materials. Over the course of this work, intrinsic catalytic properties are discussed, as well as the influences of transport phenomena and reaction environments in order to deduce the properties of an efficient Cu-based system for CO₂RR. The present work is separated in two main chapters, which include a discussion of electrochemical investigations at low currents in chapter 4 and investigations at high currents in chapter 5, see Figure 1.3.

CO₂RR investigations at low currents (chapter 4). Chapter 4 deals with the synthesis as well as the physicochemical and the catalytic characterization of cationic Cu compounds that are composed of various anions. The catalytic characterization is exclusively conducted in an H-Cell setup to allow the precise control over the reaction environment and consequently access the intrinsic properties of the investigated materials. To study how the catalytic properties of the cationic Cu compounds change with the identity of the incorporated anion, nanoparticles with crystalline phases of Cu₂O, Cu₃N, and CuS are prepared and investigated for the CO₂RR.

In 4.1 an aqueous approach is used to prepare cubic Cu₂O particles, which are successively introduced to a conductive carbon support. The catalytic properties of the supported and unsupported particles are investigated, as well as their respective change in catalyst structure after CO₂RR electrolysis. By employment of in situ XPS and operando XAS the structural changes of the unsupported catalyst are dynamically observed under reaction conditions and correlated to the catalytic selectivity.

In 4.2 the thermal decomposition of a Cu salt in an organic solvent is explored for the preparation of Cu₃N nanoparticles. The effect of the reaction temperature on nanoparticle morphology and composition is investigated as well as the catalytic selectivity during CO₂RR.

In 4.3 an anion exchange of O²⁻ by S²⁻ is explored to prepare CuS nanoparticles through exposure of Cu₂O nanocubes to aqueous solutions of (NH₄)₂S. The effect of the employed (NH₄)₂S concentration on the CuS particle morphology is investigated by electron microscopy. By use of GI-XRD, the phase transition of CuS, due to applications of reductive potentials, is traced ex situ. Finally, correlations between particle morphology, particle composition, and catalytic CO₂RR selectivity are deduced.

In 4.4, based on the promising results of subchapter 4.1, the investigations on cubic Cu₂O are extended to a bimetallic system of CeO_x and Cu₂O. Here, the effect of employing different CeCl₃/CuCl₂ ratios during particle synthesis is investigated, which is shown to strongly affect the particle structure and the catalytic selectivity during electrochemical CO₂RR.

CO₂RR investigations at high currents (chapter 5). Chapter 5 investigates the CO₂RR at high current densities of -50 to -700 mA cm⁻² in a Flow-Cell electrolyzer to develop a general understanding for the most prominent factors during CO₂RR for Cu-based catalyst at high reaction rates. Different scales of the electrolysis system are studied to evaluate the compositional integrity of the electrolyte, the influence of interfacial concentration gradients and structural changes of the catalysts. For this purpose, the nanocubic Cu₂O catalyst is chosen as model system due to the promising catalytic selectivity observed during H-Cell testing in chapter 4.

In 5.1 correlations of membrane identity and compositional electrolyte stability are deduced during CO₂RR at high currents. In this matter, the bulk pH and flow of CO₂ are monitored as proxies to evaluate the macroscopic changes that occur in the system as a function of time and current density.

In 5.2 the temporal changes in particle morphology are investigated at high currents for the carbon-supported and unsupported Cu₂O nanocubic catalyst during prolonged electrolysis. A correlation between the distinct morphological evolution of the supported catalyst to the observed selectivity during CO₂RR is deduced.

In 5.3 correlations between the structure of the gas diffusion electrode and the selectivity during high-rate CO₂RR are investigated. Variations in binder content, particle loading and KHCO₃ concentration are probed as determinants for the catalytic selectivity at high currents. Based on the results, relations between the electrode structure, the establishment of concentration gradients and the CO₂RR selectivity are proposed.

In summary, the present work aims to advance the understanding of determinants for the catalytic selectivity on cationic Cu compounds during electrochemical CO₂RR. The findings of this work range from a fundamental to a technologically relevant level and will contribute to the future development of efficient systems for the electrocatalytic CO₂RR.

2 Theoretical and scientific background

Electrocatalysis poses as an intersection between the fields of electrochemistry and heterogeneous catalysis. The inherent heterogeneous nature of the charge transport across an electrode to electrolyte interface during electrocatalysis shares many similarities with catalytic reactions in thermal processes and allows for a quite analogous discussion. In the following chapter, the scientific foundations of electrocatalysis is discussed with special focus on applications in energy storage. Here, a descriptive model of charged electrochemical interfaces, general thermodynamic and kinetic considerations for electrochemical reactions and the efficiency losses in electrochemical systems are presented.

2.1 General considerations of electrochemistry

The following discussion on the theoretical background and general considerations of electrochemistry is largely based on textbooks by Frano Barbir, Ryan O'Hayre, Patrick Moseley and Jens Nørskov. ^[11-117]

2.1.1 The electrochemical double layer

Electrochemistry considers chemical reactions at interphases that involve the transfer of charge in form of ionic and electronic species. Such an electrochemical interphase between an electrode and the surrounding electrolyte shows a characteristic structure, referred to as the electrochemical double-layer, and has been the centre of various descriptive models. Figure 2.1 shows the schematic representation of the electrochemical double layer according to the descriptive model of Bockris, Müller and Devanathan from 1963. ^[118] The submersion of a negatively charged electrode leads to the coulombic attraction of oppositely charged cations, as well as an interaction to the electric momentum of the solvent molecules. This results in the formation of a characteristically layered structure orthogonal to the charged surface of the electrode. The inner most layer, referred to as the Helmholtz layer, is separated into the inner Helmholtz plane (IHP), which is directly adjacent to the electrode surface and the outer Helmholtz plane (OHP) that is neighbouring the IHP. The IHP is composed of immobilized solvent molecules oriented to the electrical field, as well as specifically adsorbed ions. The term "specific" adsorption refers to the chemical binding of species, which show an interaction of covalent nature to the surface of the electrode. While this interaction is not driven by the electrical bias of the system, it is related to the chemical properties of the electrode surface and adsorbed ions, as well as their hydration energy. In the process of specific adsorption, the ions lose their complete or part of their hydration shell to directly interact with the surface of the electrode. In contrast, the OHP is composed of ions of opposite charge in respect to the electrode surface that possess their full hydration shell. Those ions are immobilized by the coulomb interaction with the electrode and approach the surface of the electrode as close as the thickness of their hydration shell. This rigid formation of the charged electrode surface and the opposing ions of the OHP, which are separated by a defined thickness

of solvent layer that is acting as dielectric can be described by a plate capacitor, which was reported for the first time by Helmholtz in the 19th century. ^[119] The Helmholtz layer is followed by the diffuse Gouy-Chapman-layer. This layer is characterized by a competition of electrostatic attraction to the electrode surface and the thermal energy of the ions resulting in a more mobile and diffuse distribution in contrast to the rigid structure of the Helmholtz layer. The structural combination of the molecular plate capacitor characterized by Helmholtz to the diffuse layer according to Gouy and Chapman, was firstly described by Otto Stern. ^[120]

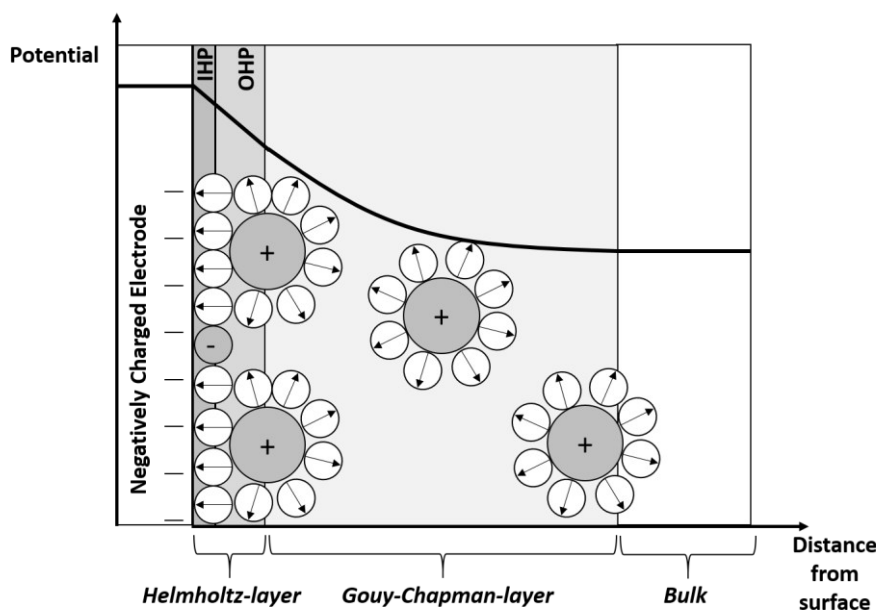


Figure 2.1 Schematic representation of the molecular arrangement within the electrochemical double layer according to the model of Bockris, Devanathan and Müller. ^[118] A simplified correlation of the change in potential with distance orthogonal to the electrode surface is also given.

Because of the similarities of the Helmholtz layer to a plate capacitor, the change in potential between surface of the electrode and OHP can be described by a linear regression under an assumption of a constant capacitance. Further increase of distance throughout the Gouy-Chapman-layer results in an exponential decrease of the potential until the bulk electrolyte is reached and a constant value is achieved. The reason for this exponential relation is given by the Poisson-Boltzmann equation, which is considering the interplay of the thermal movement of ions and the electrostatic effects of the field.

Electrochemical reactions, which involve the transfer of charged species across the electrochemical interface are sensitive to the interfacial electric field at the electrode and can be driven by it. As the Helmholtz layer can be described as a plate capacitor separated by a dielectric of molecular thickness, the potential difference across this interface results in an electric field of a magnitude strong enough to enable reactions, including the formation and breaking of chemical bonds. Such reactions are referred to inner-sphere reactions and occur in the IHP of the Helmholtz layer. Additionally, there are reactions involving only the transfer of electrons and a corresponding rearrangement of solvent molecules. Such

reactions are referred to outer-sphere reactions and proceed in the OHP of the Helmholtz layer. The vast majority of electrochemical reactions are inner-sphere reactions, which also have a higher practical relevance due to their intrinsic connection to chemical conversions.

2.1.2 Thermodynamics of electrochemistry

The fundamentals of electrochemistry can be separated into a discussion of kinetic and thermodynamic considerations for chemical redox reactions. Thermodynamics is a scientific field that deals with the transformation of energy within a defined system and the associated possibility to perform work. Hence, the field of electrochemical energy conversion is intrinsically linked to thermodynamics. In this matter, the consideration of a simple one-step electrochemical reaction from species A^+ to B helps to define some basic relations. In the considered case, species A^+ is reduced electrochemically to B by the transfer of one electron. This reaction can be inverted freely and is therefore considered to be reversible. Figure 2.2 shows a schematic energy diagram for the considered reversible reaction. Due to a difference in the internal energy of species A^+ and B the reduction is associated with a change in the energetic state and requires the transfer of energy. At constant pressure, the change in internal energy of a chemical redox system corresponds to the amount of heat transferred during the reaction and is denoted as the change in enthalpy (ΔH). For the reduction of A^+ to B this process is energetically uphill and shows a positive change in enthalpy and heat uptake, which is referred to as an endothermic process. Accordingly, the reversed oxidation reaction from B to A^+ shows a decrease in enthalpy and the release of heat, which makes the process exothermic.

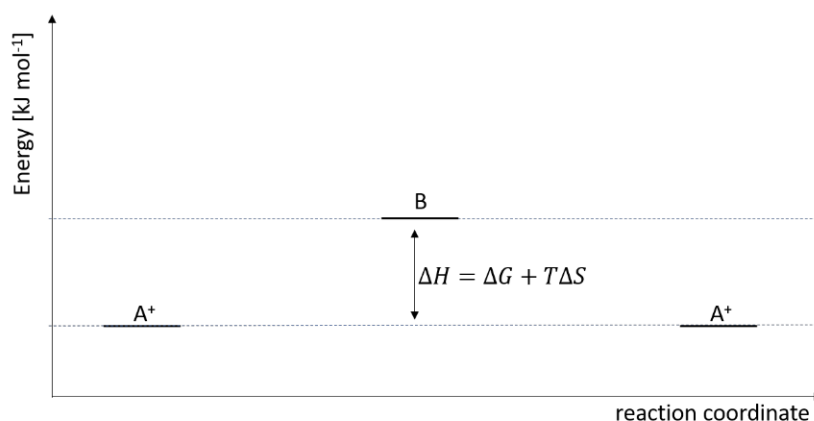


Figure 2.2 Reaction coordinate diagram depicting the change in enthalpy during a reversible reduction.

In addition to the change in enthalpy, chemical reactions also involve a change in entropy (ΔS). Entropy is a statistic measure for possible microstates of a system. According to the second law of thermodynamics, reactions within a closed system will always lead to an increase in the total entropy. Hence, the closed system will approach a state of maximum entropy. Entropy, therefore, defines a direction of spontaneous processes within a closed system. In order to evaluate if a process will occur spontaneously or requires the input of work in order to drive it, the changes in enthalpy and entropy

are combined in the Gibbs-Helmholtz equations, see Equation 2. The Gibbs-Helmholtz equation describes the maximum amount of reversible work that can be obtained from a thermodynamic system. Based on this relation, the associated Gibbs free energy of reaction (ΔG) allows a classification between spontaneous, exergonic ($\Delta G < 0$) and non-spontaneous, endergonic ($\Delta G > 0$) reactions. Under the consideration that the focus of electrochemical energy conversion lies in the storage and usage of chemical energy, the Gibbs free energy represents a central metric for the field. In this context, endergonic reactions enable the conversion of electrical energy into chemical energy and exergonic reactions can provide electrical energy using chemical energy. These cases are referred to as electrolytic and galvanic reactions, respectively.

$$\Delta G = \Delta H - T\Delta S \quad \text{Equation 2}$$

This relationship between the theoretical electrical work and the reversible thermodynamic work shows a fundamental connection between the electrochemical standard potential (E^0) of a given redox couple and the change in standard Gibbs free energy of the associated reaction. (Equation 3). Standard conditions refer to an absolute temperature of 295.15 K, an atmospheric pressure of 1 bar and an activity of the reactant of 1 mol L⁻¹ in solution. Here, F denotes the Faraday constant of 96485 C mol⁻¹ and n is the number of transferred electrons according to the stoichiometry of the considered chemical reaction.

$$\Delta G^0 = -nFE^0 \quad \text{Equation 3}$$

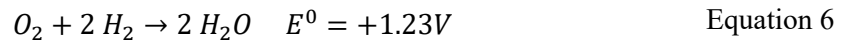
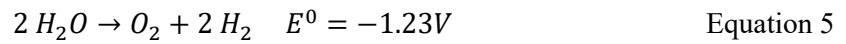
Based on this relation, for every theoretical reaction a corresponding standard potential can be assigned. It is important to note that the standard potential is referring to a state of dynamic equilibrium for a reversible reaction. It only holds true under standard conditions at constant temperature and pressure and at the absence of any net flow of current. The specification of reactant activity for standard conditions, as mentioned above, is important due to the dependence of the thermodynamic potentials on the activity of species participating in the reaction. This deviation of the potential (E) from the electrochemical standard potential as a function of reactant activity is given by the Nernst equation, see Equation 4.

$$E = E^0 + \frac{RT}{zF} \ln \frac{\prod a_{ox}^{n_{ox}}}{\prod a_{red}^{n_{red}}} \quad \text{Equation 4}$$

Theoretical background

In Equation 4, $a_{ox}^{n_{ox}}$ and $a_{red}^{n_{red}}$ refer to the activity of the oxidized and reduced form of the reactant in solution, z is the stoichiometric number of transferred electrons during the reaction, R is the ideal gas constant and T denotes the absolute temperature.

Further explanation of thermodynamic relations will consider the reactions of water electrolysis (Equation 5) and the hydrogen fuel cell (Equation 6) due to their overall importance in the field of electrochemistry. As both reactions are discussing the same process but consider different directions, the corresponding reversible standard potentials are identical in value but differ in algebraic signs.



It is not possible to measure an absolute electrode potential, which is why all values need to be referenced against a defined system. The thermodynamic standard potential of the H^+/H_2 redox couple is used as such a reference point and was deliberately set to be 0 V (at $T = 298,15 \text{ K}$, $a_{H^+} = 1$, $p_{H_2} = 1 \text{ bar}$). In doing so, it is possible to arrange all other thermodynamic reduction and oxidation potentials in a galvanic series, relative to the H^+/H_2 redox couple. This so-called standard hydrogen electrode (SHE) is practically realized by a Pt electrode submerged in a 1 M solution of a strong acid, which is assumed to show a proton activity of unity. Additionally, a hydrogen atmosphere of 1 bar is set by direct introduction of hydrogen gas to the acidic solution at atmospheric pressure. As the SHE is only valid at $pH=0$, it does not allow any changes in pH . For a practical pH -dependent reference system, the reversible hydrogen electrode (RHE) was introduced, which accounts for shifts in pH values based on the Nernstian relation, see Equation 7.

$$E_{RHE} = E_{SHE} - 0.059 \text{ V} * pH \quad \text{Equation 7}$$

The reversible standard potentials can be described either as a minimum requirement of electrical work to drive an electrolytic reaction, or as the maximum amount of electrical work that can be generated by a galvanic reaction. Such a description is, however, exclusively focused on the reversible thermodynamic work of an electrochemical system, which is associated to the change in Gibbs free energy and understate the practical importance of the involved change in entropy. The absolute change in the internal energy of a system, as stated earlier, is given by the change in enthalpy during the process. The difference between the change in energy and change in Gibbs free energy is given by the entropic contribution $T\Delta S$. This change in entropy during a reaction leads to a transfer of heat as a constant byproduct of electrochemical processes. In this, the Gibbs free energy and the associated

standard potentials show a dependence on temperature, according to the change in entropy at constant pressure (Equation 8).

$$\left(\frac{\delta G}{\delta T}\right)_p = -\Delta S \quad \text{Equation 8}$$

The nature of that entropy change has important practical implications for the transport of heat during the considered reaction. For instance, the hydrogen fuel cell reaction is always an exothermic process, whereas the electrolysis of water can be either endo- or exothermic, depending on the applied cell voltage and reaction temperature. This is visualized in Figure 2.3, which shows how the enthalpy, Gibbs free energy and the corresponding cell potentials are changing with temperature in the $\text{H}_2/\text{H}_2\text{O}$ redox system. The sudden decrease in enthalpy at a temperature of above 373 K is due to the phase change of water. This phase transition reduces the enthalpy according to the latent heat of evaporation of water. At standard conditions, the electrolysis of water needs a total energy input of $285.8 \text{ kJ mol}^{-1}$, which is often referred to as the “higher heating value” (HHV) and corresponds to a cell potential of 1.48 V. However, only $237.2 \text{ kJ mol}^{-1}$ of the total amount are necessary to be supplied as electrical energy, which correlates to the reversible cell potential of 1.23V. The difference between the two is exactly the contribution of the entropy and can be supplied to the system in the form of heat. If a potential equal to the HHV is applied to the system, there is no net exchange of heat with the surroundings and the potential is referred to as the thermoneutral potential. Those considerations are not exclusive for the $\text{H}_2/\text{H}_2\text{O}$ redox system and apply to every electrochemical conversion in the same manner.

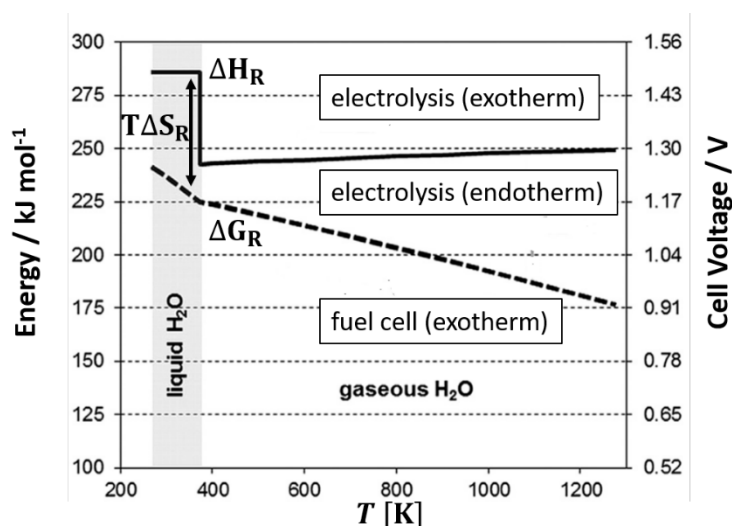


Figure 2.3 Temperature dependence of the free enthalpy, enthalpy, and their corresponding cell voltages of the $\text{H}_2/\text{H}_2\text{O}$ redox couple. Reprinted and adapted from *Electrochemical Energy Storage for Renewable Sources and Grid Balancing*, T. Smolinka, E. T. Ojong, J. Garche, *Hydrogen Production from Renewable Energies – Electrolyzer Technologies*, 106, 2015, with permission from Elsevier. ^[117]

The comparison of the potential of operation during an electrochemical reaction (E_{op}) to the change in enthalpy and Gibbs free energy during the reaction (see Equation 9 to Equation 12) allows a classification based on the total net exchange of heat.

$$\Delta G < zFE_{op} < \Delta H, \text{endothermic electrolysis} \quad \text{Equation 9}$$

$$\Delta G < \Delta H < zFE_{op}, \text{exothermic electrolysis} \quad \text{Equation 10}$$

$$zFE_{op} < \Delta G < \Delta H, \text{exothermic galvanic} \quad \text{Equation 11}$$

$$\Delta H < zFE_{op} < \Delta G, \text{endothermic galvanic} \quad \text{Equation 12}$$

2.1.3 Kinetics of electrochemistry

The previous discussion of the thermodynamic fundamentals of electrochemical redox reactions was focused on the difference in the energetic state between reactants and products. However, the thermodynamic properties of a chemical reaction do not determine the reaction rate, which is discussed as reaction kinetics. Those kinetics are not directly connected to the energy changes between two reaction states, but are determined by the energetic barrier of the transition. Such kinetic barriers are schematically depicted in Figure 2.4 and represent an activation energy (E_a), which is required to accelerate the respective reaction. The value of the activation energy is exactly the difference between the energetic state of the reactant and the energy of the reactive state at the top of the corresponding activation barrier. In Figure 2.4 it is also apparent that the forward ($E_a, A \rightarrow B$) and backward ($E_a, B \rightarrow A$) reactions differ in terms of activation energy and therefore show different reaction rates. The general concept of an activation energy was defined by Arrhenius in the 19th century, where he described an empirical correlation between the reaction temperature and the rate of a chemical reaction. ^[121]

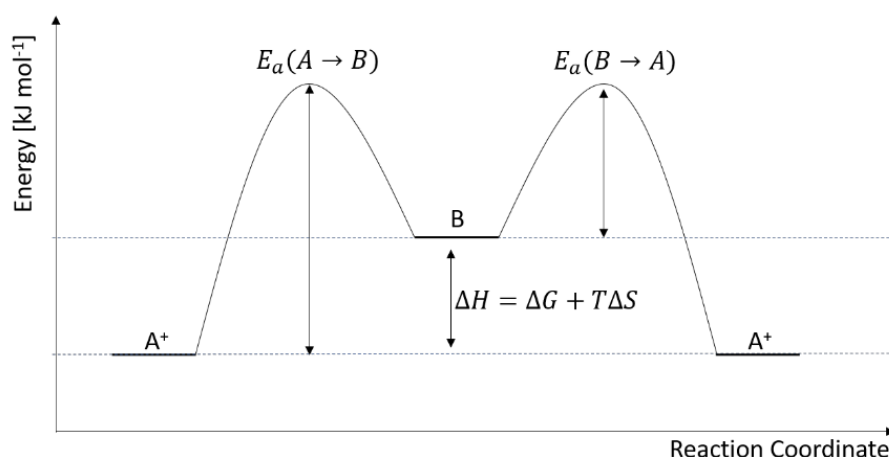


Figure 2.4 Reaction coordinate diagram depicting the change in enthalpy and activation energy during a reversible reduction.

This fundamental relation is given in Equation 13 and shows an exponential increase of the reaction rate constant (k) with a decrease in activation energy (E_a) and increase of reaction temperature (T). The preexponential factor (A) was later correlated to a collision frequency of the elementary reaction. The corresponding “collision theory” was developed by Lewis and Trautz in the 20th century and postulated a distribution of reactive collisions of idealized hard spheres, caused by their movement due to the thermal energy. ^[122] Despite the empirical nature of the Arrhenius equation, it still finds widespread application ranging from the description of reaction kinetics to various other fields, such as the determination of diffusion and adsorption barriers.

$$k = A * e^{-\frac{E_a}{RT}} \quad \text{Equation 13}$$

In a more molecular approach for discussion of reaction kinetics, the transition state theory has been developed almost simultaneously by Eyring, Evans and Polanyi. ^[123] Here, the idea of the formation of an activated complex, or transition state, is understood as the origin of activation energies. This activated complex is in quasi equilibrium with the reactants and a corresponding standard Gibbs free energy of activation (ΔG_0^\ddagger) can be assigned to it. Based on the Bell-Evans-Polanyi principle, the Gibbs free energy of activation is proportional to the Gibbs free energy of the reaction. This principle bridges thermodynamic and kinetic properties of a chemical reaction. The associated Polanyi-Hammond postulate extends the idea towards a consideration of structural properties and suggests that for exothermic reactions the transition state is structurally more similar to the reactants than the products, whereas endothermic reactions show the opposed relation. Those concepts manifests in a lower kinetic barrier for (strongly) exothermic reactions compared to (strongly) endothermic reactions, which is depicted in Figure 2.4. Those considerations pose as an important relation because they allow to make statements about the kinetic properties and rates of chemical reactions based on thermodynamic values.

Theoretical background

Electrochemistry is herein special, as kinetic and thermodynamic values are directly accessible in form of current and electrode potential, respectively. The correlation between overpotential ($E - E^0$), which is the difference of the actual electrode potential to the thermodynamic equilibrium potential, and the reaction rate in form of electric current has been described empirically in the Tafel equation, see Equation 14. Here, the value a is an electrode material specific measure for the deviation from thermodynamic equilibrium potential at a current density (j) of unity. Minimizing this intrinsic value by choice and design of electrode material is part of research in electrocatalysis. Catalysts are materials that allow the acceleration of reactions by offering alternative mechanistic pathways with favorable binding of reactants, which reduces the kinetic barrier of the overall reaction.

$$(E - E^0) = a + b \log j \quad \text{Equation 14}$$

The slope of the linear relation between overpotential and current density is given by the parameter b , which provides insight into the mechanism of the rate limiting step for the electrochemical reaction. A widespread approach to explain the Tafel equation by a thermodynamic and kinetic foundation is found in the Butler-Volmer approximation. Here, an electrochemical reaction involving the transfer of one electron, which proceeds through an outer-sphere mechanism is discussed. The reaction is assumed to occur through an activated transition state, hence can be described by an Arrhenius type relation and allows an assignment of a free Gibbs energy of activation to the transition state. Following the Bell-Evans-Polanyi principle, the free Gibbs energy of activation depends on the free Gibbs energy of reaction, which is accessible in electrochemistry by variation of the electrode potential. The effect of changes in electrode potential on reaction kinetics according to the Butler-Volmer approximation is depicted in Figure 2.5.

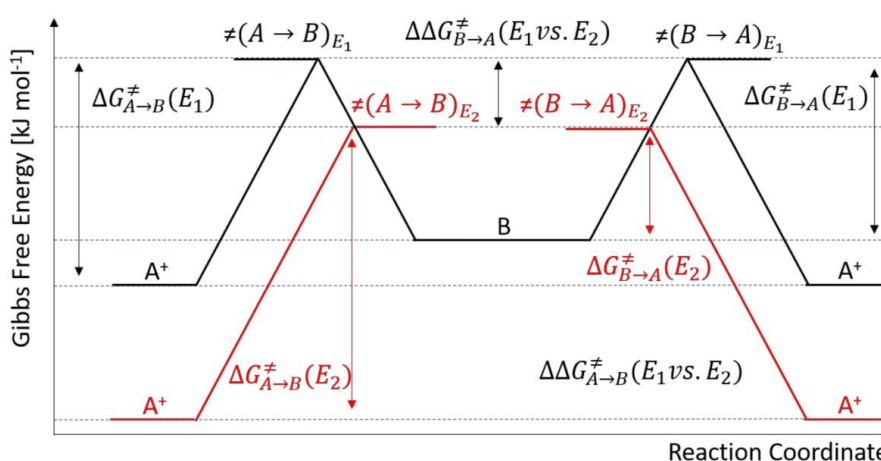


Figure 2.5 Reaction coordinate diagram showing the effect of a change in electrode potential on the kinetic barriers of a reversible electrochemical reduction.

In this context, the application of a more oxidative potential (E_2), in respect to the starting point (E_1), alters the Fermi level of the metal electrode and shows a direct influence on the relative Gibbs free energy of the charged reactant (A^+). In the depicted example of a reversible reduction of species A^+ , this change leads to a more endergonic process and a corresponding increase in Gibbs free energy of activation ($\Delta G_{A \rightarrow B}^\ddagger(E_2) > \Delta G_{A \rightarrow B}^\ddagger(E_1)$). At the same time, the reversed process or oxidation of species B shows a more exergonic value and decrease in Gibbs free energy of activation ($\Delta G_{B \rightarrow A}^\ddagger(E_2) < \Delta G_{B \rightarrow A}^\ddagger(E_1)$). Effectively, the application of an oxidative potential results in a reduced kinetic barrier and accelerated rate for the oxidation, whereas the kinetic barrier for the opposed reduction is increased. This relation between changes in electrode potential and respective acceleration as well as deceleration of the rates for the reduction and oxidation reaction are described by the general Butler-Volmer equation, see Equation 15.

$$j = j_0 \left\{ \exp \left[\frac{\alpha n F}{RT} (E - E^0) \right] - \exp \left[- \frac{(1 - \alpha) n F}{RT} (E - E^0) \right] \right\} \quad \text{Equation 15}$$

Analogously to the Tafel equation, the general Butler-Volmer equation also describes an exponential relation between the applied overpotential ($E - E^0$) and current density. However, the Bulter-Volmer approximation considers both an anodic and cathodic contribution (first and second exponential term, respectively) to the overall net current of the reversible electrochemical reaction. The parameter α is referred to as transfer coefficient derived from geometric considerations of the energetic barrier. The common assumption of $\alpha = 0.5$ represents a case of a fully symmetric intersection, which is shown in Figure 2.5. The preexponential factor (j_0) is referred to as the exchange current density. This is an intrinsic value specific for every reaction and electrode material, which is directly associated to the parameter “a” of the Tafel equation (Equation 14). It describes a current density at standard conditions, absence of any overpotential and in complete thermodynamic equilibrium. This correlates to identical contributions of anodic and cathodic currents to the reversible reaction that fully cancel each other out and result in a net current of zero. The exchange current density is also directly proportional to the standard equilibrium rate constant (k_0) and concentration of the reactant (c), as shown in Equation 16.

$$j_0 = n F k_0 c \quad \text{Equation 16}$$

Based on the transition state theory that has been discussed earlier, the rate constant is proportional to the free Gibbs enthalpy of activation. This relation is given in the Eyring equation, see Equation 17, where κ is the transmission coefficient, k_B is Boltzmann’s constant and h is Planck’s constant.

$$k_0 = \kappa * \frac{k_B T}{h} \exp\left(-\frac{\Delta G_0^\ddagger}{RT}\right) \quad \text{Equation 17}$$

This equation points out the inherent correlation between reaction kinetics and thermodynamics, as stated in the Bell-Evans-Polanyi principle, which is the theoretical foundation of the Butler-Volmer approximation.

While the Butler-Volmer approximation is a concept that finds widespread application throughout the description of electrode kinetics, one must keep in mind the limitations of the relation. For example, the simplification of a linear change in free Gibbs energy and a constant transfer coefficient has no molecular explanation. Here, the more sophisticated Marcus-Hush approach considers the transfer coefficient to be potential-dependent and incorporates the energy associated with the reorganization of solvent molecules. Furthermore, both the Butler-Volmer as well as the Marcus-Hush formalism are discussing an outer-sphere mechanism, which only applies to very few electrochemical processes. Most reactions are inner-sphere mechanism and involve the rearrangement of chemical bonds. Such electrochemical reactions are of particular interest for technological applications in the field of electrocatalysis for storage of electrical energy in small chemical molecules.

2.1.4 Efficiency of electrochemical reactions

When applying electrocatalysis as a technology for energy storage, one needs to consider the efficiency of such processes. The theoretical efficiency of an electrochemical device, e.g. electrolyzer or fuel cell, can be determined by the simple comparison of input energy in either chemical (galvanic reaction) or electrical (electrolytic reaction) form to the produced electrical (galvanic reaction) or produced chemical energy (electrolytic reaction). As discussed in the earlier section on the thermodynamic fundamentals of electrochemistry, the input or output electrical energy of an electrochemical reaction is determined by the Gibbs free energy of the reaction, whereas the change in chemical energy corresponds to the reaction enthalpy. The ratio of the two returns the thermodynamic maximum efficiency of the reaction, in which the denominator represents the energy input and the numerator the energy output. The consideration of the higher heating value (HHV) of hydrogen returns a maximum efficiency of 120 % in the case of water electrolysis and 83% for the reversed process, the hydrogen fuel cell reaction. This relation is shown for the case of water electrolysis in Equation 18. The respective offset to 100 % is caused by the exchange of heat with the environment due to the reaction entropy. This example illustrates the importance for careful consideration of the heat exchange during electrochemical reactions for calculation of thermodynamic efficiencies. In this context, the given thermodynamic efficiency of 120 % of water electrolysis would require a constant supply of free heat from the environment, which is highly unlikely under practical conditions. A more reasonable calculation of efficiency includes the entropic heat demand within the electrical energy input and

considers the stored energy to be equal to the maximum accessible work, which is the Gibbs free energy. Such an assumption reduces the maximum thermodynamic efficiency for water electrolysis to the commonly discussed value of 83 %.

$$\eta_{max} (Water\ Electrolysis) = \frac{Energy\ output}{Energy\ input} = \frac{\Delta H_{HHV}}{\Delta G} \quad \text{Equation 18}$$

This value is the maximum efficiency at which a water electrolyzer could operate from an exclusively thermodynamic point of view. However, during the actual operation many more potential losses occur due to reaction kinetics (E_{act}), mass transport (E_{conc}), charge transport (E_{Ohm}) and from reaction selectivity (FE_i). In technological devices, all phenomena show an inherent energetic demand and contribute to the overall efficiency of the system. Such merit of efficiency is referred to as the energy efficiency (η_{EE}), see Equation 19.

$$\eta_{EE} = \frac{E^0}{E^0 + E_{conc} + E_{Ohm} + E_{act}} * FE_i = \frac{E^0}{E_{op}} * FE_i \quad \text{Equation 19}$$

The energy efficiency describes the percentage agreement of the thermodynamic standard potential (E^0) and the potential of operation (E_{op}) that is composed of all voltage losses plus the thermodynamic standard potential under consideration of the reaction selectivity. An evaluation of a complete electrochemical system would require the additional consideration of auxiliary devices, e.g. pumps and compressors, which goes beyond the scope of this work. Here, the focus is put on losses associated to an electrochemical cell, which will be discussed in the following.

Selectivity induced voltage losses. In complex reactions, parallel reaction pathways and side reactions can lead to issues of selectivity. This formation of undesired products can be directly associated with an additional energetic demand and, therefore, decrease of efficiency for the target reaction. A measure of such selectivity is the dimensionless faradaic efficiency (FE), which is show in Equation 20. It describes the ratio of current that is used for an electrochemical reaction towards a target product denoted as i (j_i) in respect to the total electrochemical current of the whole system (j_{total}).

$$FE_i = \frac{j_i}{j_{total}} \quad \text{Equation 20}$$

Transport induced voltage losses. In an electrochemical system there is a constant balance between the electrical current, the interfacial transport of reactive species and their successive chemical conversion in accordance with Faraday's first law. The resistance of the underlying transport

phenomena has a considerable impact on the efficiency of the electrochemical system. A classification between transport of charged and uncharged species is common to discuss specific causes and possible mitigation strategies of corresponding voltage losses.

Transport of uncharged species. The transport of uncharged species is often referred to by the general designation mass transport. In case of a dissolved reactant, the electrode acts as a sink for the reactant, whereas the bulk electrolyte represents the well. In order to run an electrochemical conversion, the reactants need to be transported from the bulk towards the reactive sites of the electrode surface. While the transport in bulk can be driven by convection, the static electrolyte layer in vicinity of the electrode surface is limited to a strictly diffusive transport. This diffusion layer poses as a bottleneck in the transport of reactants towards the active electrode and results in concentration gradients perpendicular to its surface. In a case, where the reaction rate is fast and the diffusion layer relatively thick, the initial consumption of reactant might be higher than the diffusive transport of it towards the surface. Here, the effective concentration of reactant approaches zero and the corresponding current of the reaction becomes constant. This situation is referred to as the limiting current density, shown in Equation 21. In this relation, j_L denotes the limiting current density, D is the diffusion coefficient of the reactant in solution, δ is the thickness of the diffusion layer and c_B is the bulk concentration of the reactant. For a given reaction, the value of the limiting current density is highly dependent on the electrochemical system. For example, the thickness of the diffusive boundary layer is sensitive to the movement of the bulk solution in a way that a quiescent state results in a thicker diffusive layer in comparison to a system with strong liquid convection and therefore thinner diffusive layer.

$$j_L = \frac{nFDc_B}{\delta} \quad \text{Equation 21}$$

This relation finds widespread scientific application as rotating disc electrodes, developed by Benjamin Levich, to adjust the mass transport towards the flat surface of an electrode to study kinetic properties of an electrochemical reaction. Also, technological applications of electrocatalytic reactions are often subjected to mass transport issues, caused by the high currents necessary to meet demands of industrial productivity. Here, the more complex geometry of the porous catalytic layer cannot be as easily described as in the simplified case covered by Levich.^[124] The effect of mass transport limitations on the thermodynamic potential of the half-cell reaction can be rationalized by the Nernstian relation. In accordance with this relation, Equation 22 shows the voltage penalty associated to the mass transport (E_{conc}), which is directly proportional to the activity gradient from the bulk electrolyte (a_B) to the electrode surface (a_S). The relation also shows that the approach of a near-zero surface concentration of reactant results in an exponential increase in the thermodynamic potential, which is effectively inhibiting a further increase in reaction rate.

$$E_{conc} = \frac{RT}{nF} \ln \frac{a_B}{a_S} \quad \text{Equation 22}$$

Furthermore, the activation potential shows a sensitivity to the effect of mass transport, which adds to the effect of the Nernstian voltage loss. This dependence was discussed earlier in the subchapter on kinetics of electrochemistry. In the interest of simplification, the exact relation will not be mentioned here, but it is following the qualitative trend of the Nernstian shift. The intrigued reader is referred to the textbook on “Fuel Cell Fundamentals” by Ryan O’Hayre for an in-depth discussion of the effect.

[116]

Transport of charged species. In every electrochemical system, reactions involve the constant transport of charged species. This transport can be divided into two categories: The transport of electrons within the electronic conductors, e.g. metal electrodes and wires, and the transport of anions and cations within the ionic conductors, e.g. electrolytes and charged polymers. Independent of the charged species’ nature, the transport of it is caused by the electric field and requires the performance of work. This correlates to voltage losses associated to the transport of charged species, which is described by Ohm’s law, shown in Equation 23.

$$E_{Ohm} = i \frac{L}{A\sigma} = iR \quad \text{Equation 23}$$

Ohm’s law shows that the voltage loss (E_{Ohm}) is increasing linearly with the current (i), whereas the resistance (R) determines the slope of that change. The resistance itself is dependent on the geometric properties of the conductor, as the length (L) and the cross section (A), as well as the intrinsic conductivity of the conducting material (σ). While both electronic and ionic conductivity contribute to the total Ohmic losses within an electrochemical system, it is important to note that ionic contribution is usually much larger due to the generally lower intrinsic conductivity of ionic conductors in respect to electronic conductors.

Kinetic activation. Finally, sluggish reaction kinetics can also lead to considerable voltage losses. This effect is generally referred to as activation losses (E_{act}) and is equal to the overpotential term of the Butler-Volmer formalism. Equation 24 shows this relation based on the Butler-Volmer equation, which had been discussed previously in the earlier section of kinetics of electrochemistry.

$$E_{act} = \frac{RT}{\alpha nF} \ln \left(\frac{j}{j_0} \right) - \frac{RT}{(1 - \alpha)nF} \ln \left(\frac{j}{j_0} \right) \quad \text{Equation 24}$$

2.2 Correlation of bond strength and catalytic reaction rates – The Sabatier principle

The field of heterogeneous catalysis is shaped by the development of the Sabatier principle in the early part of the 20th century. Paul Sabatier postulated the theory that the rate of a given reaction is characterized by a surface bond strength.^[125] By variation of this bond strength a maximum rate could be achieved at an “optimal” intersection, where the bond is neither too weak nor too strong, thus allows a sufficient reactant activation without a consecutive poisoning by the products. An illustration of this relation shows a very characteristic appearance and is widely referred to as a volcano curve, which can be found in Figure 2.6. The Sabatier principle offers a guideline for catalysis research to reduce the activation losses associated to sluggish kinetics of an electrocatalytic reaction by choice of an ideal catalyst. Similar to the effect of variation in applied potential, the different electronic properties of catalysts allow a variation of the energetic states for binding of reactive intermediates and, thus, an influence on the associated catalytic reaction rates.

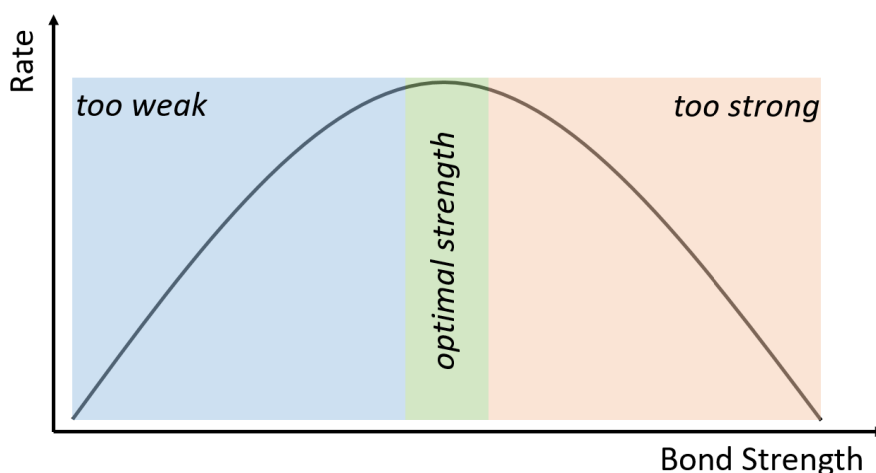


Figure 2.6 Scheme of the volcano-type relationship between the reaction rate and bond strength, which shows a region of optimal binding conditions based on the Sabatier principle.

While this model supplies a general qualitative guideline for catalysis research, it lacks a clear definition what exact bond strength is suitable for characterization and quantification of an investigated reaction. In accordance with the interfacial nature of heterogeneous catalysis, a valid descriptor needs to reflect the interaction of the relevant transition states and intermediates with the catalyst surface. While even presumably simple reactions can proceed through many transition states and intermediates along their mechanistic pathway, the individual bonding strength is often connected by scaling relations and allow the use of one descriptor for appropriate characterization.^[126-129] This is a general relation in heterogeneous catalysis and applies to thermal- and electrocatalytic processes in the same way. This is illustrated by the characterization of the ammonia production rate in thermal catalysis by the nitrogen bonding strength and the electrocatalytic OER rate by the oxygen bonding strength.^[130, 131] However, more complicated reactions and systems that involve competing pathways, as the

electrocatalytic CO₂RR, can require the use of multiple descriptors to access the catalytic behavior and lead to a higher dimensionality of the description.^[36] In any case, the proposed quantitative relations can aid in the search for new catalyst that show superior performance. In this context scaling relations can prove problematic as reaction sequences are often limited by the unfavorable bonding of one discrete intermediate, which would require individual variation for this specific elementary step in order to enhance the total conversion rate. Here, strategies to break scaling relations generally involve the introduction of surface heterogeneities to the catalyst that allow a discrimination between intermediates or a change in the catalytic environment, which can stabilize specific species.^[132]

3 Experimental section

Parts of this chapter have been reproduced from *Angew. Chem. Int. Ed.* **2020**, 59, 17974-17983, (reference^[133], DOI: [10.1002/anie.202007136](https://doi.org/10.1002/anie.202007136)) and from “Energy & Environmental Science”. *Tim Möller, Trung Ngo Thanh, Xingli Wang, Wen Ju, Zarko Jovanov and Peter Strasser*, The product selectivity zones in Gas Diffusion Electrodes during the electrocatalytic reduction of CO₂, *submitted and under revision*.

The following chapter describes all experimental procedures that were employed for the preparation and execution of synthesis, electrochemical testing, and physicochemical characterization of the various investigated systems as part of this work. Any deviations from the described procedures for distinct experiments are specifically stated at the corresponding discussion of results within chapter 4 and 5. An overview over the different materials with reference to the employed testing setup and corresponding chapter within this work is given in Table 3.1.

Material	Testing setup	Chapter
Cu ₂ O	H-Cell, Flow-Cell	4.1, 5.2, 5.3
Cu ₂ O@C	H-Cell, Flow-Cell	4.1, 5.2
Cu ₃ N	H-Cell	4.2
CuS	H-Cell	4.3
Cu ₂ O/CeO _x	H-Cell	4.4

Table 3.1 Overview over the different materials investigated within this work with reference to the employed testing setup and chapter in which they are discussed.

3.1 Synthesis of nanosized cationic Cu catalysts

In the course of this work, multiple cationic Cu compounds were synthesized as nanosized particles and investigated as catalysts for the CO₂RR. For this purpose, different synthetic procedures were followed to allow precise control over structural properties of the investigated materials. In the following subchapter, the experimental details for preparation of all investigated materials is given.

3.1.1 Preparation of cubic Cu₂O nanoparticles

Cu₂O nanoparticles were synthesized according to a prior work.^[134] In brief, a dilute solution of CuCl₂ was prepared by adding 14 mL of a 0.1 M CuCl₂*2H₂O (Sigma-Aldrich, ACS reagent) solution to 560 mL of 18 MΩ Milli-Q-water®. After a short stirring time of about 5 minutes, a solution of sodium hydroxide (42 mL, 0.2 M, Sigma-Aldrich, semiconductor grade) was poured into the reaction mixture followed by the addition of a solution of l-ascorbic acid (28 mL, 0.1 M, Sigma-Aldrich, ACS reagent). The reaction mixture was stirred during the following hour. After this time, the Cu₂O NPs were precipitated by centrifugation. The raw product was cleaned with water for two times and finally one time with ethanol. The dry particles were obtained after 12 hours of freeze drying.

3.1.2 Supporting procedure of cubic Cu₂O nanoparticles

To support the cubic Cu₂O nanoparticles on a conductive carbon support, Vulcan® XC-27R (Cabot) was dispersed in cyclohexane using a sonication horn (Branson Corp.). After 30 minutes, Cu₂O NPs were added to the suspension and the sonication was continued for one hour. Afterwards, the dispersion was stirred overnight to allow the particles to settle on the support. The catalyst was separated from the liquid phase by centrifugation, followed by washing it three times with ethanol. The final product was obtained after 12 hours of freeze drying.

3.1.3 Preparation of Cu₃N nanoparticles

Cu₃N nanoparticles were prepared by an adapted procedure of a previously published study.^[135] In a three-neck-flask 400 mg of Cu(NO₃)₂*2.5 H₂O (Sigma-Aldrich, 99.99% trace metal basis) were mixed with 20 g of 1-octadecylamine (Sigma-Aldrich, technical grade) and 25 mL of 1-octadecene (Sigma-Aldrich, technical grade). The mixture was heated under magnetic stirring and nitrogen atmosphere to four subsequent temperature steps: Initially 60 °C for 30 min in order to obtain a homogenous mixture, followed by 120 °C for 30 min to release the water contained in the metal precursor and then 150 °C for 120min under reflux. In a final step, the temperature was set for 60 min to a desired value (200, 210, 220, 230, 240 and 250 °C) under reflux to initiate the particle nucleation. After reaction, the particles were precipitated by addition of 70 mL of ethanol and subsequent centrifugation. The particles were washed for three times in a mixture of ethanol to cyclohexane of 9:1 and finally freeze dried for 12 hours.

3.1.4 Preparation of CuS nanoparticles

CuS particles were synthesized by sulfidation of cubic Cu₂O particles, which was adapted from a previously published study.^[136] In here, the cubic Cu₂O particles were synthesized following the water-based route described above (see cubic Cu₂O nanoparticles). Afterwards, roughly 50 mg of the obtained cubic Cu₂O particles were dispersed in 560 mL of milli-Q H₂O. To this dispersion, either an undiluted solution of 10 mL (NH₄)₂S (Alfa Aesar, 44 w/w aq. soln.), or 0.5 mL (NH₄)₂S in 10 mL of milli-Q H₂O were quickly added under constant magnetic stirring at room temperature. The mixture was continued to be stirred for a total of 60 min. Afterwards, the particles were separated by centrifugation and washed for two times with milli-Q H₂O and one final time with ethanol. The dry particles were obtained after freeze drying for 12 hours.

3.1.5 Preparation of CeO_x/Cu₂O nanoparticles

In order to introduce a cerium dopant to the Cu₂O nanoparticles, the synthetic route of cubic Cu₂O nanoparticles, as describes above, was modified. Here, following the addition of the CuCl₂ solution to the Erlenmeyer flask, also a solution of CeCl₃*7H₂O (0.05 M, Sigma-Aldrich, purum p.a.) was added to the mixture. The added volume of the CeCl₃ solution controlled the amount of the introduced Ce dopant. Seven different precursor ratios of Cu to Ce were prepared (10:1, 10:3, 10:5, 10:6, 10:7, 10:8, 10:10) by varying the added CeCl₃ volume and keeping the volume of CuCl₂ constant. Additionally, a sample containing only 28 mL of CeCl₃ solution was prepared for reference of a pure CeO_x phase. Besides the addition of CeCl₃ the procedure was identical to the previously described synthesis of cubic Cu₂O particles.

3.2 Electrochemical characterization

The electrochemical characterization throughout this thesis was conducted in two different cell geometries, namely: An H-Cell and a Flow-Cell. In the following subchapter, the procedure for electrode preparation is described with reference to the respective testing setups. In addition, the description of the geometrical characteristics of each setup, as well as the corresponding experimental specifications for the electrochemical investigations are given in detail.

3.2.1 Electrode preparation

Figure 3.1 shows the two procedures routinely used to prepare electrodes for electrochemical measurements. The catalyst powders were dispersed in a mixture of solvent and Nafion binder by rigorous mixing using a sonication horn. The resulting dispersion will be referred to as ink in the following. In case of H-Cell measurements, controlled volumes of the ink were drop-coated onto a surface of 1 cm² of glassy carbon plates to form a stable, catalytic layer. The mass loading of the catalyst on the glassy carbon plates was controlled by tuning the deposited volume of the catalyst-ink. Prior to catalyst deposition, the glassy carbon plates were mechanically polished with alumina paste, followed by alternating sonication in milli-Q water and acetone. In case of Flow-Cell measurements, carbon-based H2315 C2 Freudenberg gas diffusion layers were used as substrate for electrode preparation. Here, the catalyst was deposited on the microporous side of the carbon substrate by spray-coating using an airbrush pistol with pressurized nitrogen. Initial cleaning of the uncoated gas diffusion layers was realized by sonication in ethanol. During spray-coating, the gas diffusion layer was placed on a heated table at a constant temperature of 60 °C to enable a fast evaporation of the solvent. The gravimetric loading of the catalyst was determined by comparison of the electrode weight before and after the spraycoating procedure.

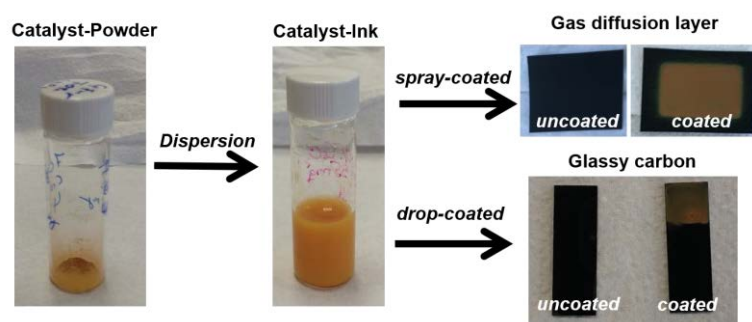


Figure 3.1 Illustration of the electrode preparation procedure showing the dispersion of catalyst-inks and coating of the substrates.

Throughout this thesis, the catalyst ink formulation and catalyst loading has been varied to cope with the different properties of the investigated materials and systems. Table 3.2 gives an overview of the used ink compositions for the different investigated systems and the resulting CuX particle loadings

Experimental section

on the prepared electrodes. Deviations from the listed parameters have been conducted to test effects of loading and ionomer content but are clearly marked in the discussion part.

Catalyst system	Measurement System	Ink Composition	CuX loading [mg cm ⁻²]
Cu ₂ O	H-Cell	4 mg catalyst, 1.6 mL H ₂ O, 0.3 mL IPA, 100 µL Nafion	0.100
Cu ₂ O @ Vulcan (23 wt%)	H-Cell	15 mg catalyst, 1.6 mL H ₂ O, 0.3 mL IPA, 100 µL Nafion	0.87
Cu ₂ O @ Vulcan (44 wt%)	H-Cell	15 mg catalyst, 1.6 mL H ₂ O, 0.3 mL IPA, 100 µL Nafion	0.167
Cu ₂ O/CeO _x	H-Cell	4 mg catalyst, 1.6 mL H ₂ O, 0.3 mL IPA, 39 µL Nafion	0.100
CuS	H-Cell	4 mg catalyst, 1.6 mL H ₂ O, 0.3 mL IPA, 100 µL Nafion	0.100
Cu ₃ N	H-Cell	4 mg catalyst, 2 mL cyclohexane	0.020
Cu ₂ O	Flow-Cell	6 mg catalyst, 4 mL H ₂ O, 2 mL IPA, 59 µL Nafion	1.00

Table 3.2 Experimental details on the ink formulation and catalyst loading during electrochemical testing (referred to the cationic Cu compound) for the various systems investigated throughout the present work.

3.2.2 Testing procedure in an H-Cell setup

The H-Cell setup. For the investigation of the intrinsic catalytic properties and the initial electrochemical characterization of the prepared Cu catalysts, a custom-made H-type Cell was used. The H-Cell is composed of an anode and a cathode compartment, which consist entirely of glass and are separated by an ion conducting membrane (either Nafion or Selemion). The cathode compartment includes connections for mounting of the working electrode, reference electrode, CO₂ feed and outlet, as well as one designated for an automated liquid sampling unit. The anode compartment offers a connection to mount the counter electrode and an additional port for the introduction of a controlled gas atmosphere or the sampling of the liquid phase. Figure 3.2 shows an image of a mounted H-Cell with indications of all relevant connections used for the electrochemical characterization.

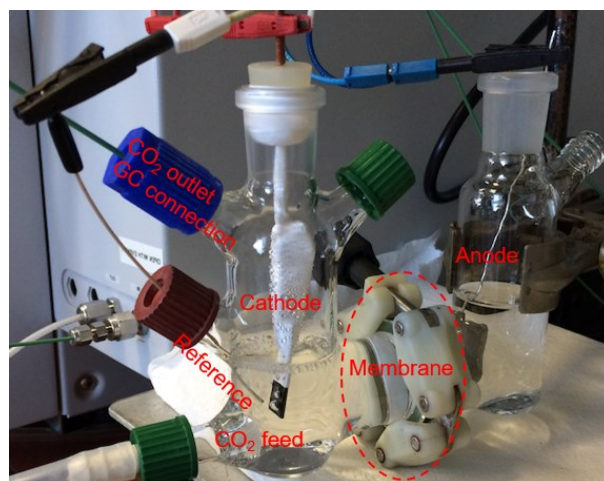


Figure 3.2 Image of a mounted H-Cell used during the electrochemical characterization. Indications for the compartments, separator and important connections are given.

H-Cell cleaning and testing procedure. Prior to electrochemical experiments the glassware was cleaned in a NOCHROMIX® bath containing sulfuric acid and afterwards in concentrated HNO₃ for 1 h, respectively. To remove remaining acid, the cell was rinsed extensively and sonicated submerged in ultra-pure water for several times. Electrochemical measurements in the H-Cell were routinely conducted in CO₂ saturated 0.1 M KHCO₃ electrolyte. Here, the anode and cathode compartment were both filled with 40 mL of the electrolyte. Before and during the electrochemical reaction, the electrolyte was purged continuously with CO₂ (30 mL min⁻¹, 4.5N) from the bottom of the cell, which was regulated using a mass flow controller (Bronkhorst). A platinum mesh 100 (Sigma-Aldrich 99.9%) was used as counter electrode (CE) and a leak-free Ag/AgCl electrode as reference electrode (Multi Channel Systems MCS GmbH). Control repeat experiments using an IrO_x counter electrode yielded identical results, suggesting that dissolved Pt ions at the CE did not affect the measurement at the working electrode (WE). General measurements of the catalytic CO₂RR activity and selectivity started with a linear voltammetric sweep, performed with a scan rate of -5 mV/s between $E = +0.05$ V_{RHE} and the working potential and was followed by a chronoamperometric step for one hour. All reported potentials are, if not further specified, corrected for Ohmic drop, which was determined by electrochemical impedance spectroscopy (EIS).

Lead under potential deposition (Pb-UPD) in an H-Cell. To evaluate the difference in accessible surface area of the electrochemically active Cu-sites, for the unsupported and supported (23 wt% metal loading), cubic Cu₂O catalysts, Pb-UPD was performed on samples that were reduced for five hours at -0.86 V vs. RHE in CO₂ saturated 0.1 M KHCO₃ prior to deposition. The deposition was performed in a degassed (N₂) solution of 0.01 M Pb(ClO₄)₂·xH₂O (Aldrich, ≥ 99.995%) in 0.1 M HClO₄ (Aldrich, 70%). The cathode-potential was cycled in between -0.40 V to -0.05 V vs Ag/AgCl at a scan rate of 10 mV s⁻¹ until a stable cyclic voltammogram (CV) could be obtained. The charge of the anodic peak at -0.24 V vs Ag/AgCl, which represents the stripping of the Pb-monolayer from the Cu surface, was

evaluated to compare both catalysts. In both cases, 100 μg of total particle mass was deposited on one cm^2 of the glassy carbon electrode.

3.2.3 Testing procedure in a Flow-Cell setup

The Flow-Cell setup. Electrochemical measurements of high-reaction rates were performed using a commercial 4-compartment, micro flow cell (ElectroCell). A solution of 1 M KHCO_3 with a respective volume of 500 mL was used routinely as electrolyte in the anode and cathode compartment, which were separated by anion conducting membrane (Selemion AMV, AGC Engineering Co., LTD.). Both electrolytes were continuously cycled at a volumetric flow rate of 100 mL min^{-1} through the respective compartments by using a peristaltic pump (PMP Ecoline, Cole-Parmer). The bulk pH values of the anode and cathode electrolyte could be simultaneously monitored during CO_2RR , realized by connecting pH-electrodes (Mettler Toledo) to the respective reservoirs. The CO_2 (4.5N) was supplied at a volumetric flow rate of 50 mL min^{-1} to the cathode and was convectively forced from the back of the GDL through the catalyst layer. As anode, a commercial IrO_x -coated Ti sheet with an active area of 10 cm^2 was used (ElectroCell). The outgoing volumetric gas flow of the CO_2 mixed with the gaseous reaction products was monitored using a mass flow controller (Bronkhorst). A schematic representation of the Flow-Cell implemented in the testing environment is given in Figure 3.3.

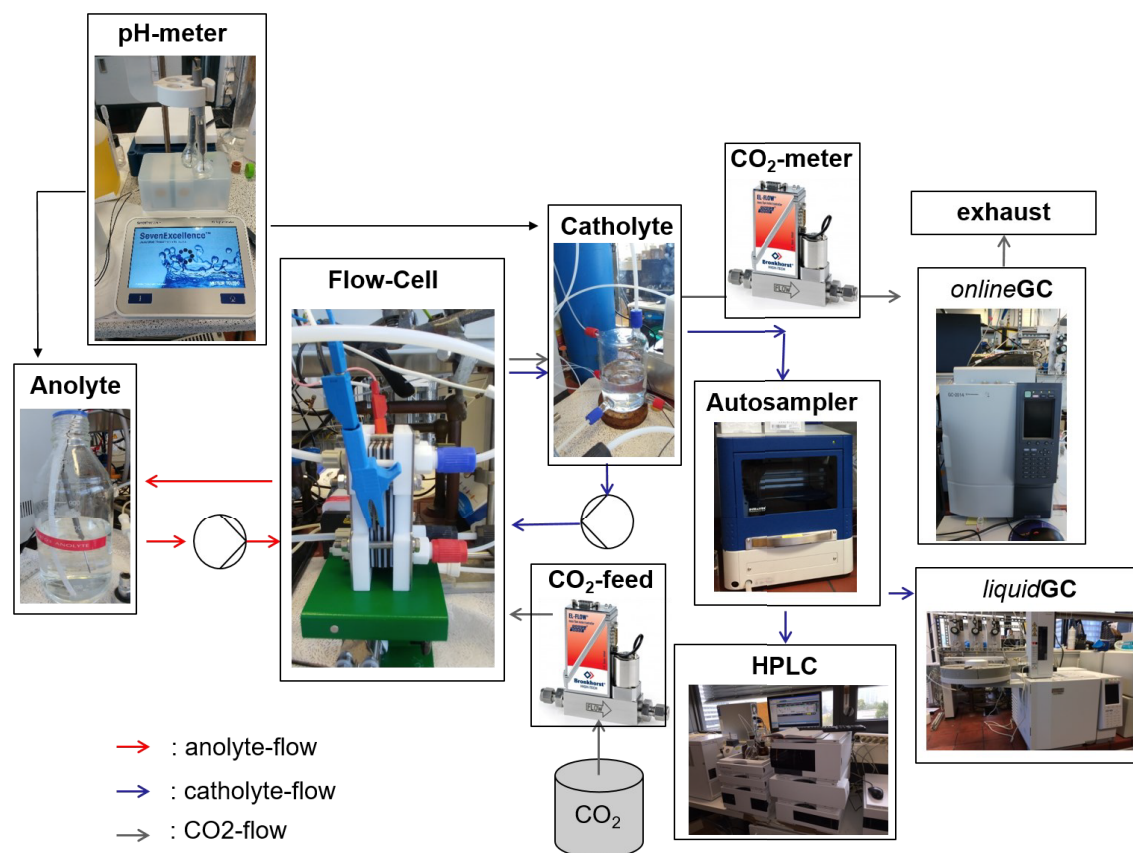


Figure 3.3 Schematic representation of the Flow-Cell testing environment. Colored arrows indicate the direction of electrolyte and CO_2 flow.

Flow-Cell testing procedure. Prior to CO₂RR experiments the system was saturated with CO₂ until the outgoing CO₂ flow was equal to the ingoing CO₂ flow. This equilibrated state occurred roughly after 30 to 60 min of constant purging. Following investigations of CO₂RR experiments were routinely conducted by galvanostatic current steps with a holding time of two hours at each investigated current and were tested from low towards increasing values. The cathode potential was measured against a leak-free Ag/AgCl electrode as reference electrode (Multi Channel Systems MCS GmbH), placed inside the cathode flow channel. In between different currents potentiostatic impedance spectroscopy at open circuit voltage was used to determine electrolyte resistivity and account for the ohmic drop in calculations of IR-free potentials.

Determination of double layer capacitance. The electrochemical double layer capacitance was determined by cycling the potential between 0.1 V_{RHE} and 0.25 V_{RHE} under variation of scan rates (20, 50, 80, 100, 150 and 200 mV s⁻¹). In this region, a purely capacitive current could be observed without any faradaic processes. Based on the linear relationship between scan rate and capacitive current the double layer capacitance was derived as the slope. The capacitance was determined for the studies of Nafion content and catalyst loading, directly after electrolysis in the testing solution of 1 M KHCO₃ electrolyte saturated with CO₂.

Oxygen reduction reaction in the flow-cell. For experiments involving the oxygen reduction reaction (ORR), a concentration of 2 M KHCO₃ was used as electrolyte in order to reduce Ohmic losses and maximize ORR currents to facilitate investigations of mass transport effects. At the start of each ORR experiment the cathode potential was cycled in N₂ saturated conditions in between – 1.3 and 0.45 V_{RHE} at 100 mV s⁻¹ to electrochemically reduce the catalyst and achieve stable starting conditions. Afterwards, the electrode potential was set to -0.45 V_{RHE} and the partial pressure of O₂ in N₂ was gradually increased in the following order: 0.05, 0.1, 0.2, 0.3, 0.5, 0.7 and finally 1.0 bar. Adjustments in O₂ partial pressure were carried out by setting mixtures of N₂ and O₂ gas flowrates, controlled by individual MFCs, while keeping the total volumetric flow at 50 mL min⁻¹. Each partial pressure was set for at least 2 min, or until a stable ORR current was observed before moving towards the next, higher value.

3.2.4 Equations used as part of electrochemical characterization

Calculation of IR-free RHE potentials. All potentials that are reported against RHE within this thesis were calculated according to Equation 25. Here, E_{RHE} refers to the calculated potential in reference to an RHE and corrected for Ohmic losses. E_{Ref} is the experimentally applied potential of the working electrode against an employed reference electrode, commonly a leak-free Ag/AgCl in 3 M KCl. $E_{Ag/AgCl}$ refers to the potential of the leak-free Ag/AgCl reference electrode measured against an NHE. The Nernstian shift was considered by $0.059 * pH$, whereas the pH is referring to the proton concentration of the bulk catholyte employed during electrochemical investigations. The Ohmic losses

Experimental section

between working and reference electrode were manually corrected by determination of the Ohmic resistance, R , derived from impedance spectroscopy, and consideration of the total electric current, I , of the experiment.

$$E_{RHE} = E_{Ref} + E_{Ag/AgCl} + 0.059 * pH + R * I \quad \text{Equation 25}$$

Calculation of the double-layer capacitance. The capacitance of the electrochemical double-layer (C_{DL}) was calculated as a measure for the electrochemically accessible surface area (ECSA) according to Equation 26. Here, j_{cap} denotes the capacitive current density derived by cycling the electrode potential in a region without any faradaic processes at a given scan rate of ν .

$$C_{DL} = \frac{j_{cap}}{\nu} \quad \text{Equation 26}$$

3.3 Physicochemical characterization

The investigations of structure-selectivity-relations require the careful analysis of the physicochemical properties of the studied materials. In this subchapter, the experimental details for the employed physicochemical characterization techniques used in this work are given.

3.3.1 Powder and grazing incidence x-ray diffraction (PXRD and GI-XRD)

The characterization of crystalline samples was routinely performed by conducting X-ray diffracting measurements.

Powder X-ray diffraction. The phase of powder samples was analyzed by X-ray diffraction using a D8 Advance Diffractometer (Bruker) equipped with a Lynx Eye detector and a KFL Cu 2 K- α anode as x-ray source. Patterns were collected in a 2θ angle range of 20 to 80 ° with a step size of 0.07 ° and a collection time of seven seconds per step.

Grazing incidence X-ray diffraction. Phase analysis of film samples were conducted by grazing incidence XRD (GI-XRD). Here a structurally identical device as in powder XRD was used to investigate the same 2θ angle range of 20 to 80 °, but the step size was decreased to 0.06°, and collection time increased to 40 s per step to achieve sufficient signal intensity. The angle of incidence was set to a constant value of 1 °.

3.3.2 X-ray absorption spectroscopy (XAS)

X-ray absorption spectroscopy (XAS) measurements were conducted on cubic Cu₂O samples. All XAS measurements were carried out at the CLÆSS beamline of Alba synchrotron radiation facility (Barcelona, Spain). A Pt-coated toroid mirror was used to reject higher harmonics in the X-ray beam and to focus it to a 500 x 500 μm^2 spot on the sample. The *operando* X-ray absorption data were recorded at the CuK- edge (8979 eV) at room temperature in fluorescence mode using a single-channel silicon drift detector (SDD). A home-built *operando* electrochemical cell was used, with a Pt foil counter electrode and Ag/AgCl reference electrode. ^[137] The Cu₂O NP powder was deposited on a graphite paper disc (Sigracet 24 BC, SGL CARBON GmbH) by filtration from a slurry containing Nafion (0.1 v/v %) as a binding agent and dissolved in ethanol. Due to low porosity of the paper, the catalyst stays on one side, while the other side stays unmodified. The paper disc was mounted in the *operando* cell so that the unmodified side was facing out, while the side containing the catalyst layer was in contact with the electrolyte. Using this approach, we successfully avoided intensity losses in the incident X-ray beam as well as fluorescence radiation emitted from the sample while passing through the electrolyte layer. The sample was measured in as prepared state, at -0.66 and at -0.95 V vs. RHE. The as prepared sample as well as commercial CuO, Cu₂O and Cu foil references were measured in transmission mode. At each applied potential, the measurements were carried out until no further changes in the XAS spectra were observed

3.3.3 X-ray photoelectron spectroscopy (XPS)

All quasi in situ X-Ray photoelectron spectroscopy (XPS) measurements were carried out with a commercial Phoibus 100 (SPECS GmbH) analyzer using an Al anode of the XR 50 X-ray source (SPECS GmbH). To prevent samples from re-oxidation in air after running the CO₂RR, our customized electrochemical cell was directly attached to the UHV XPS-analysis system, and sample transfer took place under a protective pressurized ($p=1.05$ bar) Ar atmosphere. All samples were rinsed with 10 ml of N₂-bubbled (1 hour) deionized water ($R=18.2$ M Ω) after electrochemistry to clean the samples from the residual KHCO₃ electrolyte. All reactions were run for 1h before acquiring the respective XPS spectra. The XPS data were aligned to the binding energy of carbon ($E_b=284.9$ eV) for all samples, resulting in a binding energy of the Cu 2p 3/2 spectra of $E_b=932.6$ eV, which is in agreement with the literature. ^[138]

3.3.4 Scanning and transmission electron microscopy (SEM and TEM)

The morphological investigations were conducted by measurements of scanning electron microscopy (SEM) and transmission electron microscopy (TEM).

Transmission electron microscopy. TEM measurements were performed using a Tecnai G2 microscope 20 S-Twin with a LaB6-cathode at 200 kV accelerating voltage (ZELMI Centrum, Technical University Berlin). For sample preparation, small quantities of the powder samples were dispersed in either water, ethanol or cyclohexane, depending on the nature the material, and drop casted onto TEM grids.

Scanning electron microscopy. SEM measurements were performed by using a JEOL 7401F instrument equipped with both a secondary electron detector for topological analysis and a back scattered electron detector for compositional analysis. Acceleration voltage of the electron beam was constant at 10 kV. The sample preparation for SEM measurements was analogous to TEM but Si wafers were used as substrate instead of the TEM grids. In case of morphological analysis for post electrolysis samples, the specimens were rinsed with milli-Q water to remove residual electrolyte and dried in a nitrogen stream prior to SEM imaging.

3.3.5 Inductively coupled plasma optical emission spectroscopy (ICP-OES)

An atomic emission spectrometer was used to quantify the bulk metal contents for various samples. This was performed for carbon-supported cubic Cu₂O for determination of the Cu loading and in the work on CeO_x/CuO_x mixtures for the determination of mass ratios between Ce and Cu. Sample preparation involved the digestion of roughly 10 mg of catalyst powders in a mixture of nitric acid, hydrochloric acid and sulfuric acid (1:3:1) at room temperature for 3 h. Comparison to calibration curves, derived from measurements of metals standards of a known concentration, allowed the quantitative analysis of the samples.

3.3.6 Thermogravimetric analysis and differential scanning calorimetry (TGA-DSC)

The thermal decomposition behavior of $\text{Cu}(\text{NO}_3)_2 \cdot 2.5 \text{ H}_2\text{O}$ was studied using a TGA-DSC (PerkinElmer, STA-8000). The sample was placed in a Al_2O_3 crucible and was heated in nitrogen atmosphere from 30 °C to 500 °C at a rate of 1 °C per min. The initial temperature of 30 °C, as well as the final temperature of 500 °C were kept constant over a period of 30 min to ensure stable conditions.

3.4 Product quantification

The electrocatalytic CO₂RR on Cu-based catalysts leads to the simultaneous formation of various gaseous and liquid products, which results in a diverse product spectrum. The comprehensive evaluation of the faradaic selectivity under given experimental conditions requires a careful qualitative and quantitative analysis of all possible products. For this purpose, various chromatographic techniques were employed throughout this work. This subchapter describes the experimental details and used equations, which were employed for quantification of liquid and gaseous CO₂RR products.

3.4.1 Gas phase analysis

Gaseous species produced during CO₂RR were analyzed by means of gas chromatography. Unreacted CO₂ was used as transport media to carry the gas phase from the CO₂RR measurement cell directly to a connected gas chromatograph (GC, Shimadzu GC 2014). The GC was operated using Ar as mobile phase on a combination of a HaySep Q and HaySep R column for product separation. Detection of carbon-containing species (CO, CO₂, CH₄, C₂H₄) was realized by using a combination of a methanizer and a flame ionization detector (FID). Other gaseous species (N₂, O₂, H₂) were detected by a thermal conductivity detector (TCD). Based on measurements of commercially available calibration standards, calibration curves were recorded for all CO₂RR relevant gases, which enabled the determination of the volumetric percentage composition of product gas mixtures. The Calculation of the product Faradaic Efficiency (FE_x) was conducted based on the determined volumetric concentrations, following the relation given in Equation 27.

$$FE_x = \frac{c_x * \dot{V} * z_x * F}{V_m * I} \quad \text{Equation 27}$$

In here, c_x refers to the volumetric concentration of the gaseous product determined by the GC analysis, V_m is the molar volume of an ideal gas, z_x denotes the stoichiometric number of electrons required for the reaction, \dot{V} is the total volumetric flow rate of the gas introduced to the sample loop of the GC, F is the Faraday constant, and I the value of the absolute current during the electrochemical experiment.

3.4.2 Liquid phase analysis

Liquid samples of the catholyte (between 0.5 mL and 2 mL) were taken during the electrolysis after desired periods reaction times at constant potential or current using an automatic aliquot sampling device (Duratec GmbH). The liquid samples were later introduced to a high performance liquid chromatograph (HPLC, Agilent 1200 series) equipped with an organic-acid resin column and a refractive index detector (RID) for separation and detection of carboxylic acids (e.g. Formic acid and acetic acid). Additionally, liquid samples were analyzed by a liquid gas chromatograph (liquid GC, Shimadzu 2010 plus). The liquid GC used an injector composed of a heated glass liner and quartz wool

that enabled the fast evaporation of volatile species and their subsequent introduction to the capillary column (SH-Stabilwax). Post separation, the detection was realized by an FID, enabling the analysis of aldehydes, ketones, and alcohols (e.g. ethanol, 1-proanol). HPLC and liquid GC calibration standards were prepared by dilution of pure compounds in milliQ water and used subsequently for the measurements of calibration curves for each product. Comparison of catholyte samples to the prepared calibration curves allowed qualitative and quantitative analysis of all compounds in form of molar concentrations. The Faradaic efficiency (FE_x) of liquid products was calculated based on the determined molar concentrations according to Equation 28. Here, V refers to the volume of the catholyte, Δc_x is the differential increase in product concentration over a given time, z_x denotes the stoichiometric number of electrons required for the reaction, F is the Faraday constant, and ΔQ is the electrical charge transferred during the considered period of time.

$$FE_x = \frac{V * \Delta c_x * z_x * F}{\Delta Q} * 100\% \quad \text{Equation 28}$$

4 Low-Current H-Cell investigations of copper-based catalyst systems

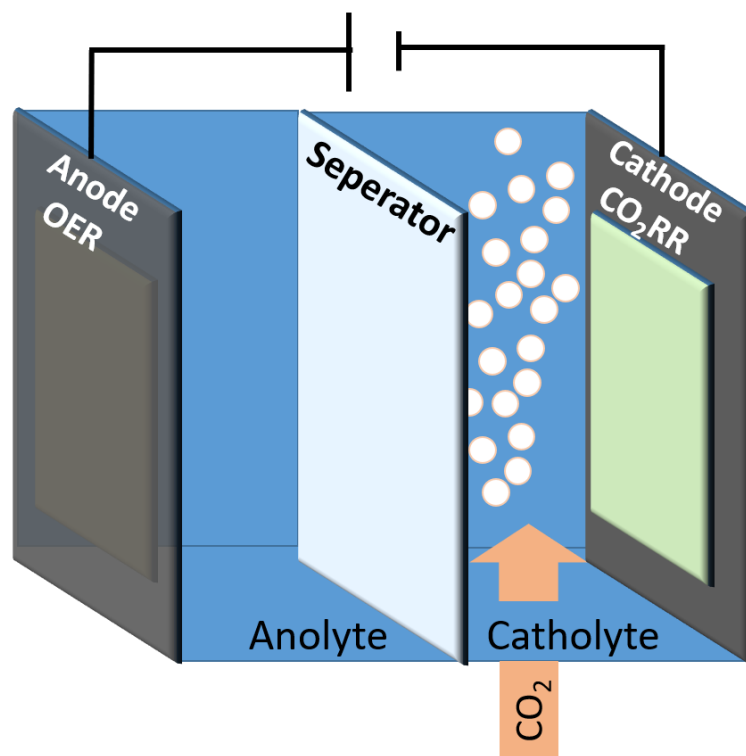


Figure 4.1 Schematic representation of an H-Cell used in common electrochemical experiments during CO₂RR.

Experimental investigations of intrinsic catalytic activities, influences of electrolyte composition, and mechanistic pathways during CO₂RR require a well controllable system. For this purpose, symmetric electrochemical cells, often referred to as H-Cells, find widespread application in experimental studies for electrocatalytic CO₂RR. While the exact geometry of the cell can vary, the basic structure usually stays unchanged and is schematically depicted in Figure 4.1. Here, two compartments for liquid electrolytes are separated by a membrane and the gaseous reactant, e.g. CO₂ or CO, is introduced near the cathode by bubbling at atmospheric pressure. This system is limited by the low solubility of the gaseous reactant in the electrolyte and the commonly non-convective transport thereof to the electrode surface. Consequently, CO₂RR experiments in H-Cells are constrained to a low current regime and are subjected to mass transport limitations if the cathodic current density exceeds around -20 to -50 mA cm⁻². Nevertheless, in the low current regime, H-Cells offer a high flexibility of parameters and excellent control over reaction conditions during electrolysis. Thus, initial characterization of novel catalysts is routinely performed in H-Cells. The following chapter 4 covers the electrocatalytic characterization of various cationic Cu catalyst and is focused exclusively on the CO₂RR in an H-Cell setup.

4.1 Electrocatalytic CO₂ reduction on CuO_x nanocubes: tracking the evolution of chemical state, geometric structure, and catalytic selectivity using *operando* spectroscopy

The direct electrochemical conversion of carbon dioxide (CO₂) into multi-carbon (C₂₊) products still faces fundamental and technological challenges. While facet-controlled and oxide-derived Cu materials have been touted as promising catalysts, their stability has remained problematic and poorly understood. The present work uncovers changes in the chemical and morphological state of supported and unsupported Cu₂O nanocubes during operation in low-current H-Cells. Operando XAS and time-resolved electron microscopy revealed the degradation of the cubic shape and, in the presence of a carbon support, the formation of small Cu-seeds during the surprisingly slow reduction of bulk Cu₂O. Here, the initially (100)-rich facet structure has presumably no controlling role on the catalytic selectivity, whereas the oxide-derived generation of under-coordinated lattice defects, as revealed by the operando Cu-Cu coordination numbers, can support the high C₂₊ product yields.

The subchapter 4.1 was reproduced from T. Möller, F. Scholten, T. N. Thanh, I. Sinev, J. Timoshenko, X. Wang, Z. Jovanov, M. Gliech, B. Roldan Cuenya, A. S. Varela, P. Strasser, *Angew. Chem. Int. Ed.* **2020**, 59, 17974-17983, (reference ^[133], DOI: [10.1002/anie.202007136](https://doi.org/10.1002/anie.202007136)). Licensed under [CC BY 4.0](https://creativecommons.org/licenses/by/4.0/).

Reproduced (adapted) from Electrocatalytic CO₂ Reduction on CuO_x Nanocubes: Tracking the Evolution of Chemical State, Geometric Structure, and Catalytic Selectivity using Operando Spectroscopy

Parts of this work have been used in the master thesis of Tim Möller entitled “Synthesis and characterization of copper-based nanoparticles as electrocatalyst for CO₂ reduction” from 2016.

T.M. and A.S.V. planned and designed the experiments. T.M. performed and analyzed the electrochemical experiments. F.S. conducted the XPS analysis. EXAFS measurements and analysis was conducted by I.S. and J.T. TEM and SEM analysis was performed by X.W. and M.G. Electrochemical investigations in the Flow-Cell electrolyzer were conducted by T.M. with the help of T.N.T. and Z.J. The manuscript was written by T.M., F.S., J.T., A.S.V., B.R.C., and P.S. All authors participated in the discussion and deduction of results.

4.1.1 Introduction

In this contribution, we explore structure and composition-selectivity relations of cubic, Cu₂O nanoparticles of about 35 nm edge-length. The nanocubes were initially tested in a two-chamber H-Cell as a carbon-supported and unsupported powder catalyst. We observed a clear effect of the carbon support, steering the selectivity away from C₂₊ of the unsupported nanocubes towards C₁ products. We correlated this difference to an altered morphological evolution of the nanocubes by spatial isolation of the particles on the conductive support. Furthermore, we monitored the surprisingly slow and incomplete electrochemical reduction of the unsupported Cu₂O particles on the molecular scale. Our *operando* XAS allowed us to trace the electrochemical reduction of the initially cubic Cu₂O into predominantly metallic particles of ill-defined morphology, showing an abundance of Cu lattice defects, which are often associated with catalytic sites of extraordinary activity. In this, we succeed at presenting the formation of a defective Cu structure by electrochemical reduction of an oxidized precursor in real time.

4.1.2 Results and discussion

Initial material characterization. The unsupported Cu₂O nanocubes will be referred to as “U-NC”, while the supported nanocubes at a loading of 23 weight% will be denoted as “S-NC”. Figure 4.2 (a,-e) and Figure A 1.1 (b) show the local TEM-based microstructural morphologies of the as-prepared unsupported and supported nanocatalysts, while the insets in Figure 4.2 (d,e) display the selected area of the electron diffraction patterns and Figure 4.2 (c) the X-ray diffraction patterns of the crystalline phases, respectively. Figure 4.2 (d,e) and Figure A 1.1 (b) confirm the targeted cubic morphology of the Cu-based NPs with an edge length of 35 ± 6 nm (see histogram in Figure 4.2 (f)), which showed no apparent change once supported on the carbon. The crystal phase analysis in Figure 4.2 (d,e,c) revealed a single Cu₂O phase for both S-NCs and the U-NCs, confirming the stability of the crystalline cubic Cu₂O phase during the supporting procedure.

In order to be able to compare catalytic activities on a real surface area basis, and include differences in roughness of the two catalysts in the discussion of their performances, we evaluated the real electrochemically accessible surface area of both supported, S-NCs, and unsupported Cu nanocubes, U-NCs, using a very specific and selective electrochemical Pb under potential deposition (Pb-UPD) technique. Under electrochemical UPD conditions, that is, at electrode potentials slightly more positive than their standard potential, Pb adatoms form a monolayer on metallic Cu surfaces in a 2-electron process. We assessed the real electrochemical surface area after five hours of continuing CO₂ electrolysis, when the surface of the Cu₂O nanocubes had chemically reduced to metallic Cu (*vide infra*). At identical geometric catalyst mass loadings, the anodic stripping charge of a single Pb monolayer deposited on the Cu nanocubes was considerably larger for the S-NCs (Figure A 1.3) than for the U-NCs, suggesting a larger real active surface area. This is well in line with the notion of dispersed nanocubes on the surface of the carbon support with accessible surface atoms, as opposed to agglomerated Cu nanocubes in case of the unsupported catalyst. Assuming a hexagonal closed packed

Pb monolayer, we can use the specific charge of $300 \mu\text{C cm}^{-2}$, known from the literature,^[139, 140] to estimate the real surface area exhibited by the U-NC (0.8 cm^2) and S-NC (2.57 cm^2) catalyst.

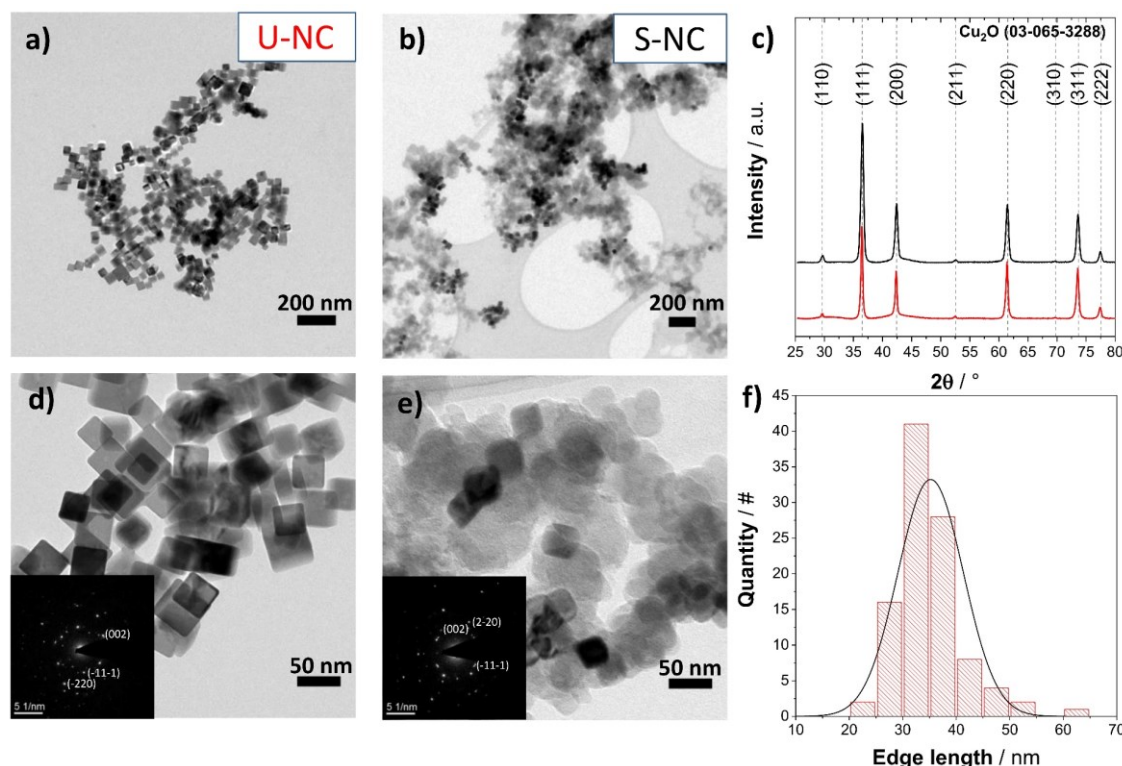


Figure 4.2 Transmission electron microscopy (TEM) images of (a,d) the unsupported Cu₂O nanocubes, U-NC, and (b,e) the carbon-supported Cu₂O nanocubes (23 wt%), S-NC. Insets (d,e) show selected area electron diffraction (SAED) patterns of the respective material. (c) X-ray diffraction (XRD) patterns of both catalysts and (f) particle size distribution histogram (edge length) derived from TEM images of the U-NC.

Catalytic performance in electrochemical CO₂RR. The supported Cu₂O nanocube catalyst, S-NC, and the unsupported Cu₂O nanocube catalyst, U-NC, were drop-casted into thin catalytic electrode layers on top of glassy carbon plates, which served as back contact electrode. The mass of the nanocubes deposited on the glassy carbon plate working electrodes is given in Table A 1.1. Subsequently, both CO₂RR electrocatalysts were tested in a two-compartment liquid-electrolyte H-Cell at constant applied electrode potentials in aqueous 0.1 M KHCO₃ buffer electrolyte saturated with CO₂. We will show further below that the Cu oxide cubes become mostly reduced to metallic Cu, therefore, in the following we will refer to the catalysts as “Cu nanocubes” rather than “Cu oxide nanocubes”. We deliberately focused on electrochemical tests in neutral pH bicarbonate buffer electrolytes, because previously reported strongly alkaline test conditions (1 M to 10 M KOH) are known not to remain sustainable in a practical flow-through electrolyzer device with CO₂ GDEs and continuously looped catholyte. While the favorable faradaic ethylene efficiencies of cubic-shaped Cu-based nanoparticles have been documented in previous works,^[77, 141, 142] catalytic support effects have been proven important but remain less studied.^[75] Therefore, we place emphasis on the comparison

between unsupported nanocubes, U-NC (red color code and symbols), and the supported ones, S-NC (black code and symbols). Figure 4.3 contrasts a few key catalytic and kinetic performance indicators of the U-NCs and the S-NCs. The displayed data report the experimental faradaic efficiencies of major reaction products (a,b), the overall polarization curves over the investigated potential range (d), the chronoamperometric current and efficiency stabilities (c), and the excess in C₂₊ products (e), all measured in bicarbonate buffer electrolyte at a bulk pH = 6.8. A significant effect of the dispersion of the nanocubes on the high surface area support is evident and will now be discussed in detail.

Catalytic CO₂RR activity. The overall geometric current density between -0.6 V_{RHE} and about -0.9 V_{RHE} showed a very similar evolution for the supported and unsupported Cu nanocube catalysts; however, at more cathodic potentials of -0.9 V_{RHE}, the geometric current density of the S-NCs exhibited a sudden, sharp increase (see Figure 4.3 d). To convince ourselves that this sudden current increase is linked to the fact that the Cu nanocubes are supported, we prepared an additional 44 wt% S-NC catalyst, which again exhibited a sudden increase in overall current density below -0.9 V_{RHE}, both on a geometric and mass-normalized basis, seen in Figure A 1.5. Closer inspection of the catalyst mass-normalized polarization curves implies improved Cu catalyst utilization with decreasing Cu cube weight loadings (23 wt% vs 44 wt%), suggesting a lower availability of active surface sites on the unsupported, agglomerated cubes in agreement with our previous results from Pb-UPD. For comparison, we have also investigated the catalytic activity and polarization behavior of the pure Vulcan carbon powder, as well as of the bare glassy carbon back contact plate in order to exclude any influence of the support or substrate. Both control catalysts displayed only negligible catalytic activity, mainly attributable to the HER (Figure A 1.4). This comparison confirmed that the controlling catalytically active sites are those on the surface of the Cu nanocubes.

Catalytic CO₂RR selectivity/faradaic efficiency. Catalytic selectivity and faradaic efficiencies (FE) of gaseous and liquid products were evaluated using online gas chromatography, high pressure liquid chromatography, and liquid injection gas chromatography. Figure 4.3 (a,b) shows the FE values of the U-NC and S-NC as function of the applied IR-corrected electrode potential. At electrode potentials of -0.65 V_{RHE}, both catalysts exhibited high CO FEs, early onset potentials of ethylene combined with a suppression of methane formation. At -0.97 V_{RHE}, the U-NCs displayed high ethylene selectivity, given the neutral pH conditions, exceeding 30 % FE. This efficiency value meets previously reported ethylene efficiency values of unsupported Cu nanocubes under comparable reaction conditions.^[77] The high C₂ gas product yield is, in principle, consistent with previous reports on CO₂ electroreduction on cubic-shaped Cu NPs in H-Cell, and is considered to constitute the key advantage of Cu(100) facet-rich nanocatalysts over electropolished Cu foils^[34].

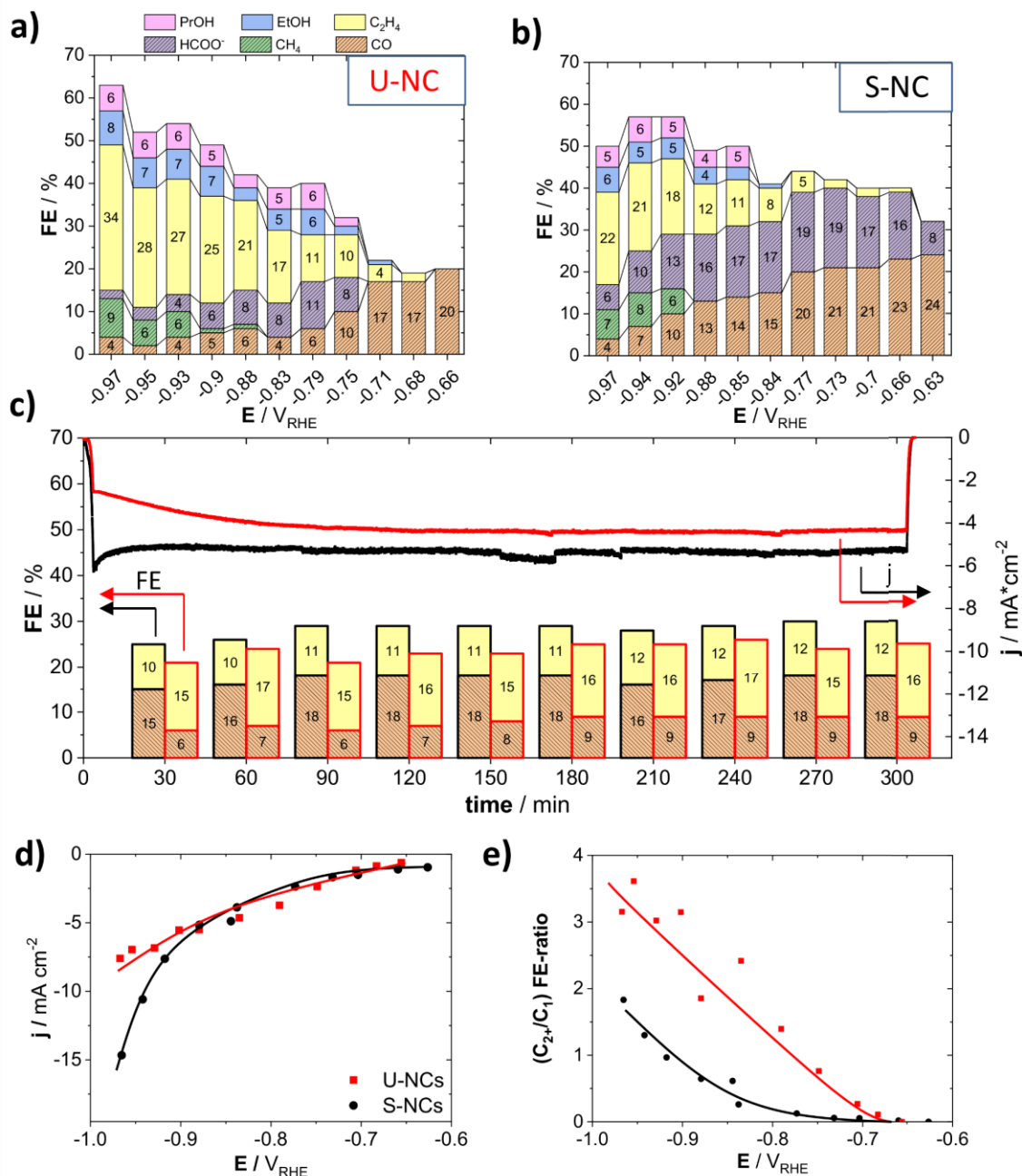


Figure 4.3 (a,b) Faradaic product efficiencies (FEs) as a function of the applied electrode potential after one hour of reaction time for (a) the unsupported Cu nanocubes, U-NC and (b) the carbon-supported Cu nanocubes (23 wt%), S-NC. Color coded bars denote products as given in the legend. (c) Chronoamperometric efficiency stability at a constant applied electrode potential of $-0.86 V_{RHE}$ for the U-NC and the S-NC catalysts. Color coded bars and curves denote time evolution of Faradaic efficiencies of gaseous species and the total geometric current density, respectively. The curve and bar-border color indicate affiliation to the respective catalyst, either U-NC, red, or S-NC, black. (d) Direct comparison of the electrochemical CO₂ reduction polarization curve (geometric current-density vs IR-corrected applied electrode potential); (e) (C_{2+}/C_1) FE ratios vs IR corrected applied electrode potential. Lines to guide the eye. Conditions: CO₂ saturated 0.1 M KHCO₃ (pH 6.8), geometric Cu₂O loading on GC plates of 100 $\mu\text{g cm}^{-1}$ and 87 $\mu\text{g cm}^{-1}$ for the U-NC and S-NC catalyst, respectively.

In addition to the distinct catalytic activity, the dispersion of the Cu nanocubes on the carbon support induced a number of important differences in terms of selectivity: The S-NC displayed a clearly lower ethylene FE, while the FEs of CO and HCOO⁻ were higher. The HCOO⁻ FE peaked at 19 %, CO at 24 %, while the C₁ FEs values generally remained at elevated levels. This observation is in good agreement with previous studies.^[75] Again, to check that that this efficiency pattern is intrinsically linked to supported Cu nanocubes, we also investigated a supported 44 wt% Cu nanocube catalyst, which showed a similar drop in ethylene FE with enhanced HCOO⁻ FE and, at larger overpotentials, enhanced CH₄ FE, see Figure A 1.1.

Next, we turn to a comparison of the time-stability of the FE values of the S-NC and the U-NC catalysts at -0.86 V_{RHE}, displayed in Figure 4.3 (c). It is evident that both catalysts displayed distinct, yet similarly time-stable trajectories of the FE values of their major gas products, resulting from CO₂RR, over at least 5 hours. The U-NC chronoamperometric trajectory showed a slow increase in current density over the first two hours, while that of the S-NC remained virtually constant over the entire time of test at slightly higher current density. Tests at other kinetic overpotentials as -0.95 V_{RHE} and -0.66 V_{RHE} showed again virtually constant FEs over 5 hours of testing time, confirming the stability of the systems (see Figure A 1.6).

Support effects. We start the discussion of the H-Cell results with our key observation, that is, that dispersion of Cu₂O-derived Cu nanocubes on a Vulcan carbon support altered their catalytic selectivity (faradaic CO₂RR efficiency) in a characteristic way: C₂₋₃ products, such as ethylene, ethanol and propanol became suppressed, whereas the production of C₁ products, such as CO, HCOO⁻ and CH₄, was favored. This resulted in a clearly smaller ratio of (C₂₊/C₁) products over the tested potential range (Figure 4.3 e). C₂₋₃ product yields, in particular that of ethylene, were exceptionally high on the unsupported, Cu₂O-derived, 35 nm Cu nanocubes, U-NC, and met or exceeded the faradic efficiencies observed previously on larger, cubic Cu catalysts or oxide-derived Cu catalysts.^[142, 143] Previously, simple physical mixing of Cu NPs with Ketjenblack carbon powder prior to electrode casting showed similar shifts in faradaic selectivities, and was attributed to a disrupted morphological particle evolution during CO₂RR from spherical to cubic morphologies.^[144] While that view placed emphasis on dynamic structural changes of Cu particles on carbon surfaces as the underlying mechanism, it neglects the contributing effect of an effectively larger mean interparticle distance on a support, associated with less likely re-adsorption of reactive intermediates such as CO, and their consecutive reaction and protonation.^[145, 146] Grosse et al. recently showed a strong dependence of the experimental CO₂RR reactivity of electrodeposited, several hundred nanometer-sized large Cu cubes on their underlying substrates, which was chosen as either a Cu foil, or a carbon paper. Their analysis suggested a difference in the morphological and chemical stability caused on the substrate. The weak interaction with the carbon was proposed to cause a stronger morphological degradation and faster chemical reduction to metallic Cu, compared to the cubes deposited on a Cu foil support, on which Cu(I) species

could still be detected. The fast, chemical reduction to metallic oxidation state of the cubes deposited on carbon was held responsible for the observed enhancements in CO and CH₄ production combined with a suppression of ethylene. Conversely, the stabilization of Cu(I) species and Cu {100} facets was deemed critical for achieving sustained high ethylene yields.^[75] Finally, the effect of interparticle distance, as suggested above, can also be an essential factor affecting the experimental selectivity and faradaic efficiency. The dispersion of the Cu nanocubes on the high surface area carbon support, as evidenced by TEM measurements and the lead-UPD based assessment of the accessible surface area, results in an effective physical separation of active surface sites of adjacent Cu cubes. A larger mean interparticle distance was previously associated with a less effective interparticle transport of intermediates by diffusion across the electrolyte. This proved detrimental for the observed C₂+ selectivity.^[145, 146]

The stability and role of {100} facets. To further deconvolute the possible origins of the difference in the catalytic reactivity and faradaic efficiency patterns, we tracked the morphological and crystal phase evolution of the S-NC and U-NC catalysts. Despite the stable high C₂H₄ efficiency, the initial cubic shape of the Cu₂O NPs was lost during the CO₂RR after one hour of applied test time. Figure 4.4 (a,b) and Figure 4.4 (d,e) show electron micrographs of both catalysts before and after 60 min of continuous CO₂ electrolysis at constant electrode potential of -0.95 V_{RHE}. The loss of the original well-defined cubic morphology is clearly visible. In addition, the particles appear to have agglomerated and merged, forming aggregates without any clearly defined preferential structure or morphology. Further microscopy of higher resolution clearly shows this strong morphological transition, as seen in Figure A 1.2. From this, we conclude that it is unlikely that the observed stable selectivity and faradaic efficiencies over 5 hours (Figure 4.3 c, Figure A 1.6), in particular, the high ethylene efficiency originate from a well-defined stable initial cubic morphology. Either the cubic morphology disappears very quickly during the first seconds or minutes, or the faradaic efficiency over the first hour is independent of the Cu NP morphology. Previous studies on metallic Cu cubes of various size, have attributed their high C₂ selectivity to the sustained stable presence of {100} facets^[77], which are known to catalyze the CO dimerization to ethylene already at low overpotentials.^[50, 147, 148] In the present study, however, in which morphologically unstable, Cu₂O-derived Cu nanocubes were deployed, yet comparable ethylene efficiencies were observed, it is clear that additional parameters besides facet- or shape selection appear to control the experimental faradaic efficiency trajectories in Figure 4.3 (a,b). In other words, it appears that a stable {100} facet-rich, cubic Cu morphology may be a sufficient, but not a necessary criterion for sustained enhanced C₂, in particular, the ethylene yield.

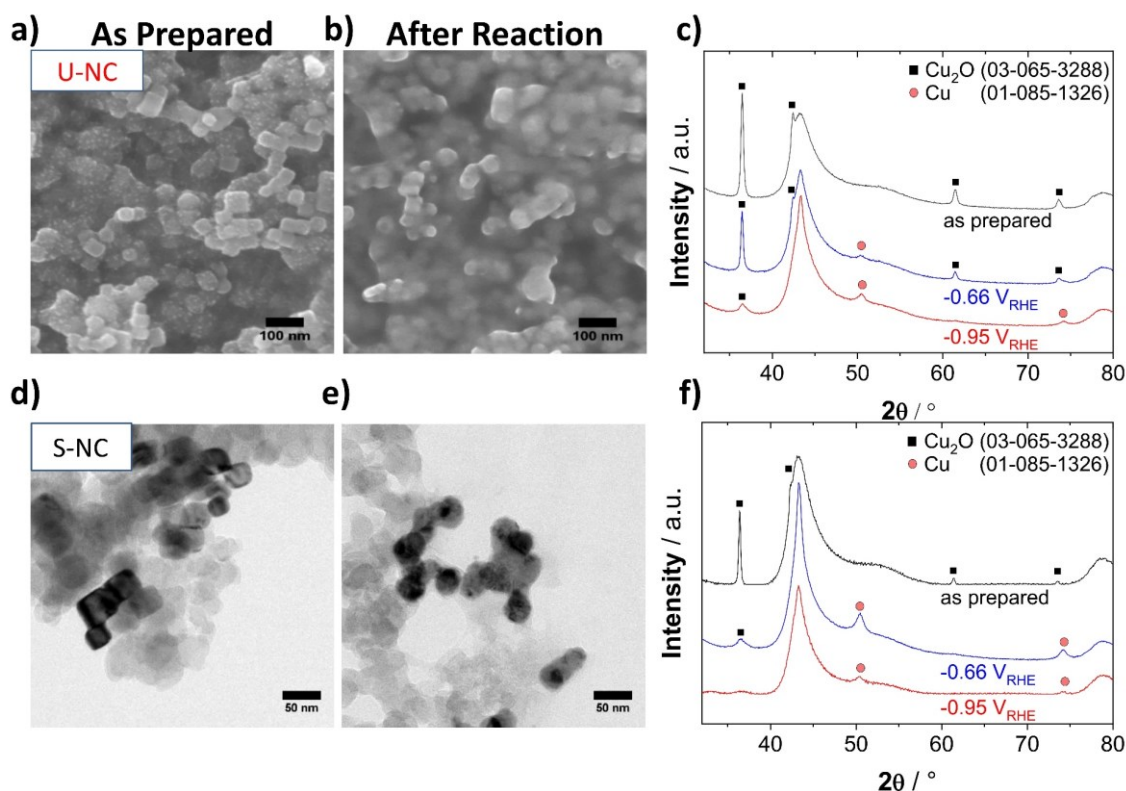


Figure 4.4 (a) SEM images of the unsupported catalyst, U-NC, as prepared and (b) after 1 hour of CO₂ electrocatalysis at an electrode potential of $-0.95 V_{RHE}$. (d) TEM images of supported Cu nanocube, S-NC, (23 wt%) catalyst, as prepared and (e) after 1 hour of CO₂RR testing at $-0.95 V_{RHE}$. (c) XRD patterns of the U-NC catalyst and (f) the S-NC catalyst after initial deposition on a glassy carbon electrode (black), after 1 hour of CO₂RR at $-0.66 V_{RHE}$ (blue) and after 1 hour at $-0.95 V_{RHE}$ (red). XRD patterns of the blank glassy carbon plate and of the as prepared catalyst powders are displayed in Figure A 1.7 as reference.

Oxide-derived Cu. In previous CO₂RR studies, the suppression of the yield and efficiency of CH₄ combined with sustained enhanced ethylene yields were reported for neither shape-controlled nor nanostructured, that is, with characteristic sizes below 100 nm, oxidized copper catalysts that chemically reduced to roughened metallic Cu surfaces under reaction conditions (referred to as oxide derived Cu, OD-Cu). While the mechanistic origins of enhanced C₂ dimerization products (mostly ethylene) on {100} facets are well described by experiments and theory, the molecular reasons for the improved performance of OD-Cu surfaces are still controversial. Different factors, such as an increase of the local pH due to large surface roughness compared to a polished non-oxidized Cu foil^[149], the presence of grain boundaries after reduction^[72, 150], remaining oxygen species within the catalyst surface^[59, 142] and the enhanced formation of undercoordinated Cu sites^[53] have all been correlated and associated with the high selectivity towards dimerized C₂ reaction products.

Origins of sustained high C₂₊ yields. Our results suggest that stable faradaic efficiency patterns similar to OD-Cu bulk catalysts can be obtained on morphologically unstable, smaller (35 nm) unsupported Cu(I) oxide nanoparticles as well.^[72] The relative real electrochemical surface areas, as

derived by Pb-UPD, of the reduced U-NCs and S-NCs (0.8 cm² vs. 2.6 cm², respectively) show that, at least for the present case, the catalyst surface roughness value alone, resulting from the reduction of the initial Cu(I) oxide cubes, is not a reliable predictor of C₂⁺ efficiency. We hypothesize that other factors, such as the detailed geometric nature of the resulting stepped OD-Cu surfaces, or the chemical state of the Cu atoms at the catalyst surface, constitute the mechanistic origin of and control the experimental product selectivity during CO₂RR. The chemical state of the Cu surface atoms may thereby depend on the presence of metallic or non-metallic adatoms at or below the surface combined with their electrochemical environment, such as the double layer structure and its ionic components.

Nilsson and co-workers proposed that an early, low overpotential onset of ethylene, that is -0.60V_{RHE} on OD-Cu vs. -0.75 V_{RHE} on polycrystalline Cu, and enhanced production during CO₂ electroreduction on electrochemically prepared Cu-based nanocubes relied on the initial, perhaps sustained, presence of Cu oxides in or near the surface.^[141, 151] Later Mistry et al. showed extraordinarily high ethylene selectivity during the CO₂RR for an oxygen-plasma treated copper foil. The oxygen plasma treatment resulted in a thick Cu oxide film. The Cu oxide layer partially reduced under reaction conditions, yet STEM-EDS analyses after the catalytic tests suggested the sustained presence of a small fraction of oxygen atoms and Cu(I).^[59] A possible theoretical explanation for this observation was provided by Xiao et al. The authors suggested that a mixed matrix of metallic and oxidized copper can facilitate the chemical dimerization of adsorbed CO.^[63] Furthermore, the possible important role of residual subsurface oxygen atoms, generated during the reduction of oxidized copper, is discussed in multiple recent publications and an amorphous metallic Cu layer was suggested as a possible stabilizing site for them.^[60-62, 64, 152] Moreover, the stabilization of Cu(I) species has also been demonstrated in the presence of Br and I.^[93, 153, 154] The highly controversial nature of this topic is reflected in another recent DFT study by Garza et al. that put forward the mechanistic role of local electric fields that would render the presence of subsurface oxygen atoms both unnecessary and unlikely due to their low stability. An experimental isotope study of the stability of oxygen atoms in O¹⁸ –labelled copper oxides by mass spectrometry confirmed the relatively low stability of subsurface oxygen atoms as well.^[65, 66] Nevertheless, the theoretical studies carried out so far have not been able to mimic the complex structure and morphological features typical of the most active oxide-derived Cu catalysts. A possible explanation for the discrepancy between some of the previously reported results might rely in the fact that Cu(I) species might be less stable on flatter Cu systems such as those accessible to theorists. Even more importantly, some of the studies available so far in the literature refuting the existence of Cu(I) species employ ex situ experiments or experimental techniques that are inherently not sensitive enough to small Cu(I) and/or oxygen contents, in particular, if they are available in the form of amorphous highly-disordered phases. This is why more direct insight in the evolution of the chemical state and the structure of initially oxidized copper under CO₂RR reaction conditions is required to unravel the mechanistic origins of the favorable C₂ efficiencies, in the present case of the unsupported Cu nanocubes, U-NC, versus the supported Cu nanocubes, S-NC.

Post-reaction, quasi *in situ* and *operando* catalyst characterization. To gain further insight into structural and chemical state of the surface and bulk of the S-NCs and U-NC we investigated first the crystalline phase structure of the nanocubes before and after CO₂RR using grazing incidence X-ray powder Diffraction (GI-XRD) (Figure 4.4 c,f). Figure A 1.7 shows additional control XRD patterns involving the catalyst powder and bare support substrates. As expected from the strongly reducing reaction environments, the characteristic metallic Cu(200) Bragg diffraction reflection at 50° indicated the formation of metallic Cu after 60 min of reaction at an applied electrode potential of -0.65 V_{RHE}. Interestingly, the presence of a cuprite Cu₂O(111) facet reflection at 36° remained visible for samples with and without carbon support. The Cu₂O pattern intensity, and thus its molar amount decreased under more negative, more strongly reducing electrode potentials (see patterns at -0.95 V_{RHE}). This observation implies a surprising chemical stability of this Cu(I) phase, contrary to thermodynamic expectations. Nevertheless, we acknowledge the limitations of *ex situ* XRD to get a proper assessment of the phase-evolution of the catalyst, especially due to the highly reactive nature of near-surface metallic copper under ambient conditions. Additionally, changes in nanoparticle orientation can also influence the intensity ratio of observed reflexes in GI-XRD. This is why we resorted to *quasi in situ* X-ray Photoelectron Spectroscopy (XPS) to trace the evolution of the chemical state of the surface of both the unsupported Cu nanocubes, U-NC, and the supported ones, S-NCs, in combination with *operando* X-ray Absorption Spectroscopy (XAS) to assess the changes in the bulk phase under reaction conditions. Those complementary techniques allow a comprehensive evaluation of phase changes (structure and composition) during the reaction.

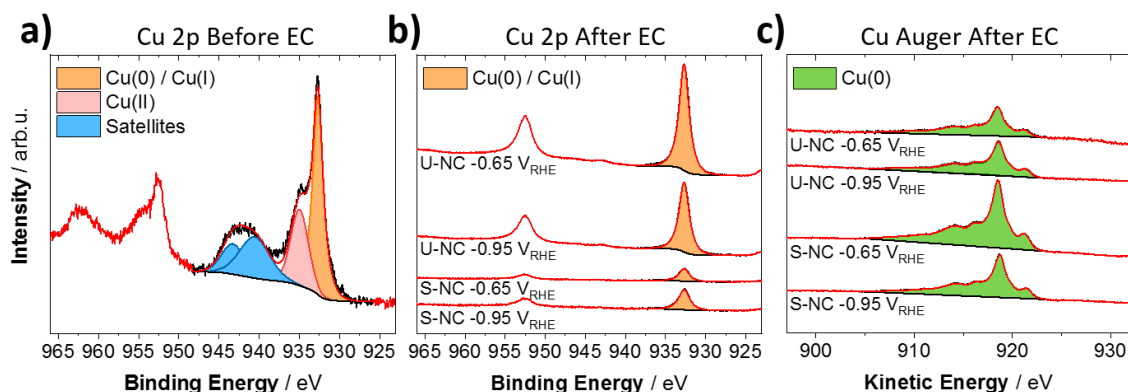


Figure 4.5 (a) XPS Cu 2p of as prepared U-NC deposited on a glassy carbon electrode. (b) Quasi in situ XPS Cu 2p and (c) Cu Auger LMM spectra of the U-NC and S-NC (23 wt%) catalyst after one hour of CO₂RR at -0.95 V_{RHE} and -0.65 V_{RHE}. Cu AES of as-prepared catalysts can be found in Figure A 1.8.

The *quasi in situ* XPS measurements (Figure 4.5 a-c) suggested a complete chemical reduction to metallic Cu of the near surface region after about one hour of reaction at low (-0.65 V_{RHE}), as well as more negative (-0.95 V_{RHE}) kinetic overpotentials. This change in redox state showed no dependence on the presence of a high surface area carbon catalyst support, thus was comparable for the U-NC and

the S-NC sample. While our XPS results show a fast reduction of the near surface region, it does not allow for a statement about possible defects introduced during the reduction or the oxidation state of deeper catalyst layers. Here, our analysis by *operando* XAS helps to add further insight into this system.

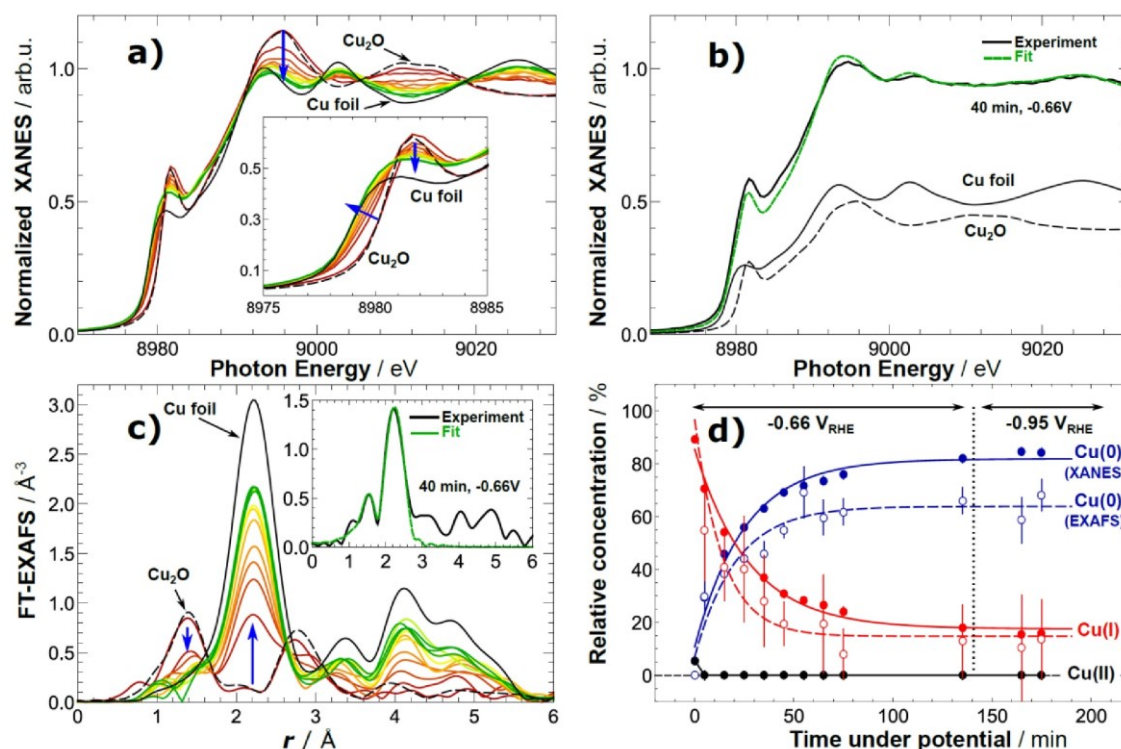


Figure 4.6 (a) Cu K-edge XANES data of U-NC sample acquired under *operando* CO₂ reduction conditions. (b) Representative example of catalyst XANES data fitting with a linear combination of reference spectra (the latter are also shown, scaled by their importance to the analyzed catalyst spectrum). (c) Fourier-transformed (FT) Cu K-edge EXAFS data of U-NC sample acquired under *operando* CO₂ reduction conditions. Representative example of EXAFS data fitting is shown in the inset. (d) Temporal evolution of the chemical composition of the Cu₂O cubes during CO₂ electroreduction obtained from the linear combination analysis of XANES data (filled circles) and coordination numbers from EXAFS data fitting (empty circles). Solid and dashed lines are guides for the eye.

The *ex situ* XAS fingerprints of the as-prepared shape-controlled Cu₂O nanocubes (see Figure A 1.9) match those of the Cu₂O reference material almost perfectly, suggesting similarity in both the Cu chemical state and the local coordination. The XANES spectrum (Figure A 1.9 a) showed an intense pre-edge feature at 8981.1 eV typical for Cu₂O (1s-3d transition). Similarly, the first feature above the edge has its maximum at 8995.5 eV and is considerably less intense than the corresponding characteristic feature of the CuO reference. The Fourier transform of the EXAFS spectrum (Figure A 1.9 b) also displayed the characteristic peaks of Cu₂O, namely at 1.4 and 2.8 Å (uncorrected for phase shift). The former peaks along with the structure, well seen between ca. 3.5 and 5.5 Å, indicate a well-developed long-range order in the sample.

Next, the Cu₂O nanocubes were deployed in an *operando* X-ray analysis cell and their chemical state and local structure was tracked during the electrochemical reduction of CO₂. Figure 4.6 shows *operando* XANES (Figure 4.6 a) and EXAFS (Figure 4.6 c) spectra recorded approximately every 10 minutes under chronoamperometric conditions at -0.66 V_{RHE} and subsequently at -0.95 V_{RHE}. There were drastic changes taking place in the sample already during the first 10 minutes under the moderate applied potential. While the electrode potential was kept constant, the pre-edge features became broader, less intense, and the absorption edge shifted to lower energy towards its position in the spectrum of a metallic foil. At the same time, the feature above the edge gradually changed its shape towards a two-peak feature characteristic of metallic Cu. The slightly higher intensity of the pre-edge feature in the *operando* XANES data as compared to that of a metallic Cu reference is a signature of self-absorption effect. However, by comparing the results of quantitative XANES and EXAFS analysis for the as-prepared sample (for which both fluorescence and transmission data were available, where the latter are not affected by self-absorption, see Table A 1.2), the obtained values agree within the uncertainties of our analysis, confirming that self-absorption does not affect the conclusions discussed below.

A linear combination fitting analysis of the *operando* XANES data, using Cu foil (metallic) and Cu₂O as basis spectra (Figure 4.6 b) evidenced a bulk reduction of the Cu₂O species in the cubes at -0.66 V_{RHE}. However, a significant fraction of Cu⁺ species (ca. 20%) can still be detected even after two hours of reduction in the H-type cell. Further increase of the potential did not induce any additional changes in the chemical state of copper, and did not result in any reduction of the Cu⁺ species. During the reduction, the Cu local environment as probed by the EXAFS spectra shows a rapid evolution of the metallic Cu-Cu distance peak at 2.2 Å (uncorrected) accompanied by an abrupt decay in the Cu₂O-related peaks (Figure 4.6 c). For quantitative analysis, we perform EXAFS data fitting (Figure A 1.10 and Table A 1.2). The metallic Cu-Cu coordination number (CN_{Cu-Cu}) increases from 3.6 after the first 10 minutes of reaction to ca. 8 within 70 minutes and the Cu-O (CN_{Cu-O}) drops from ca. 2 (as in Cu₂O) down to 0.3 within the same time (see Table A 1.2 for details). Cu-Cu CN barely changes when the catalyst was kept at -0.66 V_{RHE} for additional 60 minutes, or when, afterwards, when the potential was increased to -0.95 V_{RHE}. The findings from the EXAFS data analysis are in agreement with the XANES data. To facilitate the comparison of XANES and EXAFS results, in Figure 4.6 d we plot Cu-Cu and Cu-O coordination numbers, extracted from EXAFS data fitting, divided by respective bulk values (12 and 2, correspondingly) as estimates of concentrations of Cu⁰ and Cu(I) species. Remarkably, while for coordination number for Cu-O bond, as extracted from EXAFS, is in agreement with concentration of Cu(I) species, as obtained from XANES analysis, the Cu-Cu CN is noticeably smaller than expected from XANES analysis, indicating thus the presence of a large amount of undercoordinated Cu sites. Indeed, the final CN was distinctly different from bulk copper and showed no considerable changes even after extended periods of time or after the increase of potential. This could be indicative of an enhanced roughness or porosity in the cubes after exposure to the CO₂ electro-reduction conditions.

The presence of undercoordinated atoms or defective structures gives rise to strong binding-sites in oxide derived materials, which had repeatedly been suggested to have an influence on CO₂RR in experimental studies by Kanan and coworkers.^[55, 155] The stronger binding of possible reaction intermediates such as CO to highly defective O₂-plasma treated oxidized Cu surfaces was also demonstrated using temperature programmed desorption.^[154] In a recent theoretical study, Liu et al. supported this idea and suggested that the special performance of recent materials is actually a result of edges and steps introduced to the system^[156], which has also been proposed in an early work on polycrystalline copper.^[53] Our results are in line with these studies, and provide new evidence for a formation mechanism of undercoordinated sites by electrochemical reduction of oxidized copper. It is worth mentioning that the observed surprising stability of cationic Cu species during the catalytic testing under the strong reductive conditions, as obtained here independently both from operando XANES and EXAFS data analysis, is in line with our previous results from ex situ XRD. However, a controlling influence of Cu(I) species on the observed time trajectory of the FE values and catalytic performance cannot be irrefutably concluded. Due to the difference in probing depth of the techniques, the combination of *quasi in situ* XPS and *operando* XAS allowed for a quite complementary view on the chemical reduction of the Cu₂O nanocubes: The catalysts are undergoing a fast chemical reduction at the surface, which is progressing with time towards deeper layers. This could explain the absence of any correlation between the long-term selectivity and the loss in Cu(I) species, as the catalyst-surface became completely reduced after a relatively short reaction time.

4.1.3 Conclusions

This contribution explored and aimed to identify chemical and structural factors that control the experimentally observed catalytic selectivity of the CO₂RR on oxidized shape-controlled CuO_x particles. More precisely, this study traced the individual faradaic product efficiencies over time and linked their evolution to changes in the chemical state at the surface and bulk and in the catalyst morphology. To achieve this goal, shape-controlled crystalline, single phase Cu₂O cubes of nanometer-sized dimensions were chosen as the catalytic active phase. The nanosized cubic CO₂RR catalysts were deployed and analyzed in form of unsupported nanoparticulate catalyst films (U-NC), and compared to a format where they were supported on a high surface area carbon material (S-NC). Both U-NC and S-NC were tested in double compartment H-Cells. For both catalyst formats, the faradaic product efficiencies were recorded over time and the concomitant evolution of the physico-chemical states of the supported and unsupported nanocubes was tracked at varying time intervals, using *ex situ*, *quasi in situ* and *operando* spectroscopy, diffraction, and microscopy. Thereby, we followed the molecular transformations in the morphological structure as well as in the chemical state of the initially oxidic Cu nanocubes during the catalytic reaction and were able to arrive at new insights about the mechanism of the changes in their efficiency with time. Our main conclusions are as follows: The unsupported nanocubes catalysts prepared here displayed high C₂₊ yields in the H-Cell. Dispersion of the Cu₂O nanocubes on a high surface area carbon support, in contrast, drastically shifted their experimental

faradaic efficiencies toward C₁ products. Hence, the otherwise identical nanocubes exhibited a pronounced support effect, which we attribute, at least in part, to a larger interparticle distance that makes readsorption of CO and proton coupled dimerization less likely. There was no evidence that the surface roughness was significantly controlling the experimental C₂₊ efficiency, for instance, via enhanced local pH changes. After one hour of reaction, the cubic morphology was lost for both the unsupported and supported Cu nanocubes, while the faradic product efficiency over at least the first 5 hours remained distinct, yet very stable with time, as measured in the H-Cell experiments. This implies that the initial (100) facet- rich cubic shape appears to have no causal bearing on the distinct faradaic efficiency patterns, in particular on the sustained high C₂₊ yields of the unsupported catalyst particles. Tracking experiments using X-ray diffraction and spectroscopy suggested that the initial Cu₂O single phase gradually disappeared and gave way to metallic Cu nanoparticles. This process proceeded, however, much more slowly than previously anticipated, and a noticeable fraction (up to 20%) of cationic copper species was present in the sample even after several hours of continuous CO₂ electroreduction according to our operando XAS data. The surface of the initial oxidic nanocubes, however, reduced on shorter time scales (XPS). The transformation of the cube surface into metallic Cu justified the use of Pb underpotential deposition to assess the real electrochemical surface area. It also led us to a conclusion that the emergence of defects in the Cu lattice during the reduction of the nanocubes largely contributes to the observed stable efficiency patterns. In all, our present data and conclusions demonstrate the impact that the nature of a support (metallic self-support or carbon support) can have on the catalytic product yields.

4.2 Preparation and catalytic selectivity of Cu₃N particles for the electrochemical CO₂RR

Investigations of cationic Cu compounds as catalysts in the electrochemical CO₂RR have largely included anions from the 6th and 7th main group of the periodic table. Here, especially oxides and halides have been reported to be highly active and selective catalysts for the CO₂RR, which has often been correlated to compositional and morphological effects. To date, studies on Cu-based compounds with anionic elements of the 5th main group of the periodic table remain rare, which poses as a gap in understanding the origins of CO₂RR performance on cationic Cu compounds. The present work extends insights in CO₂RR research on cationic Cu compounds towards structures containing the N³⁻ anion. Here, Cu₃N nanoparticles are investigated as electrocatalyst for the CO₂RR and the effect of variations in phase composition on the catalytic selectivity is studied.

4.2.1 Introduction

In this study, we investigated Cu₃N nanoparticles prepared from a temperature-induced decomposition of Cu(NO₃)₂ in an organic media as the catalyst for aqueous CO₂RR. By simple variation of temperature during the synthesis, we obtained Cu₃N with different particle sizes and at the highest temperatures particles of a purely metallic Cu phase. We show that the Cu₃N nanoparticles can be selective catalysts for the production of CH₄, whereas the presence of metallic Cu shifts the selectivity to C₂H₄ generation. In this, the present work suggests that the detailed phase composition of Cu-based materials can have a large impact on the selectivity for the electrocatalytic CO₂RR.

4.2.2 Results and discussion

Thermal decomposition of Cu(NO₃)₂*2.5 H₂O in presence of ODA. In this study, we modified a previously reported procedure for the synthesis of Cu₃N particles. ^[135] Here, we used Cu(NO₃)₂*2.5 H₂O as the precursor for the thermal preparation of Cu₃N particles in the presence of octadecylamine as surfactant and octadecene as high-boiling solvent. The synthesis comprises a sequence of four temperature steps (I. to IV.) under protective nitrogen atmosphere, schematically depicted in Figure 4.7. Here, the mixture is initially heated to 70 °C (I.) to obtain a homogenous solution, followed by a step at 120 °C (II.) to remove crystal water contained in the precursor metal salt. At 150 °C (III.) we observed a change of color from an initial blue to green and finally to yellow. An early study on the thermal decomposition of Cu(NO₃)₂*3 H₂O at reduced pressure reports the formation of Cu₂(OH)₃NO₃, which is decomposed to CuO at 100-150 °C, while other work reports a temperature range of 160-235 °C for the same process. ^[157, 158] We suspect that Cu₂(OH)₃NO₃ is also formed at temperature stage III. of our experiments, which could explain the observed color change. As we did not observe the presence of a CuO phase, vide infra, and our reaction environment differs considerably to ones used in the referred studies, it is likely that the decomposition mechanism follows a different pathway. For the

final thermal step (IV.), which leads to particle nucleation and growth, we investigated the effect of temperature variation between 200 °C to 250 °C. To understand the phase evolution of the Cu(NO₃)₂ precursor with increasing temperature, we performed a thermogravimetric analysis coupled to a differential scanning calorimetry TGA-DSC measurement by varying the temperature from 30 °C to 500 °C. The results of the TGA-DSC measurement are shown in Figure 4.7 with indications for the different temperature steps used. Here, distinct changes in the heat flow indicate a thermal process, which is most evident for stage II of dehydration and stage III of decomposition. At a temperature of around 220 °C in stage IV of particle nucleation, an additional transition of lower heatflow intensity is apparent.

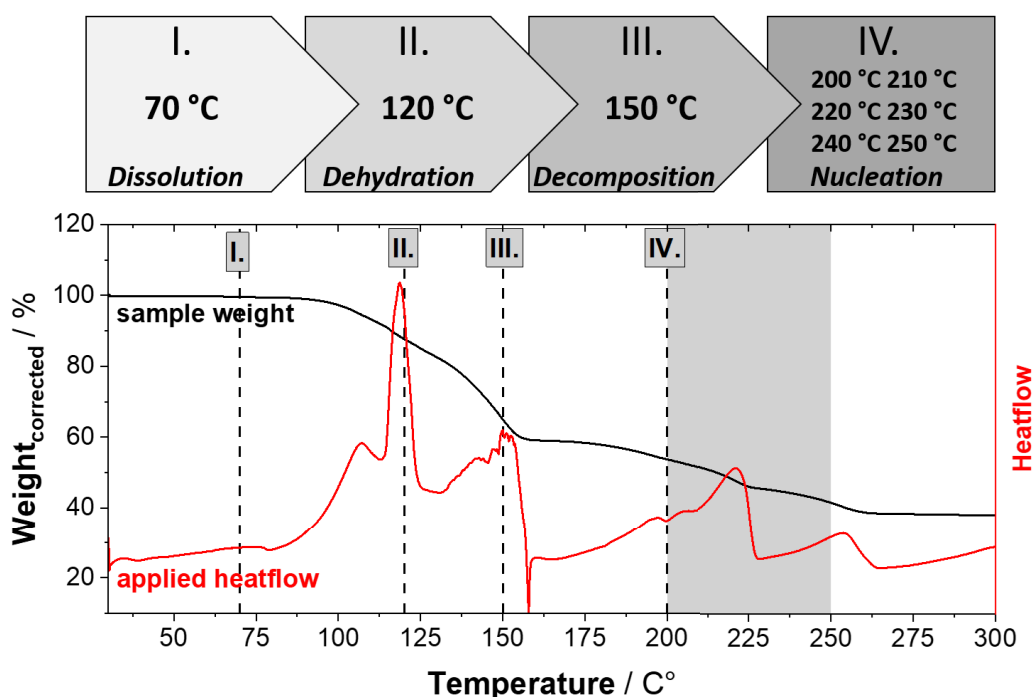


Figure 4.7 Thermogravimetric analysis coupled to a differential scanning calorimetry (TGA-DSC) measurement of the Cu(NO₃)₂ precursor used for the preparation of Cu₃N particles. Vertical lines indicate the applied heating steps during the synthesis. The shaded area at above 200 °C indicates the temperature region chosen during particle growth. The proposed sequence of underlying thermal processes is schematically depicted above.

Morphological and compositional material characterization. We used XRD to characterize the powder samples synthesized at different reaction temperatures. In Figure 4.8 (a), a clear influence of the temperature during the synthesis for the resulting composition of the crystalline phase is apparent. For the synthesis at 200 °C, we observed just a single reflection at low 2θ angles of around 20 °, which we could not assign to a specific phase and implies insufficient thermal energy for the formation of (crystalline) particles. Once we increased the temperature during synthesis to 210 °C, we observed multiple reflections in the XRD pattern, which we could assign to the formation of a Cu₃N phase. Further increase of the temperature to 220 and 230 °C, respectively, showed the sustained presence of

the Cu₃N phase, while the reflections seemed to become sharper at higher temperatures, which suggests an increased crystallite size. Interestingly, synthesis at temperatures of 240 and 250 °C revealed a drastically altered XRD pattern. Here, the reflections corresponding to the previously present Cu₃N phase diminished, and new reflections emerged, which we could assign to a metallic Cu phase. The sample prepared at 240 °C showed shoulders at 41 ° and 47 ° in the XRD pattern, which correspond to (111) and (200) facets of the Cu₃N phase, thus suggesting a minor presence thereof. In contrast, we could not observe a sustained presence of a Cu₃N phase in the XRD pattern of the sample prepared at 250 °C, which seemed to be of a purely metallic Cu nature. In Figure 4.8 (b), a blow-up of the TGA-DSC measurement of Cu(NO₃)₂*2.5 H₂O is shown for the temperature region chosen during particle nucleation. Here, vertical lines and shaded areas indicate the employed reaction temperatures and major component of the crystal phase, as derived from powder XRD measurements. The applied heat flow increased roughly between 200 °C and 225 °C, which fits well with the observed emergence of the Cu₃N phase. Subsequently, around 230 °C the heat flow shows a sudden decrease, followed by a slow increase until 255 °C. This observation is in good agreement with our observation of a phase transition from Cu₃N to metallic Cu, when we increased the reaction temperature during synthesis to 240 °C and above. Indeed, it has been reported that Cu₃N is thermally metastable and decomposes to metallic Cu by releasing gaseous nitrogen around 300 °C. [159-161] Considering the observation of a residual Cu₃N phase in the sample prepared at 240 °C, we take view that the formation of metallic Cu at high reaction temperatures originates in the thermal decomposition of a previously formed Cu₃N phase.

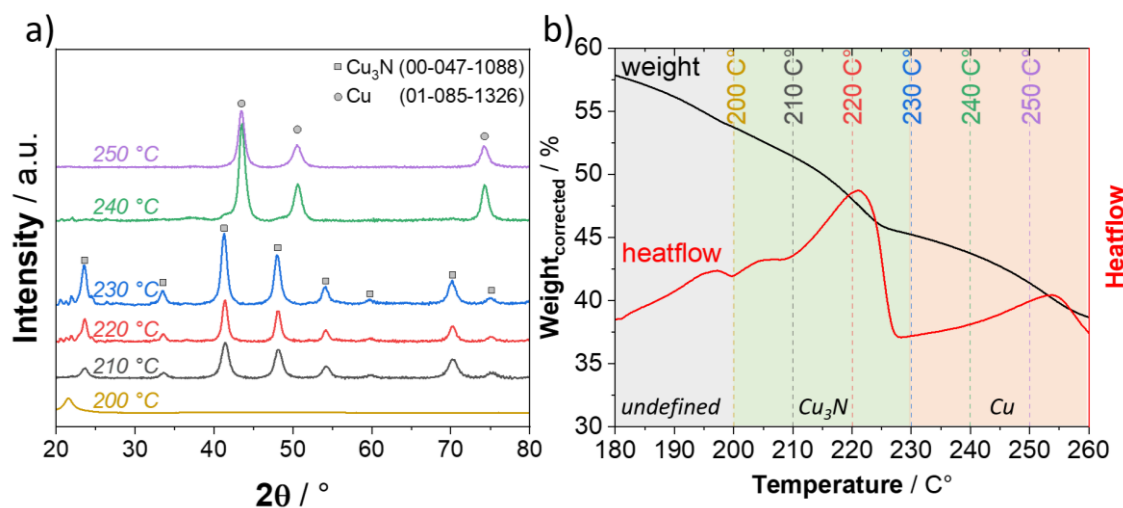


Figure 4.8 (a) Powder XRD patterns of the samples prepared by variation of the temperature during synthesis. (b) Enlarged section of the TGA-DSC measurement for the Cu(NO₃)₂*2.5 H₂O used as precursor in the particle synthesis. Here, vertical lines indicate the temperatures chosen during synthesis and shaded areas correspond to the crystalline phase of the resulting product from synthesis, as observed by powder XRD.

Next, we turned to TEM measurements to investigate the detailed morphology of the samples prepared at different reaction temperatures, which are shown in Figure 4.9. Again, we observed a pronounced influence of the reaction temperature. Here, the particles synthesized in the temperature range of 210

to 230 °C, which allowed the formation of a stable Cu₃N phase, showed a clear increase in particle size with higher reaction temperatures. Additionally, we observed a highly irregular morphology for the particles prepared at 210 °C, which became progressively more defined and seemed to approach a cubic appearance at reaction temperatures of 220 °C and 230 °C. Upon further increase of the reaction temperature to 240 °C, we observed the simultaneous presence of larger particles, comparable in size and shape to the ones prepared at 230 °C, and very small particles of highly irregular morphology. Considering the coexistence of a major metallic Cu phase and a minor Cu₃N phase, based on our previous results from powder XRD, we suspect that the small particles might be fragments of the initial Cu₃N particles, which have not yet undergone complete thermal decomposition to metallic Cu. For the particles prepared at the highest reaction temperature of 250 °C, we observed a polydispersity in size and morphology. Here some larger particles of cubic shape were visible mixed with an abundant presence of small spherical particles. In contrast to the 240 °C sample, we did not notice any small fragments supporting the perception of a complete thermal decomposition of the initial Cu₃N at this elevated temperature. Additional TEM measurements of a higher magnification are given in Figure A 1.11.

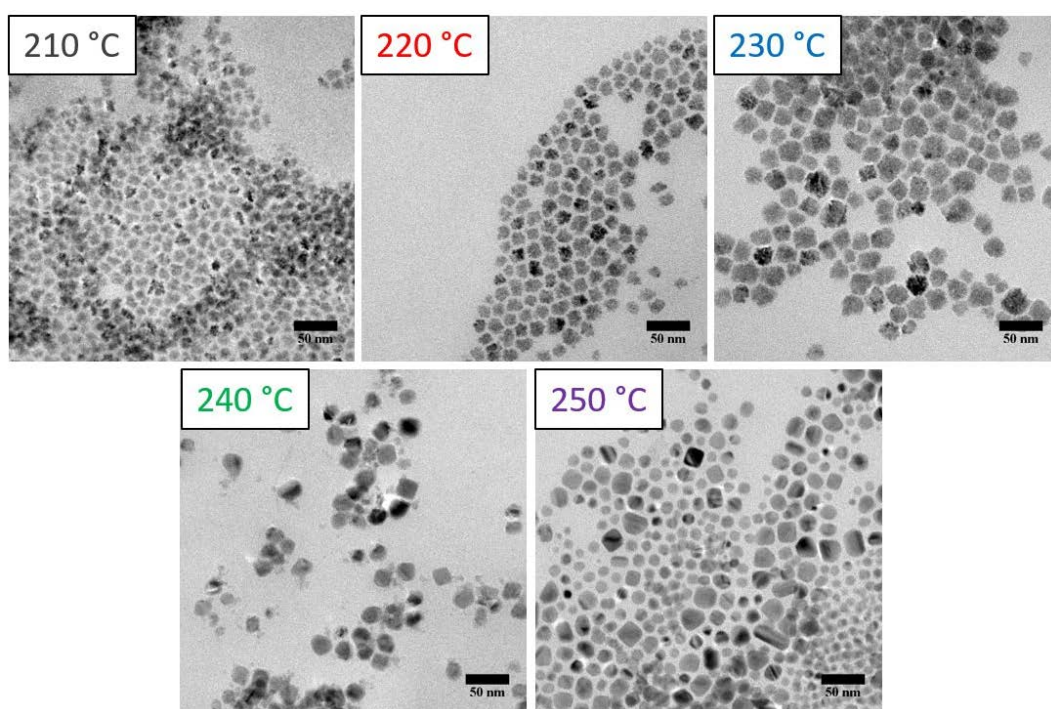


Figure 4.9 TEM images of the samples prepared at different reaction temperatures. The scale bar in each image corresponds to 50 nm.

Catalytic CO₂RR selectivity and activity. The catalytic properties during CO₂RR were investigated in an H-Cell setup in CO₂ saturated 0.1 M KHCO₃ electrolyte. Figure 4.10 shows the FE of the major products obtained during catalytic CO₂RR for particles prepared at different reaction temperatures. Here, we observed a distinct dependence of the product spectrum on the phase composition of the employed catalyst. Despite the pronounced morphological differences of the Cu₃N particles prepared

at reaction temperatures of 210 to 230 °C, we observed a high similarity in their catalytic selectivity. Here, the CH₄ FE increased in between -0.95 V_{RHE} and -1.25 V_{RHE} to a maximum of around 50 %, while C₂H₄ FE peaked at around 10 % for an electrode potential of -1.15 V_{RHE}, shown in Figure 4.10 (a,b). In contrast, the particles prepared at 240 °C, which were composed of a primarily metallic Cu phase, showed a decreased CH₄ FE peaking at 35 %, while C₂H₄ FE increased to around 18 %. The particles prepared at 250 °C, which consisted of a pure metallic Cu phase, displayed the highest C₂H₄ FE of all investigated catalysts, which exceeded 20 % FE. For the production of CO, shown in Figure 4.10 (d), there was no visible correlation to the type of employed catalyst during CO₂RR and the corresponding FE stayed below 8 % in all cases. As shown in Figure 4.10 (c), the competing HER was the dominant reaction at more positive potentials than -1.0 V_{RHE} for all catalyst and decreased to values of roughly 30 to 20 % at more cathodic electrode potentials of around -1.20 V_{RHE}. Again, all investigated catalyst displayed a comparable behavior for the FE of H₂, except for the particles prepared at 240 °C, which generally showed a more pronounced HER.

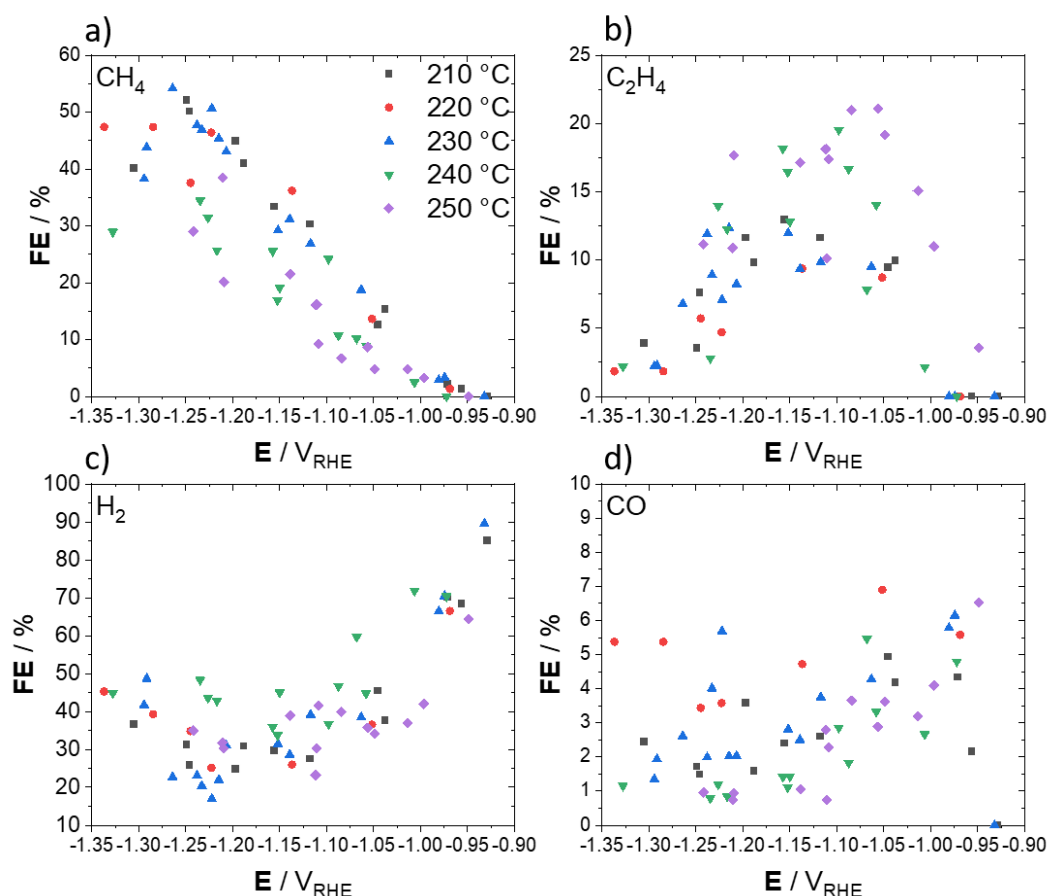


Figure 4.10 FE of the major products obtained during catalytic CO₂RR for the particles prepared at different temperatures: (a) CH₄, (b) C₂H₄, (c) H₂, and (d) CO.

Discussion on the origin of the catalytic selectivity. In contrast to the common assumption for oxide derived Cu catalyst that the presence of cationic Cu⁺ species favors C₂⁺ products during electrochemical CO₂RR, we observed that particles composed of Cu₃N tend to be more selective towards the formation of CH₄. Interestingly, the investigated metallic Cu particles obtained at higher reaction temperatures,

but otherwise identical synthesis, showed a more selective production of C₂H₄, compared to the Cu₃N particles. This relationship between phase composition and catalytic selectivity is clearly reflected in C₂H₄ to CH₄ FE-ratio of Figure A 1.12 (a). Here, catalyst prepared for from the Cu₃N temperature regime (210 – 230 °C), showed an almost identical trend in the change of C₂H₄ to CH₄ FE-ratio with electrode potential, whereas a major metallic Cu phase (240 °C) allowed a clearly higher C₂H₄ to CH₄ FE-ratio, which increased even further on the purely metallic Cu particles (250 °C). As we did not observe a comparable relationship between the catalytic activity, shown in Figure A 1.12 (b), and particle phase composition we assume that surface roughness is unlikely to cause the discussed effect. Such origin has been recently suggested for a nitride-derived Cu foil.^[162] In contrast to our work, the Cu₃N phase was grown on a Cu foil by vapor deposition in a NH₃/O₂ atmosphere at 550 °C and resulted in films with a thickness of 600 nm. The authors suggested, that a combination of local alkalization and abundance of undercoordinated reaction sites cause the observed high C₂₊ selectivity on the fully reduced Cu₃N-derived Cu films. In a different study, Cu₃N particles were prepared in a thermal synthesis of high similarity to our work and additionally modified with a CuO_x overlayer, which was later electrochemically reduced to create core-shell Cu₃N-Cu particles.^[163] The Cu₃N-Cu particles showed a higher C₂₊ selectivity compared to reference Cu₂O-Cu particles with a Cu₂O core. The authors showed a sustained presence of cationic Cu⁺ in the Cu₃N-Cu particles during application an electrode potential of -0.95 V_{RHE} over 120 min by XAS spectroscopy. An analogous XAS analysis of the Cu₂O-Cu particles showed a much faster degradation of the cationic Cu⁺ content, which they correlated to the superior C₂₊ selectivity of the Cu₃N-based system. A high resistance of the Cu₃N phase against the reduction to metallic Cu during CO₂RR could also explain our observation of a high CH₄ selectivity for our pure Cu₃N catalysts. Here, a theoretical work has suggested that the beneficial properties arise from a synergistic effect of metallic Cu embedded in an oxidized matrix and that a purely oxidized matrix is actually obstructive for electrochemical CO₂RR.^[63] An additional possibility for the observed shift in selectivity with reaction temperature could be the formation of a native, thin oxide layer on our metallic Cu particles due to their exposure to air after synthesis. Such formation of CuO_x would be hindered on the already oxidized Cu₃N particles and could influence the corresponding catalytic properties. Future work will involve surface sensitive techniques, as XPS, and in-situ phase analysis to further elucidate the origins of the composition-related shift in the catalytic selectivity during CO₂RR.

4.2.3 Conclusions

The presented study investigated a thermal approach in organic solvent for synthesis of Cu₃N and Cu nanoparticles and explored their catalytic selectivity during CO₂RR in an H-Cell setup. Herein, a simple variation of reaction temperature during the synthesis in between 210 to 230 °C, allowed the preparation of different Cu₃N particle morphologies, whereas higher reaction temperatures allowed for the partial (240 °C) or complete (250 °C) decomposition of Cu₃N to metallic Cu particles. The morphological differences of the pure Cu₃N particles were not reflected in their corresponding

selectivity during electrocatalytic CO₂RR and showed a high selectivity for CH₄ production independent on the detailed particle morphology. In conjunction with the development of a metallic phase at higher reaction temperatures of 240 °C and 250 °C a shift of the catalytic selectivity away from CH₄ directed towards C₂H₄ was apparent. Correspondingly the highest ratio in C₂H₄ to CH₄ FE was observed for the particles synthesized at 250 °C, which only showed the presence of a purely metallic phase. The results of this study suggest that, in contrast to popular belief, the use of cationic Cu compounds as catalyst during CO₂RR must not always lead to an efficient system for the production of C₂₊ species. Dependent on the anion identity such systems can instead prove to be selective catalysts for CH₄ production.

4.3 Catalytic selectivity and phase changes of CuS particles during CO₂RR prepared by anion exchange of Cu₂O structures

In Cu-based research for the electrocatalytic CO₂RR, there is a vivid discussion on the origins of the generally high selectivity towards CO₂RR observed for oxide-derived Cu catalyst. It has been suggested that the electrochemical reduction of the oxygen containing Cu precursor is incomplete and results in the residue of Cu⁺, subsurface oxygen and oxide species that can alter the binding strength towards reactive intermediates. Next to those compositional effects, structural effects as low-coordinated reaction sites and pH gradients due to high catalyst surface areas have been hypothesized to dictate the observed activity and selectivity during CO₂RR. While there are a great number of reports on oxide-derived Cu catalyst, other Cu chalcogenides are rarely considered. Further insight into the origins of efficient and selective CO₂RR could be derived by extending the basis of Cu catalysts towards other chalcogenides anions and understanding their specific phase changes under reductive conditions and corresponding catalytic selectivity. In this context, this study investigates CuS as catalytic material for the electrochemical CO₂RR. The present work illustrates how the presence of S²⁻ anions in Cu structures greatly influences the catalytic selectivity observed for the CO₂RR and enables a selective production of HCOO⁻ by suppression of the CO-related reaction pathways.

4.3.1 Introduction

Within this work we have investigated CuS as catalytic material for the electrochemical CO₂RR. Here, we used previously discussed cubic Cu₂O material as precursor in the synthesis of CuS particles, that were prepared in aqueous conditions by means of anion exchange using (NH₄)₂S as the source of S²⁻. We observed a drastically changed CO₂RR selectivity of the CuS material, which primarily produced HCOO⁻ in contrast to the CO related pathway of the cubic CuO_x material. Structural investigations of the crystalline phase by GI-XRD revealed a two-stage transformation of the CuS material under reductive potentials, which proceeded through initially coexisting phases of Cu₂S and Cu₂O towards a final resulting mixture composed of Cu₂O and metallic Cu. This transformation occurred at potentials more positive than bulk CO₂ electrolysis. The obtained results are suggesting that the identity of chalcogenide species within a Cu-chalcogenide structure is an important parameter for CO₂RR that can critically influence the prevailing reaction pathway and control the observed catalytic selectivity during the CO₂RR.

4.3.2 Results and discussion

Material preparation and structural characterization. The preparation of the sulfur-modified Cu catalysts was adapted from a previously reported procedure for sulfidation of transition metals ^[136]. In short, cubic Cu₂O particles were dispersed in milli-Q water and exposed to an aqueous solution of (NH₄)₂S at room temperature. Two different catalyst were prepared by variation of the added volume of (NH₄)₂S: The first catalyst was prepared by addition of 0.5 mL of the sulfidating reagent diluted in

10 mL of water, the second catalyst by addition of 10 mL of the undiluted reagent. In the following, the two catalyst are referred to by their corresponding volume of $(\text{NH}_4)_2\text{S}$ addition during preparation. We observed strong morphological changes of the initially cubic Cu_2O particles upon addition of $(\text{NH}_4)_2\text{S}$, shown in Figure 4.11 (a). The 0.5 mL catalyst was composed of agglomerated particles having an ill-defined morphology and a particle size exceeding 100 nm. Interestingly, the addition of a higher volume of $(\text{NH}_4)_2\text{S}$ induced a rather different morphological evolution. Here, the 10 mL catalyst showed the presence of sheet-like particles, which were also subjected to the effect of agglomeration. To get a clearer understanding of the detailed morphology for the 10 mL catalyst, we used TEM for additional microscopy images of higher magnification, shown in Figure A 1.13. The closer inspection revealed that the sheets tend to form a hexagonal shape with a thickness of below 10 nm and edge-to-edge length of around 100 nm. A scheme of the morphological transition upon addition of $(\text{NH}_4)_2\text{S}$ for the 0.5 mL and 10 mL catalyst is shown in Figure 4.11 (b). The occurrence of two-dimensional morphologies have been repeatedly reported for Cu chalcogenides compounds, as Cu_xS and Cu_xSe , and have been correlated to their inherent anisotropic crystal structure. Here, usually strong ligands as octylamine are used to control the growth mechanism in order to prevent crystal aggregation.^[164-167] As we do not include additional ligands in the presented synthesis, it is feasible that the observed aggregates originate in the merging of smaller crystallites. Nevertheless, ligands are known to interfere with the electrocatalytic properties of a materials surface, which is why we specifically refrain from using them within this work. The phase structure of both catalysts was investigated by powder-XRD, which is displayed in Figure 4.11 (c). Both catalysts showed XRD patterns that were in good agreement with a reference of a pure CuS phase, suggesting a bulk conversion of the initial Cu_2O phase. However, it is important to consider the limitations of XRD, which is a bulk sensitive technique, unable to detect near-surface or amorphous structures. Therefore, we cannot guarantee a complete absence of any oxides at this point.

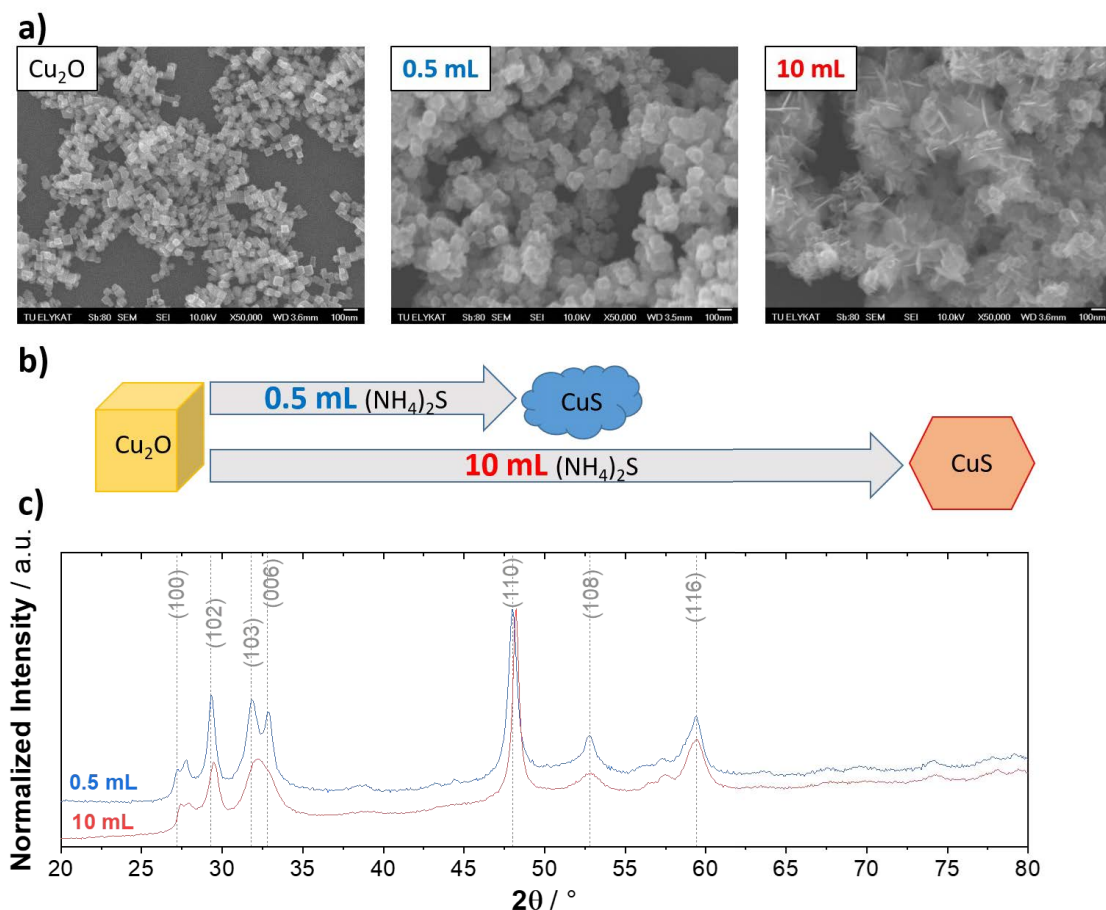


Figure 4.11 SEM images of the initial state of the cubic Cu₂O particles, after addition of 0.5 mL and 10 mL of (NH₄)₂S (a). Schematic representation of the morphological transition induced during the sulfidation (b). Powder-XRD patterns of the 0.5 mL and 10 mL catalyst with marks corresponding to the most intense signals of a CuS reference pattern, PDF-number:01-078-0877 (c).

Catalytic CO₂RR selectivity and activity. The performance of both catalysts was investigated in an H-Cell configuration using a CO₂ saturated solution of 0.1 M KHCO₃ as the electrolyte. Figure 4.12 (a) shows the geometric current density as a function of applied electrode potential for both synthesized CuS materials. The materials were comparable in catalytic activity, whereas the 0.5 mL catalyst showed a slightly steeper increase in current density with increasing potentials. The major compounds produced during CO₂RR are shown in Figure 4.12 (b), while minor products are shown in Figure 4.12 (c). Both investigated CuS materials displayed an almost exclusive production of HCOO⁻ from CO₂RR, which increased from around 40 % FE at an electrode potential of -0.67 V_{RHE} to a maximum of around 55 % FE at an electrode potential of roughly -0.85 V_{RHE}. Further increase of potential resulted in a decrease in FE for HCOO⁻ production and showed an increase in FE of the competing HER. Other CO₂RR products, as CO, CH₄, and C₂H₄ were evolved only in small quantities and showed low FE values of below 5 % over the whole investigated potential range.

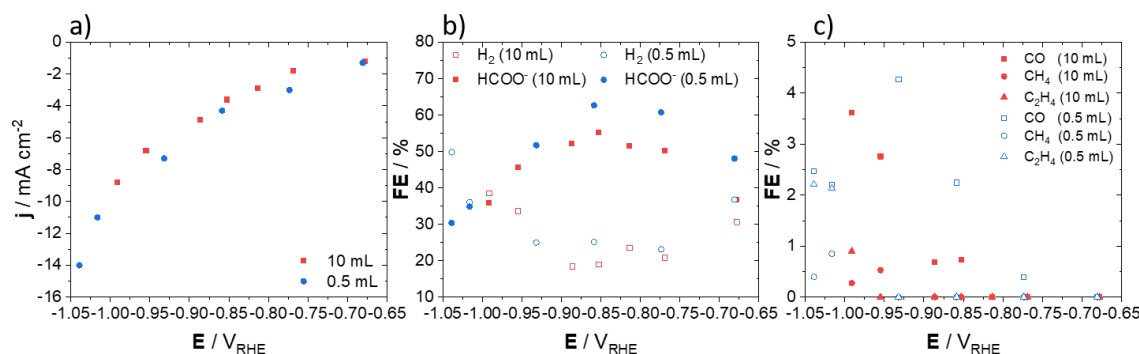


Figure 4.12 Geometric current density (a), faradaic efficiency of the main products, H_2 and HCOO^- , (b) and faradaic efficiency of the minor products, CO , CH_4 , and C_2H_4 (c), as a function of applied electrode potential obtained during catalytic testing of the CuS catalysts.

The observed electrocatalytic selectivity during CO_2RR is in large contrast to the selectivity of the initial cubic Cu_2O particles, as previously discussed in subchapter 4.1, and polycrystalline Cu foil. [34] The characteristic feature of Cu-based catalysts is the reaction pathway, which enables considerable amounts of post-CO reduction products, such as ethylene, methane, and alcohols. However, these products show an obvious suppression on the investigated CuS catalysts, whereas the production of HCOO^- is instead strongly favored. This observation is remarkable, as it suggests that the presence of S^{2-} can impact the dominance of one reaction pathway at the first branching point during the electrocatalytic CO_2RR . Here, the mechanism of the first electron transfer step during CO_2RR is suspected to determine the direction towards either HCOO^- or CO and all CO-related products (ethylene, methane, etc.). This has been suggested to occur from an oxygen-down binding mode for the production of HCOO^- and a C-down binding mode for CO related products. The observed shift in selectivity, therefore, could be an indication of an altered binding of reactive intermediates caused by the presence of sulfides or result from the specific surface structure of the CuS-derived material during CO_2RR .

Post-reduction GI-XRD investigations of CuS phase stability. To probe the electrochemical resilience of the CuS phase against the reductive environment during CO_2RR we used GI-XRD after applications of controlled electrode potentials to the 0.5 mL catalyst. Here, the tests were performed under identical conditions to the ones used during investigations of the catalytic selectivity. Figure 4.13 (a) shows the observed response of the current density as a function of the varied electrode potential. During routine testing of CO_2RR , we observed two reduction features during the scan of electrode potential towards the desired working potential (in between $-0.7 V_{RHE}$ to $-1.05 V_{RHE}$). The first reduction peak was situated at a $-0.15 V_{RHE}$ and the second at $-0.515 V_{RHE}$, whereas both peaks showed a shoulder at slightly more cathodic potentials. To investigate the underlying reduction process, we prepared two electrodes with the 0.5 mL catalyst, which were used to scan the potential in between $0.02 V_{RHE}$ to $-0.33 V_{RHE}$ and to $-0.68 V_{RHE}$, respectively, and were subsequently measured in GI-XRD. Both samples showed reduction features, during the first CV, that were in qualitative agreement with

the previously observed features during CO₂RR. Repetitive cycling of the potential within the mentioned segment did not reveal any additional features and only showed a slow increase in current, most likely associated to the onset of catalytic CO₂RR or HER. This observation suggests an irreversible reduction of the sample that occurred during the first potential cycle. Figure 4.13 (b) shows the results of GI-XRD measurements which were mentioned above. Here, the left panel shows the initial, as-prepared pattern of the 0.5 mL catalyst deposited on the glassy carbon substrate without application of a reductive potential. The pattern is in well agreement with the most prominent features of a CuS reference superimposed with the features of the glassy carbon substrate. For a reference GI-XRD measurement of a pure glassy carbon substrate see Figure A 1.7. Upon application of an electrode potential of $-0.33\text{ V}_{\text{RHE}}$, we observed a clear change in the GI-XRD pattern of the corresponding sample, displayed in the middle panel. Here, in contrast to the initial state of a pure CuS phase, we observed features that we assigned to a coexistence of a Cu₂S and a Cu₂O phase. This observation could be explained either by a competition of two parallel electrochemical reductions path from CuS towards Cu₂O and Cu₂S, respectively, or by an initial electrochemical reduction of CuS to Cu₂S and a subsequent chemical conversion of Cu₂S to Cu₂O. The right panel of Figure 4.13 (b) shows the GI-XRD pattern after application of an electrode potential of $-0.68\text{ V}_{\text{RHE}}$. Here, we observed a further change in the diffraction pattern with respect to the $-0.33\text{ V}_{\text{RHE}}$ sample. At this potential, the Cu₂S has been completely converted and coexisting phases of Cu₂O and metallic Cu are apparent. The observed presence of metallic Cu is thermodynamically expected, considering the reductive potential, whereas Cu₂O should not be stable. A possible explanation for the sustained presence of the Cu₂O phase could originate in kinetic considerations, or an oxidation of metallic Cu due to the inevitable exposure to atmospheric oxygen during GI-XRD experiments.

Taking into account our previous observation of shoulders for the reduction features at $-0.15\text{ V}_{\text{RHE}}$ and at $-0.515\text{ V}_{\text{RHE}}$ during CO₂RR testing, we propose a reduction mechanism that involves two superimposed electrochemical processes. Matching this assumption to our observations from GI-XRD measurements, we propose following phase-transition sequence (see Figure 4.13 (c)): First, the initial CuS phase is electrochemically reduced in parallel towards Cu₂O and Cu₂S. Second, both phases, Cu₂O and Cu₂S, are further reduced towards metallic Cu. Finally, a hypothetical third one, in which part of the metallic Cu is chemically reoxidized under air to Cu₂O.

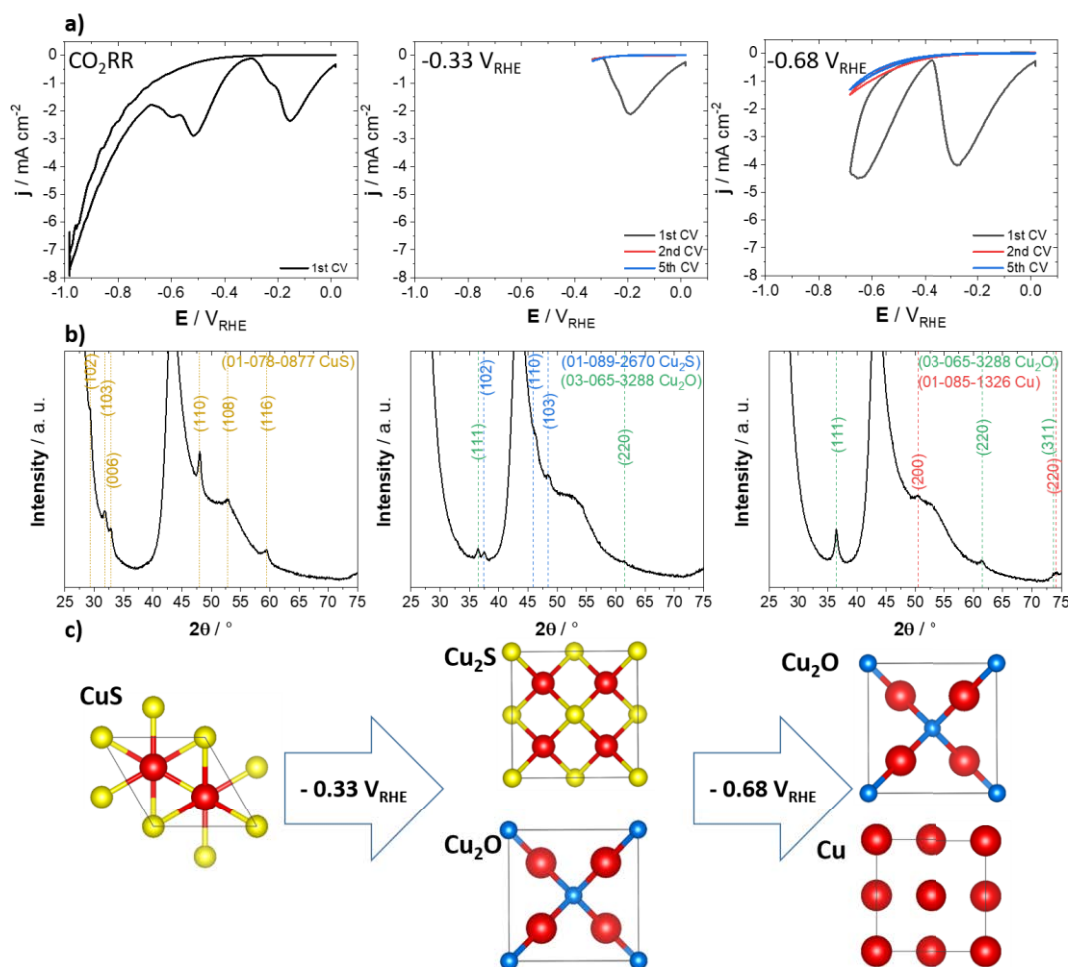


Figure 4.13 Cyclovoltamograms obtained during routine testing of catalytic CO₂RR and for scans towards an upper potential of -0.33 V_{RHE} and -0.68 V_{RHE} (a). GI-XRD patterns obtained for the as-prepared catalyst, left, after scanning the potential towards -0.33 V_{RHE}, middle, and after scanning the potential towards -0.68 V_{RHE}, right, (b). Schematic representation of the change in crystal phase of the initial CuS catalyst upon application of reductive potentials (c). All tests were performed using the 0.5 mL catalyst.

Origins of sustained HCOO⁻ selectivity. It is a remarkable observation, that even though the initial CuS phase was completely reduced at electrode potential more positive than applied during CO₂RR, the observed catalytic selectivity is still in stark contrast to that observed on common Cu and OD-Cu materials. Apparently, the phase composition of the bulk material is not a reliable descriptor for its catalytic CO₂RR selectivity. A possible cause of the observed absence of a correlation between catalytic selectivity and bulk composition after reaction conditions could lie within a different near-surface composition. Here, a remaining presence of sulfides or sulfur could influence the electronic structure and the associated catalytic properties of the surface region. Such a surface population of nanometric Cu_xS domains have been reported after electrochemical CO₂RR tests of CuS particles with varying compositional ratios of Cu_xS to Cu_xO. Here, they observed a detectable near-surface content of sulfides after CO₂RR tests by XPS measurements, while the Cu_xS concentration in the bulk dropped to a value of around 1 at%, which was independent on the initial Cu_xS content.^[168] While sulfides seem

to show a certain stability at the electrochemical interface during CO₂RR the mechanistic origins of the associated HCOO⁻ selectivity is still on debate. In a mechanistic study, an altered electronic structure of the S-containing Cu surface was suggested. Here, a weakened binding of the *OCHO and *COOH intermediate was reported to allow a more favorable pathway towards HCOO⁻ over CO during electrochemical CO₂RR.^[169] A different explanation lies in a more direct participation of S in form of an adatom. Here, the authors suggested an alternate reactions mechanism, which involved S acting as a hydride shuttle or active site for tethering of CO₂ molecules.^[170] In general, the electrochemical CO₂RR is known to be highly sensitive to the presence of adatoms on the metallic Cu surface. We have previously reported, that a sub monolayer coverage of 16 % Pb on a polycrystalline Cu surface is enough to dramatically suppress the mechanistic *COOH pathway and enable a selective production of HCOO⁻.^[171] The observation that even presumably low coverages of adatoms is sufficient to completely alter the CO₂RR selectivity could be indicative towards the important role of undercoordinated Cu sites that largely contribute to the observed CO₂RR activity and product spectrum. It is conceivable that CO₂RR on sulfide-derived Cu catalyst could also be subjected to a similar, site-specific positioning of the surface sulfur or sulfides. Such selective coverage of otherwise highly active reactions sites could therefore cause the dominance of alternative reaction channels. Although the techniques presented in this study are not providing the necessary surface sensitivity to directly verify the presence of S in the near-surface region, it is nevertheless very likely, considering the strong difference in catalytic properties for CO₂RR compared to metallic Cu.

4.3.3 Conclusions

In the presented study the catalytic selectivity and phase transition of CuS materials during CO₂RR were investigated. For this, a facile water-based synthesis method for preparation of surfactant-free CuS nanoparticles by anion exchange of Cu₂O nanostructures has been utilized. The synthesis method resulted in a pure CuS phase, based on XRD analysis, in accordance with a complete exchange of O²⁻ anions by S²⁻. By changing the concentration of the employed sulfidating reactant ((NH₄)₂S) during the anion exchange, either hexagonal platelets or morphologically ill-defined particles were obtained. The catalytic selectivity during CO₂RR tests proved to be largely independent from the specific particle morphology and showed a generally high tendency for the formation of HCOO⁻. GI-XRD measurements of CuS particles after exposure to cathodic potentials of -0.33 V_{RHE} and -0.68 V_{RHE}, revealed a multi-stage reduction of the CuS phase, which proceeded through an intermediate stage of Cu₂S and Cu₂O and resulted in final production of metallic Cu. Despite this presumably complete reduction of the initially cationic bulk phase, nearly exclusive production of HCOO⁻ was observed combined with almost total suppression of CO and CO-derived products in between electrode potentials of -0.65 V_{RHE} to -1.05 V_{RHE}. Based on the sustained change in catalytic performance by the introduction of the S²⁻ anion, it has been established that there is a high probability of (meta-)stable S species present in the near-surface region of the catalyst during CO₂RR. In this, the work exemplifies

that the catalytic selectivity during CO₂RR on cationic Cu compounds can be largely dominated by the identity of the (chalcogenide) anion.

4.4 Introduction of CeO_x to Cu₂O nanocubes: a bimetallic CuO_x/CeO_x system for the electrocatalytic CO₂RR

The presence of residual oxygen in oxide-derived Cu structures has been suggested to largely improve the catalytic selectivity for C₂₊ products from electrochemical CO₂RR. However, such oxides are naturally short-lived under the highly reductive conditions during the cathodic CO₂RR. Here, the addition of second oxides has been hypothesized to aid in the stabilization of such structures through catalyst support interactions and has been suspected to act as reservoirs for oxygen. For this purpose, ceria have been introduced to Cu structures and have been reported to enable a selective production of hydrocarbons in the electrochemical CO₂RR. While ceria are well characterized for applications in fuel cells and water electrolyzers as electrode and electrolyte materials, their applications in CO₂RR remain scarce and relatively poorly understood. The present study investigates the synthesis and catalytic CO₂RR performance of nanostructured materials composed of Cu₂O and CeO_x. Changes in particle morphology and composition are observed because of the introduction of a Ce(III) salt during particle synthesis and those changes are correlated to the catalytic CO₂RR selectivity.

4.4.1 Introduction

The present study investigated a facile preparation route for mixed materials composed of Cu₂O and CeO_x by an aqueous surfactant-free procedure. It was shown that the synthesis at higher Ce/Cu precursor ratios leads to changes in particle morphology and composition. Here, the use of low CeCl₃ concentrations during synthesis allowed a prevalence of the cubic Cu₂O morphology, whereas higher CeCl₃ concentrations lead to a stepwise degradation and eventually complete loss of the cubic morphology. The investigation of the CO₂RR selectivity during catalytic tests in an H-Cell revealed a sensitivity to those structural changes and showed a general increase in pH-dependent products with raised Ce/Cu precursor ratios. Here, an increase in particle size, a degradation of the cubic morphology, and an increase in CeO_x content have been suggested to contribute to the observed catalytic behavior. In this, the present study shows how the addition of Ce(III) salts can influence the structural properties of Cu₂O catalysts and their consequential catalytic selectivity for the electrochemical CO₂RR.

4.4.2 Results and discussion

Material preparation and physicochemical characterization. The investigated materials within this study were prepared from a modified synthesis of previously described cubic Cu₂O particles. Here, the particles were prepared by a precipitation through alkalization of an aqueous CuCl₂ solution and the consequential reduction with ascorbic acid. In the current study, various amounts of CeCl₃ were added to an aqueous CuCl₂ solution of constant concentration to obtain CuO_x materials doped with CeO_x. The employed CeCl₃/CuCl₂ molar precursor-ratio was varied in between 1/10 and an equimolar ratio of 10/10. Additionally, synthesis was performed with pure CuCl₂ and CeCl₃ solutions to obtain

monometallic materials for reference. In the following, the prepared materials are referred to by the molar precursor-ratio (Ce/Cu) employed during synthesis.

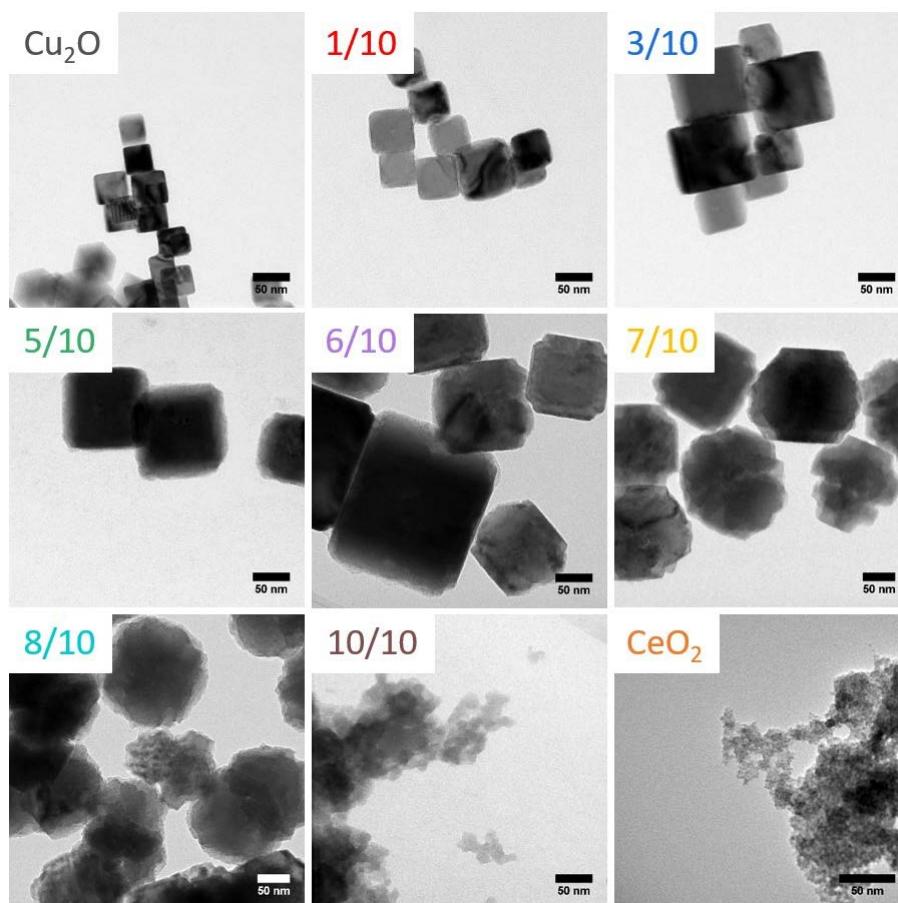


Figure 4.14 TEM images of the materials prepared under employment of different CeCl₃ to CuCl₂ molar precursor-ratios during synthesis. The respective value is given in each panel and the labels Cu₂O and CeO₂ refer to a preparation route including only CuCl₂ or CeCl₃, respectively.

The morphology of the prepared materials was investigated by TEM, shown in Figure 4.14. A clear influence of the employed precursor-ratio on the particle morphology was apparent. Here, an increase in CeCl₃ concentration during synthesis up until a 3/10 ratio primarily led to an increase in particle size under the general preservation of the cubic morphology. When the ratio was increased further towards 5/10 and 6/10 the particle growth was paired with a starting degradation of the cubic morphology. This degradation manifested itself in truncated edges of the cubic particles, indicating that the {110} facets were particularly susceptible to the process. The morphological degradation became more drastic, when the ratio was increased further towards 7/10 and 8/10. At this point, the entire morphology was affected and only a fleeting resemblance to the original cubic structure remained. For equimolar employment of Ce and Cu precursors (10/10), the cubic morphology was completely lost and showed high similarities to the pure CeO₂ reference material. Additional TEM images of this morphological transition can be found in Figure A 1.14.

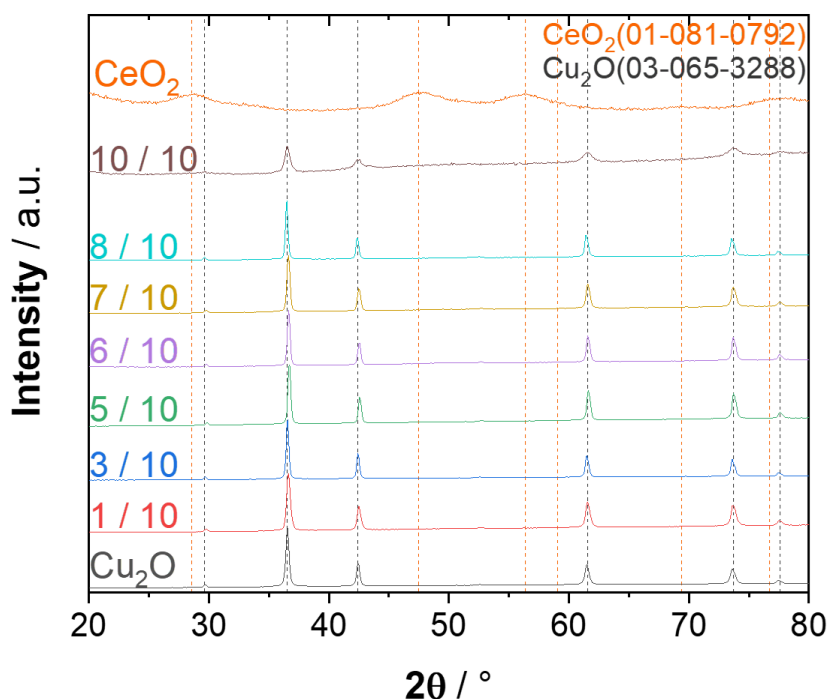


Figure 4.15 Powder-XRD analysis of the particles prepared from employment of different CeCl₃ to CuCl₂ molar precursor-ratios during synthesis.

The crystalline phase of the prepared materials was analyzed by powder-XRD, shown in Figure 4.15. Interestingly, the patterns of the samples prepared at various precursor ratios showed only reflections that could be assigned to a Cu₂O phase. Furthermore, the increased share of CeCl₃ during sample preparation showed no obvious influence on the crystallinity of the samples, except in the case of 10/10. Here, the observed reflections appeared broadened, thus, suggesting a reduced crystallite size in accordance to the Debye-Scherrer equation. Considering the large differences in signal intensity observed for the monometallic reference materials, e.g. Cu₂O and CeO₂, the absence of an observable CeO_x phase in the mixed materials could originate from an amorphous structure of the CeO_x. In order to avoid this limitation of the XRD and probe the total Ce content, an ICP-OES analysis was conducted for all samples, shown in Figure A 1.15. Interestingly, the mass content of Ce in the samples 1/10, 3/10 and 5/10 remained at very low values of clearly below 1 wt%. Even a further increase of Ce precursor concentration to 6/10, 7/10 and 8/10 only increased the mass content of Ce in the prepared materials to 1-2 wt%, as derived from OES analysis. The only case, which showed a considerable content of Ce was the 10/10 sample with roughly 22 wt%.

Origin of the size and morphological evolution with precursor Ratio. Two major effects on the particle structure were observable for the continuous increase in CeCl₃ to CuCl₂ precursor ratio during synthesis: Initially an increase in particle size under general preservation of the cubic morphology at low CeCl₃ to CuCl₂ ratios of up to 5/10, which was coinciding with almost no detectable Ce content in the final particles. Secondly, a progressive degradation of the cubic morphological at higher ratios of

6/10 to 8/10, which originated at the {110} facets of the cubes and eventually resulted in the complete loss of the cubic morphology at a ratio of 10/10. This loss of morphology was also accompanied with a clear increase in resulting Ce content for the obtained particles.

Particle size evolution for ratios up to 5/10. It is possible that the observed increase in particle size up to the 5/10 sample might originate from a kinetic effect caused by the higher concentration of Cl⁻ anions due to the addition of CeCl₃ to the reaction mixture. The size and shape of nanoparticles has been reported to be sensitive to the identity and concentration of anions due to surface adsorption and interference with facet-specific growth rates, as well as interactions during nucleation.^[172, 173] Here, the size of particles prepared by solvothermal approaches and formed from a homogenous solution was suggested to be determined by the ratio between nucleation and growth rate. Essentially, a kinetic dominance of the nucleation rate over the growth rate would result in smaller particles and vice versa. However, in the present study the alkaline environment caused the precursors to precipitate in their insoluble hydroxide forms, e.g. Cu(OH)₂ and Ce(OH)₃, which was later converted upon addition of the ascorbic acid and is, therefore, closer related to a heterogeneous nucleation. Nevertheless, the size of particles formed through heterogeneous nucleation has also been reported to show a similar sensibility to the presence of anions.^[174] It is unclear if the Ce³⁺ cation is also interfering with the nucleation and growth process, however, considering the extremely low mass content of Ce in the final structure, it seems less likely. In this line of thoughts, the hampered nucleation by increased Cl⁻ concentration is suspected to largely cause the observed particle size dependence on the employed precursor ratio of up to 5/10.

Morphological evolution for ratios higher than 5/10. There are two different approaches that could explain the observation that the degradation of the cubic morphology at higher CeCl₃ concentrations is coinciding with the formation of {110} facets. The first case involves a specific adsorption at the {110} facets during particle growth, which leads to a passivation and slows down the growth rate of the {110} facets, relative to other facets. The second case is a specific etching of the {110} facets after formation of the cubic morphology. Such a selective etching of the {110} facets has been reported for larger Cu₂O cubes by control of NH₂OH·HCl concentration, which enabled the stepwise transition towards Cu₂O rhombic dodecahedra.^[175] Generally, the observation that the morphological degradation is initially confined to the {110} facets can be explained by the higher surface energy relative to {111} and {100} facets for Cu₂O, which correspond to a higher reactivity.^[176] Interestingly, the degradation of the cubic morphology is coinciding with a clearly heightened mass content of Ce in the obtained materials. Furthermore, a comparison of the structures obtained at mixed Ce/Cu ratios to the structure of the pure Cu₂O and CeO₂ reference materials appears to show a successive transition from the Cu₂O to the CeO₂ morphology with increasing CeCl₃ to CuCl₂ precursor ratio. Those observations suggest a direct interaction between Cu₂O and CeO₂ precursors during the particle formation. A hypothesis for the nature of this interaction lies in a galvanic replacement of the Cu(I)oxide high energy {110} facets

by Ce(III) under production of Cu(0) and Ce(IV)oxide. Such “etching” mechanism could explain why the morphological degradation is conceding with an increased presence of CeO_x and is feasible according to Pourbaix diagrams of Cu and Ce in water. [177-180] However, the detailed nature and temporal sequence of this interaction is very elusive. Based on the current results it is difficult to unambiguously deconvolute the formation process of the particles, which would require a more in-depth morphological analysis and is not the main focus of this work.

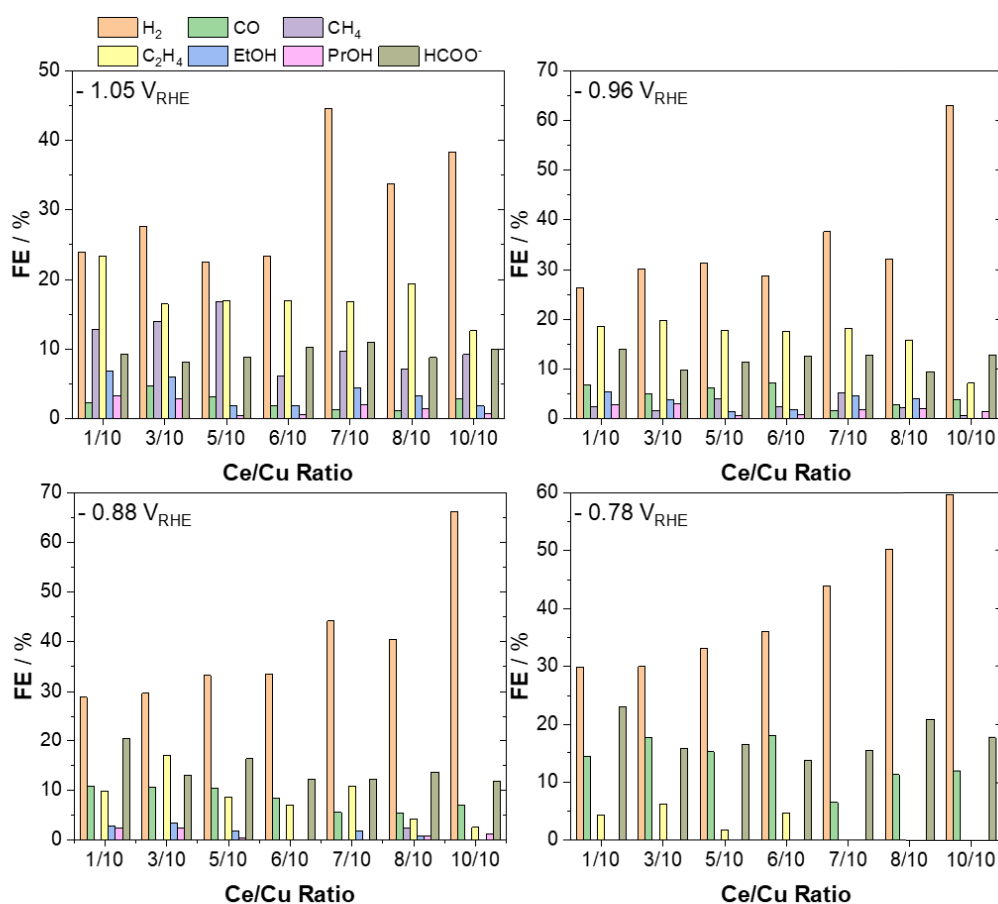


Figure 4.16 Faradaic efficiency for catalysts prepared from various Ce/Cu precursor ratios during electrocatalytic CO₂RR observed at different cathodic potentials.

Electrocatalytic CO₂RR selectivity. The electrocatalytic properties of the different materials during CO₂RR were characterized in an H-Cell setup using an aqueous solution of 0.1 M KHCO₃ as electrolyte. The catalysts were investigated in a potential range of around -0.65 V_{RHE} to -1.05 V_{RHE}. In Figure 4.16 the faradaic efficiency for all observed products are shown for the catalyst prepared at different precursor ratios. For the sake of simplicity, only four different cathodic potentials, namely -1.05 V_{RHE}, -0.96 V_{RHE}, -0.88 V_{RHE}, and -0.78 V_{RHE}, are shown, but additional data can be found in Figure A 1.16. The most obvious effect of an increased Ce/Cu ratio is a pronounced HER. This trend of an increase in H₂ FE with higher Ce/Cu ratios can be seen clearly at more positive potentials (-0.88 V_{RHE}, and -0.78 V_{RHE}), but is generally also present at more cathodic potentials. In accordance with a more pronounced HER, the FE towards C₂⁺ species (C₂H₄, EtOH, PrOH) showed also a decrease at

higher Ce/Cu ratios. In contrast, the FE of C₁ products (CH₄, CO, HCOO⁻) did not show a clear dependence on Ce/Cu ratios. Here, CH₄ and CO production seemed to be preferred at ratios of 3/10 and 5/10 and showed strong decrease when exceeding a ratio of 6/10, whereas HCOO⁻ production appeared to be largely independent from the nature of the employed catalysts.

Origins of the electrocatalytic CO₂RR selectivity. As the variation of Ce/Cu precursor ratio from 1/10 to 10/10 introduced changes in particle size, morphology and composition it is unlikely that one single effect can explain the observed changes in catalytic selectivity for all catalysts. In an effort to allow a clearer discussion of the observations and origins, a correlation of catalytic selectivity to the most prominent structural changes observed for a range of precursor ratios is plausible. In here, changes in catalytic CO₂RR selectivity for the materials 1/10 to 5/10 are suggested to be primarily correlated to the observed increase in particle size and for the materials 6/10 to 10/10 to the morphological degradation of the cubic shape and increase of CeO_x content.

Here, the initial increase of particle size at low precursor ratios showed no significant effect on H₂ and CO FE, whereas at larger potentials the production of CH₄ was enhanced at cost of C₂₊ and HCOO⁻ FE. In contrast to the presented results, the increase of particle size for small cubes of metallic Cu from 24 to 63 nm has been reported to decrease CH₄ in favor of C₂H₄, which was correlated to a changed ratio of edge to plane sites.^[77] The origin of this effect was correlated to beneficial kinetics of a COH-CO coupling pathway, proceeding at the an (110)/(100) intersection.^[78] However, in the present case Cu₂O structures are employed, which are known to be subjected to rigorous restructuring during CO₂RR and it is questionable to what degree the initial morphology can be sustained. Such restructuring has been previously shown to cause the formation of low-coordinated Cu sites, which have been hypothesized to aid in the conversion of CO₂ towards C₂₊ products.^[133] For larger Cu₂O cubes with an edge length of 220 – 580 nm the CO₂RR selectivity has been reported to be sensitive to the particle size and suggested to correlate to a more stable morphology of larger particles.^[75] Likewise, the origin of the correlation between Cu₂O cube size and increased CH₄ production, as observed in the present study, potentially originates in an altered morphological evolution, which lead to less favorable reaction sites for CO dimerization. At this state it is not possible to give a final explanation of the effect and further morphological investigations after and during reaction are required to grasp the cause.

The morphological degradation of the cubic shape and increased CeO_x content at larger precursor ratios of 6/10 to 10/10, showed a general increase of all proton dependent products (H₂, CH₄ and HCOO⁻), whereas CO and C₂H₄ production was hampered. The observation that the suppression of C₂₊ products coincided with a degradation of the cubic morphology fits well to the general believe that {100} facets facilitate the rate limiting step of CO dimerization. However, as discussed earlier, the extensive restructuring of CuO_x materials during CO₂RR makes a direct correlation of the initial morphology to the observed selectivity after prolonged time of catalytic testing difficult. A different reason for the observed selectivity shift could be caused by the increased presence of CeO_x. Here, CeO_x particles

have been shown to produce primarily H₂ during CO₂RR with minor amounts of CO. It is conceivable that CeO_x acts as a source of protons and therefore facilitates the production of all proton dependent species, as well as their prevalence over C₂₊ compounds. Such a similar effect has been observed for cubic Cu nanoparticles, which have been grown on CeO_x seeds and showed an intersection between the two materials. Here, they observed a strong increase in CH₄ selectivity for the bimetallic structure in contrast to pure Cu particles.^[181] For the pure CeO_x reference material that was prepared from an exclusive use of the CeCl₃, we observed a very low catalytic activity and could only detect H₂ during CO₂RR, see Figure A 1.17. As both processes, degradation of {100} facets and increased presence of CeO_x, are suggested to cause a similar effect for the catalytic CO₂RR selectivity and are superimposed in the present study it is difficult to conclude a dominant contribution at the current state of this work.

4.4.3 Conclusions

In the present study nanoparticles composed of different Cu₂O to CeO_x ratios were investigated for the electrocatalytic CO₂RR. Here, a previously reported aqueous synthesis of Cu₂O nanocubes was modified by introduction of various CeCl₃/CuCl₂ ratios to the reaction mixture. By adjusting the employed CeCl₃/CuCl₂ ratio during synthesis, morphological and compositional changes could be introduced to the particles. Here, the increased CeCl₃/CuCl₂ ratio initially led to an increase in particle size under preservation of a cubic morphology and the predominant Cu₂O phase. However, at higher CeCl₃/CuCl₂ ratios the cubic morphology started to degrade, which was starting at the high energy Cu₂O(110) facet, and lead to a complete loss of the initial morphology at the highest investigated CeCl₃ content. This observation was coincident with an increased presence of CeO_x in the final structure and was hypothesized to originate from an etching of the Cu₂O structure by Ce(III). The observed CO₂RR selectivity was proven to be sensitive to these structural changes and generally showed an increased production of pH dependent species (CH₄, H₂, HCOO⁻) with increasing CeCl₃/CuCl₂ ratios. In this, the present work shows how the structural and catalytic properties during CO₂RR of Cu₂O-derived catalysts can be affected by addition of Ce(III)-salts during particle synthesis.

5 High-Current Flow-Cell investigations of copper-based catalyst systems

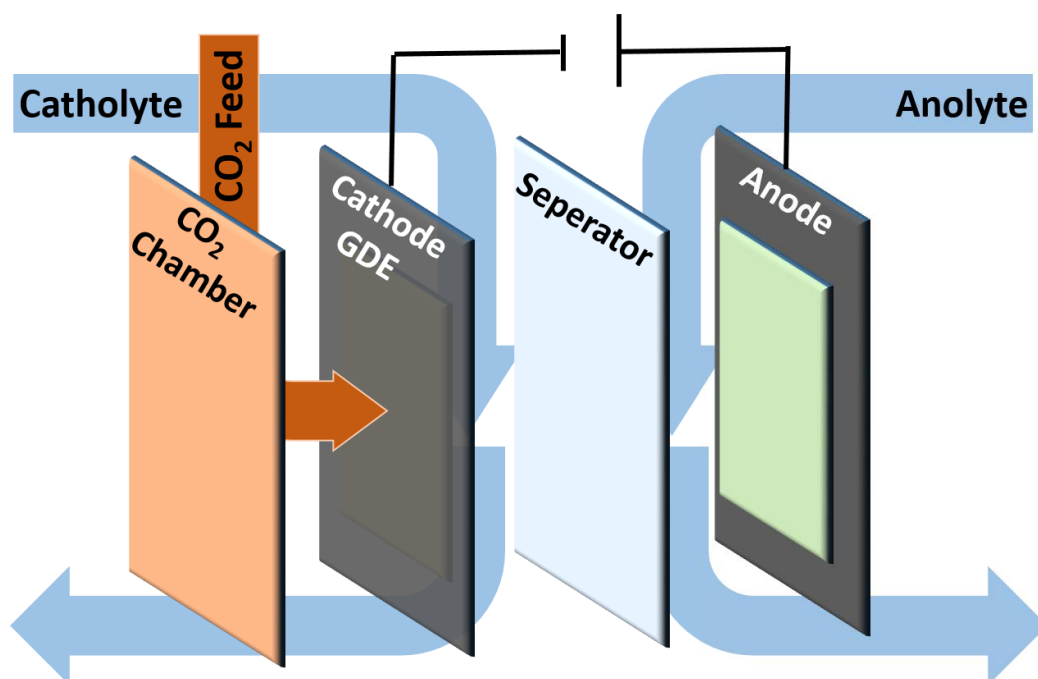


Figure 5.1 Schematic representation of a CO₂RR Flow-Cell electrolyzer including a gas diffusion electrode (GDE) with indicated directions for gas and liquid transport.

For a technological application of the CO₂ electrolysis current densities are required to exceed a certain threshold to enable an industrial relevant productivity. In here, a minimum of around 200 mA cm^{-2} is often suggested to allow reasonable conversion rate.^[15, 29, 106] While H-Cells provide a good system for fundamental investigations, they are unsuitable to even approach the required conversion rates because of an insufficient reactant transport to the cathode. Here, the use of gas diffusion electrodes (GDE) in combination with Flow-Cell electrolyzers have proven as suitable systems to accelerate the reactant transport to appropriate levels. In such systems, the liquid transport of the electrolyte and the gaseous reactant transport are decoupled, as schematically shown in Figure 5.1, and allow the direct introduction of gaseous CO₂ to the porous structure of the cathode GDE. While the CO₂ is likely to be dissolved prior to electrocatalytic reduction, the convective feed of gaseous reactant offers a much shorter associated mean path of transportation and a higher reactant flux. However, the application of high currents in Flow-Cell electrolyzers can lead to pronounced concentration gradients between the region near the electrode surface and the bulk of the electrolyte. Thus, measurements at high currents can lead to large differences in the electrocatalytic environment compared to the case of low currents in H-Cells and need to be included for a comprehensive investigation of an efficient system. The following chapter primarily involved the use of cubic Cu₂O particles, which have been presented in subchapter 4.1, and is exclusively focused on electrocatalytic characterizations at high currents in a Flow-Cell electrolyzer.

5.1 Correlation of membrane conductivity, acid-base equilibria, and electrolyte stability during prolonged CO₂ electrolysis in aqueous solutions of KHCO₃

Upon transition from the low-rate electrocatalytic CO₂RR in H-Cells to the high-rate CO₂RR in Flow-Cells, the current related transport effects become progressively more pronounced. For example, the migration of charged species across the separator between cathodic and anodic compartment usually shows only minor effects in H-Cells due to the generally low currents and reaction times, thus, are often overlooked or neglected. In contrast, the electrolysis at technological currents in Flow-Cells lead to considerably higher migration rates, which can interfere with the bulk composition of the electrolyte and the electrocatalytic properties of the system. Accordingly, an understanding of the underlying interactions between the electrode reactions, the electrolyte composition and the reactant transportation are crucial to allow the design of efficient and stable CO₂RR electrolyzers. The following work focuses on the analysis of these profound interrelations and proposes a suitable system for a sustained CO₂ electrolysis over long reaction times.

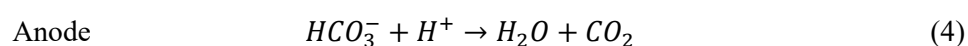
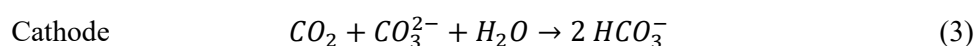
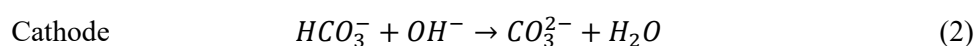
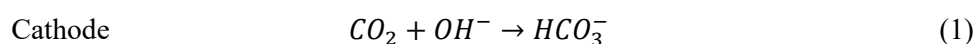
5.1.1 Introduction

Here, we show how the identity of the membrane, either anion or cation conducting, can profoundly alter the transport of CO₂ and associated electrolyte stability within a CO₂ electrolyzer. This effect is investigated in a Flow-Cell electrolyzer under the deployment of a widely used buffering KHCO₃ electrolyte of neutral pH. We then focus on an anion exchange membrane (AEM) and show how the bulk pH, as a proxy of electrolyte composition, of anode and cathode compartment remains stable even at high currents of up to 1500 mA and long reaction time of up to 48 h. We correlated this observation to the directed transport and constant regeneration of the pH buffering HCO₃⁻ anions. In this, the balance of the transported, generated and consumed HCO₃⁻ anions within the CO₂ electrolyzer mediates the pH changes in the anode and cathode compartment and determines the compositional stability for the whole system.

5.1.2 Results and discussion

The effect of membrane identity on the transport of CO₂. Within this work, we routinely used a Cu-based GDE as the cathode and a commercial Ir-MMO as the anode in a Flow-Cell setup to investigate the membrane dependent effects of ion migration in 1 M KHCO₃ electrolyte. Here, we started by monitoring the outgoing cathodic CO₂ flow in a current range of 150 mA to 2100 mA with a constant CO₂ feed of 50 mL min⁻¹, shown in Figure 5.2 (a). The current was kept constant at each step for a duration of two hours before moving towards the next, higher value. The use of Nafion and Selemion membranes show a distinct difference for the outgoing (CO₂) gas flow of the cathode chamber. In the case of Selemion, an anion exchange membrane (AEM), we observed a successive decrease in outgoing cathode gas flow with increasing currents. In contrast, the use of Nafion, a cation exchange membrane (CEM), led to a largely constant outgoing cathode gas flow that was largely

independent from the applied current up to a value of 1200 mA. At this point, a larger current led to an increase in outgoing gas flow. It is apparent, that the AEM enables a pathway for the CO₂ to be transported out of the cell in non-gaseous form, which seems to be inaccessible under the use of a CEM. Considering the use of 1 M KHCO₃ as the electrolyte, the most abundantly present ions in the system are K⁺ and HCO₃⁻, thus both species should be the major ions transported for CEMs and AEMs, respectively. We suspect that the HCO₃⁻ can act as an intermediate for gaseous CO₂, which can move freely through the AEM and shuttles the CO₂ from the cathode to the anode compartment. This transport mechanism is schematically depicted in Figure 5.2 (b) and is largely based on acid-base equilibria of carbonate species. Here, OH⁻, which is a constant side product during CO₂RR and HER from water reduction, is generated on the cathode GDE and directly reacts with dissolved CO₂ to form HCO₃⁻, as shown below in reaction (1). Alternatively, OH⁻ could also react with the abundantly present HCO₃⁻ anion (2) to CO₃²⁻, which could later equilibrate with CO₂ in the presence of water (3). In sum, both reaction pathways either (1) or (2+3) lead to the consumption of CO₂ and production of HCO₃⁻. In the case of an AEM, the HCO₃⁻ is transported across the membrane to the anode chamber, where the OER causes a constant supply of H⁺ from water oxidation. The acidic conditions near the anode shifts carbonate equilibria towards CO₂ and leads to its gaseous release, see reaction (4) below.



In contrast, the use of a CEM denies this transport channel of CO₂. Here, K⁺ is the dominant ion transported across the membrane, which leads to a largely unaffected gas flow. A comparison of the measured outgoing gas flow to one that is calculated based on a consumption of CO₂ exclusively by alkaline conversion through cathodically generated OH⁻, depicted in Figure A 2.2, generally shows a good agreement between the two. This observation suggests that the major sink for CO₂ is the formation of carbonate species in the alkaline environment near the cathode and not the actual CO₂RR. Here, deviations in the measured flow for CEM and AEM systems at higher currents are most likely correlated to an increasing contribution of the HER.

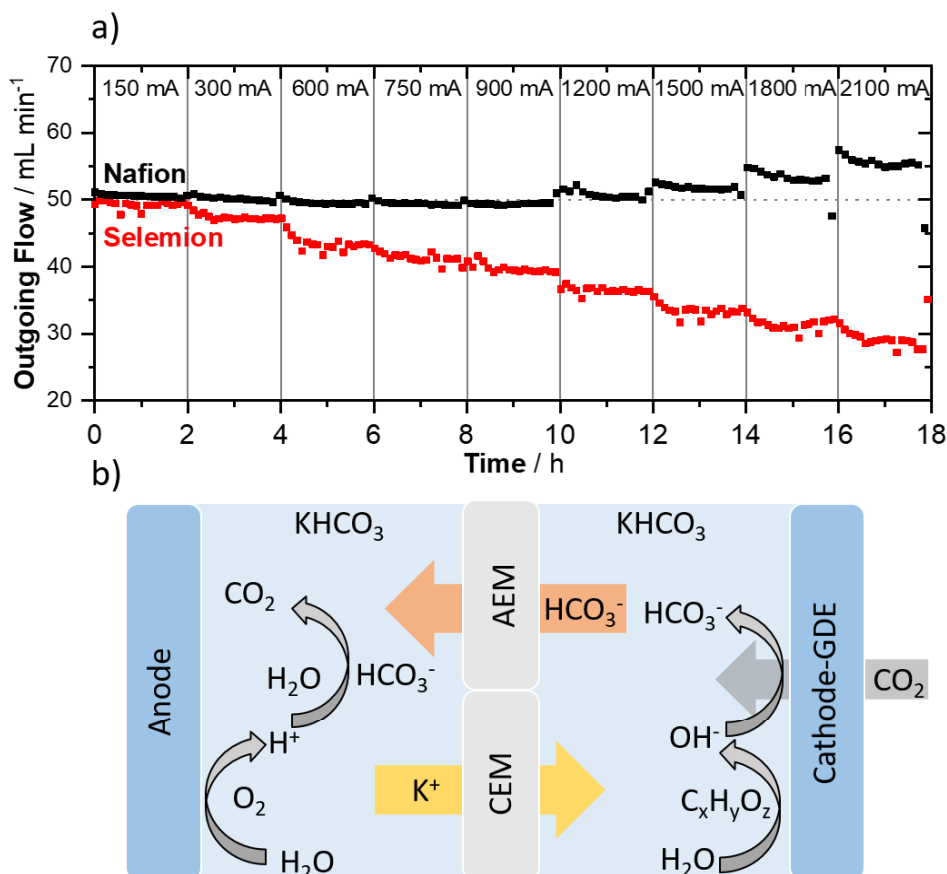


Figure 5.2 (a) Time dependent, outgoing gas flow of the cathodic chamber for a Flow-Cell setup including a Nafion and a Selemion membrane, respectively, in 1 M KHCO₃. Every two hours the current was increased while the gas feed was held constant at 50 mL min⁻¹. (b) Schematic depiction of the ion migration for anion (AEM) and cation (CEM) conduction membranes and pH related reactions.

In case of the CEM, the HCO₃⁻ is unlikely to be transported across the membrane, however, the cathodic production and anodic consumption of HCO₃⁻ still occur. This causes an increase in cathode KHCO₃ concentration and decrease of anode KHCO₃ concentration. We traced this effect in an H-Cell using 40 mL of 0.1 M KHCO₃ anolyte at constant current of 100 mA, shown in Figure A 2.1. Here, the anode potential showed a continuous rise due to the progressive increase in Ohmic resistance and associated IR losses. Interestingly, the measured charge, which passed through the system before the anode potential became limiting, is close to the theoretical value that is required to fully convert the anolyte HCO₃⁻ to CO₂ by anodic production of H⁺ (410 C_{mes} vs. 386 C_{theo}). This observation suggests that the continuous depletion of HCO₃⁻ due to its acidic conversion to CO₂ is quite likely to be the underlying process, which reduces the conductivity of the anolyte. Such a relation between current and loss in conductivity would require a constant external regeneration of the bicarbonate electrolyte for CEM-based electrolyzers and speaks against the use of CEMs for extended electrolysis in carbonate electrolytes.

The effect of membrane identity on the bulk pH. Next, we focused on the exclusive use of the AEM and monitored the respective bulk pH in the anolyte and catholyte reservoirs, which contained a solution of 1 M KHCO_3 as the electrolyte, to trace their compositional stability during electrolysis. Here, we first increased the current gradually from 150 mA to a maximum of 1500 mA in two-hour intervals, after which we reversed the steps to return to a current of 150 mA. The temporal evolution of the pH for anolyte and catholyte is shown in Figure 5.3 (a). We observed that the bulk pH in the cathode reservoir is tracing the stepped current during electrolysis. Here, the increase of current lead to a simultaneous increase of the catholyte pH, which seemed to be reversible, as the successive decrease in current also lead to a decrease of catholyte pH. Interestingly, the anolyte pH did not reflect the current profile and showed only a continuous decrease over the first two hours, after which the pH remained fairly stable. Also, during a prolonged electrolysis at a current of 450 mA, shown in Figure 5.3 (b), we observed only minor changes in bulk pH for both electrolytes, which suggested a high compositional stability. Tracing the outgoing cathode gas flow, shown in Figure A 2.3, agreed well with the employed current profile and dynamics of the catholyte pH.

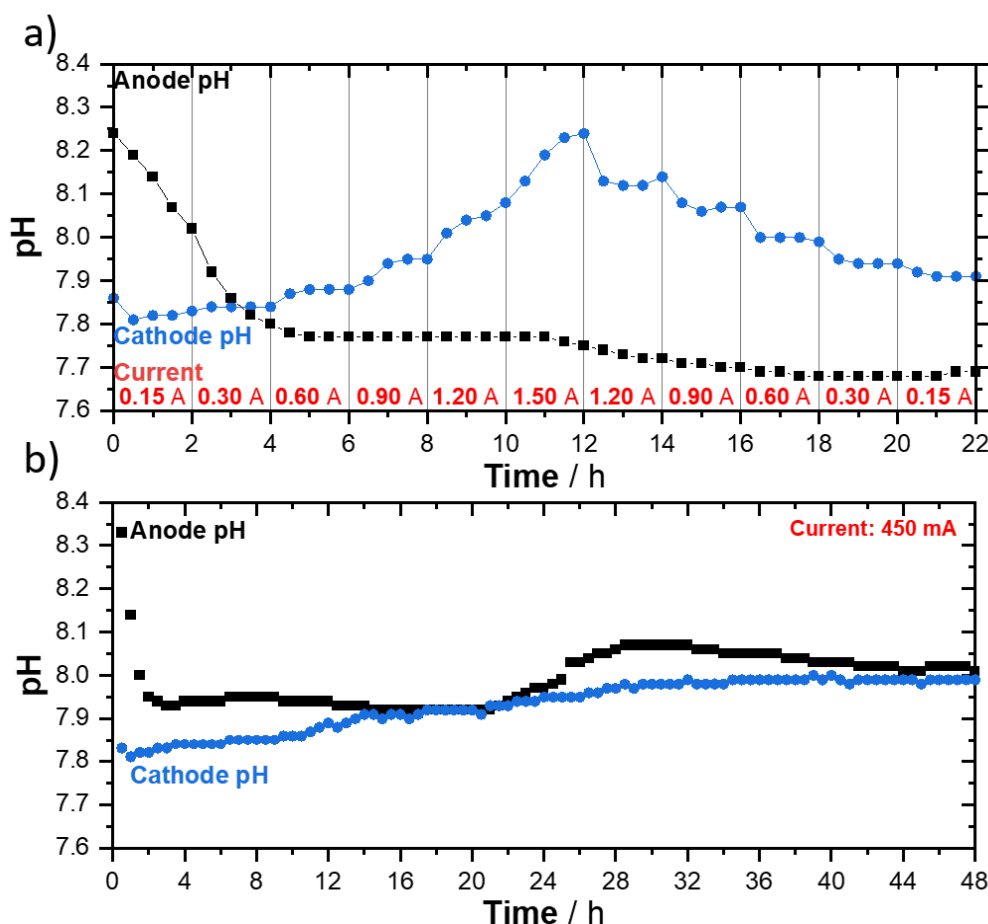


Figure 5.3 Anolyte and catholyte pH as a function of time during CO_2RR electrolysis in 1 M KHCO_3 (a) under variation of the applied current and (b) at a constant current of 450 mA.

We take the view that the changes in catholyte and anolyte bulk pH during electrolysis can also be rationalized by a discussion of acid-base equilibria of carbonate species, as was done for the consideration of the gas flow. Here, increasing the applied current leads to a proportional increase of the production rates for anodic H^+ and cathodic OH^- . Considering the high concentration and corresponding abundance of HCO_3^- , it is feasible that OH^- reacts according to (2) under production of CO_3^{2-} . This reaction is also kinetically highly favored over path (1).^[182] The subsequent equilibration with CO_2 according to reaction (3) is kinetically sluggish, which could explain the slopes at current steps observed in Figure 5.3 (a) when the current was increased to values above 900 mA. Such an effect of differences in reaction kinetics of reaction (3) to the direct buffering by HCO_3^- , see reaction (2) and (4), might also cause the general insensitivity of the anode pH to the applied current. Here, the buffering of H^+ according to (4) and the replenishment of HCO_3^- by migration through the AEM are fast enough to completely negate an effect on the bulk electrolyte composition by anodic H^+ production. The initial pH decrease can be explained by an effective saturation of the anolyte with CO_2 released by HCO_3^- decomposition, as CO_2 saturation is only performed on the cathode side prior to electrolysis. In contrast, reaction (3) acts as a kinetic bottleneck on the cathode side and could allow a certain buildup of CO_3^{2-} concentration, which leads to the observed temporal evolution of the pH. Recent work on a Cu-based CO_2RR electrolyzer also reported this transport mechanism but showed a strong alkalization of the 1 M KHCO_3 with time, which suggests that the effect is dependent on the setup and extend of interaction between CO_2 and electrolyte.^[183]

5.1.3 Conclusions

Here, we have investigated the influence of ion migration for the compositional stability of aqueous KHCO_3 solutions during CO_2RR electrolysis in a Flow-Cell under employment of a CEM (Nafion) and an AEM (Sustainion). We monitored temporal changes of anolyte and catholyte bulk pH, variations in outgoing gas flow of the cathode compartment and cell potential as proxies for compositional electrolyte stability. We showed that the use of AEMs led to a HCO_3^- mediated transportation of CO_2 from the cathode to the anode compartment. While this transportation mechanism led to considerable losses of CO_2 from the gaseous reactant feed, which was directly proportional to the applied current, it also allowed for a stable long-term composition of anolyte and catholyte. In contrast, the use of a CEM denied the transportation channel of HCO_3^- , which resulted in a constant anodic decrease and cathodic increase of HCO_3^- concentration due to acid-base reactions near the electrode surfaces. Ultimately, an electrolyzer using a CEM in KHCO_3 electrolyte will suffer from large Ohmic losses due to the inevitable anodic depletion of electrolyte under CO_2 evolution in the acidic proximity of the anode. Our results show that ionic migration is an important factor to consider in evaluation of suitable membrane and electrolyte combinations for CO_2RR at high rates. We take view that commonly employed KHCO_3 solutions require the use of AEMs for long-term and high-rate electrolysis in systems of continuously looped electrolytes and that CEMs are unsuitable to be employed in combination with carbonate-based anolytes.

5.2 High-rate CO₂RR on carbon-supported and unsupported cubic Cu₂O nanoparticles

There is an inherent gap between the electrochemical investigations of intrinsic catalyst properties and their technological application. Here, large differences in the electrochemical conditions during operation can occur because of the mismatch in current densities, which can deviate by multiple orders of magnitude. This raises the question to what degree the insight from fundamental investigations can be transferred to experiments on an electrolyzer level. The present work investigates the catalytic properties of previously discussed cubic Cu₂O nanoparticles at technological relevant currents. Here, qualitative agreement with results from tests at 10 to 100 times lower current densities in an H-Cell could be observed, but also differences in temporal selectivity variations during prolonged electrolysis.

The subchapter 5.2 was reproduced from T. Möller, F. Scholten, T. N. Thanh, I. Sinev, J. Timoshenko, X. Wang, Z. Jovanov, M. Gliech, B. Roldan Cuenya, A. S. Varela, P. Strasser, *Angew. Chem. Int. Ed.* **2020**, 59, 17974-17983, (reference ^[133], DOI: [10.1002/anie.202007136](https://doi.org/10.1002/anie.202007136)). Licensed under [CC BY 4.0](https://creativecommons.org/licenses/by/4.0/)

T.M. and A.S.V. planned and designed the experiments. T.M. performed and analyzed the electrochemical experiments. F.S. conducted the XPS analysis. EXAFS measurements and analysis was conducted by I.S. and J.T. TEM and SEM analysis was performed by X.W. and M.G. Electrochemical investigations in the Flow-Cell electrolyzer were conducted by T.M. with the help of T.N.T. and Z.J. The manuscript was written by T.M., F.S., J.T., A.S.V., B.R.C., and P.S. All authors participated in the discussion and deduction of results.

5.2.1 Introduction

To investigate the catalytic CO₂RR properties of supported Cu₂O nanocubes, S-NC, and unsupported Cu₂O nanocubes, U-NC, under high-rate reaction rates, we deployed the catalysts in a Flow-Cell electrolyzer at neutral pH catholyte. The performance of both catalysts was investigated over a broad current range from 50 mA cm⁻² to 700 mA cm⁻². In good agreement with previous results at low currents, we observed a strong effect for the presence of a carbon support. Here, the C₂₊ selectivity for the unsupported Cu₂O nanocubes shifted towards a high C₁ selectivity for the supported system. During investigations over extended periods of electrolysis, we observed a distinct difference in the temporal evolution of the FE for the supported system at 300 mA cm⁻², which was not visible for the lower currents used during previous investigations. A SEM analysis of both catalysts after reaction revealed a difference in the morphological evolution over prolonged electrolysis, which is suspected to contribute to the observed differences in catalytic properties. This study illustrates the importance of complementary investigations at high currents to access the catalytic capabilities of Cu-based materials for selective CO₂RR.

5.2.2 Results and discussion

The Cu₂O nanocube-loaded GDEs (loading of about 1 mg_{Cu₂O} / cm² active geometric area) were tested in a commercial 4-chamber membrane Flow-Cell electrolyzer. The ambient CO₂ reactant pressure minimized mass transport limitations and enabled catalytic tests at very high currents, as depicted schematically in Figure 5.4 (a). Unlike experiments in the H-Cell, the electrolyzer tests were routinely performed galvanostatically. More precisely, a constant current was applied for two hours for each current step in the range of 50 to 700 mA cm⁻² in 1 M KHCO₃. Figure 5.4 (b,c) shows the change in the FEs of the major CO₂RR products with variation of the applied total current. The supported Cu nanocubes, S-NC, as well as the unsupported ones, U-NCs, exhibited a high catalytic selectivity towards CO₂RR products, exceeding 70 % at 200 mA cm⁻². Indeed, the U-NC displayed an exceptionally high efficiency for C₂₊ products, which gradually increased with the applied current to a maximum of 59 % at 300 mA cm⁻². Even at 500 mA cm⁻², the production yield remained high and only upon further increase to current densities exceeding today's typical industrial applications a gradual decrease due to the dominant HER was visible.

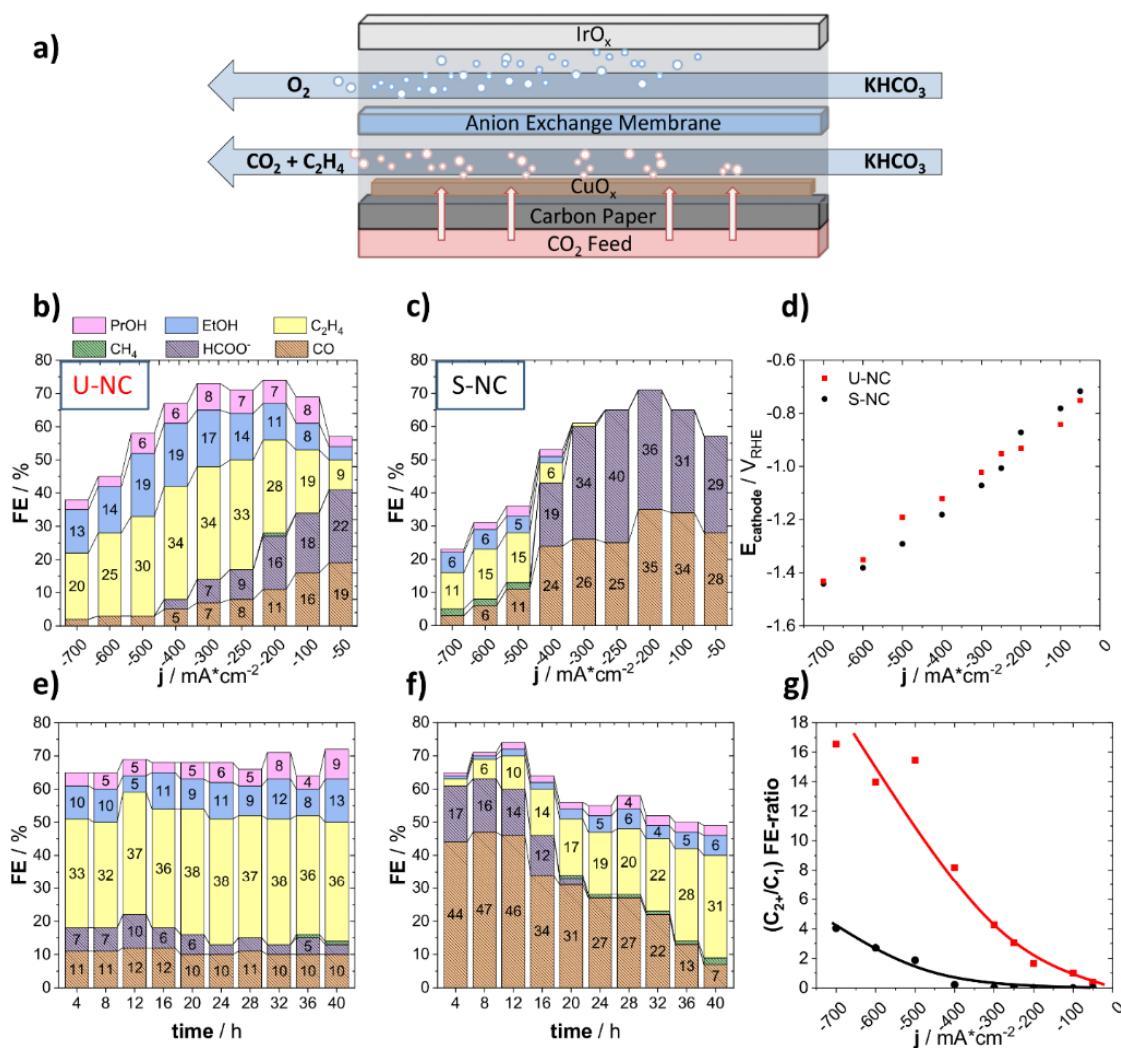


Figure 5.4 (a) Schematic representation of the membrane electrolyzer flow cell, visualizing the direction of electrolyte and gas flow. Faradaic product efficiencies as a function of applied geometric current density for (b) the unsupported Cu nanocubes, U-NC, and (c) the supported (23 wt%) Cu nanocubes, S-NC. (e) 40 h faradaic efficiency stability test at -300 mA cm⁻², displaying the Faradaic efficiency as a function of time for the unsupported, U-NC, and (f) the supported (23 wt%) Cu nanocubes, S-NC. (d) Direct comparison of the electrolyzer polarization curves of U-NC and S-NC; (g) Plot of the (C₂₊ / C₁) product FE-ratio for both catalysts. All electrolyzer tests were performed in CO₂ saturated 1 M KHCO₃ (pH 7.6) with an active geometric cathode-area of 3 cm² and 1 mg cm⁻² particle loading. CO₂ was supplied at 50 sccm to the cathode and the electrolyte was cycled at 100 mL min⁻¹ through each respective compartment.

Again, our data evidenced a pronounced support effect of high similarity to the one observed in an H-Cell setup at low rates. The S-NCs (23 wt%) produced mainly HCOO⁻ and CO up to a current density of 400 mA cm⁻². Currents above 400 mA cm⁻² then favored C₂₊ selectivity, yet also caused the HER to dominate the overall faradaic processes, which resulted in a gradual decrease in CO₂RR selectivities. The electrolyzer results are in excellent agreement with our H-Cell results, confirming the significant shift in the experimental CO₂RR selectivity caused by the carbon support (Figure 5.4 g). In an effort to pinpoint the origin of the selectivity change, we first carefully analyzed the resulting IR-corrected overpotentials of the supported and the unsupported catalyst cathodes at the applied currents. Since the

electrolyzer polarization curves showed almost identical catalytic reactivities for both catalysts, we believe we can safely exclude overpotential differences as the origin of the experimental selectivity differences (Figure 5.4 d).

Next, during long-term stability tests over 40 hours at -300 mA cm^{-2} , shown in Figure 5.4 (e,f), we uncovered a remarkably stable selectivity behavior (constant product FEs) for the U-NC, whereas the S-NC displayed a clear time-dependent variation in its catalytic selectivity. Here, the initially high FEs of CO and HCOO^- were continuously dropping, whereas the C_{2+} selectivity was constantly rising. Importantly, over 40 hours of reaction time, the catalytic CO_2RR selectivities of the S-NC approached those of the U-NC. Again, the two measured cathode potentials of the U-NC and S-NC during the 40 h stability tests showed no obvious differences that could account for the observed behavior (Figure A 2.4). As a result of this, we then hypothesized that some molecular chemical or structural characteristics of the two catalysts may have been matched over the 40 h tests, which would explain the identical performance. To search for such characteristics, we carried out SEM imaging of the GDEs after the reaction to better understand the difference in the respective catalyst surface evolution of the two catalysts (Figure A 2.5). While the U-NC formed a rough, continuous surface after testing, the S-NC displayed the presence of highly dispersed spherically shaped Cu particles after the polarization test, which transformed into irregular Cu nanoparticle aggregates after the 40 h stability test. Note that the newly formed spherical Cu NPs were smaller than the initial Cu_2O nanocubes. We suspect that the high mobility of these Cu nanoparticles on the carbon support surface is aiding in the observed morphological evolution. Particle mobility is a well-known issue in water electrolyzers or fuel cells; it affects Pt catalyst particles that are supported on high surface area carbons.^[184, 185] The agglomeration and growth of the reaction-generated small spherical Cu NPs results in the formation of larger particles decreasing the effective particle dispersion. Previous studies of Cu particle size effects in the CO_2RR revealed enhanced C_{2+} FEs, in particular ethylene, with increasing Cu particle size and decreasing dispersion on carbon substrates.^[145, 146, 186] It is conceivable that such a lowered particle dispersion effect contributed to our experimental data, accounting for the gradual change in the faradaic efficiency values, eventually matching those of the unsupported Cu nanoparticles. Moreover, recent studies have discussed similar morphological changes for systems of unsupported, metallic Cu cubes^[79] and supported oxidized copper particles^[187]. Interestingly, the first study shows a temporal decrease in C_{2+} efficiency, caused by a potential-driven structural degradation of metallic Cu cubes and loss of the (100) facet during CO_2RR , whereas the second study reports on a temporal increase of C_{2+} efficiency, caused by fragmentation and successive reconstruction resulting in a boundary-rich Cu structure. This shows the need for carefully distinction between effects of exposed crystal facets and the abundance of defects for shaped CuO_x catalysts in CO_2RR , which we help to address here.

To trace this particle growth in more detail, we performed stepwise SEM analyses after 4 and 20 hours of constant electrolysis at -300 mA cm^{-2} using the supported Cu_2O nanocubes, S-NCs (Figure A 2.6).

While already after 4 hours the presence of emerging Cu particle aggregates was visible, we could also observe clear evidence of their precursors, that is, very small, isolated particles (indicated by a red cycle in Figure A 2.6). We note that these tiny Cu seed particles were considerably smaller than the initial Cu₂O nanocubes, suggesting a partial break-up of the original Cu₂O cubes during the catalytic reaction and electrochemical Cu₂O reduction process. Based on the complementary analysis from our previous spectroscopic investigations combined with the presented morphological investigation, we can schematically depict the temporal evolution of shaped Cu₂O nanocubes during CO₂RR and the effect of dispersion on a carbon support (Figure 5.5).

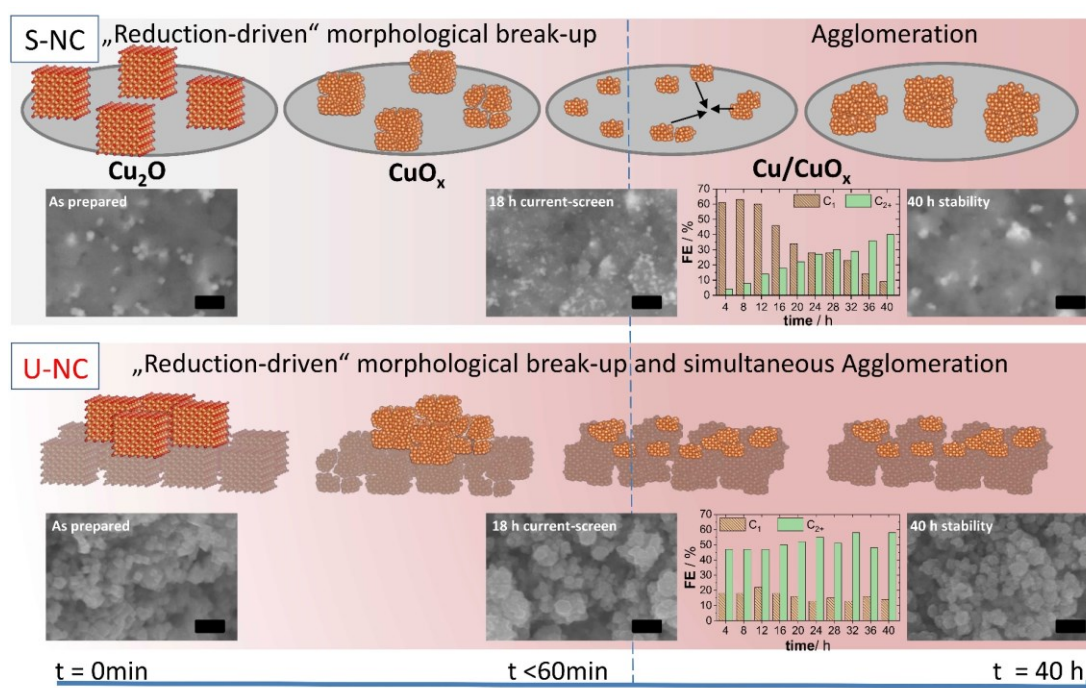


Figure 5.5 Schematic representation of the morphological and structural degradation of the supported Cu nanocubes (23 wt%), S-NC, and unsupported Cu nanocubes, U-NC, during CO₂RR in a flow-electrolyzer. Top-view SEM images of the gas diffusion electrode as prepared, after 18 h of selectivity screen and after 40 h of stability test at -300 mA cm⁻², as well as the temporal evolution of the C₂₊ and C₁ Faradaic efficiency during 40 h of stability test at -300 mA cm⁻² are displayed for U-NC and S-NC, respectively.

As our *quasi in situ* XPS in Figure 4.5 results suggested, negative potentials during reaction cause a complete reduction of the near-surface region of the catalyst. This process is fast in the case of the unsupported, as well as the supported nanocubes and progresses towards a completely metallic overlayer within one hour of reaction time. Nevertheless, our *operando* XAS results in Figure 4.6 show that the unsupported nanocubes are not fully reduced during reaction and can retain a significant fraction of 20 % Cu(I) in the sub-surface structure for extended periods of time. Additionally, during this process a defect-rich structure is formed displayed by a clearly lower CN than that expected of bulk Cu, based on our analysis of EXAFS data. The nanocubes are generally morphologically unstable under those conditions and start to merge with adjacent NPs to form larger intertwined structures. Here,

the dispersion on the carbon support shows a distinct effect for the morphological evolution, allowing for a structural break-up into smaller Cu clusters compared to the initial particle size. This strong difference in behavior is expected to be caused by the isolation of particles on the support, which decreases the probability for immediate formation of aggregates during the “reduction-driven” morphological break-up. At longer reaction times, however, the dispersed Cu-seeds start to sinter to minimize surface energy, facilitated by their high mobility on the weak-interacting carbon support, and, in turn, their performance aligns to the unsupported system. Our experimental results and their interpretations provide surprising new insights into the morphological and chemical dynamics of supported oxidic nanocubes and how they affect their catalytic selectivity during the electrochemical CO₂RR (see Figure 5.5). A recent in situ TEM analysis of electrochemically deposited Cu cubes is in good agreement with our observation of an unstable particle morphology during CO₂RR and also report on consecutive shrinkage and agglomeration. ^[188].

5.2.3 Conclusions

Here, we explored the catalytic properties of unsupported, U-NC, and carbon-supported Cu₂O nanocubes, S-NC, for CO₂RR at high-current operation in a flow electrolyzer. The unsupported nanocubes catalysts displayed high C₂₊ yields in previous H-Cell tests, but exceptionally high C₂₊ yields in the Gas Diffusion Electrolyzer cell tests at neutral pH conditions, in particular at around -300 mA cm⁻². In agreement with our previous H-Cell results, we again observed a pronounced influence of the carbon support for the obtained catalytic selectivity. Here the presence of a carbon support shifted the observed catalytic selectivity from C₂₊ products for the U-NC, towards C₁ products for the S-NC during CO₂RR at currents in between 50 to 700 mA cm⁻² in a 1 M KHCO₃ electrolyte. The S-NC catalyst exhibit a significant evolution in their faradaic efficiencies toward those of the unsupported catalyst over a 40 h electrolyzer test. Concomitant tracking of the catalyst state led us to conclude that carbon-dispersed Cu₂O nanocubes are morphologically unstable, generate small seed particles, which subsequently agglomerate and grow into a structure that resembles the unsupported sample. As a result of this evolution, the efficiencies of C₂₊ products increase, while those of C₁ products decline. Carbon appears unable to suppress the tendency of Cu nanoparticles to form seeds, to grow and to ripen into a more unsupported morphology. Other support materials such as oxides, nitrides or carbides may be able to achieve this objective better. Finally, while catalytic performance patterns obtained from thin film electrodes deployed in H-Cell tests are qualitatively in line with those from Gas Diffusion Electrodes in a Flow-Cell electrolyzer, their magnitude varied considerably. Also, the short term (5 h tests) of the H-Cells could not reveal the structural and selectivity changes revealed in the 40h electrolyzer tests. This underlines that H-Cell catalyst screening results, similar to the translation of Rotating Disk Electrode (RDE) catalyst screenings into Membrane Electrode Assembly (MEA) tests for the purpose of fuel cell cathode catalysts development, should always be validated and complemented by single cell GDE electrolyzer tests for a reliable development and scale up of CO₂RR catalysts

5.3 Influence of concentration gradients and electrode structure on the electrocatalytic CO₂RR selectivity during high rate electrolysis in pH buffering media

Recently, the field of CO₂RR has progressively moved towards studies of the high current regime in pH neutral and alkaline, gas-feed flow-electrolyzers to approach technological rates. As the cathodic production of OH⁻ is a function of the current, flow-electrolyzers have been suggested to be particularly affected by local alkalization due to insufficient mass transport and the observed high selectivity for C₂₊ products has been, at least in part, associated to that effect. While the electrode structure and the active surface area of the catalyst have been shown to be the crucial parameters determining mass transport in low-current H-Cells, similar correlations remain underexplored for gas diffusion electrodes in flow-electrolyzers. In this study, we use a previously reported cubic Cu₂O catalyst to systematically alter the structure of the catalytic layer of a gas diffusion electrode (GDE) for tests in a flow-electrolyzer. By changing macroscopic parameters, as the particle loading and ionomer content (Nafion), we influence the accessibility of catalytically active sites and the mass transport throughout the porous structure of the catalytic layer. In this, the present work correlates the electrode structure with restriction in mass transport, manifesting in local concentration gradients and alkalization, which in turn influences the selectivity of CO₂RR during a high current density operation in a bulk neutral bicarbonate electrolyte.

The subchapter 5.3 has been largely reproduced from a submitted manuscript that is currently under revision in the journal “Energy & Environmental Science” with permission from the Royal Society of Chemistry. *Tim Möller, Trung Ngo Thanh, Xingli Wang, Wen Ju, Zarko Jovanov and Peter Strasser*, The product selectivity zones in Gas Diffusion Electrodes during the electrocatalytic reduction of CO₂, Energy & Environmental Science **2021**, submitted.

T.M., T.N.T. and Z.J. planned and designed the experiments. T.M. and T.N.T. performed and analyzed the electrochemical experiments. X.W. conducted SEM measurements. The manuscript was written by T.M., Z.J. and P.S. All authors participated in the discussion and deduction of results.

5.3.1 Introduction

Here we report on the most prominent factors influencing the performance of a Cu-based CO₂ electrolyzer operating at high currents. Using a flow-electrolyzer design where CO₂ gas feed passes directly through the electrode interacting with the Cu catalyst layer, we observed that the selectivity of the electrochemical CO₂ reduction in (bulk) pH neutral media can greatly be influenced by adjusting the structure of the electrode. In this, the variations in catalyst loading and ionomer content can profoundly affect the selectivity of CO₂RR. We explore the hypothesis that this originates from the overall mass transport variations within the porous catalytic layer of the gas diffusion electrode. As further evidence for this, apart from the CO₂ electrolysis results, we propose a special method to benchmark the reactant mass transport in flow-cells using oxygen reduction reaction (ORR) limiting current measurements. Our analysis suggests that a restriction of mass transport is highly desirable due to its connection to a local alkalization and corresponding suppression of pH-dependent reaction products, given the absence of local CO₂ concentration limitations. We further show how the electrode structure can be used to push the observed catalytic CO₂ reduction selectivity either towards C₁ or C₂₊ products, dependent on the ionomer content and catalyst loading in a cathodic current range of 50 to 700 mA cm⁻². Measurements at various KHCO₃ electrolyte concentrations agree with the notion of the local pH dictating the overall selectivity and point towards the presents of pronounced concentration gradients within the system. Overall, our work suggests that the differences in electrocatalytic CO₂ reduction selectivity at high currents (in a range of pH neutral buffering electrolytes) largely originate from the local concentration gradients defined by the initial catalyst ink formulation and architecture of the catalytic layer, both of which represent a powerful tool for optimization in the production of selected value-added products.

5.3.2 Results and discussion

Mass Transport in Flow-Cell Electrolyzers and Gas Diffusion Electrodes. We employed a commercial Flow-Cell electrolyzer in a setup consisting of three compartments to investigate CO₂RR electrolysis at high rates, which is schematically depicted in Figure 5.6 (a). Here, two separated solutions of 1 M KHCO₃ were used as electrolytes and continuously looped through two compartments divided by an anion conducting membrane. Anodic and cathodic reaction products were transported out of the respective compartments with the flow of the electrolytes. A convective stream of CO₂ was feed form the third compartment through the backside of the porous cathode towards the catalytic layer, which allowed a fast supply of reactant to the cathodic reaction sites. The cathode catalyst layer was deposited by airbrushing an ink containing a mixture of Nafion and cubic Cu₂O nanoparticles on a carbon-based Freudenberg H23C2 gas diffusion layer serving as substrate. As anode, a commercially available dimensionally stable electrode composed of a Ti sheet covered by an Ir-MMO was routinely used. Throughout this study, we will refer to the uncoated Freudenberg H23C2 by gas diffusion layer, GDL, and to the particle-coated Freudenberg H23C2 by gas diffusion electrode, GDE. Figure 5.6 (b) shows the schematic structure of a GDE prepared by spraycoating. In this system, the different

elements of the GDE are spatially separated and can be assigned to different layers. The lowest layer consists of carbon fibers and acts as mechanical and conductive backbone of the entire structure. Next, the microporous layer (MPL) functions as conductive and hydrophobic substrate, which allows the electronic and CO_2 transport towards the adjoining catalytic layer. The catalytic layer represents the uppermost element of the GDE and is the interface between gaseous transports of CO_2 and liquid transport of electrolyte. Within the catalytic layer, the electronic, ionic and reactant transport intersect and define the reaction environment of the electrocatalytic CO_2RR and the reactivity of the system. The morphology of the catalytic layer, as obtained by spraycoating, showed a porous, 3-dimensional appearance with a rough surface, visible in cross-section and top-view SEM images of Figure 5.6 (b).

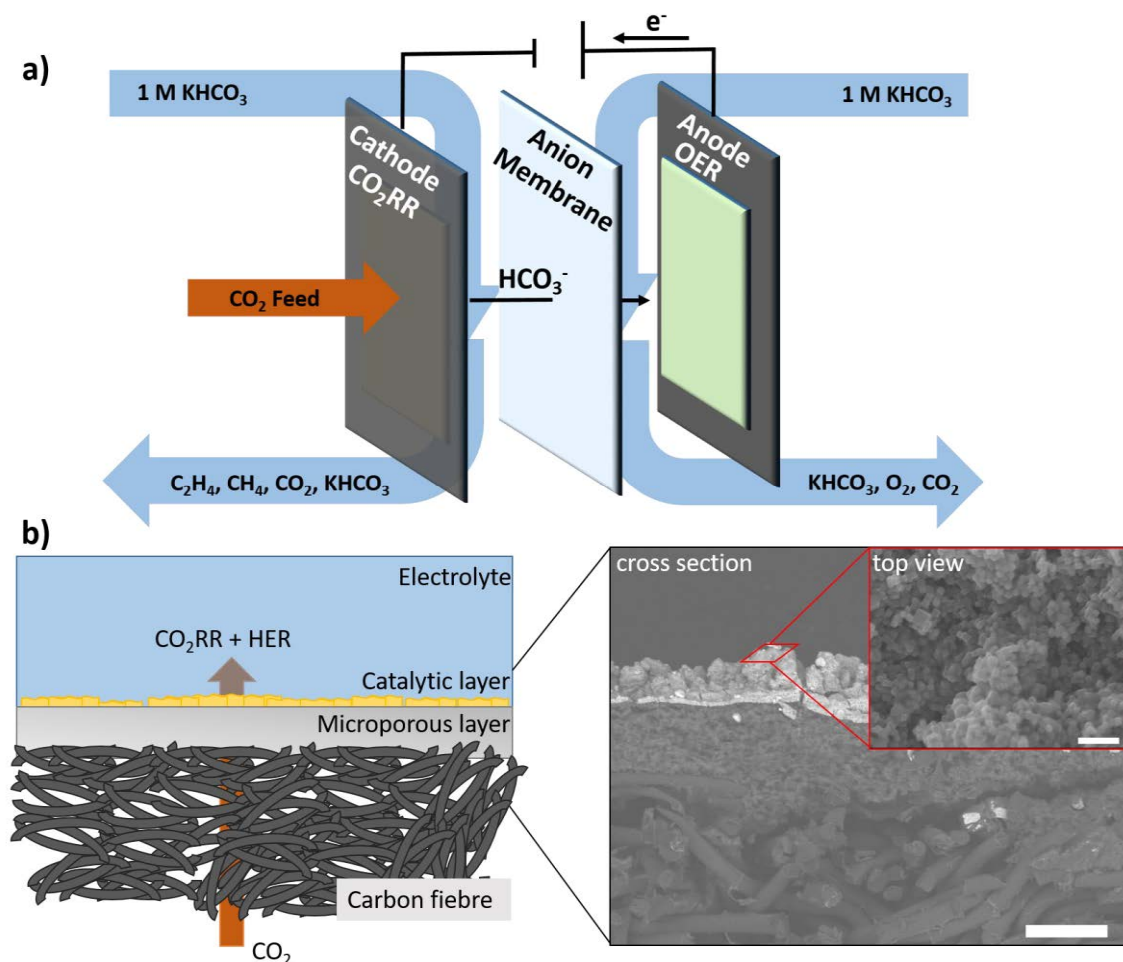


Figure 5.6 Schematic representation of a 3-compartment flow-cell electrolyzer with indications of the transport directions for reactants, products and electrolyte (a). Schematic representation of carbon-based gas diffusion electrode with cross-section (50 μm scalebar) and top view SEM images (400 nm scalebar) of a GDE prepared by spray-coating a dispersion of a cubic Cu_2O catalyst with Nafion binder onto a carbon gas diffusion layer.

For H-type setups, effects of variations in the structure of the catalytic layer have been repeatedly reported influence the mass transport, critically altering the reaction environment and therefore determining the observed selectivity of the system during electrochemical CO_2RR . Here, the mass

transport can be divided into a transport of reactants directed towards the surface and a transport of product leaving the surface. On the reactant site, in the aqueous electrolyte dissolved CO_2 is transported towards the catalytic sites, where abundantly available water supplies the protons to form reduced carbon compounds under production of OH^- . The generated OH^- can readily react with the commonly used HCO_3^- electrolyte acting as a buffer. However, HCO_3^- transport from the bulk towards the surface is not sufficiently fast to keep up with the OH^- production rate, which locally shifts the pH and bicarbonate-equilibrium near the reaction sites. This effect of local alkalization during CO_2RR was observed experimentally at already moderate potentials by surface enhanced IR and Raman spectroscopy, simulated based on bicarbonate equilibria and often suggested to be the origin of a high selectivity for multi-carbon products during electrochemical CO_2RR . [68, 81, 82] [72, 189, 190] On the products site, carbon compounds need to be transported away from the surface to allow for further reactants to fill in. However, the sustained presence of reactive intermediates such as CO have also been reported to show a beneficial effect on production of ethylene and oxygenates, and was also suggested to show a suppression for the competing HER from water reduction due to the occupation of reactive sites. [191-195] Generally, an increasing thickness of the catalytic layer and the associated electrochemically active surface area (ECSA) increases the mean path of transportation for the reactants and products. This impedes a homogeneous through-plane mass transport within the catalytic layer, which results in more pronounced concentration gradients throughout the system. [68, 70, 82] Accordingly, it has been suggested for mesoporous Ag electrodes of various thicknesses that the CO_2RR selectivity is sensitive to the concentration gradients and shows the strongest suppression of the competing HER for the thickest electrode at the lowest part of the catalytic layer, where the effect of alkalization was pronounced most. [196, 197]

It is feasible that, high rate CO₂RR on GDEs in flow-cell electrolyzers shows the same fundamental correlations of mass transport and catalytic selectivity as those reported for H-Cell setups. Indeed, as the local pH is a function of the OH⁻ production rate and associated to the current density, high rate CO₂RR was already suggested to be strongly influenced by the effect of local alkalization.^[106] Additionally, a recent study also discussed the local CO₂ concentration as selectivity determining criteria in a neutral CO₂RR electrolyzer.^[110] We take view, that the catalytic selectivity of Cu during high rate CO₂RR in pH buffering KHCO₃ electrolyte is largely defined by the mass transport, which can be rationalized by a discussion of CO₂ transport and transport of pH buffering HCO₃⁻ anions. We chose our previously reported cubic Cu₂O catalyst as a model system to investigate the influence of concentration gradients by variation of three macroscopic parameters:

- *Particle catalyst loading.* First, we varied the amount of deposited catalyst particles to obtain GDEs with various catalyst loadings that show differences in layer thickness, roughness and ECSA. In doing so, we affect the mean path of transportation from the bulk sources of CO₂ and KHCO₃ towards the catalytic sites.
- *Ionomer to particle catalyst ratio.* To introduce an impediment for the mass transport, we varied the Nafion content of the ink formulation to obtain GDEs that show different ionomer to catalyst ratios for a constant absolute catalyst loading. Nafion acts as a strong adhesive to introduce a mechanical stability to the catalytic layer, however, the ionomer distribution is a known issue in fuel cell research due to its influence on local reactant transportation and associated mass (oxygen) transport resistances.^[198] Likewise, the transport of reactants in CO₂RR towards the active sites should also be sensitive to the local distribution of the ionomer, acting as a barrier for the CO₂ and HCO₃⁻ transport.
- *Buffer capacity.* To induce various buffer capacities, we varied the concentration of the KHCO₃ electrolyte to alter the buffer capacity within our system. A higher concentration of HCO₃⁻ offers more buffer capacity, in turn resulting in decreased pH gradients at the interface and counteracting the effect of alkalization.

The present work is not about setting new number records in product selectivity, but to pinpoint the major controlling factors for the product selectivity in an industrial scale electrode under more realistic reaction conditions. To characterize the mass transport properties of CO₂RR GDE, we employ oxygen reduction limiting current measurements typically used in the hydrogen fuel cell community as diagnostic tool in the field of CO₂ reduction.

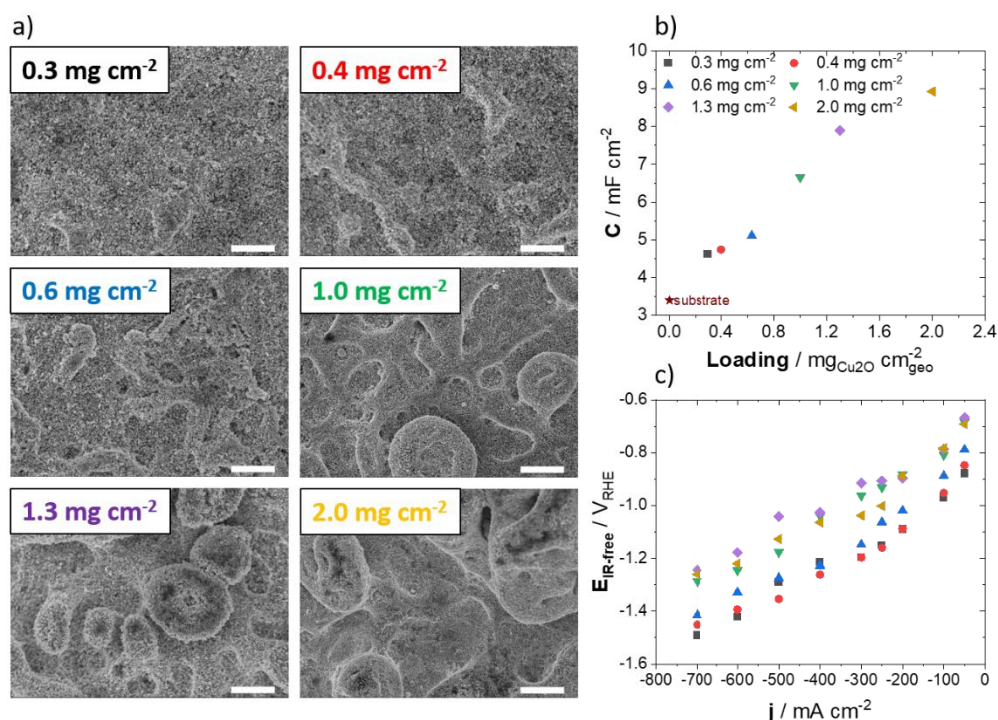


Figure 5.7 Top view SEM images after electrolysis (a), electrochemical double layer capacitance after electrolysis (b) and polarization curves (c) of GDEs with various catalyst mass loadings. Conditions were 3 cm² of geometric surface area, 1 M KHCO₃ and 10 wt% of Nafion binder. Scale bars in SEM images represent 10 μm.

Effect of catalyst loading. We started with a morphological investigation of the GDEs prepared by deposition of various catalyst loadings. Here, top-view SEM images after electrolysis are given in Figure 5.7 (a) and show a clear influence of the particle loading. We observed a progressive roughening and introduction of pores to the surface upon increase of particle loading. Such structural changes suggest an increase in electrochemically accessible surface area (ECSA), which we have investigated by quantification of the electrochemical charging of the double layer (see Figure A 2.9). As a measure of the ECSA, we calculated the double-layer capacitance, shown in Figure 5.7 (b), which showed an increase with particle loading and agrees with our observation of a progressive surface roughening in SEM images. In accordance with an increased ECSA, we noticed a higher catalytic activity during CO₂RR for the high particle loadings visible in the polarization curves of Figure 5.7 (c).

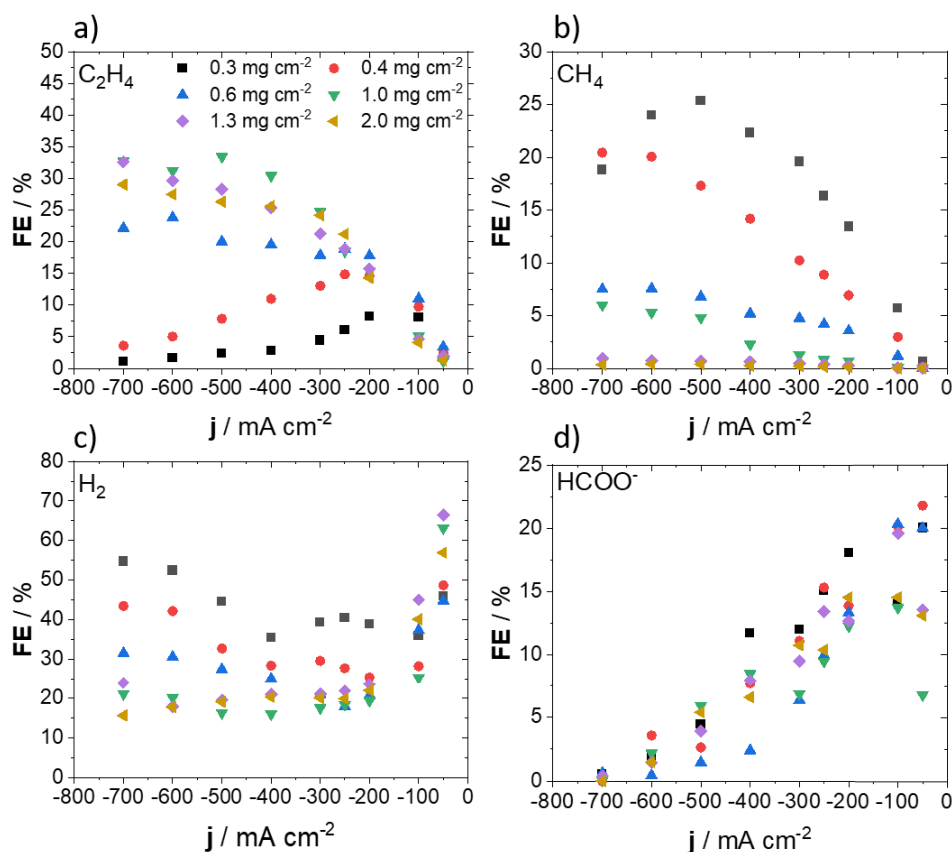


Figure 5.8 Faradaic efficiency as a function of applied current density at varying catalyst mass loadings for C_2H_4 (a), CH_4 (b), H_2 (c) and HCOO^- (d). Reactions were conducted under following Conditions: 3 cm^2 of geometric surface area of cathode, 1 M KHCO_3 and 10 wt\% of Nafion used as binder in catalyst ink.

In Figure 5.8 we tested the influence of catalyst loading on the product distribution in a fixed electrolyte and at const. binder content. Here, the FE of C_2H_4 , CH_4 , H_2 and HCOO^- is displayed as a function of the applied current density for catalyst mass loadings ranging from 0.3 mg cm^{-2} to 2.0 mg cm^{-2} . We specifically focus on these products, as they have distinctly different rate-limiting reaction steps, which show either a strong pH-dependence (CH_4 , HCOO^- and H_2) or primarily independence (C_2H_4) and can therefore provide insight in the local reaction environment.^[51, 199] We observed a clear suppression of all pH-dependent products (CH_4 , HCOO^- and H_2) at high loadings of the catalyst, which was accompanied by a favored production of ethylene. CH_4 , which is regarded to be a preferred product from CO_2RR at high proton concentration, shows a negligible FE of below 1% , once catalyst loading was increased to 1.3 mg cm^{-2} and higher. In contrast, in experiments using very low catalysts loadings of below 0.4 mg cm^{-2} the FE for CH_4 raised to above 20% , see Figure 5.8 (b). While this trend was qualitatively in line with the production of H_2 and HCOO^- (Figure 5.8 (c,d)) the change in FE for C_2H_4 showed a reversed behavior, see Figure 5.8 (a). Here, the decrease of catalyst loading below 0.4 mg cm^{-2} resulted in a FE for C_2H_4 of below 15% , whereas higher loadings allowed for a more selective C_2H_4 production and increased FE to around 30% . Due to the well-known sensibility of CO_2RR selectivity to the electrode potential, we plotted the product FE against IR-free RHE potentials in Figure

A 2.7. As the shift in selectivity is also visible on an IR-free potential scale, we exclude variations in electrode potential as the sole origin of the observed effect. Additional information of FE for the remaining CO₂RR products (EtOH, PrOH and CO) are given in Figure A 2.8 and agree with the observed favorable production C₂₊ compounds at high catalyst loadings. Our observation suggests that the catalytic selectivity during high-rate CO₂RR is sensitive to the structure of the catalytic layer, which can be affected by variation of the catalyst loading. We suspect that the correlation between catalytic selectivity and catalyst loading originates in changes of the mass transport, which in turn affect the local pH near the electrode.

Effect of Nafion content. In order to further investigate the mass transport as potential origin of the observed shift in selectivity, we turned towards varying the binder content within the catalytic layer. Inspired by fuel cell research, we suspect that increasing amounts of ionomer within the catalytic layer represents a barrier for the mass transport of reactive species as dissolved CO₂ and HCO₃⁻ towards reaction sites. Figure 5.9 shows the effect of an increase in Nafion content within the catalytic layer of a GDE on the selectivity during CO₂RR. A suppression of CH₄ and HCOO⁻ is evident in samples of high Nafion loading, see Figure 5.9 (b,d), similar to what we have observed at high catalyst mass loadings. Interestingly, samples of high Nafion loading (30 and 50 wt%) show a suppression of HER and increased C₂H₄ FE only at a relatively low current density of more positive than -200 mA cm⁻² (Figure 5.9 (a,c)). A further increase of current density, results in a strong rise of FE for HER at the cost of total CO₂RR FE. We suspect that this change in selectivity at high currents is caused by an excessive content of Nafion, which reduces the mass transport to a point, where the reactant (CO₂) transport becomes limiting for CO₂RR and causes the HER to dominate in the process. While such a correlation between the Nafion content and the limited reactant transport is restricting for CO₂RR selectivity at currents above -200 mA cm⁻², it shows an increase at lower rates. Excessive amounts of ionomer could also influence the electrical accessibility of particles, which is why we investigated the change in electrochemical double layer capacitance and catalytic activity. Here, we only observed minor changes in double layer capacitance with varied Nafion loading, but a lower catalytic activity of the 50 wt% Nafion sample was apparent (see Figure 5.9 (e,f)). Again, to exclude differences in electrode overpotential as cause of the observed trend, we plotted IR-free RHE electrode potentials against the product FE in Figure A 2.10, which still clearly shows the binder induced shift in selectivity.

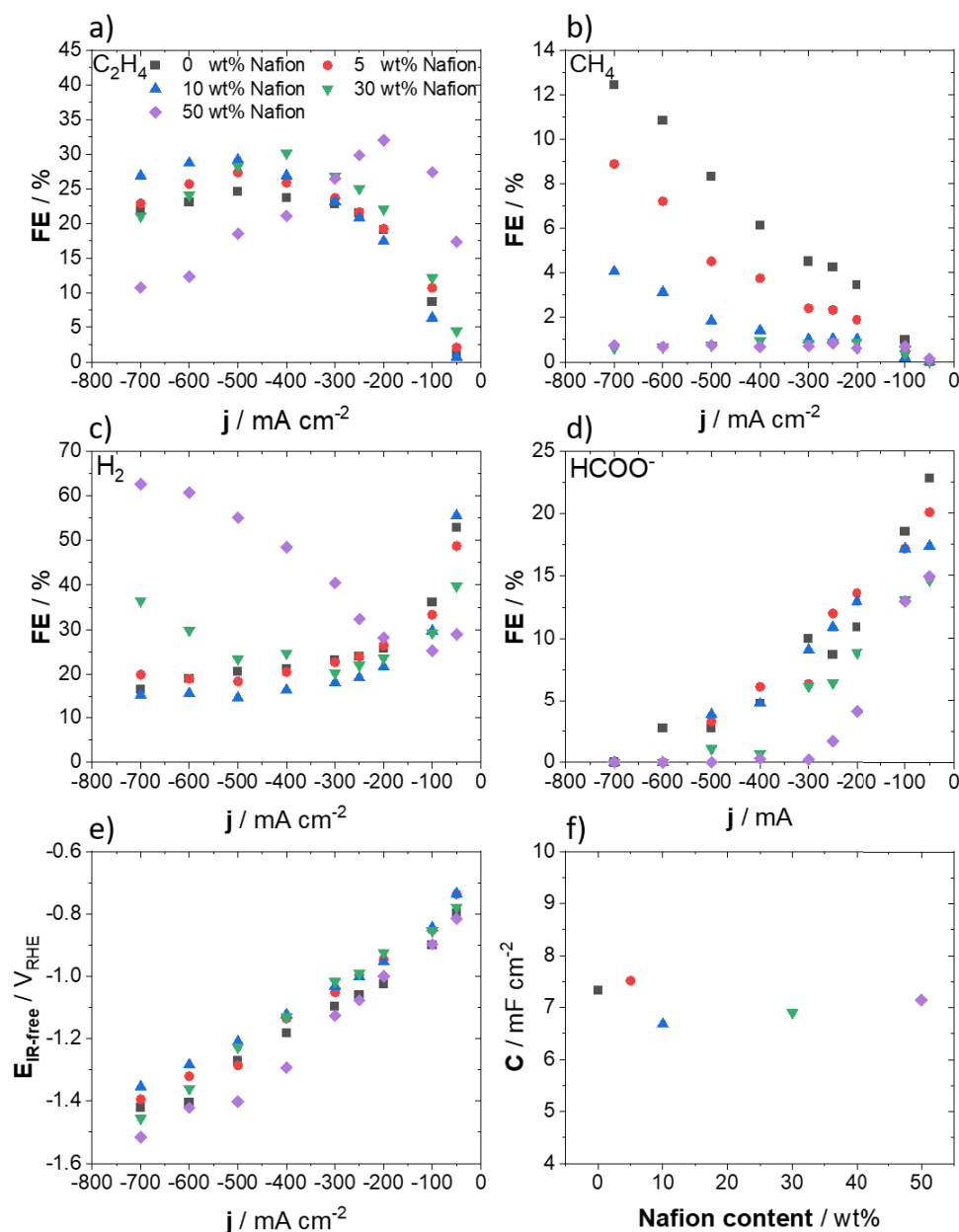


Figure 5.9 Faradaic efficiency as a function of applied current density with Nafion loadings for C_2H_4 (a), CH_4 (b), H_2 (d) and $HCOO^-$ (e). Measurements of double layer capacitance (c) and IR-free electrode potentials (f) as function of applied current density with various Nafion loadings. Conditions were as follows: $3\ cm^2$ of geometric surface area, $1\ M\ KHCO_3$ and $0.7\ mg\ cm^{-2}$ catalyst mass loading.

Furthermore, we have also investigated the change in surface structure at different Nafion contents by SEM, shown in Figure A 2.11. Here, an intermediate content of Nafion (10 and 30 wt%) resulted in a rough surface of the catalytic layer, whereas the extreme cases of 0 wt% and 50 wt% showed a relatively smooth surface. Noteworthy is the pronounced coverage of the Cu_2O cubes supposedly by the ionomer in the 50 wt% Nafion sample, visible in images of higher magnification, consistent with the idea of representing a distinct barrier for the mass transport. Additional CO_2RR products (CO , $EtOH$ and $PrOH$) are given in Figure A 2.12, which showed a higher selectivity for $EtOH$ with increased Nafion content at moderate currents. Our observations on the effects of increased Nafion

content are qualitatively in line with the effect of particle loading. In both cases, we generally observed a higher selectivity for C_{2+} products when either binder content or particle loading was increased. It seems feasible that a similar origin causes the observed selectivity shifts, given their high qualitative agreement.

Effect of $KHCO_3$ concentration. Figure 5.10 (a-f) shows the influence of the bulk $KHCO_3$ concentration on the C_{2+} (C_2H_4 , EtOH and PrOH) and C_1 (CH_4 , $HCOO^-$) selectivity during CO_2 electrolysis in the Flow-Cell. Here, we used different Nafion contents of 10 wt% to 50 wt% and a constant catalyst loading of about 0.7 mg cm^{-2} . For the 50 wt% Nafion sample we observed no significant change in catalytic selectivity, when increasing electrolyte concentration from 0.1 M to 1.0 M $KHCO_3$, see Figure 5.10 (a,d). Both concentrations showed the highest C_{2+} selectivity of roughly 40 % FE at -200 mA cm^{-2} , whereas a more cathodic current density resulted in the increase of the competing HER (Figure A 2.13). Further increase of $KHCO_3$ electrolyte to 3 M lowered the C_{2+} FE and favored HER over the whole investigated current range. In contrast, the FE for C_1 products seemed largely unaffected by the change in $KHCO_3$ concentration. Next, the 30 wt% Nafion sample showed a clear dependence of C_{2+} and C_1 FE on the $KHCO_3$ concentration during CO_2RR , see Figure 5.10 (b,e). While we were able to achieve a combined C_{2+} FE of around 70 % at -600 mA cm^{-2} , the use of higher $KHCO_3$ concentrations of 1 and 3 M lead to a decreased C_{2+} FE to around 50 % and 30 %, respectively. For the FE of C_1 products we observed an inverse behavior, here 3 M $KHCO_3$ showed the highest combined C_1 FE of roughly 17 %, while the use of 1 M and 0.1 M $KHCO_3$ lead to a subsequent decrease to as low as 10 % C_1 FE at 0.1 M $KHCO_3$. Our observations during CO_2RR , using a 10 wt% Nafion sample were quite similar to the case of a 30 wt% Nafion sample, see Figure 5.10 (c,f). Again, we achieved the highest C_{2+} selectivity at the lowest $KHCO_3$ concentration of 0.1 M, which enabled a combined FE of around 60 % over a broad range of cathodic currents. The use of an increased $KHCO_3$ concentration of 1 and 3 M resulted in a dramatically decreased C_{2+} FE of 40 % and 5 %, respectively. At the same time the highest C_1 FE observed on the 10 wt% Nafion sample increased from a maximum of 10 %, towards 17 % and roughly 23 % for respective $KHCO_3$ concentrations of 0.1 M, 1.0 M and 3.0 M. In parallel to the CO_2RR , the HER also proved sensitive to $KHCO_3$ concentration and showed an overall increase with $KHCO_3$ concentration, whereas the 50 wt% sample seemed to be generally less sensitive to the buffer concentration (Figure A 2.13 (a-c)). At all Nafion contents we observed a higher selectivity for C_{2+} products and generally lower HER and C_1 FE, when we employed $KHCO_3$ electrolytes of a lower concentration during electrolysis, however, this effect seemed to be dependent on Nafion content and was most pronounced for the lowest Nafion content of 10 wt%.

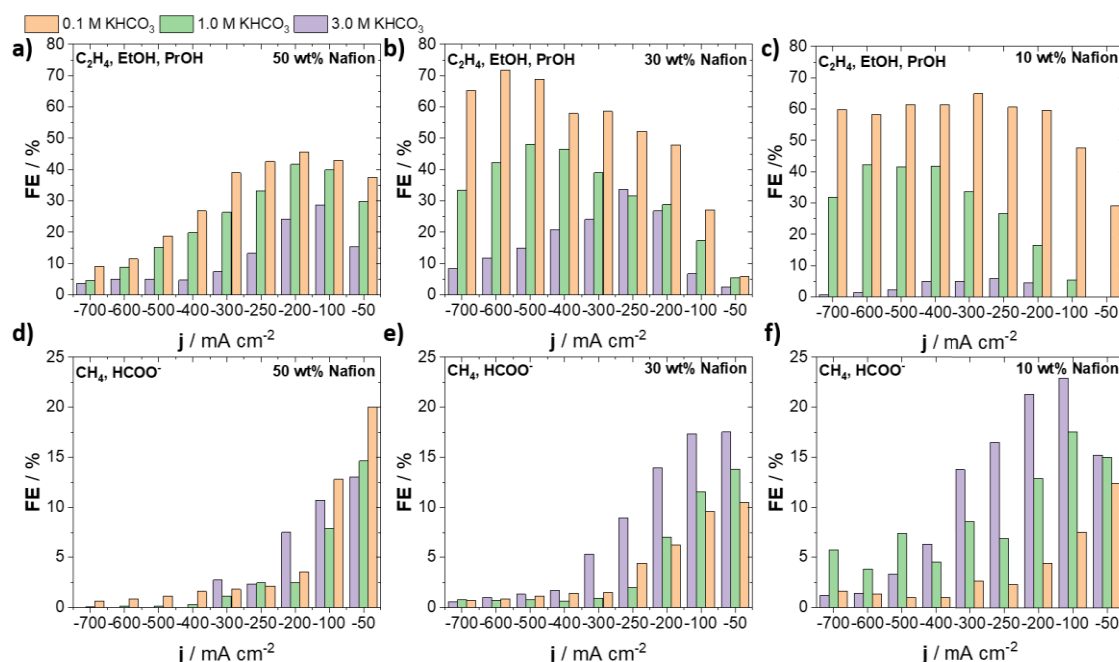


Figure 5.10 Effect of variations in KHCO₃ concentration on the CO₂RR selectivity towards C₂+ products using 50 wt% (a), 30 wt% (b), and 10 wt% (c) of Nafion. Effect of variations in KHCO₃ concentration on the CO₂RR selectivity towards C₁ products using 50 wt% (d), 30 wt% (e), and 10 wt% (f) of Nafion. In all cases Cu₂O loading was const. at 0.7 mg cm⁻². Additional information on FE of H₂ and CO are given in Figure A 2.13.

ORR as Measure of Mass Transport Limitations. As the effects of the local pH, the mass transport and the catalyst kinetics are superimposed and, therefore, often difficult to be unambiguously deconvoluted, especially due to parallel reaction pathways of CO₂RR on Cu and the competing HER, we resorted to the oxygen reduction reaction (ORR) for further discussion of the correlation between binder content and mass transport. In doing so, we were able to exploit the more positive standard reduction potential of the ORR, in respect to CO₂RR, to cancel out the HER and decrease the overall complexity, schematically depicted in Figure 5.11 (a). We take view that such an approach allows for a more direct investigation of the mass transport limitations within our system. To probe the mass transport towards the catalytically active centers of the Cu₂O particles, we varied the partial pressure of O₂ in an N₂ feed at a constant electrode potential of -0.45 V_{RHE}. We chose this potential to achieve the highest possible rate of ORR, while avoiding a region of considerable HER activity, indicated in Figure 5.11 (b). By tracing the change in ORR current as a function of O₂ partial pressure at a fixed electrode potential, we can directly access changes in mass transport caused by variations in binder content. In Figure 5.11 (c), we can see a rise in ORR current with increase in partial pressure of O₂ until around 0.3 bar, where the ORR current of the 10 wt% Nafion sample approaches a plateau. This transition supposedly originates in a change from a primarily mass transport dominated regime, towards one, where reaction kinetics are denying higher reduction rates. The regimes of mass transport and catalytic kinetics are indicated by different levels of shading in Figure 5.11 (c), but should be rather understood as a visual orientation and not as a strict border between the two. A comparison of three

samples with Nafion loadings ranging from 10 to 50 wt% shows an increased ORR current in the mass transport domain of below 0.3 bar of O_2 partial pressure for lower loadings of the ionomer, however, this difference seemed to decrease progressively with a higher partial O_2 pressure (Figure A 2.14). The observed behavior suggests that the mass transport remains limiting even at higher O_2 partial pressure for samples of high Nafion content, whereas samples of reduced binder content showed primarily kinetic limitations at a similar partial pressure of O_2 and constant electrode potential. Our results suggest that the binder content of the catalytic layer of a GDE interferes with the reactant transport. Here, a high binder content induce resistances for the reactant transport and can lead to mass transport limitations.

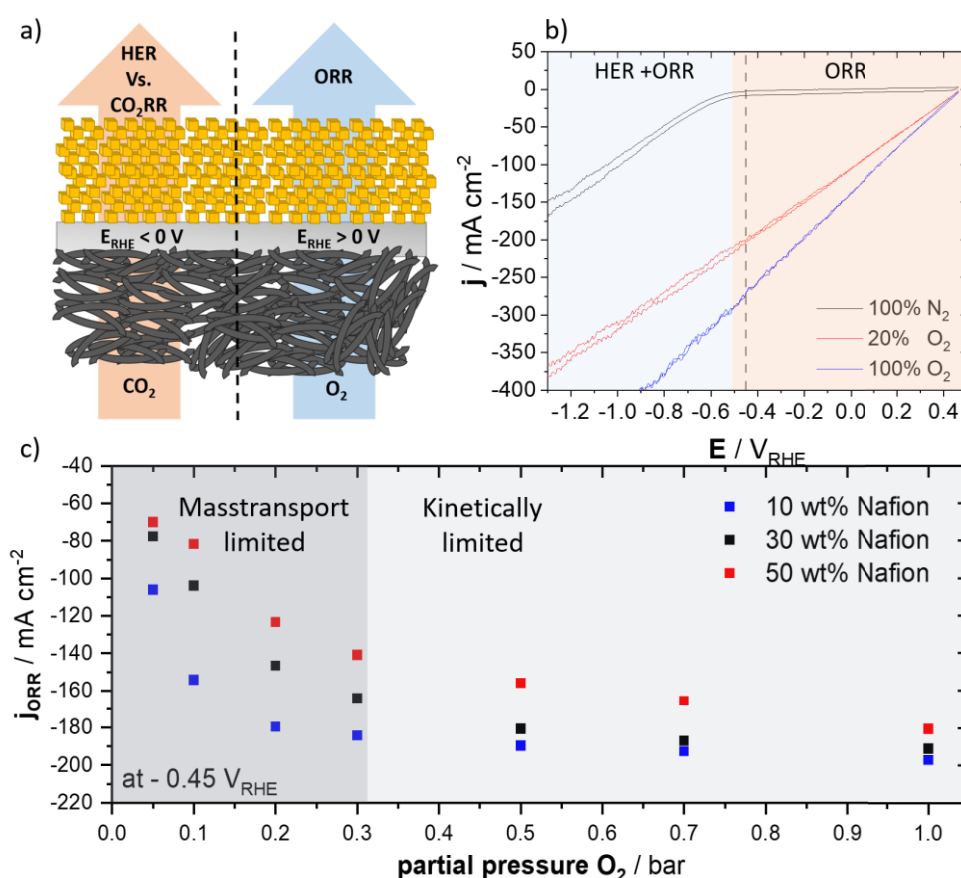


Figure 5.11 Schematic representation of CO₂RR and ORR on the Cu surface of a GDE (a). Cyclic voltammetry under different ratios of N₂/O₂ saturated gas atmosphere in 2 M KHCO₃ for a 10 wt% of Nafion GDE. Different colors are indicating a potential regime of pure ORR or mixed regime of HER and ORR (b). ORR current as a function of partial O₂ pressure from N₂/O₂ mixtures in 2 M KHCO₃ for different Nafion contents in the catalytic layer at a constant electrode potential of -0.45 V_{RHE}. Different levels of shading indicate the primary limitation, either mass transport or reaction kinetics (c).

Electrode structure determines concentration gradients during CO₂ electrolysis. Combining our observations, we can schematically depict the proposed influence of the catalytic layer structure on the selectivity during high-rate CO₂RR electrolysis in a pH-neutral, buffering media. Figure 5.12 (a),

shows a schematic GDE and depicts the relevant reactions, as well as the transport of reactants and products throughout the catalytic layer during CO₂RR. While CO₂ is feed in a gaseous state to the GDE, we take view that a dissolution in the electrolyte prior to reaction on the catalyst surface is highly likely due to the presumable presence of a native solvent layer caused by the hydrophilicity of charged electrodes. On the catalyst, OH⁻ is being produced during the reductive reaction of CO₂ and H₂O, which equilibrates readily with the present, buffering HCO₃⁻ anions, supplied from the bulk electrolyte. This buffer reaction creates CO₃²⁻ and shifts the pH towards alkaline near the electrode surface. In the bulk of the electrolyte the CO₃²⁻ concentration can equilibrate with excess CO₂ to regenerate the buffer and create HCO₃⁻, therefore, approaching a neutral pH. It is important to note that in contrast to H-Cell setups the source of CO₂ and buffer, e.g. bicarbonate, are on opposing sides as indicated by opposed directions of arrows in Figure 5.12 (a). This asymmetric feed implies a largely decoupled transport of dissolved CO₂ and HCO₃⁻ for GDEs in contrast to H-Cell setups and affects the formation of concentration gradients throughout the system. The proposed effect for variation of Nafion content and particle loading is depicted in Figure 5.12 (b). Here, by increasing the particle loading, and consequentially the layer thickness, the mean path of transportation for CO₂ and HCO₃⁻ through the layer is increased. The longer distance of transportation results in a stronger decrease of both species and causes regions of high alkalinity and depletion of CO₂, respectively. We suspect that the increase in Nafion content causes a quite similar drop in reactant concentration throughout the layer. Here, as we have shown from our ORR measurements, an extensive content of Nafion in the catalytic layer presents a barrier for the mass transport of reactants, e.g. O₂ or CO₂, towards the Cu sites. Such impediment of the mass transport can be rationalized by a slower through-plane transport of reactants and steeper decrease in concentration perpendicular to the catalytic layer. Essentially, the outcome is similar to the increased particle loading and results in regions of high alkalinity and depletion of CO₂ at high binder content. Finally, the increase in the bulk concentration of KHCO₃ and, accordingly, the near-(electrode) surface concentration of HCO₃⁻, provides a higher pH buffer capacity and can in turn reduce the pH gradient throughout the catalytic layer. Such increased buffer capacity would therefore lead to lesser alkalization within the porous layer structure. Additionally, the physical solubility of CO₂ is decreasing with the ionic strength, which could lead to a more drastically depletion of CO₂ reactant in regions of the catalytic layer.

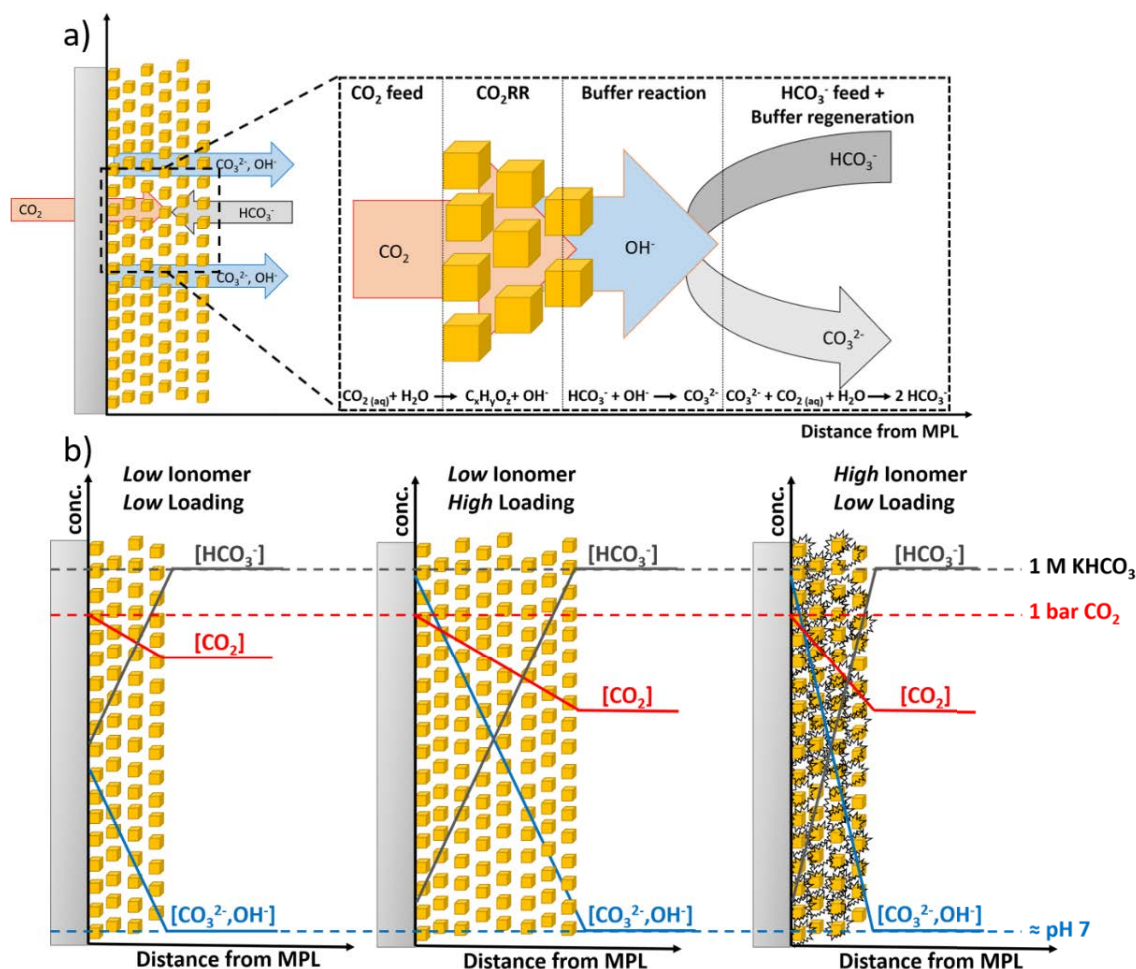


Figure 5.12 Scheme visualizing the transport of reactive species and products with indications of their respective directions throughout the structure of a Cu-GDE during CO_2RR in KHCO_3 (a). Schematic representation of how variations in the Nafion content and particle loading influence concentration gradients throughout the catalytic layer (b).

Concentration gradients establish “selectivity zones”. As a consequence of the through plane concentration gradients for CO_2 and pH within the catalytic layer, we propose zones of different CO_2RR selectivity as a function of distance from the MPL substrate, shown in Figure 5.13. Here, the lowest level of the catalytic layer shows the highest proximity to the gaseous CO_2 feed and furthest distance from the bulk KHCO_3 electrolyte, which results in a region of high pH and CO_2 concentration. With increasing distance from the MPL, those conditions invert and can result in CO_2 deficient regions and relatively lower pH value. The observed catalytic CO_2 selectivity directly correlates to those conditions. Here, the region of high pH and CO_2 concentration directly adjacent to the MPL gives optimal conditions for selective production of pH independent, multi-carbon CO_2RR (C_{2+}) products, as ethylene. With further distance from the MPL, the pH value decreases and the catalytic selectivity can shift towards CO_2RR products, which are preferred at higher proton concentration (C_1), e.g. CH_4 . Finally, in the outermost region of the catalytic layer CO_2 concentration might become deficient, which shifts the catalytic selectivity towards an increased contribution of the HER. Based on the proposed

selectivity zones, a selective CO₂RR electrolyzer for production of C₂₊ compounds in buffering electrolytes would require the deliberate introduction of an impediment for the transport of buffering anions. This could be realized by controlling the structure of the GDE through an increased thickness and a higher density of the catalytic layer, if the transport of CO₂ remains sufficient. Additionally, operation conditions could achieve a similar effect and contribute for further increase in C₂₊ selectivity. Here, lowering electrolyte flow-rates and avoiding bubble formation at the electrode to electrolyte interface could reduce the interfacial convection and in turn lead to creation of an increased hydrodynamic boundary layer thickness, further limiting the transport of buffering anions.

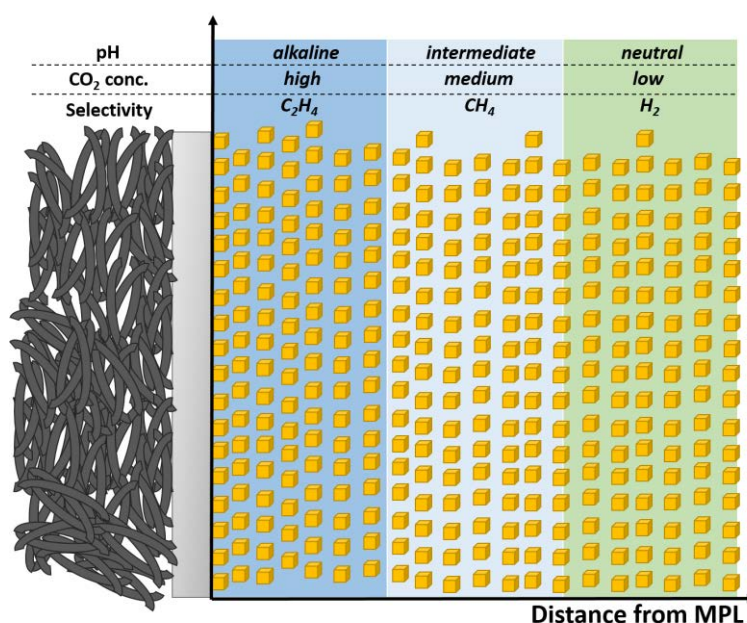


Figure 5.13. Schematic cross section of a GDE, which shows the proposed through-plane CO₂RR selectivity distribution in the catalytic layer due to concentration gradients of pH and CO₂.

5.3.3 Conclusions

In this study, we have investigated relations between electrode structure, more specifically, catalyst loading and Nafion content, and the resulting product selectivity of Cu-based CO₂RR electrolysis at high currents in a bulk pH-neutral flow-electrolyzer. We found that with increasing catalyst loading, that is catalyst layer thickness, or Nafion content the production of pH-sensitive products (e.g. H₂, CH₄ and HCOO⁻) could be suppressed and C₂₊ species were produced more selectively. To explain this, we showed that the Nafion content influences the mass transport using an ORR limiting current analysis at varying oxygen partial pressure as a diagnostic tool. We concluded that such changes in mass transport define and control the local reaction environment in form of pH and CO₂ concentration, and hence can be used to deliberately tune the reaction selectivity. Here, concentration gradients in through-plane directions of the porous catalytic layer are more pronounced and shift the observed catalytic selectivity during the CO₂RR electrolysis. Varying the KHCO₃ electrolyte concentrations showed that the selectivity of the system is highly sensitive to the concentration of the buffering media and agreed

with our proposal that the local pH variations are crucial in determining the CO₂RR selectivity. Our study demonstrates how the structure of the catalytic layer is a key parameter to influence local mass transport and provides an effective way to tune the selectivity during pH neutral (bulk) CO₂RR electrolysis at high currents.

6 Summary and perspective

The goal of this thesis was to extend the knowledge of the underlying factors that determine the catalytic selectivity observed for cationic Cu compounds during the electrochemical CO₂RR. For this purpose, different nanosized cationic Cu catalysts were prepared and investigated under the variation of the anion identity (Cu₂O, Cu₃N, CuS) and the catalyst environment (carbon-supported, self-supported). Structure-selectivity relations were proposed based on a combination of physicochemical characterization techniques and electrochemical tests in an H-Cell setup at low current densities. Furthermore, the electrochemical investigations were extended towards a current regime of technological relevance under employment of a cubic Cu₂O catalyst as a model system to deduce the most prominent factors that govern the CO₂RR selectivity at high CO₂ conversion rates. Here, the use of a Flow-Cell electrolyzer and gas diffusion electrodes allowed the proposition of correlations between the detailed catalyst structure, effects of reaction environment, architecture of the catalytic layer and catalytic selectivity

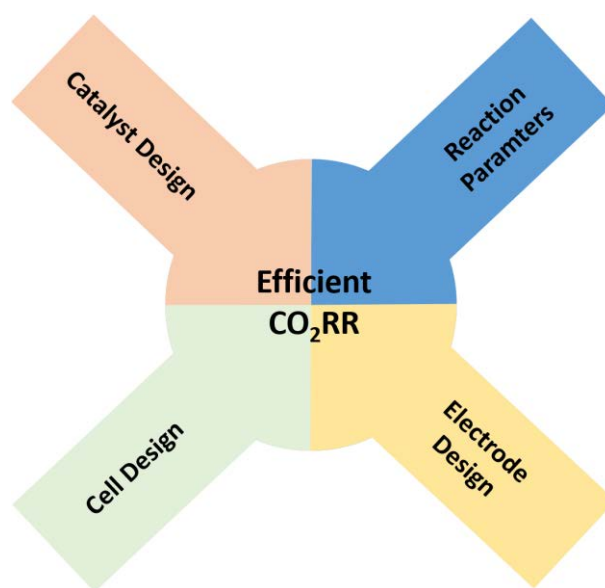


Figure 6.1 Schematic illustration of the factors determining an electrochemical system for efficient CO₂RR.

In conclusion, the present work established determinants for the electrochemical CO₂RR selectivity of Cu-based systems in a buffering, pH neutral electrolyte. Dynamic changes of the catalyst structure and the presence of interfacial concentration gradients as a consequence of the cathodic currents have been deduced and guidelines proposed that can contribute to the efficient production of multi-carbon species. The identification of selectivity determining factors as part of the present work, illustrated in Figure 6.1, will aid in future design of novel systems for the efficient electrolysis of CO₂. The insights provided by this work add to the identification of the necessary elements to compose an industrial CO₂ electrolyzer and contribute to the overall technological maturity of the reaction.

6.1 Summary of results from H-Cell investigations

Chapter 4 of the present work set out to investigate the structural features of cationic Cu compounds that dictate the electrocatalytic CO₂RR selectivity at low reaction rates. For that purpose, cationic Cu-based nanoparticles composed of different anions (S²⁻, N³⁻ and O²⁻) and within different environments (Cu₂O@Cu₂O, Cu₂O@C and Cu₂O/CeO_x) have been synthesized, physicochemically characterized and catalytically tested in an H-Cell setup within pH-neutral solutions of 0.1 M KHCO₃ electrolyte. In this, both, the identity of the anion as well as the detailed catalytic environment proved to be highly decisive for the observed catalytic selectivity during the CO₂RR, which is schematically depicted in Figure 6.2.

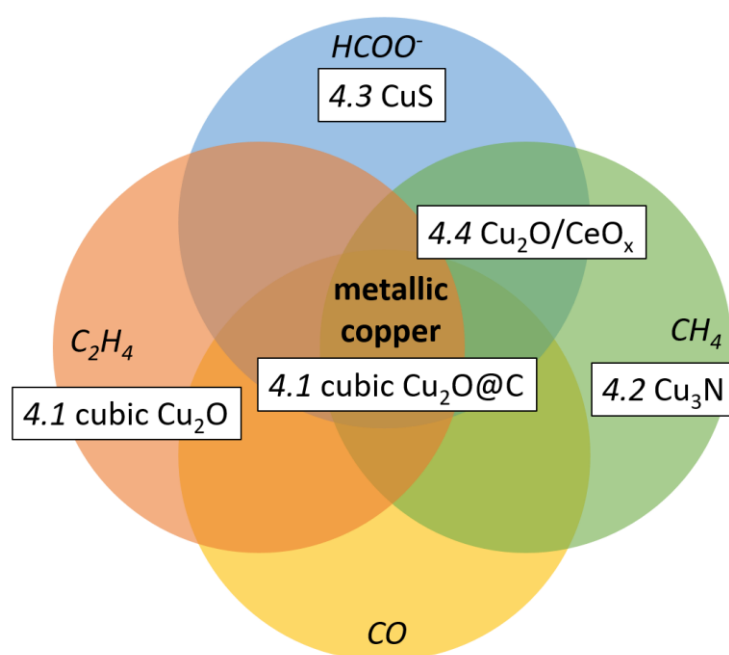


Figure 6.2 Schematic illustration of the CO₂RR selectivity observed for the different catalyst systems investigated throughout chapter 4.

Unsupported and carbon supported Cu₂O nanocubes (chapter 4.1). The temporal evolution of the structural properties of Cu₂O nanocubes during the CO₂RR has been studied and correlated to the observed catalytic selectivity. In this process, compositional investigations of the unsupported Cu₂O nanocubes by operando XAS and in situ XPS revealed a fast and complete reduction of the near-surface region, while for the bulk material a sustained presence of cationic Cu could be detected during prolonged CO₂RR electrolysis. Furthermore, an abundance of undercoordinated Cu sites as a consequence of the reductive conversion of the Cu₂O material to a mostly metallic Cu structure in course of the electrolysis has been deduced. A morphological investigation showed a complete loss of the cubic morphology already after short reaction times, while a high selectivity for C₂₊ products could be maintained over prolonged times of electrolysis. It has been concluded that the formation and sustained presence of undercoordinated Cu sites are decisive for the observed high selectivity for C₂₊.

products of the unsupported Cu₂O nanocubes. Additionally, the presence of a carbon support has been shown to strongly influence the catalytic selectivity of the Cu₂O nanocubes by shifting it towards C₁ products. This observation has been suggested to be, at least in part, correlated to a spatial separation of reaction sites and, thus, the reduced probability for (re)adsorption of reactive intermediates. The study showed that Cu₂O nanocubes can be selective catalysts for the production of C₂₊ species during the CO₂RR and that the selectivity is highly sensitive to the presence of (carbon)-supports.

Thermally prepared Cu₃N nanoparticles (chapter 4.2). The study investigated the morphological and compositional properties, as well as the associated catalytic CO₂RR selectivity of nanoparticles prepared by the thermal decomposition of a Cu(NO₃)₂ precursor. It has been shown that by controlling the reaction temperature either Cu₃N particles with different sizes and, at higher temperatures, metallic Cu particles can be synthesized under otherwise identical reaction conditions. It has been deduced that this emergence of a metallic Cu phase resulted from the successive decomposition of the thermally labile Cu₃N phase. The CO₂RR selectivity has been shown to be rather insensitive to the detailed morphology of the prepared Cu₃N particles, however, highly sensitive to the phase composition of the employed catalyst. As a consequence, all tested Cu₃N nanoparticles proved to be selective catalysts for the production of CH₄, whereas the presence of metallic Cu shifted the catalytic selectivity towards the production of C₂H₄. This work showed that cationic Cu compounds in form of Cu₃N nanoparticles can be selective catalysts for the formation of CH₄ in the electrochemical CO₂RR.

Sulfidation of Cu₂O nanocubes by anion exchange (chapter 4.3). In the presented study CuS nanoparticles were shown to be highly selective catalysts for the CO₂RR towards HCOO⁻. Here, CuS nanoparticles were prepared by an exchange of O²⁻ anions by S²⁻ anions in a nanocubic Cu₂O structure through addition of (NH₄)₂S as a sulfidating reagent. The concentration of the (NH₄)₂S reactant during the anion exchange was shown to influence the resulting nanoparticle morphology, however, this morphological change showed no large effect on the observed CO₂RR selectivity during electrocatalytic tests. Ex situ investigations by GI-XRD after applications of different potentials revealed the successive reduction of the CuS phase that proceeded through an intermediate stage of Cu₂S and Cu₂O and finally resulted in the production of metallic Cu. In contrast to the observation of a metallic bulk state, the catalytic selectivity during CO₂RR was distinctly different from Cu(0) and showed an almost complete suppression for all CO-related products. This observation was rationalized by the sustained presence of CuS_x species in the near surface region of the material enabling this distinct catalytic selectivity. The study presented a facile synthetic procedure for preparation of an HCOO⁻-selective Cu-based catalyst during CO₂RR by introduction of S²⁻ anions. Furthermore, the work illustrated how decisive the detailed identity of the anion in cationic Cu structures can be for steering the CO₂RR selectivity towards selected value-added products.

Investigation of CeO_x doped nanostructured Cu₂O catalysts (chapter 4.4). A nanostructured system composed of Cu₂O with various amounts of CeO_x has been investigated during the

electrocatalytic CO₂RR. By adjustment of the ratio between CeCl₃ and CuCl₃ during the aqueous synthesis, morphological and compositional changes could be introduced to the obtained nanoparticles. Here, the increase of the CeCl₃ concentration was shown to lead to the stepwise degradation of the cubic Cu₂O morphology and the elevated presence of a CeO_x phase. Investigations of the catalytic selectivity during the CO₂RR revealed a general increase in the HER and a shift towards pH-dependent products (HCOO⁻ and CH₄) for the catalysts prepared from higher CeCl₃ concentrations. The work demonstrated how structural properties of Cu₂O can be modified by addition of Ce(III) salts during particle synthesis and that alterations in the particle morphology, as well as the presence of a second metal oxide can impact the catalytic selectivity during CO₂RR

6.2 Summary of results from Flow-Cell investigations

Chapter 5 of the present work set out to investigate the parameters on different length scales (macro, meso and micro), shown in Figure 6.3, that dictate the electrocatalytic CO₂RR selectivity at high reaction rates for CuO_x catalysts in KHCO₃ electrolytes. For this purpose, the presented studies ranged from an investigation of the macroscale compositional electrolyte integrity, over the determination of mesoscale diffusion-limited mass transport effects at electrode/electrolyte interfaces towards the observation of microscale structural changes of the employed CuO_x catalysts.

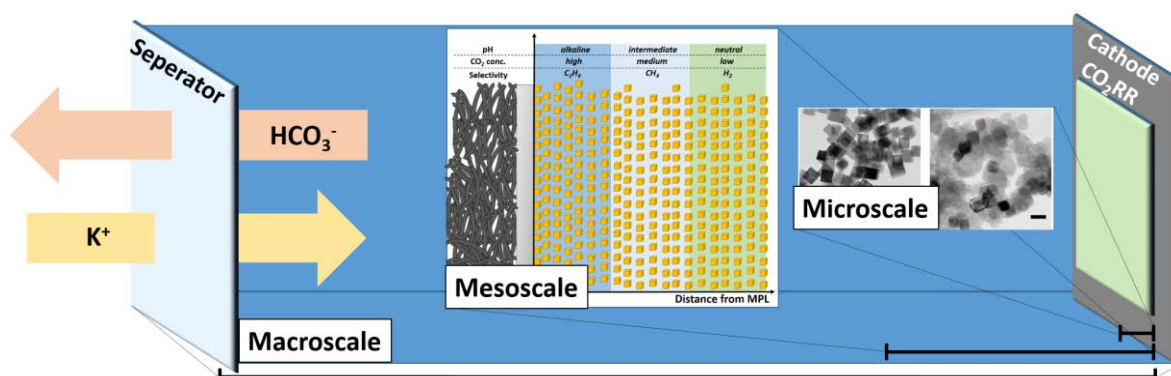


Figure 6.3 Schematic representation of the different length scales relevant to the CO₂RR in a Flow-Cell electrolyzer.

Macroscale investigation of KHCO₃ electrolyte integrity during CO₂RR (chapter 5.1). The correlation of membrane identity, anolyte and catholyte pH, and CO₂ consumption during prolonged electrolysis at elevated currents was explored. It was shown that the transport of the HCO₃⁻ anion across the anion exchange membrane (AEM) can counteract changes in electrolyte composition due to its anodic decomposition and cathodic production. This HCO₃⁻ mediated transport of CO₂ through the AEM from the cathode to the anode compartment allowed for stable operation conditions during the CO₂ electrolysis in between 50 to 500 mA cm⁻² in 1 M KHCO₃ electrolyte. It was deduced that a cation exchange membrane (CEM) does not allow for this transport channel. Instead, the exclusive transport of K⁺ from anode to cathode resulted in a complete depletion of the anolyte in cause of the electrolysis. Consequently, it was established that CEMs are unsuitable for prolonged and high current CO₂RR electrolysis in continuously looped HCO₃⁻ electrolytes. In summary, the study showed how anion migration in AEMs can allow stable operation conditions during CO₂RR through the establishment of a self-regulating system and pH buffering properties of carbonate species.

Microscale investigation of morphological changes for cubic Cu₂O catalysts during CO₂RR (chapter 5.2). Two catalytic motifs of cubic Cu₂O nanoparticles, carbon-supported and unsupported, were investigated for CO₂RR at currents of 50 to 700 mA cm⁻² in 1 M KHCO₃. It was shown that the catalytic selectivity observed at high currents in a flow electrolyzer was qualitatively in line with tests at low currents in an H-Cell, as derived from previous investigations. Here, the carbon-supported

particles showed a shift in catalytic selectivity towards C_1 products in comparison to the C_2 selective unsupported particles independent of the testing setup. However, the usage of a flow electrolyzer generally led to a favored CO_2RR over HER with respect to tests in H-Cells, which points towards a higher availability of CO_2 in the gas-feed Flow-Cell electrolyzer. Additionally, during prolonged electrolysis at 300 mA cm^{-2} for 40 h, a distinct temporal evolution in catalytic selectivity for the supported catalysts was observed, which was not visible over shorter time spans and at lower currents employed during H-Cell tests. Here, the carbon-supported catalyst showed a high selectivity for C_1 products at the start of the reaction, which progressively decreased and gave rise to a selective production of C_2 species. This change in catalytic behavior was accompanied by an initial morphological fragmentation into small Cu particles, followed by agglomeration to larger structures of ill-defined morphology. Such temporal changes could not be observed for the unsupported catalyst, neither for morphology nor for catalytic selectivity. This study shows how the nature of support, either carbon-supported or self-supported, can critically affect the morphological stability of a catalysts and its selectivity observed during high rate CO_2RR . Furthermore, it also exemplified that while H-Cells are suitable for an initial characterization of catalytic properties, they cannot substitute the use of a flow electrolyzer in evaluation of catalytic performance under industrial relevant conditions.

Mesoscale investigations of interfacial concentration gradients, electrode structure and catalytic performance during CO_2RR (chapter 5.3). The study aimed towards the identification of selectivity-determining relations for the CO_2RR at high currents of 50 to 700 mA cm^{-2} in aqueous solutions of $KHCO_3$ electrolyte. Correlations were drawn between the structure of a gas diffusion electrode (GDE) based on nanocubic Cu_2O particles and the selectivity observed during the CO_2RR . Variations in the ionomer (Nafion) to particle catalyst ratio and the particle catalyst loading was shown to allow control over the structural properties of the catalytic layer and in turn push the catalytic selectivity towards pH dependent or independent products. It has been established that both, low binder content and particle loading, are beneficial for production of pH dependent species by minimizing the concentration gradients associated to the high conversion rate at the electrode's surface under elevated currents. In contrast, a high binder content and particle loading led to improved production of pH independent species through pronounced concentration gradients. This correlation was probed by measurements of the diffusion-limited oxygen reduction current at low partial O_2 pressure and through the variation of the $KHCO_3$ electrolyte concentrations. Based on the given results, a layered distribution profile of the catalytic selectivity perpendicular to the GDE has been proposed for the CO_2RR at high rates. In summary, the study showed that mass transport contributes significantly to the observed catalytic selectivity during CO_2RR in $KHCO_3$ electrolytes and that the electrode structure allows for an indirect control over it.

6.3 Perspective

While the pronounced structural and catalytic effect of the introduction of a carbon support to the cubic Cu₂O nanoparticles has been demonstrated within this work, it raises the question of how other supports might perform. Here, carbon supports of different porosity, surface area and with the presence of heteroatom dopants could largely influence the catalytic properties of the supported Cu catalysts. Additionally, support materials of a different chemical nature, such as nitrides and oxides could provide pronounced catalyst-support interactions and modulate the structural stability for cationic Cu catalysts. Overall, the important role of support materials is widely recognized for other areas of electrocatalysis, such as for research on fuel cells and on water electrolysis, but is poorly investigated for the CO₂RR. Further research needs to address this lack of knowledge and, thus, could considerably contribute to the development of more efficient systems.

The anion identity in cationic Cu structures has been shown in the present work to be a highly influential parameter for the catalytic properties of the material. However, for the case of Cu₃N and CuS structures the exact origin of the performance remains elusive. While in chapter 4 the structural investigations at ambient conditions allowed for a proposal of causes, the inherent reactive nature of metallic Cu under ambient conditions weakens the conclusions drawn from any *ex situ* characterization techniques. On that matter, further research will require the incorporation of *in situ* or *operando* spectroscopic and microscopic techniques to help resolve the structural changes of those cationic Cu compounds under reactive conditions and allow for additional insights.

The established importance of the detailed electrochemical environment for the catalytic selectivity, as revealed by Flow-Cell studies of the nanocubic Cu₂O catalyst, has many implications for future investigations. Here, the structural design of the gas diffusion electrode is highly likely to allow an enhanced control over the electrochemical environment and in turn lead to a higher efficiency of the cathodic reaction. Different design strategies could address the wetting properties and gas permeability of the GDE by introduction of hydrophobic binders and additional structuring of the electrode. Beyond the sole consideration of the CO₂RR, a functional system will need to show a suitable energy efficiency and single pass conversions of CO₂ to enable an industrial application of a CO₂RR electrolyzer. In this context, cell design, similar to research on water electrolysis and fuel cells, is required to progress the energy efficiency to appropriate levels. For this purpose, future investigations need to include the choice of suitable membranes, electrolytes, and reaction temperatures for cells of a minimized distance between electrodes, potentially in form of MEAs, to reduce Ohmic resistances and activation losses in order to allow an energy efficient production of carbon compounds from the CO₂RR.

7 References

- [1] C. Mora, D. Spirandelli, E. C. Franklin, J. Lynham, M. B. Kantar, W. Miles, C. Z. Smith, K. Freel, J. Moy, L. V. Louis, E. W. Barba, K. Bettinger, A. G. Frazier, J. F. Colburn IX, N. Hanasaki, E. Hawkins, Y. Hirabayashi, W. Knorr, C. M. Little, K. Emanuel, J. Sheffield, J. A. Patz, C. L. Hunter, *Nature Climate Change* **2018**, *8*, 1062-1071.
- [2] IPCC, *Climate Change 2014: Synthesis Report* **2014**, 151.
- [3] J. Chow, R. J. Kopp, P. R. Portney, *Science* **2003**, *302*, 1528-1531.
- [4] P. Friedlingstein, M. W. Jones, M. O'Sullivan, R. M. Andrew, J. Hauck, G. P. Peters, W. Peters, J. Pongratz, S. Sitch, C. Le Quéré, D. C. E. Bakker, J. G. Canadell, P. Ciais, R. B. Jackson, P. Anthoni, L. Barbero, A. Bastos, V. Bastrikov, M. Becker, L. Bopp, E. Buitenhuis, N. Chandra, F. Chevallier, L. P. Chini, K. I. Currie, R. A. Feely, M. Gehlen, D. Gilfillan, T. Gkritzalis, D. S. Goll, N. Gruber, S. Gutekunst, I. Harris, V. Haverd, R. A. Houghton, G. Hurtt, T. Ilyina, A. K. Jain, E. Joetzjer, J. O. Kaplan, E. Kato, K. Klein Goldewijk, J. I. Korsbakken, P. Landschützer, S. K. Lauvset, N. Lefèvre, A. Lenton, S. Lienert, D. Lombardozi, G. Marland, P. C. McGuire, J. R. Melton, N. Metzl, D. R. Munro, J. E. M. S. Nabel, S.-I. Nakaoka, C. Neill, A. M. Omar, T. Ono, A. Peregon, D. Pierrot, B. Poulter, G. Rehder, L. Resplandy, E. Robertson, C. Rödenbeck, R. Séférian, J. Schwinger, N. Smith, P. P. Tans, H. Tian, B. Tilbrook, F. N. Tubiello, G. R. van der Werf, A. J. Wiltshire, S. Zaehle, *Earth System Science Data* **2019**, *11*, 1783-1838.
- [5] M. Lenzen, *Energy Convers. Manage.* **2008**, *49*, 2178-2199.
- [6] G. Luderer, V. Krey, K. Calvin, J. Merrick, S. Mima, R. Pietzcker, J. Van Vliet, K. Wada, *Climatic Change* **2014**, *123*, 427-441.
- [7] O. Krishan, S. Suhag, *International Journal of Energy Research* **2019**, *43*, 6171-6210.
- [8] T. M. Gür, *Energy & Environmental Science* **2018**, *11*, 2696-2767.
- [9] M. Aneke, M. Wang, *Applied Energy* **2016**, *179*, 350-377.
- [10] P. Nejat, F. Jomehzadeh, M. M. Taheri, M. Gohari, M. Z. Abd. Majid, *Renewable and Sustainable Energy Reviews* **2015**, *43*, 843-862.
- [11] T. Brown, D. Schlachtberger, A. Kies, S. Schramm, M. Greiner, *Energy* **2018**, *160*, 720-739.
- [12] Y. Zhou, M. Wang, H. Hao, L. Johnson, H. Wang, H. Hao, *Mitigation and Adaptation Strategies for Global Change* **2015**, *20*, 777-795.
- [13] X. Cui, C. Tang, Q. Zhang, *Advanced Energy Materials* **2018**, *8*, 1800369.
- [14] S. Nitopi, E. Bertheussen, S. B. Scott, X. Liu, A. K. Engstfeld, S. Horch, B. Seger, I. E. L. Stephens, K. Chan, C. Hahn, J. K. Nørskov, T. F. Jaramillo, I. Chorkendorff, *Chem. Rev.* **2019**, *119*, 7610-7672.
- [15] P. De Luna, C. Hahn, D. Higgins, S. A. Jaffer, T. F. Jaramillo, E. H. Sargent, *Science* **2019**, *364*, eaav3506.
- [16] T. E. Teeter, P. V. Rysselberghe, *The Journal of Chemical Physics* **1954**, *22*, 759-760.
- [17] A. Lieben, *Monatsch. Chem.* **1895**, *16*, 211.
- [18] N. Klobukow, *J. Prakt. Chem.* **1887**, *34*, 126.
- [19] E. Royer, *Compt. rend.* **1870**, *70*, 731.

-
- [20] Y. Hori, R. Takahashi, Y. Yoshinami, A. Murata, *The Journal of Physical Chemistry B* **1997**, *101*, 7075-7081.
- [21] Y. Hori, A. Murata, Y. Yoshinami, *J. Chem. Soc., Faraday Trans.* **1991**, *87*, 125-128.
- [22] A. Murata, Y. Hori, *Bull. Chem. Soc. Jpn.* **1991**, *64*, 123-127.
- [23] Y. Hori, A. Murata, R. Takahashi, S. Suzuki, *J. Chem. Soc., Chem. Commun.* **1988**, 17-19.
- [24] Y. Hori, A. Murata, R. Takahashi, S. Suzuki, *J. Am. Chem. Soc.* **1987**, *109*, 5022-5023.
- [25] H. Yoshio, K. Katsuhei, M. Akira, S. Shin, *Chem. Lett.* **1986**, *15*, 897-898.
- [26] H. Yoshio, K. Katsuhei, S. Shin, *Chem. Lett.* **1985**, *14*, 1695-1698.
- [27] J. M. Spurgeon, B. Kumar, *Energy & Environmental Science* **2018**, *11*, 1536-1551.
- [28] D. U. Nielsen, X.-M. Hu, K. Daasbjerg, T. Skrydstrup, *Nat. Catal.* **2018**, *1*, 244-254.
- [29] M. Jouny, W. Luc, F. Jiao, *Industrial & Engineering Chemistry Research* **2018**, *57*, 2165-2177.
- [30] P. J. A. Kenis, A. Dibenedetto, T. Zhang, *Chemphyschem* **2017**, *18*, 3091-3093.
- [31] S. Verma, B. Kim, H. R. Jhong, S. Ma, P. J. Kenis, *ChemSusChem* **2016**, *9*, 1972-1979.
- [32] X. Li, P. Anderson, H.-R. M. Jhong, M. Paster, J. F. Stubbins, P. J. A. Kenis, *Energy & Fuels* **2016**, *30*, 5980-5989.
- [33] H.-R. M. Jhong, S. Ma, P. J. A. Kenis, *Current Opinion in Chemical Engineering* **2013**, *2*, 191-199.
- [34] K. P. Kuhl, E. R. Cave, D. N. Abram, T. F. Jaramillo, *Energy & Environmental Science* **2012**, *5*, 7050-7059.
- [35] Y. Y. Birdja, E. Pérez-Gallent, M. C. Figueiredo, A. J. Göttle, F. Calle-Vallejo, M. T. M. Koper, *Nature Energy* **2019**, *4*, 732-745.
- [36] A. Bagger, W. Ju, A. S. Varela, P. Strasser, J. Rossmeisl, *ChemPhysChem* **2017**, *18*, 3266-3273.
- [37] C. Shi, H. A. Hansen, A. C. Lausche, J. K. Nørskov, *PCCP* **2014**, *16*, 4720-4727.
- [38] K. P. Kuhl, T. Hatsukade, E. R. Cave, D. N. Abram, J. Kibsgaard, T. F. Jaramillo, *J. Am. Chem. Soc.* **2014**, *136*, 14107-14113.
- [39] R. P. S. Chaplin, A. A. Wragg, *J. Appl. Electrochem.* **2003**, *33*, 1107-1123.
- [40] W. J. Durand, A. A. Peterson, F. Studt, F. Abild-Pedersen, J. K. Nørskov, *Surf. Sci.* **2011**, *605*, 1354-1359.
- [41] A. A. Peterson, F. Abild-Pedersen, F. Studt, J. Rossmeisl, J. K. Nørskov, *Energy & Environmental Science* **2010**, *3*, 1311-1315.
- [42] J. H. Montoya, C. Shi, K. Chan, J. K. Nørskov, *The Journal of Physical Chemistry Letters* **2015**, *6*, 2032-2037.
- [43] R. Kortlever, J. Shen, K. J. P. Schouten, F. Calle-Vallejo, M. T. M. Koper, *The Journal of Physical Chemistry Letters* **2015**, *6*, 4073-4082.
- [44] K. J. P. Schouten, E. Pérez Gallent, M. T. M. Koper, *ACS Catalysis* **2013**, *3*, 1292-1295.
- [45] J. H. Montoya, A. A. Peterson, J. K. Nørskov, *ChemCatChem* **2013**, *5*, 737-742.

References

-
- [46] F. Calle-Vallejo, M. T. M. Koper, *Angew. Chem. Int. Ed.* **2013**, *125*, 7423–7426.
- [47] K. J. P. Schouten, Z. Qin, E. P. Gallent, M. T. M. Koper, *J. Am. Chem. Soc.* **2012**, *134*, 9864–9867.
- [48] K. J. P. Schouten, Y. Kwon, C. J. M. van der Ham, Z. Qin, M. T. M. Koper, *Chemical Science* **2011**, *2*, 1902–1909.
- [49] K. J. P. Schouten, E. Pérez Gallent, M. T. M. Koper, *J. Electroanal. Chem.* **2014**, *716*, 53–57.
- [50] Y. Hori, I. Takahashi, O. Koga, N. Hoshi, *The Journal of Physical Chemistry B* **2002**, *106*, 15–17.
- [51] A. Bagger, W. Ju, A. S. Varela, P. Strasser, J. Rossmeisl, *ACS Catalysis* **2019**, *9*, 7894–7899.
- [52] A. J. Garza, A. T. Bell, M. Head-Gordon, *ACS Catalysis* **2018**, *8*, 1490–1499.
- [53] W. Tang, A. A. Peterson, A. S. Varela, Z. P. Jovanov, L. Bech, W. J. Durand, S. Dahl, J. K. Nørskov, I. Chorkendorff, *PCCP* **2012**, *14*, 76–81.
- [54] C. W. Li, M. W. Kanan, *J. Am. Chem. Soc.* **2012**, *134*, 7231–7234.
- [55] A. Verdager-Casadevall, C. W. Li, T. P. Johansson, S. B. Scott, J. T. McKeown, M. Kumar, I. E. L. Stephens, M. W. Kanan, I. Chorkendorff, *Journal of the American Chemical Society* **2015**, *137*, 9808–9811.
- [56] R. G. Mariano, K. McKelvey, H. S. White, M. W. Kanan, *Science* **2017**, *358*, 1187–1192.
- [57] Y. Chen, C. W. Li, M. W. Kanan, *J. Am. Chem. Soc.* **2012**, *134*, 19969–19972.
- [58] M. Ma, B. J. Trzeźniewski, J. Xie, W. A. Smith, *Angew. Chem. Int. Ed.* **2016**, *55*, 9748–9752.
- [59] H. Mistry, A. S. Varela, C. S. Bonifacio, I. Zegkinoglou, I. Sinev, Y.-W. Choi, K. Kisslinger, E. A. Stach, J. C. Yang, P. Strasser, B. R. Cuenya, *Nature Communications* **2016**, *7*, 12123.
- [60] M. Favaro, H. Xiao, T. Cheng, W. A. Goddard, J. Yano, E. J. Crumlin, *Proceedings of the National Academy of Sciences* **2017**, *114*, 6706–6711.
- [61] A. Eilert, F. Cavalca, F. S. Roberts, J. Osterwalder, C. Liu, M. Favaro, E. J. Crumlin, H. Ogasawara, D. Friebe, L. G. M. Pettersson, A. Nilsson, *The Journal of Physical Chemistry Letters* **2017**, *8*, 285–290.
- [62] F. Cavalca, R. Ferragut, S. Aghion, A. Eilert, O. Diaz-Morales, C. Liu, A. L. Koh, T. W. Hansen, L. G. M. Pettersson, A. Nilsson, *The Journal of Physical Chemistry C* **2017**, *121*, 25003–25009.
- [63] H. Xiao, W. A. Goddard, T. Cheng, Y. Liu, *Proceedings of the National Academy of Sciences* **2017**, *114*, 6685–6688.
- [64] C. Liu, M. P. Lourenço, S. Hedström, F. Cavalca, O. Diaz-Morales, H. A. Duarte, A. Nilsson, L. G. M. Pettersson, *The Journal of Physical Chemistry C* **2017**, *121*, 25010–25017.
- [65] Y. Lum, J. W. Ager, *Angew. Chem. Int. Ed.* **2018**, *57*, 551–554.
- [66] A. J. Garza, A. T. Bell, M. Head-Gordon, *The Journal of Physical Chemistry Letters* **2018**, *9*, 601–606.
- [67] M. Fields, X. Hong, J. K. Nørskov, K. Chan, *The Journal of Physical Chemistry C* **2018**, *122*, 16209–16215.
- [68] K. Yang, R. Kas, W. A. Smith, *J. Am. Chem. Soc.* **2019**, *141*, 15891–15900.
- [69] X. Liu, P. Schlexer, J. Xiao, Y. Ji, L. Wang, R. B. Sandberg, M. Tang, K. S. Brown, H. Peng, S. Ringe, C. Hahn, T. F. Jaramillo, J. K. Nørskov, K. Chan, *Nature Communications* **2019**, *10*, 32.
- [70] R. David, M. Mark, P. J. Ha, W. Chao, *J. Electrochem. Soc.* **2018**, *165*, 799–804.

- [71] K. Jiang, Y. Huang, G. Zeng, F. M. Toma, W. A. Goddard, A. T. Bell, *ACS Energy Letters* **2020**, *5*, 1206-1214.
- [72] D. Ren, Y. Deng, A. D. Handoko, C. S. Chen, S. Malkhandi, B. S. Yeo, *ACS Catalysis* **2015**, *5*, 2814-2821.
- [73] K. D. Yang, W. R. Ko, J. H. Lee, S. J. Kim, H. Lee, M. H. Lee, K. T. Nam, *Angew. Chem. Int. Ed.* **2017**, *56*, 796-800.
- [74] F. S. Roberts, K. P. Kuhl, A. Nilsson, *Angew. Chem. Int. Ed.* **2015**, *127*, 5268-5271.
- [75] P. Grosse, D. Gao, F. Scholten, I. Sinev, H. Mistry, B. Roldan Cuenya, *Angew. Chem. Int. Ed.* **2018**, *57*, 6192-6197.
- [76] R. Reske, H. Mistry, F. Behafarid, B. Roldan Cuenya, P. Strasser, *J. Am. Chem. Soc.* **2014**, *136*, 6978-6986.
- [77] A. Loiudice, P. Lobaccaro, E. A. Kamali, T. Thao, B. H. Huang, J. W. Ager, R. Buonsanti, *Angew. Chem. Int. Ed.* **2016**, *55*, 5789-5792.
- [78] G. Mangione, J. Huang, R. Buonsanti, C. Corminboeuf, *J Phys Chem Lett* **2019**, *10*, 4259-4265.
- [79] J. Huang, N. Hormann, E. Oveisi, A. Loiudice, G. L. De Gregorio, O. Andreussi, N. Marzari, R. Buonsanti, *Nature Communications* **2018**, *9*, 3117.
- [80] Y. Hori, A. Murata, R. Takahashi, *J. Chem. Soc., Faraday Trans. 1* **1989**, *85*, 2309-2326.
- [81] N. Gupta, M. Gattrell, B. MacDougall, *J. Appl. Electrochem.* **2006**, *36*, 161-172.
- [82] K. Klingan, T. Kottakkat, Z. P. Jovanov, S. Jiang, C. Pasquini, F. Scholten, P. Kubella, A. Bergmann, B. Roldan Cuenya, C. Roth, H. Dau, *ChemSusChem* **2018**, *11*, 3449-3459.
- [83] M. Dunwell, X. Yang, B. P. Setzler, J. Anibal, Y. Yan, B. Xu, *ACS Catalysis* **2018**, *8*, 3999-4008.
- [84] M. Schreier, Y. Yoon, M. N. Jackson, Y. Surendranath, *Angew. Chem. Int. Ed.* **2018**, *57*, 10221-10225.
- [85] A. S. Varela, M. Kroschel, T. Reier, P. Strasser, *Catal. Today* **2016**, *260*, 8-13.
- [86] M. R. Singh, Y. Kwon, Y. Lum, J. W. Ager, A. T. Bell, *J. Am. Chem. Soc.* **2016**, *138*, 13006-13012.
- [87] Y. H. Akira Murata, *Bull. Chem. Soc. Jpn.* **1991**, *64*, 123-127.
- [88] E. Pérez-Gallent, G. Marcandalli, M. C. Figueiredo, F. Calle-Vallejo, M. T. M. Koper, *J. Am. Chem. Soc.* **2017**, *139*, 16412-16419.
- [89] R. B. Sandberg, J. H. Montoya, K. Chan, J. K. Nørskov, *Surf. Sci.* **2016**, *654*, 56-62.
- [90] L. D. Chen, M. Urushihara, K. Chan, J. K. Nørskov, *ACS Catalysis* **2016**, *6*, 7133-7139.
- [91] S. Ringe, E. L. Clark, J. Resasco, A. Walton, B. Seger, A. T. Bell, K. Chan, *Energy & Environmental Science* **2019**, *12*, 3001-3014.
- [92] Y. Huang, C. W. Ong, B. S. Yeo, *ChemSusChem* **2018**, *11*, 3299-3306.
- [93] D. Gao, F. Scholten, B. Roldan Cuenya, *ACS Catalysis* **2017**, *7*, 5112-5120.
- [94] A. S. Varela, W. Ju, T. Reier, P. Strasser, *ACS Catalysis* **2016**, *6*, 2136-2144.
- [95] D. T. Whipple, E. C. Finke, P. J. A. Kenis, *Electrochem. Solid-State Lett.* **2010**, *13*, B109.
- [96] S. Verma, X. Lu, S. Ma, R. I. Masel, P. J. Kenis, *Phys. Chem. Chem. Phys.* **2016**, *18*, 7075-7084.

References

-
- [97] H.-R. M. Jhong, F. R. Brushett, P. J. A. Kenis, *Advanced Energy Materials* **2013**, 3, 589-599.
- [98] M. R. Thorson, K. I. Siil, P. J. A. Kenis, *J. Electrochem. Soc.* **2012**, 160, F69-F74.
- [99] S. Ma, M. Sadakiyo, R. Luo, M. Heima, M. Yamauchi, P. J. A. Kenis, *J. Power Sources* **2016**, 301, 219-228.
- [100] C.-T. Dinh, T. Burdyny, M. G. Kibria, A. Seifitokaldani, C. M. Gabardo, F. P. García de Arquer, A. Kiani, J. P. Edwards, P. De Luna, O. S. Bushuyev, C. Zou, R. Quintero-Bermudez, Y. Pang, D. Sinton, E. H. Sargent, *Science* **2018**, 360, 783.
- [101] U. O. Nwabara, E. R. Cofell, S. Verma, E. Negro, P. J. A. Kenis, *ChemSusChem* **2020**, 13, 855-875.
- [102] J. J. Lv, M. Jouny, W. Luc, W. Zhu, J. J. Zhu, F. Jiao, *Adv. Mater.* **2018**, 30, e1803111.
- [103] M. G. Kibria, C. T. Dinh, A. Seifitokaldani, P. De Luna, T. Burdyny, R. Quintero-Bermudez, M. B. Ross, O. S. Bushuyev, F. P. Garcia de Arquer, P. Yang, D. Sinton, E. H. Sargent, *Adv. Mater.* **2018**, e1804867.
- [104] Y. Wang, H. Shen, K. J. T. Livi, D. Raciti, H. Zong, J. Gregg, M. Onadeko, Y. Wan, A. Watson, C. Wang, *Nano Lett.* **2019**, 19, 8461-8468.
- [105] G. L. De Gregorio, T. Burdyny, A. Loiudice, P. Iyengar, W. A. Smith, R. Buonsanti, *ACS Catal* **2020**, 10, 4854-4862.
- [106] T. Burdyny, W. A. Smith, *Energy & Environmental Science* **2019**, 12, 1442-1453.
- [107] D. Bohra, J. H. Chaudhry, T. Burdyny, E. A. Pidko, W. A. Smith, *Energy & Environmental Science* **2019**, 12, 3380-3389.
- [108] D. M. Weekes, D. A. Salvatore, A. Reyes, A. Huang, C. P. Berlinguette, *Acc. Chem. Res.* **2018**, 51, 910-918.
- [109] X. Wang, A. Xu, F. Li, S. F. Hung, D. H. Nam, C. M. Gabardo, Z. Wang, Y. Xu, A. Ozden, A. S. Rasouli, A. H. Ip, D. Sinton, E. H. Sargent, *J. Am. Chem. Soc.* **2020**, 142, 3525-3531.
- [110] Y. C. Tan, K. B. Lee, H. Song, J. Oh, *Joule* **2020**, 4, 1104-1120.
- [111] P. Strasser, H. Ogasawara, in *Chemical Bonding at Surfaces and Interfaces* (Eds.: A. Nilsson, L. G. M. Pettersson, J. K. Nørskov), Elsevier, Amsterdam, **2008**, pp. 397-455.
- [112] F. Barbir, in *PEM Fuel Cells (Second Edition)* (Ed.: F. Barbir), Academic Press, Boston, **2013**, pp. 17-32.
- [113] R. O'Hayre, S.-W. Cha, W. Colella, F. Prinz, in *Fuel Cell Fundamentals*, **2016**, pp. 25-76.
- [114] R. O'Hayre, S.-W. Cha, W. Colella, F. Prinz, in *Fuel Cell Fundamentals*, **2016**, pp. 77-116.
- [115] R. O'Hayre, S.-W. Cha, W. Colella, F. Prinz, in *Fuel Cell Fundamentals*, **2016**, pp. 117-166.
- [116] R. O'Hayre, S.-W. Cha, W. Colella, F. Prinz, in *Fuel Cell Fundamentals*, **2016**, pp. 167-202.
- [117] T. Smolinka, E. T. Ojong, J. Garche, in *Electrochemical Energy Storage for Renewable Sources and Grid Balancing* (Eds.: P. T. Moseley, J. Garche), Elsevier, Amsterdam, **2015**, pp. 103-128.
- [118] J. O. m. Bockris, M. A. V. Devanathan, K. Müller, J. A. V. Butler, *Proceedings of the Royal Society of London. Series A. Mathematical and Physical Sciences* **1963**, 274, 55-79.
- [119] H. Helmholtz, *Annalen der Physik* **1879**, 243, 337-382.
- [120] O. Stern, *Zeitschrift für Elektrochemie und angewandte physikalische Chemie* **1924**, 30, 508-516.

-
- [121] S. Arrhenius, *Z. Phys. Chem.* **1889**, *4U*, 226-248.
- [122] M. Trautz, *Z. Anorg. Allg. Chem.* **1916**, *96*, 1-28.
- [123] K. J. Laidler, M. C. King, *The Journal of Physical Chemistry* **1983**, *87*, 2657-2664.
- [124] S. Treimer, A. Tang, D. C. Johnson, *Electroanalysis* **2002**, *14*, 165-171.
- [125] P. Sabatier, *Berichte der deutschen chemischen Gesellschaft* **1911**, *44*, 1984-2001.
- [126] J. K. Nørskov, T. Bligaard, A. Logadottir, S. Bahn, L. B. Hansen, M. Bollinger, H. Bengaard, B. Hammer, Z. Sljivancanin, M. Mavrikakis, Y. Xu, S. Dahl, C. J. H. Jacobsen, *J. Catal.* **2002**, *209*, 275-278.
- [127] M. P. Andersson, T. Bligaard, A. Kustov, K. E. Larsen, J. Greeley, T. Johannessen, C. H. Christensen, J. K. Nørskov, *J. Catal.* **2006**, *239*, 501-506.
- [128] T. Bligaard, J. K. Nørskov, S. Dahl, J. Matthiesen, C. H. Christensen, J. Sehested, *J. Catal.* **2004**, *224*, 206-217.
- [129] J. K. Nørskov, J. Rossmeisl, A. Logadottir, L. Lindqvist, J. R. Kitchin, T. Bligaard, H. Jónsson, *The Journal of Physical Chemistry B* **2004**, *108*, 17886-17892.
- [130] H. Dau, C. Limberg, T. Reier, M. Risch, S. Roggan, P. Strasser, *ChemCatChem* **2010**, *2*, 724-761.
- [131] J. Rossmeisl, Z. W. Qu, H. Zhu, G. J. Kroes, J. K. Nørskov, *J. Electroanal. Chem.* **2007**, *607*, 83-89.
- [132] Y. Li, Q. Sun, *Advanced Energy Materials* **2016**, *6*, 1600463.
- [133] T. Möller, F. Scholten, T. N. Thanh, I. Sinev, J. Timoshenko, X. Wang, Z. Jovanov, M. Gliech, B. Roldan Cuenya, A. S. Varela, P. Strasser, *Angew. Chem. Int. Ed.* **2020**, *59*, 17974-17983.
- [134] X.-W. Liu, F.-Y. Wang, F. Zhen, J.-R. Huang, *RSC Advances* **2012**, *2*, 7647-7651.
- [135] H. Wu, W. Chen, *J. Am. Chem. Soc.* **2011**, *133*, 15236-15239.
- [136] H. Zhang, B.-R. Hyun, F. W. Wise, R. D. Robinson, *Nano Lett.* **2012**, *12*, 5856-5860.
- [137] N. Leonard, W. Ju, I. Sinev, J. Steinberg, F. Luo, A. S. Varela, B. Roldan Cuenya, P. Strasser, *Chem Sci* **2018**, *9*, 5064-5073.
- [138] M. C. Biesinger, L. W. M. Lau, A. R. Gerson, R. S. C. Smart, *Appl. Surf. Sci.* **2010**, *257*, 887-898.
- [139] A. Łukomska, J. Sobkowski, *J. Electroanal. Chem.* **2004**, *567*, 95-102.
- [140] G. M. Brisard, E. Zenati, H. A. Gasteiger, N. Markovic, P. N. Ross, *Langmuir* **1995**, *11*, 2221-2230.
- [141] F. S. Roberts, K. P. Kuhl, A. Nilsson, *Angew. Chem. Int. Ed.* **2015**, *127*, 5268-5271.
- [142] D. Gao, I. Zegkinoglou, N. J. Divins, F. Scholten, I. Sinev, P. Grosse, B. Roldan Cuenya, *ACS Nano* **2017**, *11*, 4825-4831.
- [143] C. S. Chen, A. D. Handoko, J. H. Wan, L. Ma, D. Ren, B. S. Yeo, *Catalysis Science & Technology* **2015**, *5*, 161-168.
- [144] D. Kim, C. S. Kley, Y. Li, P. Yang, *Proceedings of the National Academy of Sciences* **2017**, *114*, 10560-10565.
- [145] X. Wang, A. S. Varela, A. Bergmann, S. Köhl, P. Strasser, *ChemSusChem* **2017**, *10*, 4642-4649.

References

-
- [146] H. Mistry, F. Behafarid, R. Reske, A. S. Varela, P. Strasser, B. Roldan Cuenya, *ACS Catalysis* **2016**, *6*, 1075-1080.
- [147] K. J. P. Schouten, Z. Qin, E. Pérez Gallent, M. T. M. Koper, *Journal of the American Chemical Society* **2012**, *134*, 9864-9867.
- [148] E. Pérez-Gallent, M. C. Figueiredo, F. Calle-Vallejo, M. T. M. Koper, *Angewandte Chemie International Edition* **2017**, *56*, 3621-3624.
- [149] Y. Lum, B. Yue, P. Lobaccaro, A. T. Bell, J. W. Ager, *The Journal of Physical Chemistry C* **2017**, *121*, 14191-14203.
- [150] C. W. L. Yihong Chen, Matthew W. Kanan, *J. Am. Chem. Soc* **2012**, *134*, 19969–19972.
- [151] A. Eilert, F. S. Roberts, D. Friebe, A. Nilsson, *The Journal of Physical Chemistry Letters* **2016**, *7*, 1466-1470.
- [152] C. Liu, S. Hedström, J. H. Stenlid, L. G. M. Pettersson, *The Journal of Physical Chemistry C* **2019**, *123*, 4961-4968.
- [153] D. Gao, I. Sinev, F. Scholten, R. M. Aran-Ais, N. J. Divins, K. Kvashnina, J. Timoshenko, B. Roldan Cuenya, *Angewandte Chemie International Edition* **2019**, *58*, 17047-17053.
- [154] D. Gao, I. T. McCrum, S. Deo, Y.-W. Choi, F. Scholten, W. Wan, J. G. Chen, M. J. Janik, B. Roldan Cuenya, *ACS Catalysis* **2018**, *8*, 10012-10020.
- [155] X. Feng, K. Jiang, S. Fan, M. W. Kanan, *ACS Central Science* **2016**, *2*, 169-174.
- [156] X. Liu, J. Xiao, H. Peng, X. Hong, K. Chan, J. K. Nørskov, *Nature Communications* **2017**, *8*, 15438.
- [157] I. V. Morozov, K. O. Znamenkov, Y. M. Korenev, O. A. Shlyakhtin, *Thermochim. Acta* **2003**, *403*, 173-179.
- [158] I. Schildermans, J. Mullens, B. J. Van der Veken, J. Yperman, D. Franco, L. C. Van Pucke, *Thermochim. Acta* **1993**, *224*, 227-232.
- [159] C. M. Caskey, R. M. Richards, D. S. Ginley, A. Zakutayev, *Materials Horizons* **2014**, *1*, 424-430.
- [160] R. Gonzalez-Arrabal, N. Gordillo, M. S. Martin-Gonzalez, R. Ruiz-Bustos, F. Agulló-López, *J. Appl. Phys.* **2010**, *107*, 103513.
- [161] T. Nosaka, M. Yoshitake, A. Okamoto, S. Ogawa, Y. Nakayama, *Appl. Surf. Sci.* **2001**, *169–170*, 358-361.
- [162] M. Ebaid, K. Jiang, Z. Zhang, W. S. Drisdell, A. T. Bell, J. K. Cooper, *Chem. Mater.* **2020**, *32*, 3304-3311.
- [163] Z.-Q. Liang, T.-T. Zhuang, A. Seifitokaldani, J. Li, C.-W. Huang, C.-S. Tan, Y. Li, P. De Luna, C. T. Dinh, Y. Hu, Q. Xiao, P.-L. Hsieh, Y. Wang, F. Li, R. Quintero-Bermudez, Y. Zhou, P. Chen, Y. Pang, S.-C. Lo, L.-J. Chen, H. Tan, Z. Xu, S. Zhao, D. Sinton, E. H. Sargent, *Nature Communications* **2018**, *9*.
- [164] R. Lesyuk, E. Klein, I. Yaremchuk, C. Klinke, *Nanoscale* **2018**, *10*, 20640-20651.
- [165] X. J. Wu, X. Huang, X. Qi, H. Li, B. Li, H. Zhang, *Angew. Chem. Int. Ed. Engl.* **2014**, *53*, 8929-8933.
- [166] Y.-Q. Liu, F.-X. Wang, Y. Xiao, H.-D. Peng, H.-J. Zhong, Z.-H. Liu, G.-B. Pan, *Scientific Reports* **2014**, *4*, 5998.
- [167] X.-J. Wu, X. Huang, J. Liu, H. Li, J. Yang, B. Li, W. Huang, H. Zhang, *Angew. Chem. Int. Ed.* **2014**, *53*, 5083-5087.

- [168] T. Shinagawa, G. O. Larrazábal, A. J. Martín, F. Krumeich, J. Pérez-Ramírez, *ACS Catalysis* **2018**, *8*, 837-844.
- [169] Y. Deng, Y. Huang, D. Ren, A. D. Handoko, Z. W. Seh, P. Hirunsit, B. S. Yeo, *ACS Appl Mater Interfaces* **2018**, *10*, 28572-28581.
- [170] R. García-Muelas, F. Dattila, T. Shinagawa, A. J. Martín, J. Pérez-Ramírez, N. López, *The Journal of Physical Chemistry Letters* **2018**, *9*, 7153-7159.
- [171] C. Kim, T. Möller, J. Schmidt, A. Thomas, P. Strasser, *ACS Catalysis* **2018**, *9*, 1482-1488.
- [172] B. Lv, Z. Liu, H. Tian, Y. Xu, D. Wu, Y. Sun, *Adv. Funct. Mater.* **2010**, *20*, 3987-3996.
- [173] S. Mozaffari, W. Li, C. Thompson, S. Ivanov, S. Seifert, B. Lee, L. Kovarik, A. M. Karim, *Nanoscale* **2017**, *9*, 13772-13785.
- [174] Y. Hu, B. Lee, C. Bell, Y.-S. Jun, *Langmuir* **2012**, *28*, 7737-7746.
- [175] W.-C. Huang, L.-M. Lyu, Y.-C. Yang, M. H. Huang, *J. Am. Chem. Soc.* **2012**, *134*, 1261-1267.
- [176] Y. Shang, L. Guo, *Advanced Science* **2015**, *2*, 1500140.
- [177] D. Channei, S. Phanichphant, A. Nakaruk, S. S. Mofarah, P. Koshy, C. C. Sorrell, *Catalysts* **2017**, *7*, 45.
- [178] P. Yu, S. A. Hayes, T. J. O'Keefe, M. J. O'Keefe, J. O. Stoffer, *J. Electrochem. Soc.* **2006**, *153*, C74.
- [179] S. A. Hayes, P. Yu, T. J. O'Keefe, M. J. O'Keefe, J. O. Stoffer, *J. Electrochem. Soc.* **2002**, *149*, C623.
- [180] G. Bianchi, P. Longhi, *Corros. Sci.* **1973**, *13*, 853-864.
- [181] S. B. Varandili, J. Huang, E. Oveisi, G. L. De Gregorio, M. Mensi, M. Strach, J. Vavra, C. Gadiyar, A. Bhowmik, R. Buonsanti, *ACS Catalysis* **2019**, *9*, 5035-5046.
- [182] L. C. Weng, A. T. Bell, A. Z. Weber, *Phys. Chem. Chem. Phys.* **2018**, *20*, 16973-16984.
- [183] M. Ma, E. L. Clark, K. T. Therkildsen, S. Dalsgaard, I. Chorkendorff, B. Seger, *Energy & Environmental Science* **2020**, *13*, 977-985.
- [184] P. Paciok, M. Schalenbach, M. Carmo, D. Stolten, *J. Power Sources* **2017**, *365*, 53-60.
- [185] L. Dubau, L. Castanheira, G. Berthomé, F. Maillard, *Electrochim. Acta* **2013**, *110*, 273-281.
- [186] R. Reske, H. Mistry, F. Behafarid, B. Roldan Cuenya, P. Strasser, *J. Am. Chem. Soc.* **2014**, *136*, 6978-6986.
- [187] H. Jung, S. Y. Lee, C. W. Lee, M. K. Cho, D. H. Won, C. Kim, H.-S. Oh, B. K. Min, Y. J. Hwang, *J. Am. Chem. Soc.* **2019**, *141*, 4624-4633.
- [188] R. M. Arán-Ais, R. Rizo, P. Grosse, G. Algara-Siller, K. Dembélé, M. Plodinec, T. Lunkenbein, S. W. Chee, B. R. Cuenya, *Nature Communications* **2020**, *11*, 3489.
- [189] R. Kas, R. Kortlever, A. Milbrat, M. T. Koper, G. Mul, J. Baltrusaitis, *Phys. Chem. Chem. Phys.* **2014**, *16*, 12194-12201.
- [190] R. Kas, R. Kortlever, H. Yilmaz, M. T. M. Koper, G. Mul, *ChemElectroChem* **2015**, *2*, 354-358.
- [191] J. Gao, H. Zhang, X. Guo, J. Luo, S. M. Zakeeruddin, D. Ren, M. Gratzel, *J. Am. Chem. Soc.* **2019**, *141*, 18704-18714.
- [192] Y. Lum, J. W. Ager, *Energy & Environmental Science* **2018**, *11*, 2935-2944.

References

- [193] X. Wang, J. F. de Araujo, W. Ju, A. Bagger, H. Schmies, S. Kuhl, J. Rossmeisl, P. Strasser, *Nature Nanotechnology* **2019**, *14*, 1063-1070.
- [194] C. G. Morales-Guio, E. R. Cave, S. A. Nitopi, J. T. Feaster, L. Wang, K. P. Kuhl, A. Jackson, N. C. Johnson, D. N. Abram, T. Hatsukade, C. Hahn, T. F. Jaramillo, *Nat. Catal.* **2018**, *1*, 764-771.
- [195] H. Ooka, M. C. Figueiredo, M. T. M. Koper, *Langmuir* **2017**, *37*, 9307-9313.
- [196] Y. Yoon, A. S. Hall, Y. Surendranath, *Angew. Chem. Int. Ed.* **2016**, *55*, 15282-15286.
- [197] S. Suter, S. Haussener, *Energy & Environmental Science* **2019**, *12*, 1668-1678.
- [198] S. Ott, A. Orfanidi, H. Schmies, B. Anke, H. N. Nong, J. Hübner, U. Gernert, M. Gliech, M. Lerch, P. Strasser, *Nature Materials* **2020**, *19*, 77-85.
- [199] T. Cheng, H. Xiao, W. A. Goddard, *J. Am. Chem. Soc.* **2016**, *138*, 13802-13805.

Appendix

A 1 Supplementary information to CO₂RR in an H-Cell

Supplementary information to chapter 4.1

The supplementary information to subchapter 4.1 has been reproduced from T. Möller et al., *Angew. Chem. Int. Ed.* **2020**, *59*, 17974-17983, (reference ^[133], DOI: [10.1002/anie.202007136](https://doi.org/10.1002/anie.202007136)). Licensed under [CC BY 4.0](#).

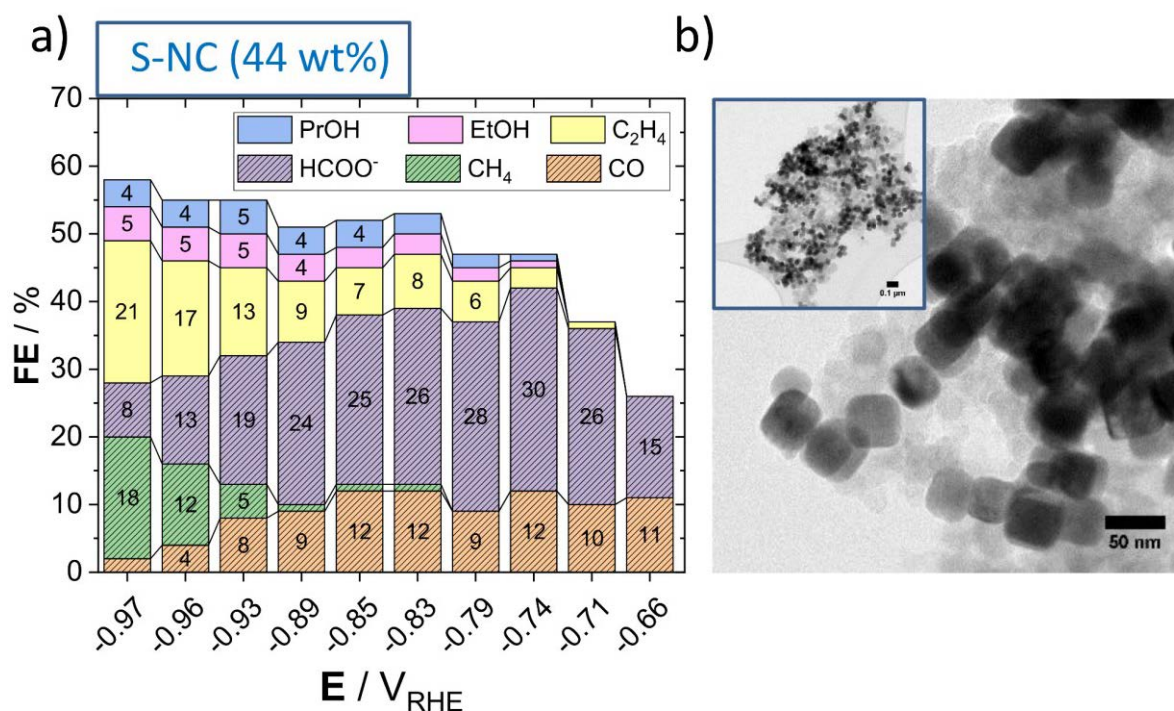


Figure A 1.1 (a) Faradaic product efficiencies (FEs) as a function of IR-free applied electrode potential after one hour of reaction time. (b) Transmission electron microscopy (TEM) images of the S-NC (44 wt%) catalyst, a low magnification TEM is given in the inset.

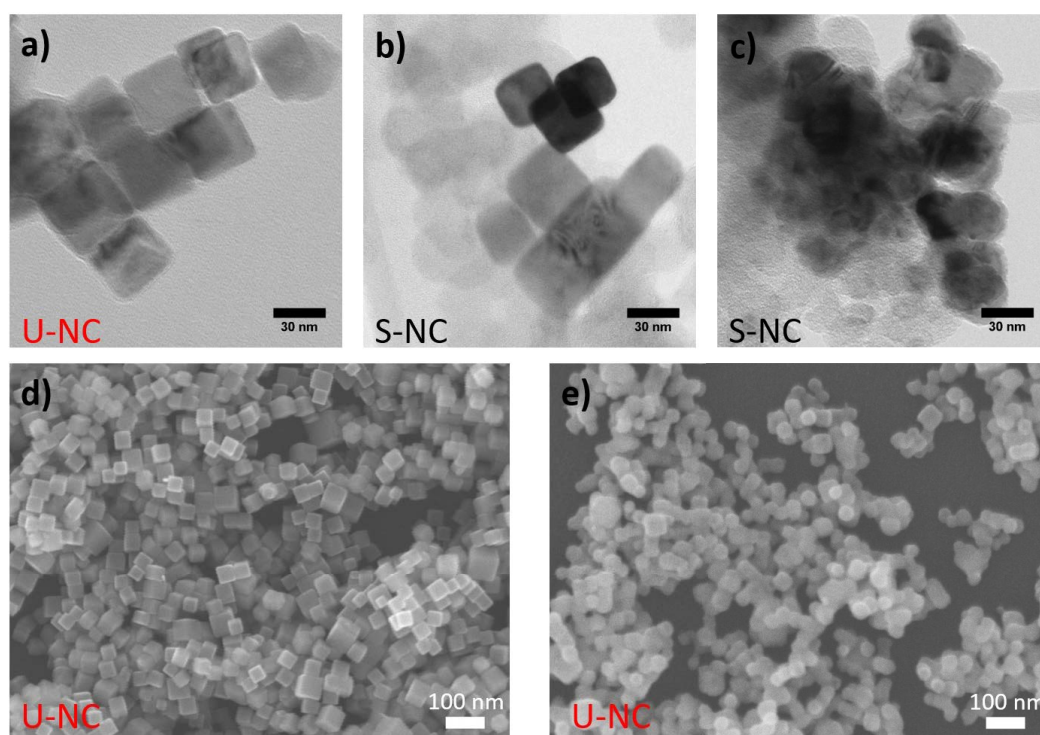


Figure A 1.2 Transmission electron microscopy (TEM) images of the U-NC (a) and S-NC (b) catalyst in as prepared state and for the S-NC after CO₂RR at an electrode potential of $-0.95 V_{\text{RHE}}$ in H-Cell (c). Scanning electron microscopy (SEM) images of the U-NC catalyst on a glassy carbon electrode, in as prepared state (d) and after CO₂RR at an electrode potential of $-0.95 V_{\text{RHE}}$ in H-Cell (e). In case of the U-NC catalyst no Nafion was used and the loading was reduced to $20 \mu\text{g cm}^{-2}$ to allow a clearer imaging of the particles. Time of electrolysis was 60 min in all cases.

	U-NC	23 wt% S-NC	44 wt% S-NC
Total amount of catalyst deposited on GC plate [$\mu\text{g/cm}^2$]	100	380	380
Total Cu ₂ O particle loading on GC plate [$\mu\text{g/cm}^2$]	100	87	167

Table A 1.1 Total amount of catalyst-powder and respective Cu₂O particles deposited on the glassy carbon (GC) plates for CO₂RR experiments in H-Cell.

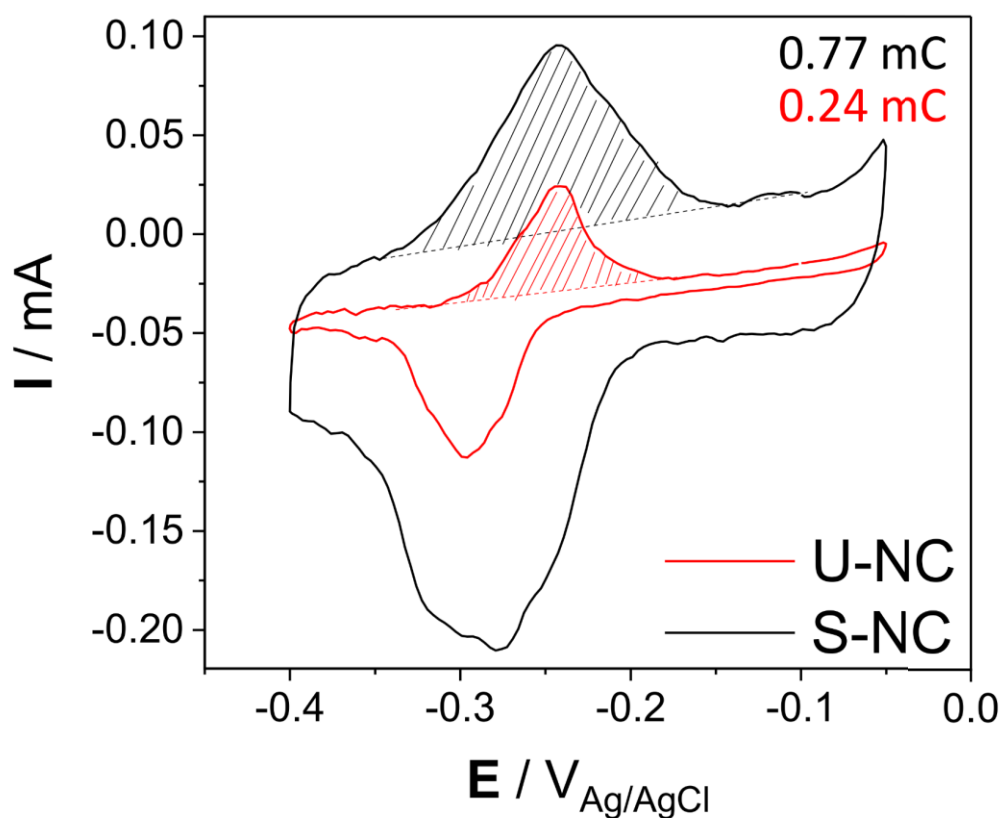


Figure A 1.3 Final CVs obtained for the unsupported nanocubes, U-NC, and supported nanocubes, S-NC, (23 wt%) catalyst after cycling in an aqueous solution of 0.01 M $\text{Pb}(\text{ClO}_4)_2$ and 0.1 M HClO_4 at 10 mV s^{-1} in between -0.40 V and -0.05 V vs Ag/AgCl. Prior to Pb-UPD both samples have been reduced for 5 h at $-0.86 \text{ V}_{\text{RHE}}$ during CO_2RR to ensure a purely metallic material. The given value represents the charge derived from the anodic stripping peak at -0.24 V vs Ag/AgCl, indicated by the shaded area.

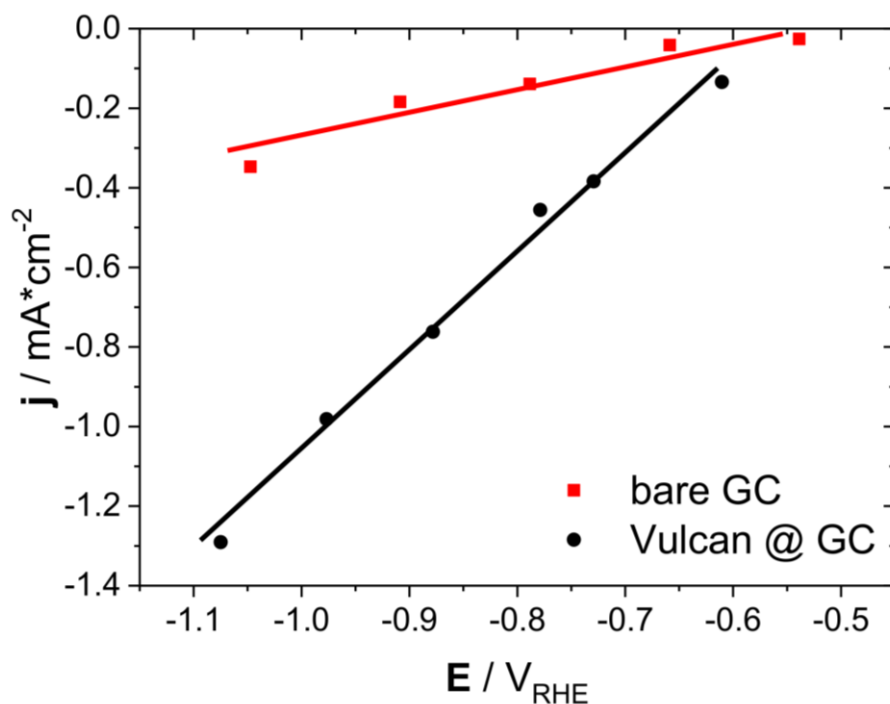


Figure A 1.4 Current density achieved by using the bare glassy carbon plate (GC) or 300 $\mu\text{g cm}^{-2}$ of Vulcan carbon deposited on a GC plate. The conditions were equal to the CO₂RR tests including the Cu₂O particles. Lines to guide the eye.

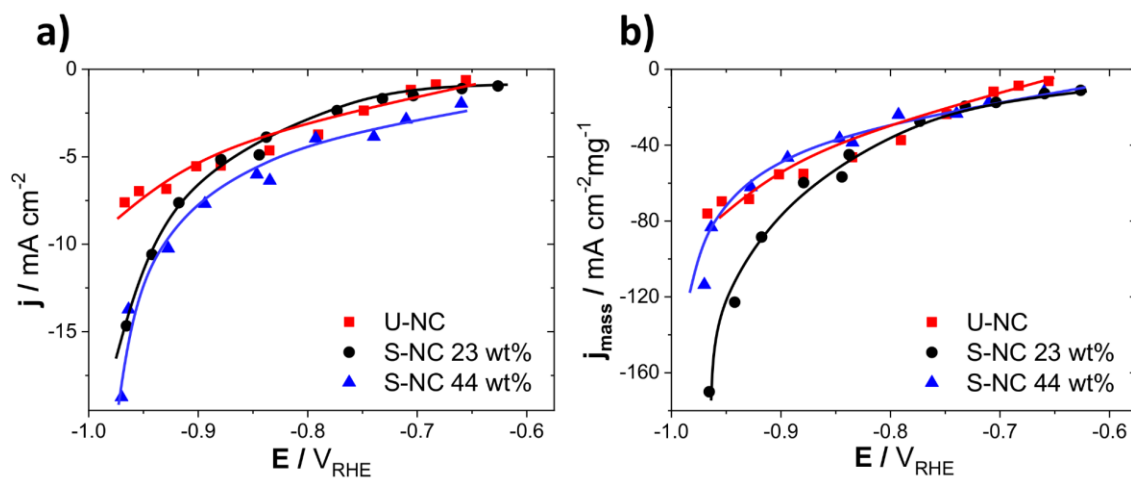


Figure A 1.5 Current density normalized to geometric area (a) and to deposited mass of Cu (b) after one hour of constant potential. The reported value resulted from the averaged current during the last minute of reaction. Lines to guide the eye.

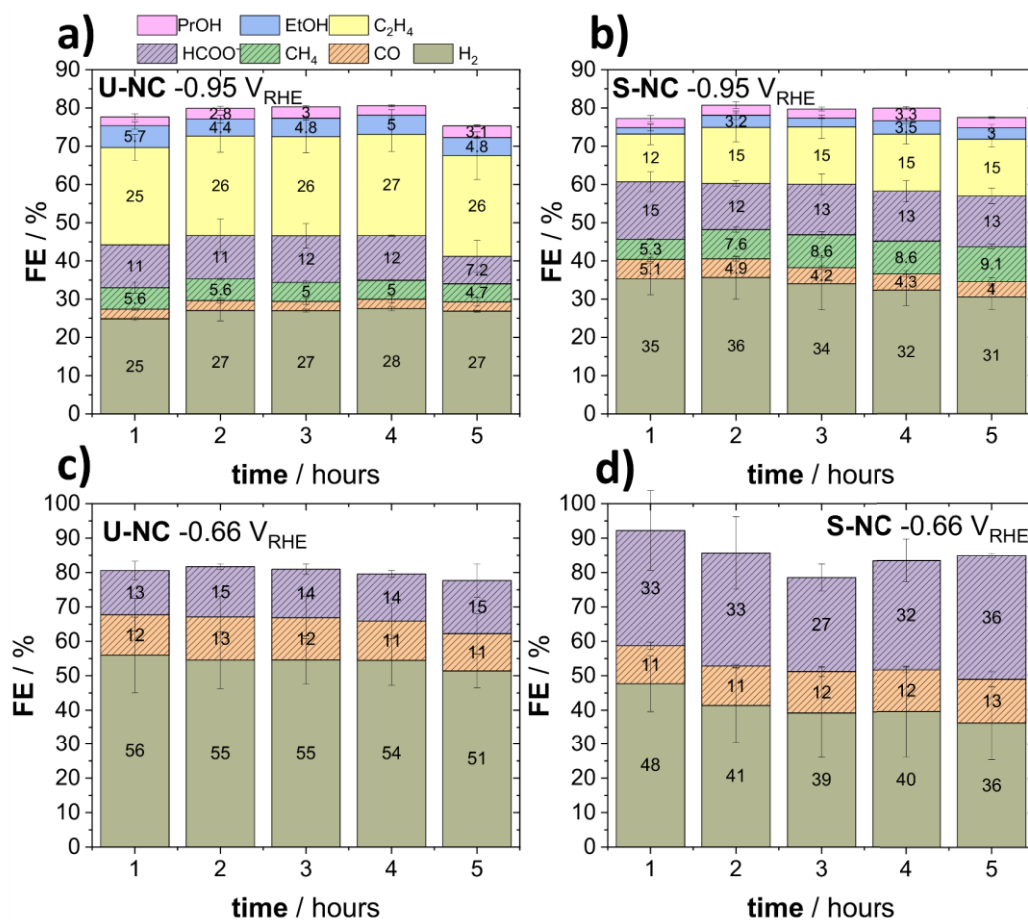


Figure A 1.6 Faradaic efficiency during CO₂RR over 5 hours for the U-NC catalyst at -0.95 V_{RHE} (a) and -0.66 V_{RHE} (c), as well as for S-NC catalyst at -0.95 V_{RHE} (b) and -0.66 V_{RHE} (d). Values are the average of 2 independent measurements and error bars represent the respective standard deviation. The electrolyte is 0.1 M KHCO₃ saturated with CO₂ (pH = 6.8).

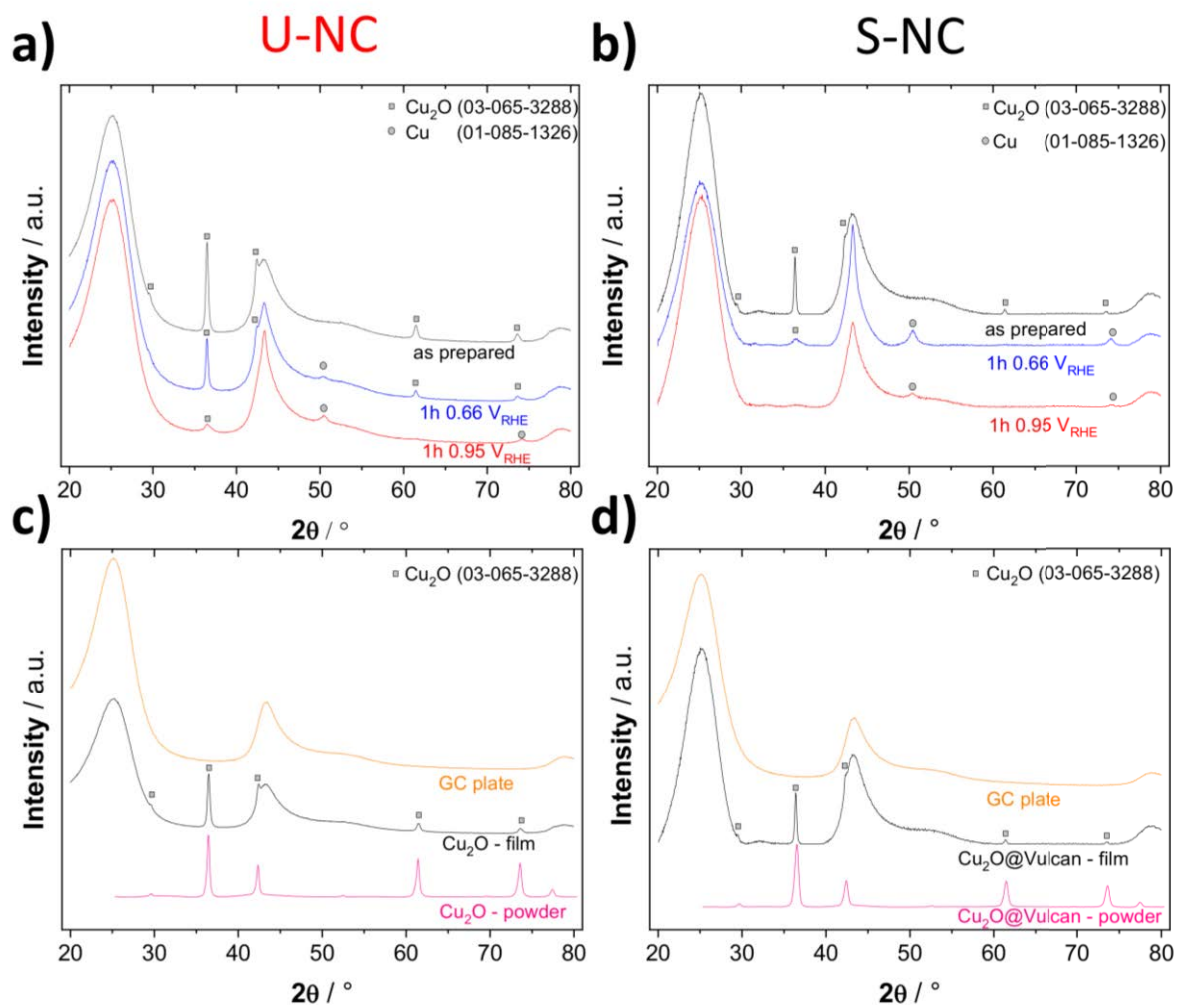


Figure A 1.7 XRD measurements of the unsupported (a) and 23 wt% supported catalyst (b) on GC plate as prepared (black), after one hour of CO_2RR conditions at $-0.66 \text{ V}_{\text{RHE}}$ (blue) and at $-0.95 \text{ V}_{\text{RHE}}$ (red). Comparison of a XRD measurement for the GC plate substrate (orange) and catalyst powder (pink) for the unsupported catalyst (c) and the 23 wt% catalyst (d) illustrating the origin of the film-XRD pattern of the respective catalyst (black).

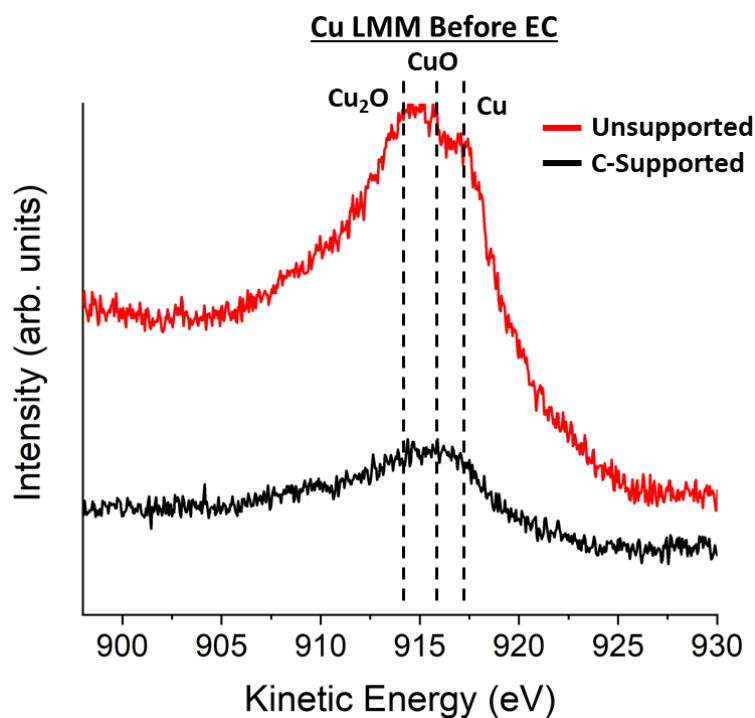


Figure A 1.8 Cu-AES measurements of the as-prepared supported (23 wt%) and unsupported catalyst.

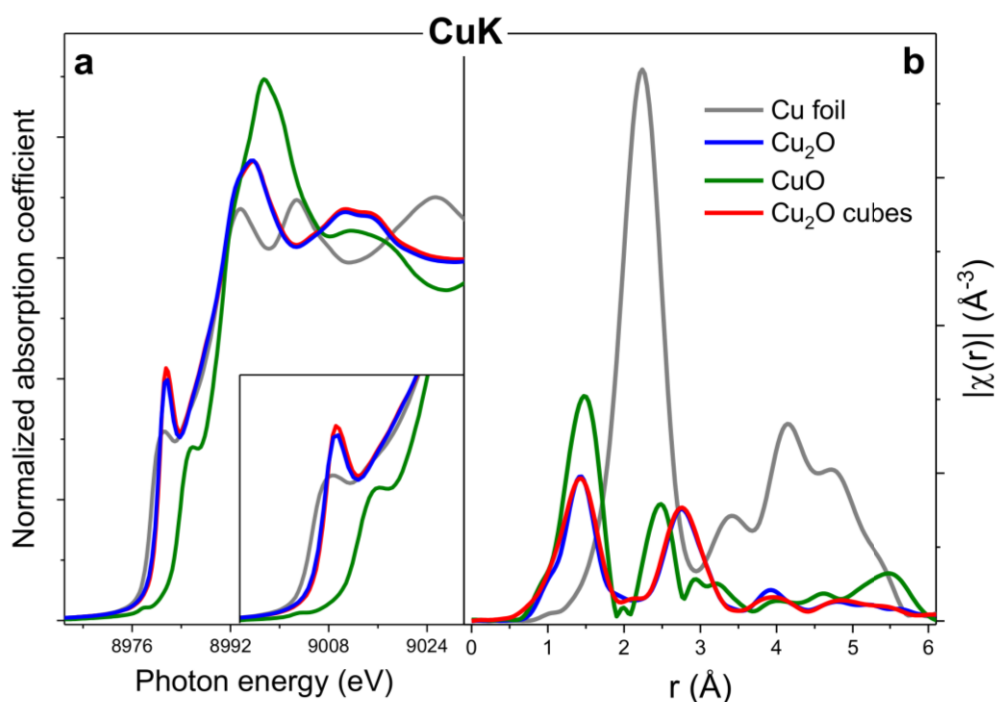


Figure A 1.9 The initial as-prepared state of Cu_2O cube sample is displayed and compared with references. (a) Cu K-edge X-ray absorption near edge structure (XANES) spectra. The inset shows the pre-edge feature. (b) – Fourier transformed Cu K-edge extended X-ray absorption fine structure (EXAFS) spectra.

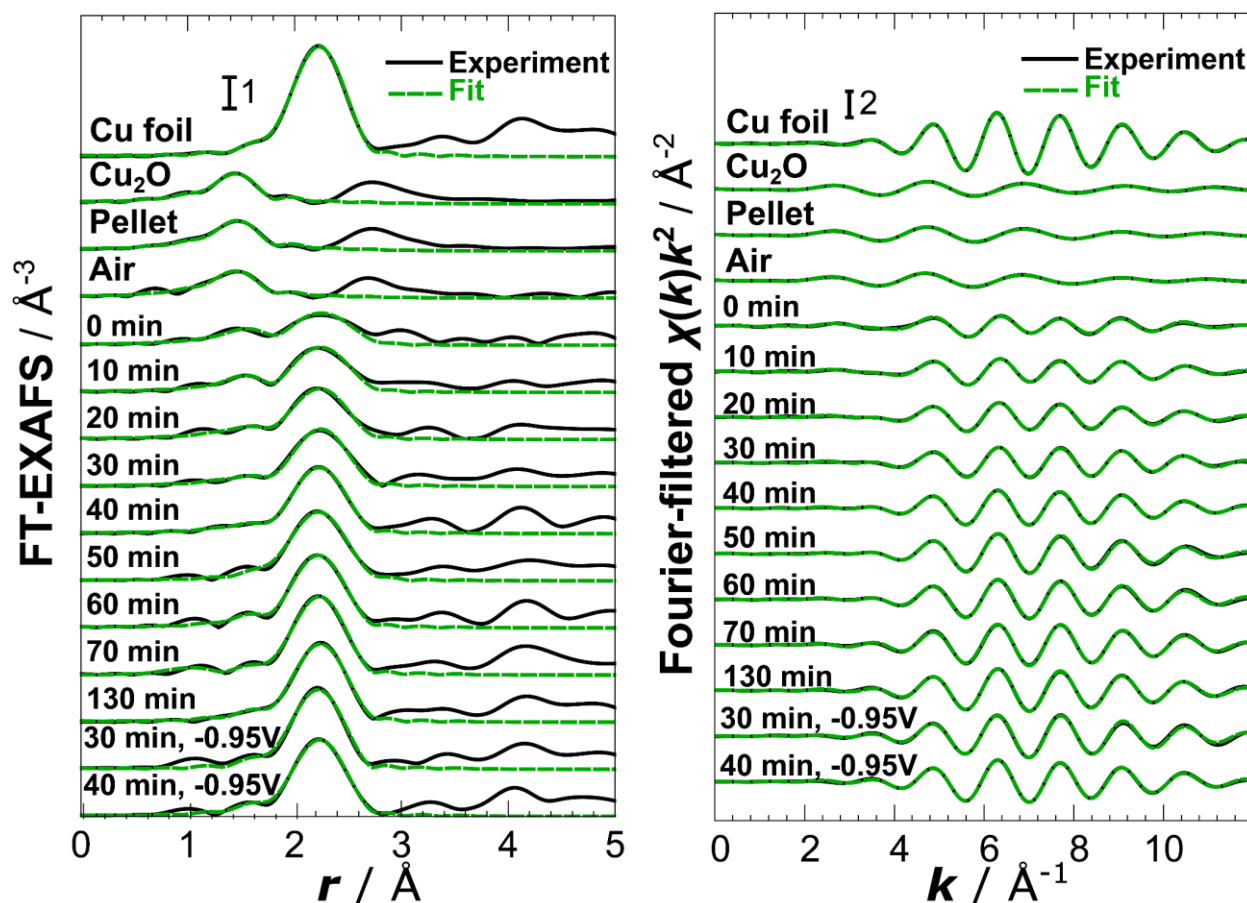


Figure A 1.10 Fits of EXAFS spectra of the Cu_2O cubes and references in r and k -spaces Spectra for the initial as-prepared state of Cu_2O cube sample measured in transmission (“Pellet”) and in fluorescence mode in electrochemical cell without electrolyte (“Air”) are compared with the spectra for reference samples (Cu foil and Cu_2O) and with time-dependent *operando* EXAFS data collected at $-0.66\text{V}_{\text{RHE}}$ (spectra for 0 min - 130 min) and at $-0.95\text{V}_{\text{RHE}}$. Fitting of EXAFS spectra $\chi(k)k^2$ was carried out in r -space in the range from 1.0 Å up to 2.8 Å (2.1 Å for Cu_2O). Fourier transform was carried out in the k range from 3 Å^{-1} up to 12 Å^{-1} .

Appendix – Supplementary information to H-Cell investigations

Sample	N_{Cu-Cu}	R_{Cu-Cu} (Å)	σ_{Cu-Cu}^2 (Å ²)	N_{Cu-O}	R_{Cu-O} (Å)	σ_{Cu-O}^2 (Å ²)	ΔE_0 (eV)	R-factor
Cu foil	12	2.541(3)	0.009(4)	0	-	-	2.0(5)	0.002
Cu₂O	0	-	-	2	1.836(8)	0.002(1)	1.1(1)	0.011
As-prepared (pellet, transmission)	0	-	-	2.2(2)	1.848(6)	0.003(1)	2(1)	0.006
As-prepared (air, fluorescence)	0	-	-	2.1(2)	1.846(9)	0.003(1)	0(1)	0.011
-0.66 V_{RHE}, 0 min	3.6(8)	2.56(1)	0.009(2)	1.1(4)	1.90(3)	0.003(5)	7(2)	0.028
-0.66 V_{RHE}, 10 min	4.6(6)	2.553(8)	0.008(1)	0.8(3)	1.88(2)	0.001(3)	5(1)	0.01
-0.66 V_{RHE}, 20 min	5.3(8)	2.545(9)	0.000(1)	0.8(5)	1.89(3)	0.005(9)	4(1)	0.014
-0.66 V_{RHE}, 30 min	5.5(6)	2.548(7)	0.0078(9)	0.6(3)	1.87(3)	0.004(8)	4(1)	0.008
-0.66 V_{RHE}, 40 min	6.6(3)	2.542(3)	0.0082(4)	0.4(2)	1.86(2)	0.002(5)	3(1)	0.002
-0.66 V_{RHE}, 50 min	7.6(7)	2.54(6)	0.0090(8)	0.4(3)	1.89(4)	0.001(9)	2(1)	0.005
-0.66 V_{RHE}, 60 min	7.2(8)	2.536(7)	0.0082(9)	0.4(4)	1.90(4)	0.01(1)	3(1)	0.009
-0.66 V_{RHE}, 70 min	7.3(5)	2.539(5)	0.0077(6)	0.5(6)	1.86(6)	0.01(2)	2.6(8)	0.003
-0.66 V_{RHE}, 130 min	7.9(6)	2.545(5)	0.0084(7)	0.3(3)	1.91(5)	0.01(1)	3.3(8)	0.004
-0.95 V_{RHE}, 30 min	7(1)	2.53(1)	0.007(1)	0.2(6)	2.1 (1)	0.01(3)	1(2)	0.015
-0.95 V_{RHE}, 40 min	8.2(7)	2.543(6)	0.0088(8)	0.3(3)	1.92(5)	0.01(1)	3(1)	0.005

Table A 1.2 Evolution of coordination numbers and interatomic distances from EXAFS. Coordination numbers (N), interatomic distances (R) and disorder factors (σ^2) of Cu-O and Cu-Cu nearest neighbors from EXAFS, as well as corrections to photoelectron reference energies ΔE_0 .

Supplementary information to chapter 4.2

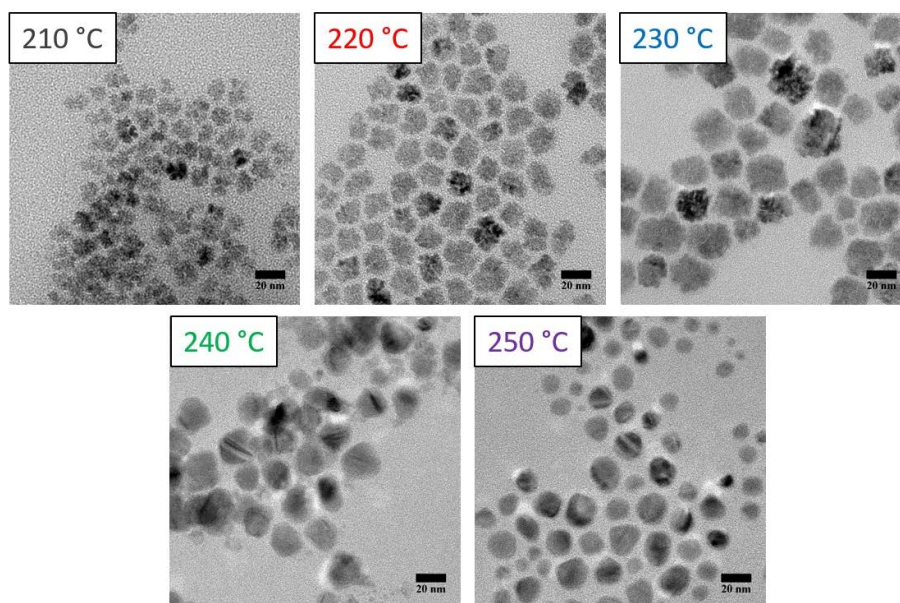


Figure A 1.11 TEM images for the particles prepared at different temperatures from thermal decomposition of $\text{Cu}(\text{NO}_3)_2 \cdot 2.5 \text{H}_2\text{O}$ in presence of octadecylamine. The scale bar in each image corresponds to 20 nm.

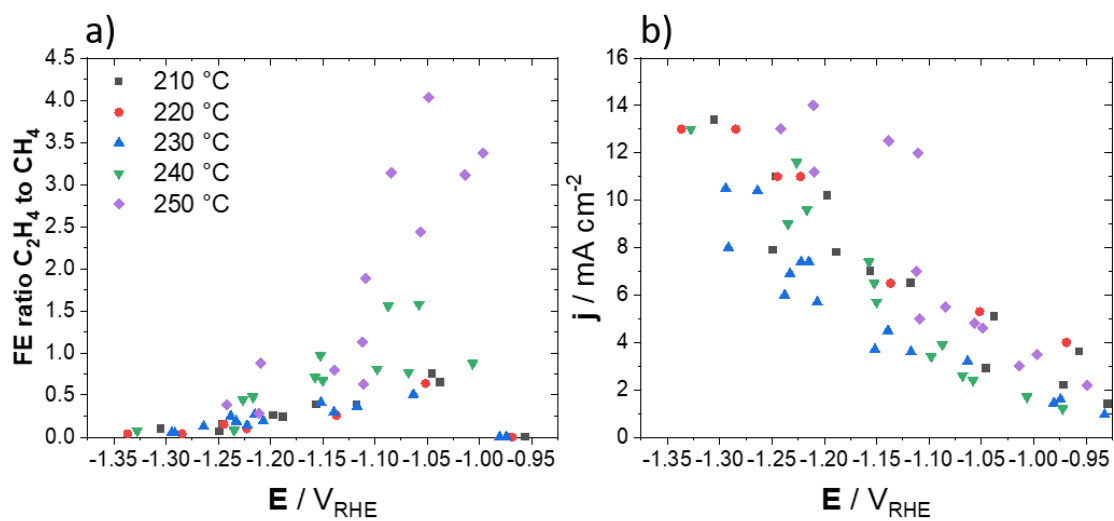


Figure A 1.12 (a) FE-ratio of C_2H_4 to CH_4 and (b) geometric current density as a function of electrode potential obtained for catalysts prepared at different reaction temperatures during CO_2RR .

Supplementary information to chapter 4.3

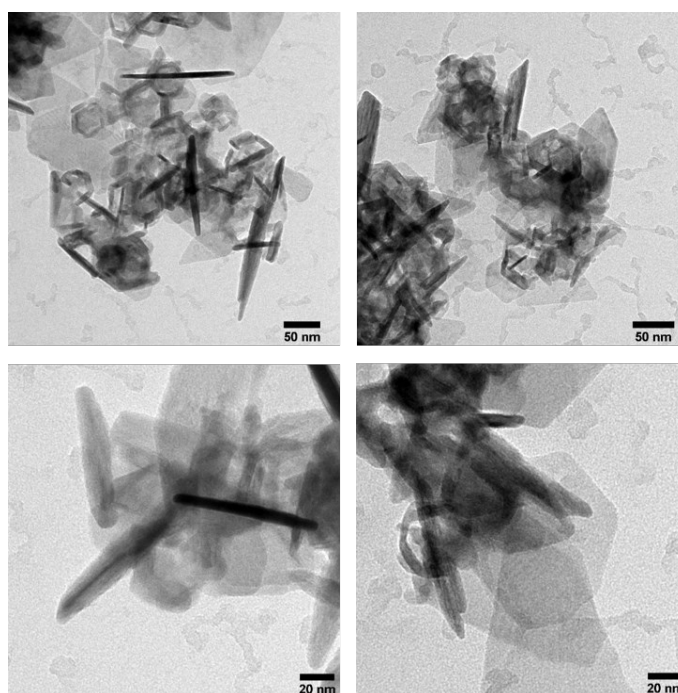


Figure A 1.13 TEM images of the 10 mL CuS catalyst prepared by sulfidation of cubic Cu₂O particles.

Supplementary information to chapter 4.4

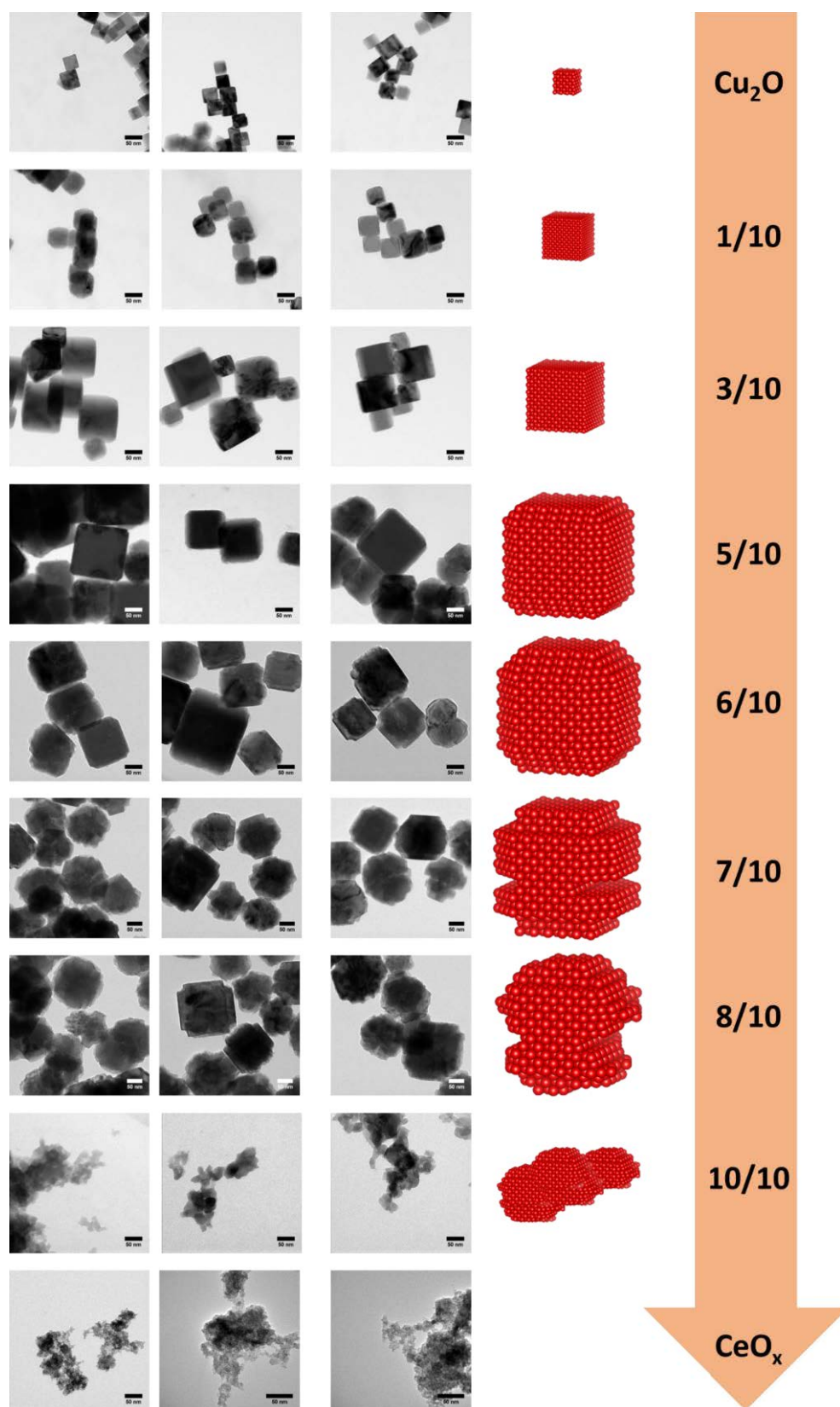


Figure A 1.14 TEM images and schematic illustration of the morphological influence for the employed Ce/Cu ratio during synthesis. Scale bars of the images are 50 nm.

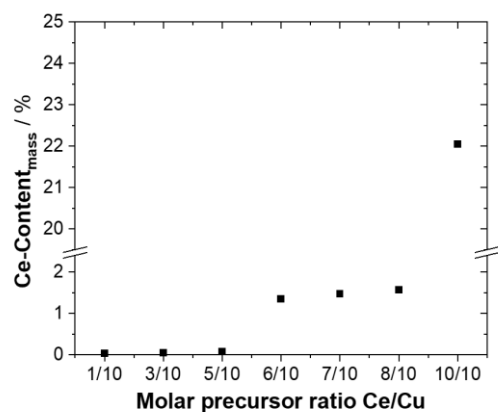


Figure A 1.15 Mass content of Ce for the materials prepared under employment of different CeCl_3 to CuCl_2 molar precursor-ratios during synthesis, as derived from ICP-OES analysis.

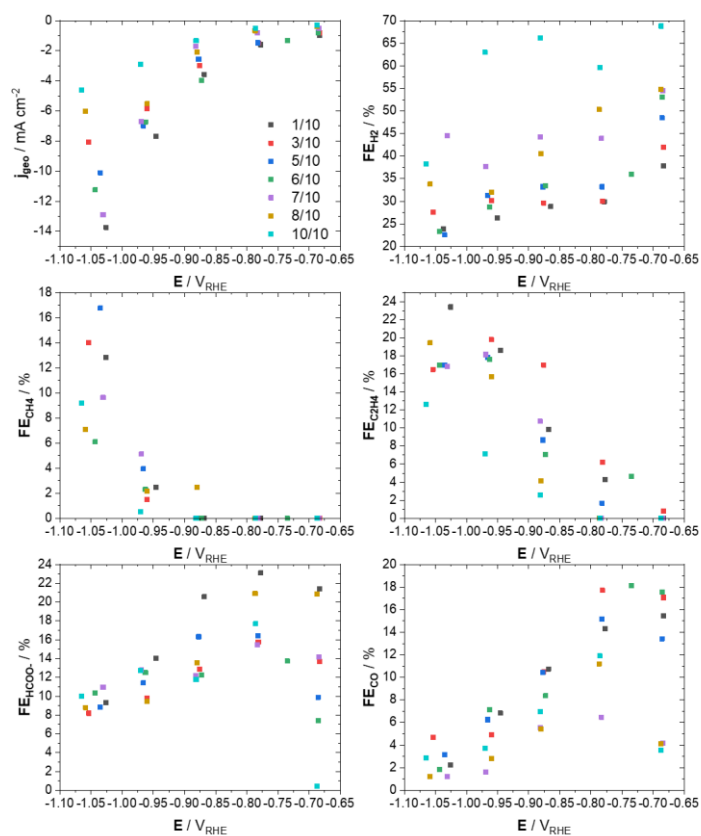


Figure A 1.16 Faradaic efficiency and geometric current density observed for catalysts prepared from various Ce/Cu precursor ratios during electrocatalytic CO_2RR .

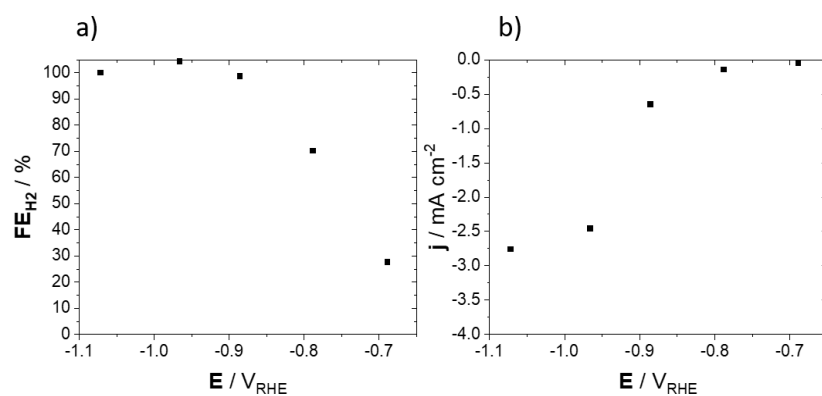


Figure A 1.17 (a) FE for the production of H₂ and (b) geometric current density observed during CO₂RR for the pure CeO_x material prepared from exclusive use of CeCl₃ as precursor.

A 2 Supplementary information to CO₂RR in a Flow-Cell

Supplementary information to chapter 5.1

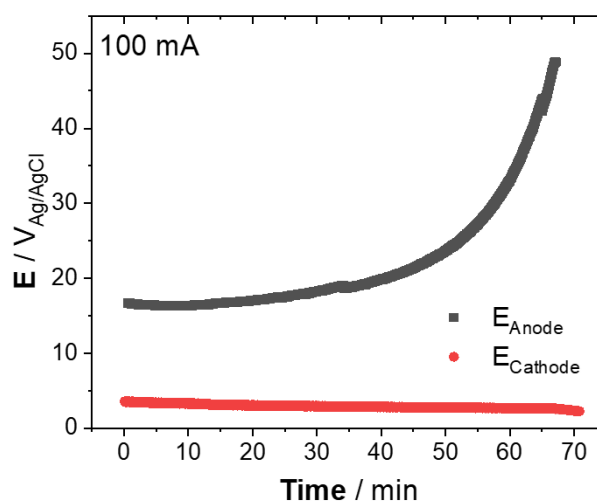


Figure A 2.1 Potential measurement as a function of time at a constant current of 100 mA conducted in an H-Cell. The measurement was performed in 0.1 M KHCO₃ electrolyte with respective volume of 40 mL for anolyte and catholyte. As cathode Cu foil of 1 cm² was used and the catholyte was saturated with CO₂ during electrolysis. The use anode was a commercial Ir-MMO electrode with 2 cm².

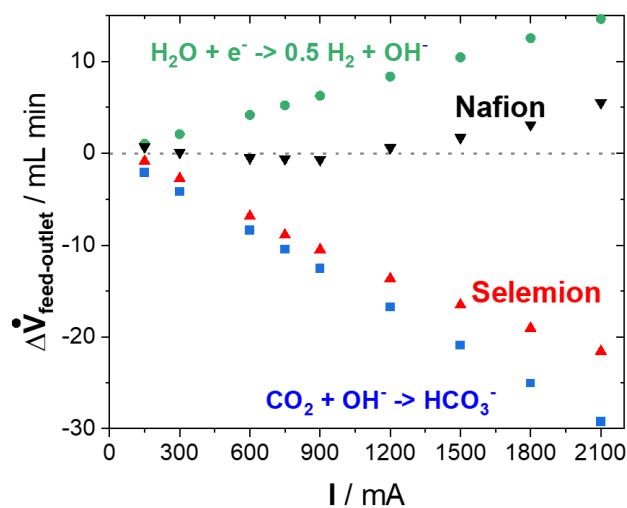


Figure A 2.2 Difference of the cathode feed and outlet flow as a function of applied current as measured for a Nafion and Selemion membrane in 1 KHCO₃ electrolyte. Additionally the theoretic values based on the HER and CO₂ consumption in the alkaline environment are shown

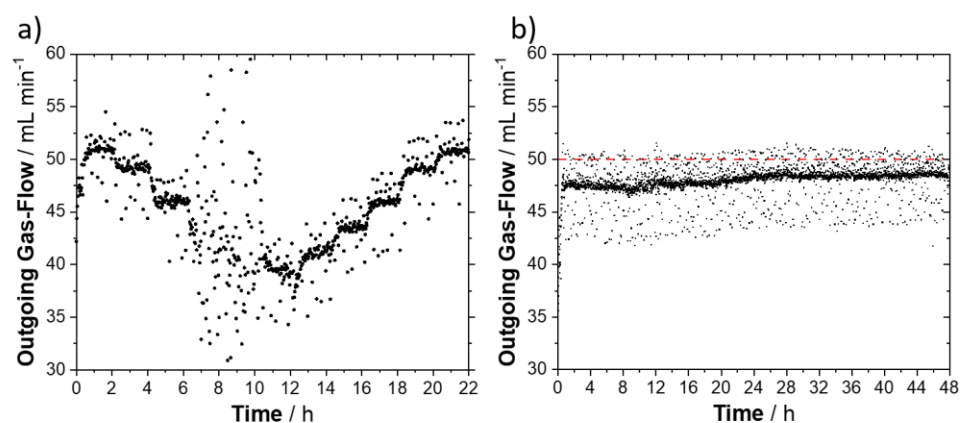


Figure A 2.3 Outgoing gas-flow of the cathode chamber as a function of time during CO₂RR in 1 M KHCO₃ under (a) variation of the applied current in between 150 mA and 1500 mA and (b) at a constant current of 450 mA.

Supplementary information to chapter 5.2

The supplementary information to subchapter 5.2 has been reproduced from T. Möller et al., *Angew. Chem. Int. Ed.* **2020**, 59, 17974-17983, (reference ^[133], DOI: [10.1002/anie.202007136](https://doi.org/10.1002/anie.202007136)). Licensed under [CC BY 4.0](https://creativecommons.org/licenses/by/4.0/).

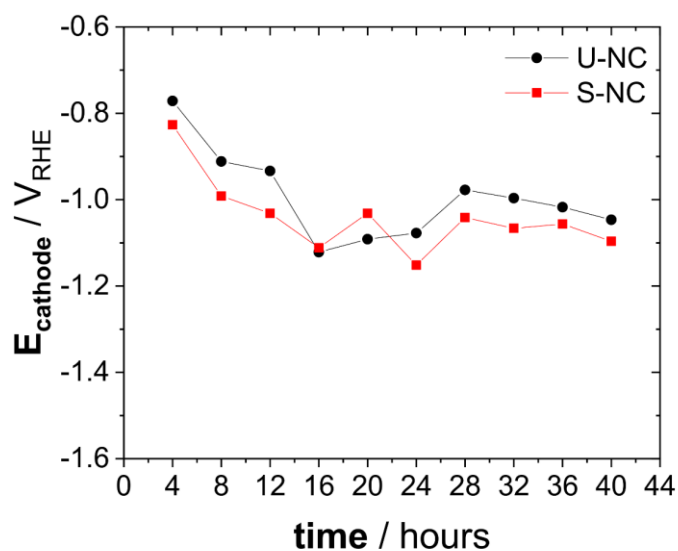


Figure A 2.4 The cathode potential vs. IR-free RHE as a function of time for the unsupported, U-NC, and supported, S-NC, (23 wt% metal loading) catalyst at -300 mA cm^{-2} over the duration of 40 h. Every 4 h the resistance was determined by a PEIS measurement, which was used to account for the ohmic drop. Lines to guide the eye

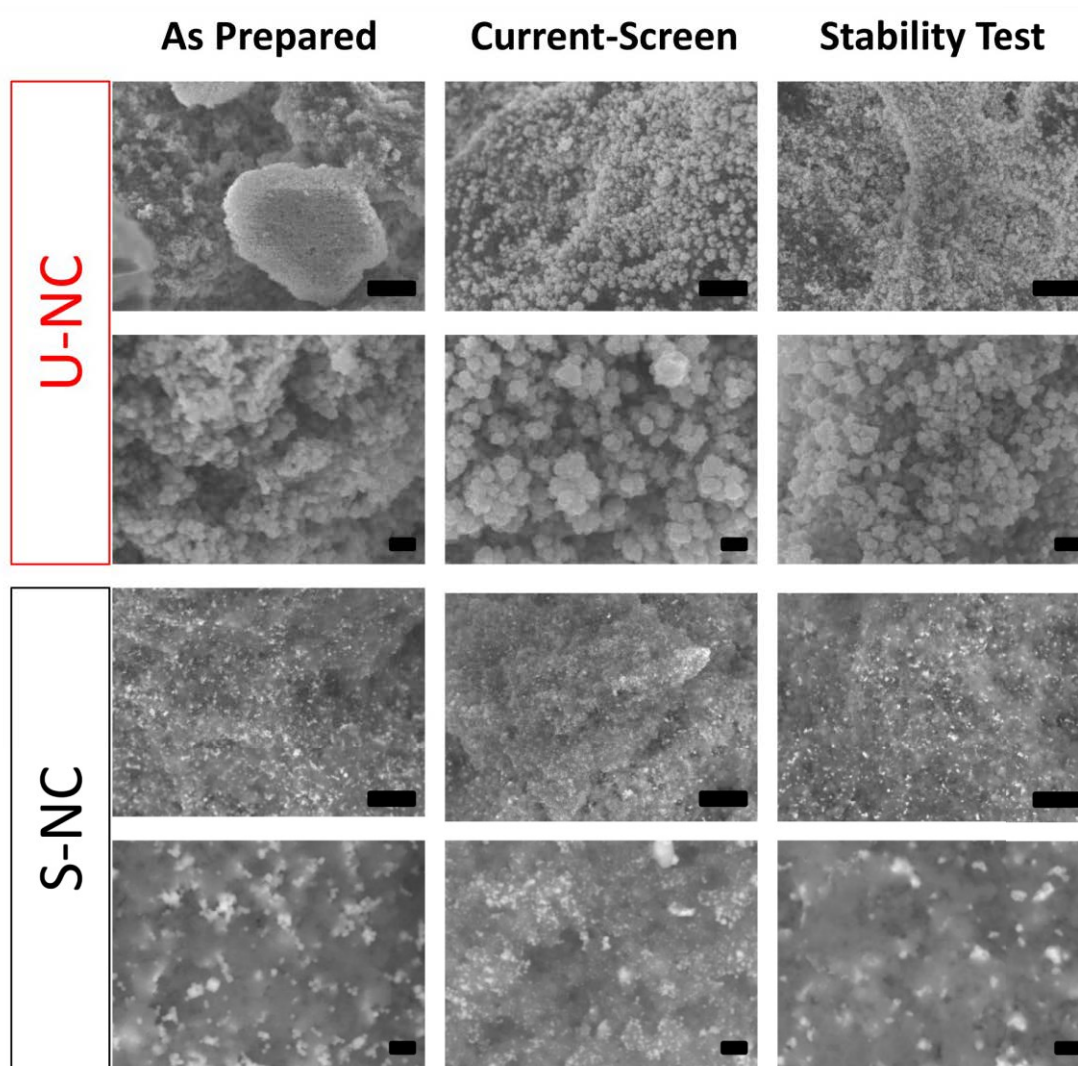


Figure A 2.5 SEM images of the unsupported particles (top two rows) and SEM-COMPO images of the supported particles (bottom two rows) in as prepared state, after the current-screen in between -50 to -700 mA cm⁻² and 40 h stability test in the flow-cell at -300 mA cm⁻². Scale bars in the low-magnification images (first and third row) represent 2000 nm and represent 200 nm in the high-magnification images (second and fourth row).

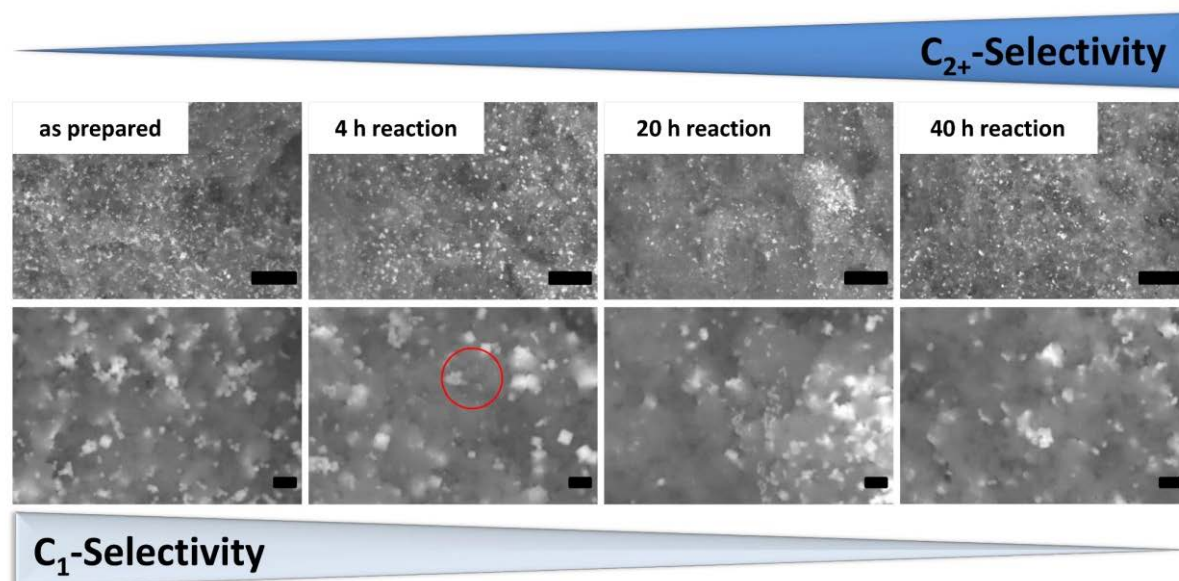


Figure A 2.6. SEM-COMPO images of the supported (23 wt% metal loading) after different times of reduction at constant current of -300 mA cm^{-2} in the Flow-Cell. Scale bars represent 2000 nm in the first row and 200 nm in the second row. The formation of small particle is indicated by a red circle in the image after four hours of reaction time.

Supplementary information to chapter 5.3

The supplementary information to subchapter 5.3 has been largely reproduced from a submitted manuscript that is currently under revision in the journal “Energy & Environmental Science” with permission from the Royal Society of Chemistry. *Tim Möller, Trung Ngo Thanh, Xingli Wang, Wen Ju, Zarko Jovanov and Peter Strasser*, The product selectivity zones in Gas Diffusion Electrodes during the electrocatalytic reduction of CO₂, Energy & Environmental Science **2021**, submitted.

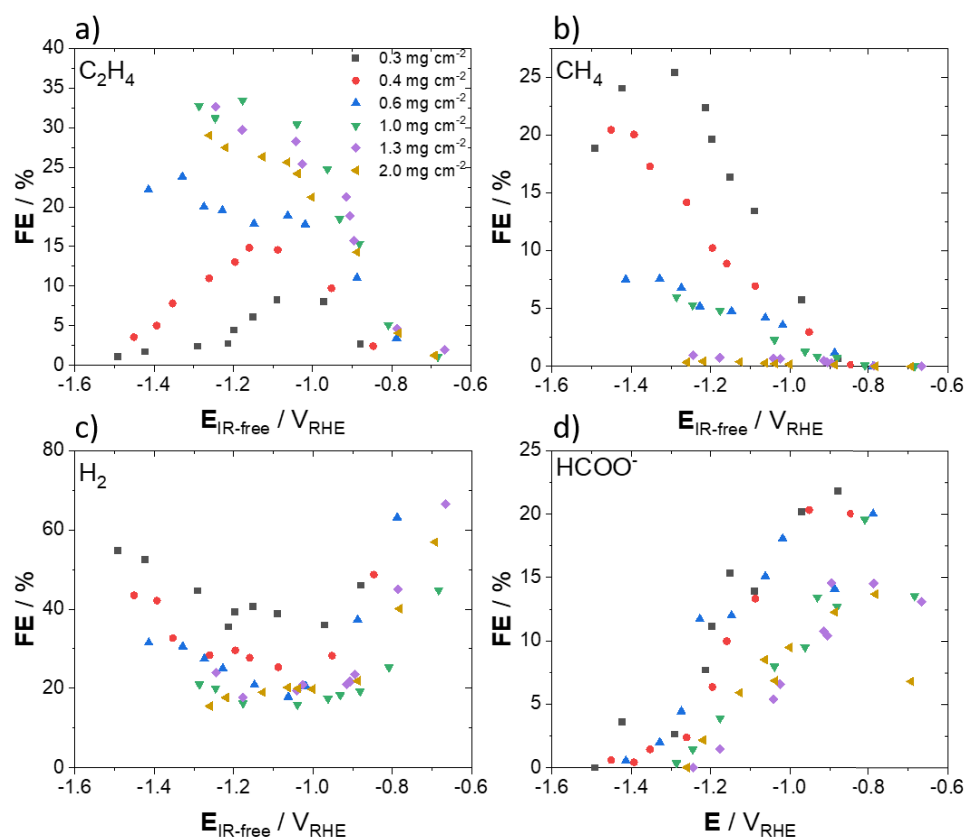


Figure A 2.7 Faradaic efficiency as a function of applied IR-free RHE potentials for C₂H₄ (a), CH₄ (b), H₂ (c) and HCOO⁻ (d) during tests in the flow-cell for different catalyst loadings. Test were performed in 1 M KHCO₃ with constant Nafion content of 10 wt% and an active geometric area of 3 cm².

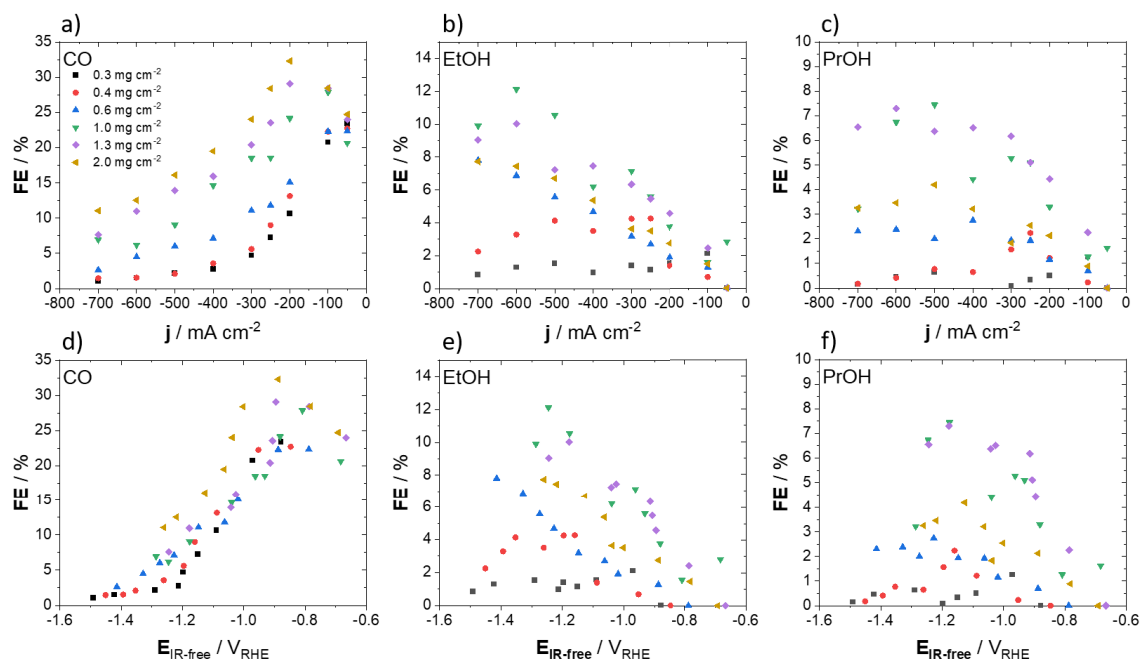


Figure A 2.8 Faradaic efficiency as a function of applied current density for CO (a), EtOH (b) and PrOH (c). Faradaic efficiency as a function of applied IR-free RHE potentials for CO (d), EtOH (e) and PrOH (f). Test were performed in 1 M KHCO_3 with constant Nafion content of 10 wt%, various catalyst loadings and an active geometric area of 3 cm^2 .

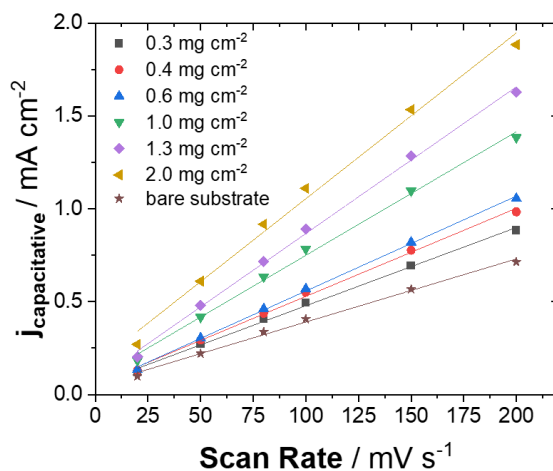


Figure A 2.9 Electrochemical capacitance measurements for various catalyst loadings after CO_2RR electrolysis. The potential was cycled in between $0.1 \text{ V}_{\text{RHE}}$ and $0.25 \text{ V}_{\text{RHE}}$ at different scan rates directly after screening the catalytic selectivity during CO_2RR . The sample “bare substrate” is referring to an uncoated Freudenberg C2 gas diffusion layer. Test were performed in 1 M KHCO_3 with constant Nafion content of 10 wt% and an active geometric area of 3 cm^2 .

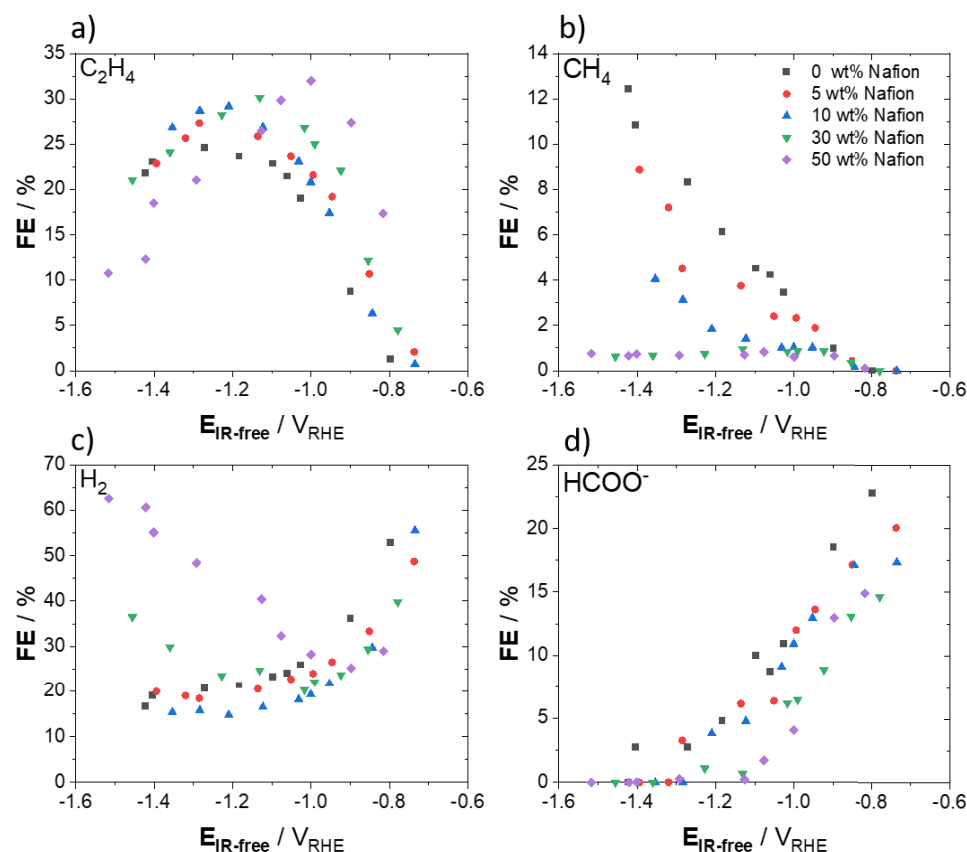


Figure A 2.10 Faradaic efficiency as a function of applied IR-free RHE potentials for C_2H_4 (a), CH_4 (b), H_2 (c) and HCOO^- (d) during tests in the flow-cell for various different Nafion contents. Tests were performed in 1 M KHCO_3 with constant catalyst loading of 0.7 mg cm^{-2} and an active geometric area of 3 cm^2 .

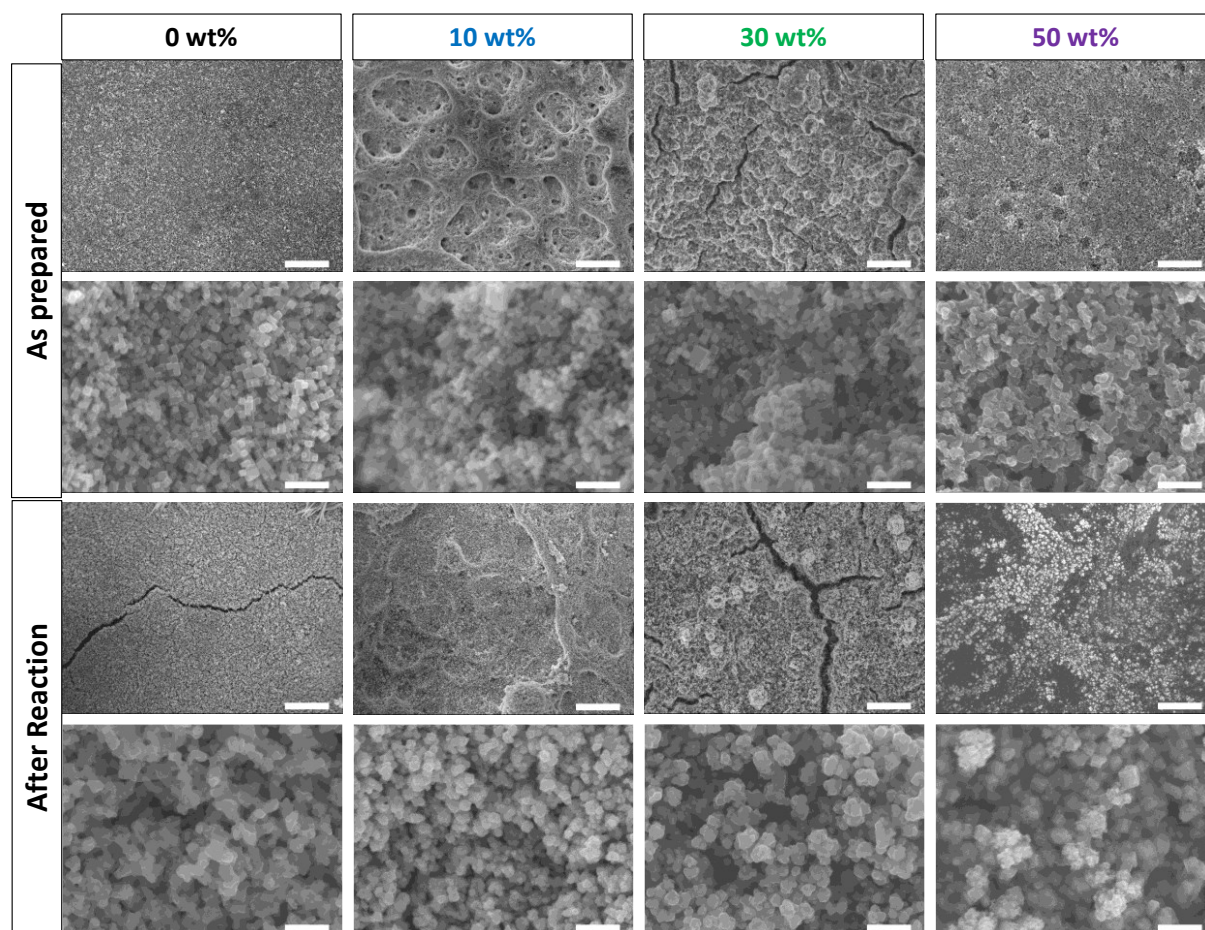


Figure A 2.11 Top-view SEM images of GDEs with different Nafion contents, as prepared and after reaction. Test were performed in 1 M KHCO_3 with constant catalyst loading of 0.7 mg cm^{-2} , various Nafion contents and an active geometric area of 3 cm^2 . Low magnification images of the first rows for after reaction and as prepared show a scale bar of $10 \text{ } \mu\text{m}$ and higher magnification images of the second rows show a scale bar of 400 nm .

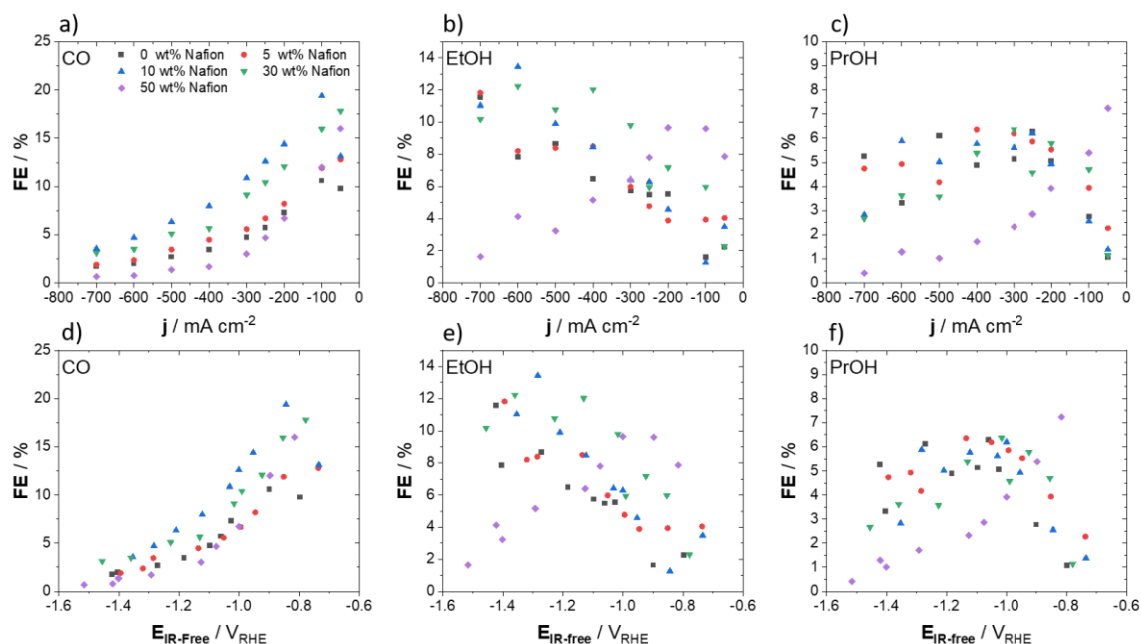


Figure A 2.12 Faradaic efficiency as a function of applied current density for CO (a), EtOH (b) and PrOH (c). Faradaic efficiency as a function of applied IR-free RHE potentials for CO (d), EtOH (e) and PrOH (f). Tests were performed in 1 M KHCO_3 with constant catalyst loading of 0.7 mg cm^{-2} , various Nafion contents and an active geometric area of 3 cm^2 .

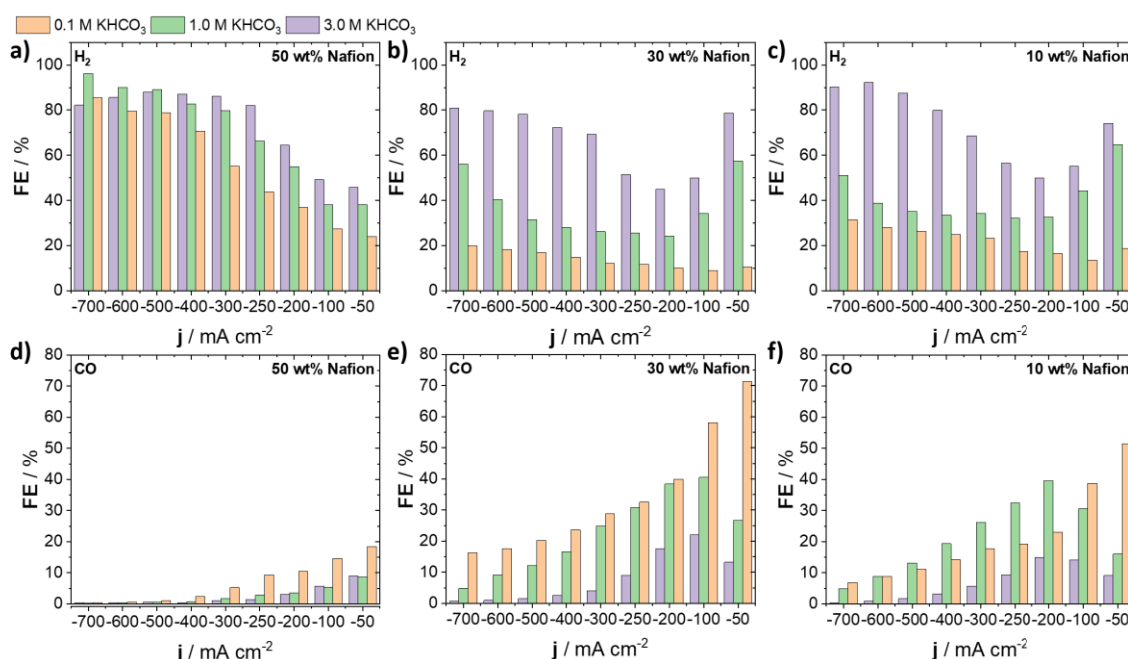


Figure A 2.13 Effect of variations in KHCO_3 concentration on the CO_2RR selectivity towards HER products using 50 wt% (a), 30 wt% (b), and 10 wt% (c) of Nafion. . Effect of variations in KHCO_3 concentration on the CO_2RR selectivity towards CO using 50 wt% (d), 30 wt% (e), and 10 wt% (f) of Nafion. In all cases Cu_2O loading was const. at 0.7 mg cm^{-2} .

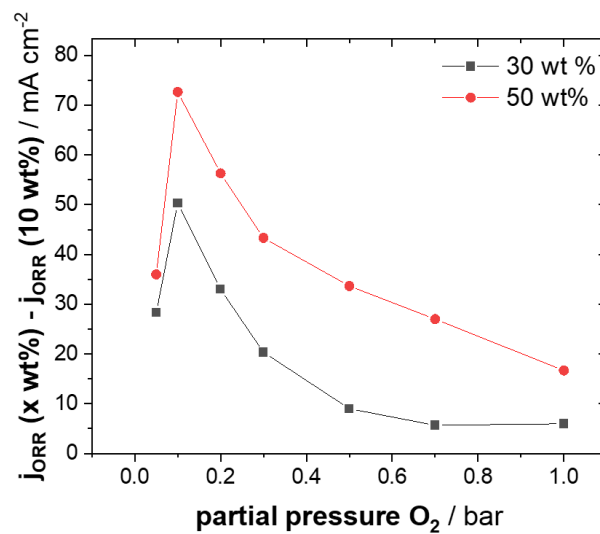


Figure A 2.14 Measurements of oxygen reduction reaction (ORR) currents in 2 M KHCO₃ as a function of partial O₂ pressure at various Nafion contents. Shown is the difference of the ORR current on the 10 wt% Nafion sample to the 30 wt% sample (black) and the 50 wt% sample (red).

List of figures

Figure 1.1 Illustration of the overall perturbation of the global carbon cycle caused by anthropogenic activities, averaged globally for the decade 2009-2018. The figure was reproduced from P. Friedlingstein et al., <i>Earth System Science Data</i> 2019, 11, 1783-1838 (reference ^[4]).	2
Figure 1.2 (a) Classification of electrode materials according to the major product generated during CO ₂ RR in 0.1 M KHCO ₃ . (b) Binding energies for CO* and H* on various electrode materials. Reproduced with permission from <i>ChemPhysChem</i> 2017, 18, 3266-3273 (reference ^[36]). Copyright 2017 Wiley-VCH Verlag GmbH & Co. KGaA, Weinheim.	5
Figure 1.3 Schematic outline of the present work with reference to the different investigated materials and systems within each chapter.	11
Figure 2.1 Schematic representation of the molecular arrangement within the electrochemical double layer according to the model of Bockris, Devanathan and Müller. ^[118] A simplified correlation of the change in potential with distance orthogonal to the electrode surface is also given.	16
Figure 2.2 Reaction coordinate diagram depicting the change in enthalpy during a reversible reduction.	17
Figure 2.3 Temperature dependence of the free enthalpy, enthalpy, and their corresponding cell voltages of the H ₂ /H ₂ O redox couple. Reprinted and adapted from <i>Electrochemical Energy Storage for Renewable Sources and Grid Balancing</i> , T. Smolinka, E. T. Ojong, J. Garche, <i>Hydrogen Production from Renewable Energies – Electrolyzer Technologies</i> , 106, 2015, with permission from Elsevier. ^[117]	20
Figure 2.4 Reaction coordinate diagram depicting the change in enthalpy and activation energy during a reversible reduction.	22
Figure 2.5 Reaction coordinate diagram showing the effect of a change in electrode potential on the kinetic barriers of a reversible electrochemical reduction.	23
Figure 2.6 Scheme of the volcano-type relationship between the reaction rate and bond strength, which shows a region of optimal binding conditions based on the Sabatier principle.	29
Figure 3.1 Illustration of the electrode preparation procedure showing the dispersion of catalyst-inks and coating of the substrates.	34
Figure 3.2 Image of a mounted H-Cell used during the electrochemical characterization. Indications for the compartments, separator and important connections are given.	36
Figure 3.3 Schematic representation of the Flow-Cell testing environment. Colored arrows indicate the direction of electrolyte and CO ₂ flow.	37
Figure 4.1 Schematic representation of an H-Cell used in common electrochemical experiments during CO ₂ RR.	45
Figure 4.2 Transmission electron microscopy (TEM) images of (a,d) the unsupported Cu ₂ O nanocubes, U-NC, and (b,e) the carbon-supported Cu ₂ O nanocubes (23 wt%), S-NC. Insets (d,e) show selected area electron diffraction (SAED) patterns of the respective material. (c) X-ray diffraction (XRD) patterns of both catalysts and (f) particle size distribution histogram (edge length) derived from TEM images of the U-NC.	49
Figure 4.3 (a,b) Faradaic product efficiencies (FEs) as a function of the applied electrode potential after one hour of reaction time for (a) the unsupported Cu nanocubes, U-NC and (b) the carbon-supported Cu nanocubes (23 wt%), S-NC. Color coded bars denote products as given in the legend. (c) Chronoamperometric efficiency stability at a constant applied electrode potential of -0.86 V _{RHE} for the U-NC and the S-NC catalysts. Color coded bars and curves denote time evolution of Faradaic efficiencies of gaseous species and the total geometric current density, respectively. The curve and bar-border color indicate affiliation to the respective catalyst, either U-NC, red, or S-NC, black. (d) Direct comparison of the electrochemical CO ₂ reduction polarization curve (geometric current-density vs IR-corrected applied electrode potential); (e) (C ₂₊ /C ₁) FE ratios vs IR corrected applied	

electrode potential. Lines to guide the eye. Conditions: CO₂ saturated 0.1 M KHCO₃ (pH 6.8), geometric Cu₂O loading on GC plates of 100 µg cm⁻¹ and 87 µg cm⁻¹ for the U-NC and S-NC catalyst, respectively.....51

Figure 4.4 (a) SEM images of the unsupported catalyst, U-NC, as prepared and (b) after 1 hour of CO₂ electrocatalysis at an electrode potential of -0.95 V_{RHE}. (d) TEM images of supported Cu nanocube, S-NC, (23 wt%) catalyst, as prepared and (e) after 1 hour of CO₂RR testing at -0.95 V_{RHE}. (c) XRD patterns of the U-NC catalyst and (f) the S-NC catalyst after initial deposition on a glassy carbon electrode (black), after 1 hour of CO₂RR at -0.66 V_{RHE} (blue) and after 1 hour at -0.95 V_{RHE} (red). XRD patterns of the blank glassy carbon plate and of the as prepared catalyst powders are displayed in Figure A 1.7 as reference.54

Figure 4.5 (a) XPS Cu 2p of as prepared U-NC deposited on a glassy carbon electrode. (b) Quasi in situ XPS Cu 2p and (c) Cu Auger LMM spectra of the U-NC and S-NC (23 wt%) catalyst after one hour of CO₂RR at -0.95 V_{RHE} and -0.65 V_{RHE}. Cu AES of as-prepared catalysts can be found in Figure A 1.8.....56

Figure 4.6 (a) Cu K-edge XANES data of U-NC sample acquired under operando CO₂ reduction conditions. (b) Representative example of catalyst XANES data fitting with a linear combination of reference spectra (the latter are also shown, scaled by their importance to the analyzed catalyst spectrum). (c) Fourier-transformed (FT) Cu K-edge EXAFS data of U-NC sample acquired under operando CO₂ reduction conditions. Representative example of EXAFS data fitting is shown in the inset. (d) Temporal evolution of the chemical composition of the Cu₂O cubes during CO₂ electroreduction obtained from the linear combination analysis of XANES data (filled circles) and coordination numbers from EXAFS data fitting (empty circles). Solid and dashed lines are guides for the eye.57

Figure 4.7 Thermogravimetric analysis coupled to a differential scanning calorimetry (TGA-DSC) measurement of the Cu(NO₃)₂ precursor used for the preparation of Cu₃N particles. Vertical lines indicate the applied heating steps during the synthesis. The shaded area at above 200 °C indicates the temperature region chosen during particle growth. The proposed sequence of underlying thermal processes is schematically depicted above.....62

Figure 4.8 (a) Powder XRD patterns of the samples prepared by variation of the temperature during synthesis. (b) Enlarged section of the TGA-DSC measurement for the Cu(NO₃)₂*2.5 H₂O used as precursor in the particle synthesis. Here, vertical lines indicate the temperatures chosen during synthesis and shaded areas correspond to the crystalline phase of the resulting product from synthesis, as observed by powder XRD.63

Figure 4.9 TEM images of the samples prepared at different reaction temperatures. The scale bar in each image corresponds to 50 nm.....64

Figure 4.10 FE of the major products obtained during catalytic CO₂RR for the particles prepared at different temperatures: (a) CH₄, (b) C₂H₄, (c) H₂, and (d) CO.....65

Figure 4.11 SEM images of the initial state of the cubic Cu₂O particles, after addition of 0.5 mL and 10 mL of (NH₄)₂S (a). Schematic representation of the morphological transition induced during the sulfidation (b). Powder-XRD patterns of the 0.5 mL and 10 mL catalyst with marks corresponding to the most intense signals of a CuS reference pattern, PDF-number:01-078-0877 (c).....71

Figure 4.12 Geometric current density (a), faradaic efficiency of the main products, H₂ and HCOO⁻, (b) and faradaic efficiency of the minor products, CO, CH₄, and C₂H₄ (c), as a function of applied electrode potential obtained during catalytic testing of the CuS catalysts.72

Figure 4.13 Cyclovoltamograms obtained during routine testing of catalytic CO₂RR and for scans towards an upper potential of -0.33 V_{RHE} and -0.68 V_{RHE} (a). GI-XRD patterns obtained for the as-prepared catalyst, left, after scanning the potential towards -0.33 V_{RHE}, middle, and after scanning the potential towards -0.68 V_{RHE}, right, (b). Schematic representation of the change in crystal phase of the initial CuS catalyst upon application of reductive potentials (c). All tests were performed using the 0.5 mL catalyst.74

Figure 4.14 TEM images of the materials prepared under employment of different CeCl₃ to CuCl₂ molar precursor-ratios during synthesis. The respective value is given in each panel and the labels Cu₂O and CeO₂ refer to a preparation route including only CuCl₂ or CeCl₃, respectively.78

Figure 4.15 Powder-XRD analysis of the particles prepared from employment of different CeCl₃ to CuCl₂ molar precursor-ratios during synthesis.79

List of figures

Figure 4.16 Faradaic efficiency for catalysts prepared from various Ce/Cu precursor ratios during electrocatalytic CO ₂ RR observed at different cathodic potentials.	81
Figure 5.1 Schematic representation of a CO ₂ RR Flow-Cell electrolyzer including a gas diffusion electrode (GDE) with indicated directions for gas and liquid transport.....	85
Figure 5.2 (a) Time dependent, outgoing gas flow of the cathodic chamber for a Flow-Cell setup including a Nafion and a Selemion membrane, respectively, in 1 M KHCO ₃ . Every two hours the current was increased while the gas feed was held constant at 50 mL min ⁻¹ . (b) Schematic depiction of the ion migration for anion (AEM) and cation (CEM) conduction membranes and pH related reactions.	89
Figure 5.3 Anolyte and catholyte pH as a function of time during CO ₂ RR electrolysis in 1 M KHCO ₃ (a) under variation of the applied current and (b) at a constant current of 450 mA.	90
Figure 5.4 (a) Schematic representation of the membrane electrolyzer flow cell, visualizing the direction of electrolyte and gas flow. Faradaic product efficiencies as a function of applied geometric current density for (b) the unsupported Cu nanocubes, U-NC, and (c) the supported (23 wt%) Cu nanocubes, S-NC. (e) 40 h faradaic efficiency stability test at -300 mA cm ⁻² , displaying the Faradaic efficiency as a function of time for the unsupported, U-NC, and (f) the supported (23 wt%) Cu nanocubes, S-NC. (d) Direct comparison of the electrolyzer polarization curves of U-NC and S-NC; (g) Plot of the (C ₂₊ / C ₁) product FE-ratio for both catalysts. All electrolyzer tests were performed in CO ₂ saturated 1 M KHCO ₃ (pH 7.6) with an active geometric cathode-area of 3 cm ² and 1 mg cm ⁻² particle loading. CO ₂ was supplied at 50 sccm to the cathode and the electrolyte was cycled at 100 mL min ⁻¹ through each respective compartment.	95
Figure 5.5 Schematic representation of the morphological and structural degradation of the supported Cu nanocubes (23 wt%), S-NC, and unsupported Cu nanocubes, U-NC, during CO ₂ RR in a flow-electrolyzer. Top-view SEM images of the gas diffusion electrode as prepared, after 18 h of selectivity screen and after 40 h of stability test at -300 mA cm ⁻² , as well as the temporal evolution of the C ₂₊ and C ₁ Faradaic efficiency during 40 h of stability test at -300 mA cm ⁻² are displayed for U-NC and S-NC, respectively.....	97
Figure 5.6 Schematic representation of a 3-compartment flow-cell electrolyzer with indications of the transport directions for reactants, products and electrolyte (a). Schematic representation of carbon-based gas diffusion electrode with cross-section (50 μm scalebar) and top view SEM images (400 nm scalebar) of a GDE prepared by spray-coating a dispersion of a cubic Cu ₂ O catalyst with Nafion binder onto a carbon gas diffusion layer.	101
Figure 5.7 Top view SEM images after electrolysis (a), electrochemical double layer capacitance after electrolysis (b) and polarization curves (c) of GDEs with various catalyst mass loadings. Conditions were 3 cm ² of geometric surface area, 1 M KHCO ₃ and 10 wt% of Nafion binder. Scale bars in SEM images represent 10 μm.....	104
Figure 5.8 Faradaic efficiency as a function of applied current density at varying catalyst mass loadings for C ₂ H ₄ (a), CH ₄ (b), H ₂ (c) and HCOO ⁻ (d). Reactions were conducted under following Conditions: 3 cm ² of geometric surface area of cathode, 1 M KHCO ₃ and 10 wt% of Nafion used as binder in catalyst ink.....	105
Figure 5.9 Faradaic efficiency as a function of applied current density with Nafion loadings for C ₂ H ₄ (a), CH ₄ (b), H ₂ (d) and HCOO ⁻ (e). Measurements of double layer capacitance (c) and IR-free electrode potentials (f) as function of applied current density with various Nafion loadings. Conditions were as follows: 3 cm ² of geometric surface area, 1 M KHCO ₃ and 0.7 mg cm ⁻² catalyst mass loading.....	107
Figure 5.10 Effect of variations in KHCO ₃ concentration on the CO ₂ RR selectivity towards C ₂₊ products using 50 wt% (a), 30 wt% (b), and 10 wt% (c) of Nafion. Effect of variations in KHCO ₃ concentration on the CO ₂ RR selectivity towards C ₁ products using 50 wt% (d), 30 wt% (e), and 10 wt% (f) of Nafion. In all cases Cu ₂ O loading was const. at 0.7 mg cm ⁻² . Additional information on FE of H ₂ and CO are given in Figure A 2.13.	109
Figure 5.11 Schematic representation of CO ₂ RR and ORR on the Cu surface of a GDE (a). Cyclic voltammetry under different ratios of N ₂ /O ₂ saturated gas atmosphere in 2 M KHCO ₃ for a 10 wt% of Nafion GDE. Different colors are indicating a potential regime of pure ORR or mixed regime of HER and ORR (b). ORR current as a function of partial O ₂ pressure from N ₂ /O ₂ mixtures in 2 M KHCO ₃ for different Nafion contents in the catalytic layer at a constant electrode potential of -0.45 V _{RHE} . Different levels of shading indicate the primary limitation, either mass transport or reaction kinetics (c).	110

Figure 5.12 Scheme visualizing the transport of reactive species and products with indications of their respective directions throughout the structure of a Cu-GDE during CO ₂ RR in KHCO ₃ (a). Schematic representation of how variations in the Nafion content and particle loading influence concentration gradients throughout the catalytic layer (b).....	112
Figure 5.13. Schematic cross section of a GDE, which shows the proposed through-plane CO ₂ RR selectivity distribution in the catalytic layer due to concentration gradients of pH and CO ₂	113
Figure 6.1 Schematic illustration of the factors determining an electrochemical system for efficient CO ₂ RR.	115
Figure 6.2 Schematic illustration of the CO ₂ RR selectivity observed for the different catalyst systems investigated throughout chapter 4.	116
Figure 6.3 Schematic representation of the different length scales relevant to the CO ₂ RR in a Flow-Cell electrolyzer.	119
Figure A 1.1 (a) Faradaic product efficiencies (FEs) as a function of IR-free applied electrode potential after one hour of reaction time. (b) Transmission electron microscopy (TEM) images of the S-NC (44 wt%) catalyst, a low magnification TEM is given in the inlet.	133
Figure A 1.2 Transmission electron microscopy (TEM) images of the U-NC (a) and S-NC (b) catalyst in as prepared state and for the S-NC after CO ₂ RR at an electrode potential of -0.95 V _{RHE} in H-Cell (c). Scanning electron microscopy (SEM) images of the U-NC catalyst on a glassy carbon electrode, in as prepared state (d) and after CO ₂ RR at an electrode potential of -0.95 V _{RHE} in H-Cell (e). In case of the U-NC catalyst no Nafion was used and the loading was reduced to 20 µg cm ⁻² to allow a clearer imaging of the particles. Time of electrolysis was 60 min in all cases.	134
Figure A 1.3 Final CVs obtained for the unsupported nanocubes, U-NC, and supported nanocubes, S-NC, (23 wt%) catalyst after cycling in an aqueous solution of 0.01 M Pb(ClO ₄) ₂ and 0.1 M HClO ₄ at 10 mV s ⁻¹ in between -0.40 V and -0.05 V vs Ag/AgCl. Prior to Pb-UPD both samples have been reduced for 5 h at -0.86 V _{RHE} during CO ₂ RR to ensure a purely metallic material. The given value represents the charge derived from the anodic stripping peak at -0.24 V vs Ag/AgCl, indicated by the shaded area.	135
Figure A 1.4 Current density achieved by using the bare glassy carbon plate (GC) or 300 µg cm ⁻² of Vulcan carbon deposited on a GC plate. The conditions were equal to the CO ₂ RR tests including the Cu ₂ O particles. Lines to guide the eye.	136
Figure A 1.5 Current density normalized to geometric area (a) and to deposited mass of Cu (b) after one hour of constant potential. The reported value resulted from the averaged current during the last minute of reaction. Lines to guide the eye.....	136
Figure A 1.6 Faradaic efficiency during CO ₂ RR over 5 hours for the U-NC catalyst at -0.95 V _{RHE} (a) and -0.66 V _{RHE} (c), as well as for S-NC catalyst at -0.95 V _{RHE} (b) and -0.66 V _{RHE} (d). Values are the average of 2 independent measurements and error bars represent the respective standard deviation. The electrolyte is 0.1 M KHCO ₃ saturated with CO ₂ (pH = 6.8).....	137
Figure A 1.7 XRD measurements of the unsupported (a) and 23 wt% supported catalyst (b) on GC plate as prepared (black), after one hour of CO ₂ RR conditions at -0.66 V _{RHE} (blue) and at -0.95 V _{RHE} (red). Comparison of a XRD measurement for the GC plate substrate (orange) and catalyst powder (pink) for the unsupported catalyst (c) and the 23 wt% catalyst (d) illustrating the origin of the film-XRD pattern of the respective catalyst (black).....	138
Figure A 1.8 Cu-AES measurements of the as-prepared supported (23 wt%) and unsupported catalyst.	139
Figure A 1.9 The initial as-prepared state of Cu ₂ O cube sample is displayed and compared with references. (a) Cu K-edge X-ray absorption near edge structure (XANES) spectra. The inset shows the pre-edge feature. (b) – Fourier transformed Cu K-edge extended X-ray absorption fine structure (EXAFS) spectra.	139

List of figures

Figure A 1.10 Fits of EXAFS spectra of the Cu ₂ O cubes and references in <i>r</i> and <i>k</i> -spaces Spectra for the initial as-prepared state of Cu ₂ O cube sample measured in transmission (“Pellet”) and in fluorescence mode in electrochemical cell without electrolyte (“Air”) are compared with the spectra for reference samples (Cu foil and Cu ₂ O) and with time-dependent <i>operando</i> EXAFS data collected at -0.66V _{RHE} (spectra for 0 min - 130 min) and at -0.95 V _{RHE} . Fitting of EXAFS spectra $\chi(k)k^2$ was carried out in <i>r</i> -space in the range from 1.0 Å up to 2.8 Å (2.1 Å for Cu ₂ O). Fourier transform was carried out in the <i>k</i> range from 3 Å ⁻¹ up to 12 Å ⁻¹	140
Figure A 1.11 TEM images for the particles prepared at different temperatures from thermal decomposition of Cu(NO ₃) ₂ *2.5 H ₂ O in presence of octadecylamine. The scale bar in each image corresponds to 20 nm.....	142
Figure A 1.12 (a) FE-ratio of C ₂ H ₄ to CH ₄ and (b) geometric current density as a function of electrode potential obtained for catalysts prepared at different reaction temperatures during CO ₂ RR.....	142
Figure A 1.13 TEM images of the 10 mL CuS catalyst prepared by sulfidation of cubic Cu ₂ O particles.	143
Figure A 1.14 TEM images and schematic illustration of the morphological influence for the employed Ce/Cu ratio during synthesis. Scale bars of the images are 50 nm.	144
Figure A 1.15 Mass content of Ce for the materials prepared under employment of different CeCl ₃ to CuCl ₂ molar precursor-ratios during synthesis, as derived from ICP-OES analysis.....	145
Figure A 1.16 Faradaic efficiency and geometric current density observed for catalysts prepared from various Ce/Cu precursor ratios during electrocatalytic CO ₂ RR.	145
Figure A 1.17 (a) FE for the production of H ₂ and (b) geometric current density observed during CO ₂ RR for the pure CeO _x material prepared from exclusive use of CeCl ₃ as precursor.	146
Figure A 2.1 Potential measurement as a function of time at a constant current of 100 mA conducted in an H-Cell. The measurement was performed in 0.1 M KHCO ₃ electrolyte with respective volume of 40 mL for anolyte and catholyte. As cathode Cu foil of 1 cm ² was used and the catholyte was saturated with CO ₂ during electrolysis. The use anode was a commercial Ir-MMO electrode with 2 cm ²	147
Figure A 2.2 Difference of the cathode feed and outlet flow as a function of applied current as measured for a Nafion and Selemion membrane in 1 KHCO ₃ electrolyte. Additionally the theoretic values based on the HER and CO ₂ consumption in the alkaline environment are shown.....	147
Figure A 2.3 Outgoing gas-flow of the cathode chamber as a function of time during CO ₂ RR in 1 M KHCO ₃ under (a) variation of the applied current in between 150 mA and 1500 mA and (b) at a constant current of 450 mA.....	148
Figure A 2.4 The cathode potential vs. IR-free RHE as a function of time for the unsupported, U-NC, and supported, S-NC, (23 wt% metal loading) catalyst at -300 mA cm ⁻² over the duration of 40 h. Every 4 h the resistance was determined by a PEIS measurement, which was used to account for the ohmic drop. Lines to guide the eye	149
Figure A 2.5 SEM images of the unsupported particles (top two rows) and SEM-COMPO images of the supported particles (bottom two rows) in as prepared state, after the current-screen in between -50 to -700 mA cm ⁻² and 40 h stability test in the flow-cell at -300 mA cm ⁻² . Scale bars in the low-magnification images (first and third row) represent 2000 nm and represent 200 nm in the high-magnification images (second and fourth row).	150
Figure A 2.6. SEM-COMPO images of the supported (23 wt% metal loading) after different times of reduction at constant current of -300 mA cm ⁻² in the Flow-Cell. Scale bars represent 2000 nm in the first row and 200 nm in the second row. The formation of small particle is indicated by a red circle in the image after four hours of reaction time.....	151
Figure A 2.7 Faradaic efficiency as a function of applied IR-free RHE potentials for C ₂ H ₄ (a), CH ₄ (b), H ₂ (c) and HCOO ⁻ (d) during tests in the flow-cell for different catalyst loadings. Test were performed in 1 M KHCO ₃ with constant Nafion content of 10 wt% and an active geometric area of 3 cm ²	152
Figure A 2.8 Faradaic efficiency as a function of applied current density for CO (a), EtOH (b) and PrOH (c). Faradaic efficiency as a function of applied IR-free RHE potentials for CO (d), EtOH (e) and PrOH (f). Test were	

performed in 1 M KHCO_3 with constant Nafion content of 10 wt%, various catalyst loadings and an active geometric area of 3 cm^2 .	153
Figure A 2.9 Electrochemical capacitance measurements for various catalyst loadings after CO_2RR electrolysis. The potential was cycled in between $0.1 \text{ V}_{\text{RHE}}$ and $0.25 \text{ V}_{\text{RHE}}$ at different scan rates directly after screening the catalytic selectivity during CO_2RR . The sample “bare substrate” is referring to an uncoated Freudenberg C2 gas diffusion layer. Test were performed in 1 M KHCO_3 with constant Nafion content of 10 wt% and an active geometric area of 3 cm^2 .	153
Figure A 2.10 Faradaic efficiency as a function of applied IR-free RHE potentials for C_2H_4 (a), CH_4 (b), H_2 (c) and HCOO^- (d) during tests in the flow-cell for various different Nafion contents. Test were performed in 1 M KHCO_3 with constant catalyst loading of 0.7 mg cm^{-2} and an active geometric area of 3 cm^2 .	154
Figure A 2.11 Top-view SEM images of GDEs with different Nafion contents, as prepared and after reaction. Test were performed in 1 M KHCO_3 with constant catalyst loading of 0.7 mg cm^{-2} , various Nafion contents and an active geometric area of 3 cm^2 . Low magnification images of the first rows for after reaction and as prepared show a scale bar of $10 \mu\text{m}$ and higher magnification images of the second rows show a scale bar of 400 nm .	155
Figure A 2.12 Faradaic efficiency as a function of applied current density for CO (a), EtOH (b) and PrOH (c). Faradaic efficiency as a function of applied IR-free RHE potentials for CO (d), EtOH (e) and PrOH (f). Tests were performed in 1 M KHCO_3 with constant catalyst loading of 0.7 mg cm^{-2} , various Nafion contents and an active geometric area of 3 cm^2 .	156
Figure A 2.13 Effect of variations in KHCO_3 concentration on the CO_2RR selectivity towards HER products using 50 wt% (a), 30 wt% (b), and 10 wt% (c) of Nafion. . Effect of variations in KHCO_3 concentration on the CO_2RR selectivity towards CO using 50 wt% (d), 30 wt% (e), and 10 wt% (f) of Nafion. In all cases Cu_2O loading was const. at 0.7 mg cm^{-2} .	156
Figure A 2.14 Measurements of oxygen reduction reaction (ORR) currents in 2 M KHCO_3 as a function of partial O_2 pressure at various Nafion contents. Shown is the difference of the ORR current on the 10 wt% Nafion sample to the 30 wt% sample (black) and the 50 wt% sample (red).	157

List of tables

Table 3.1 Overview over the different materials investigated within this work with reference to the employed testing setup and chapter in which they are discussed.....	31
Table 3.2 Experimental details on the ink formulation and catalyst loading during electrochemical testing (referred to the cationic Cu compound) for the various systems investigated throughout the present work.....	35
Table A 1.1 Total amount of catalyst-powder and respective Cu ₂ O particles deposited on the glassy carbon (GC) plates for CO ₂ RR experiments in H-Cell.	134
Table A 1.2 Evolution of coordination numbers and interatomic distances from EXAFS. Coordination numbers (N), interatomic distances (R) and disorder factors (σ^2) of Cu-O and Cu-Cu nearest neighbors from EXAFS, as well as corrections to photoelectron reference energies ΔE_0	141

List of chemicals

List of chemicals

Name	Acronym	Purity/Concentration	Supplier
Ultra-pure water	Milli-Q water	16.8 M Ω cm	-
Methanol	MeOH	anhydrous, 99.9 %	Alfa Aesar
Ethanol	EtOH	99.8 %	VWR Chemicals
Isopropanol	IPA	99.5 %	Sigma Aldrich
n-Propanol	PrOH	99.9 %	Sigma Aldrich
Nafion	-	5 wt%	Sigma Aldrich
Nafion membrane	-		Sigma Aldrich
Selemion membrane	-		AGC Eng. Co.
Lead(II) perchlorate	Pb(ClO ₄) ₂	99.995 %	Sigma Aldrich
Copper(II) chloride	CuCl ₂	99.0%	Sigma-Aldrich
L-Ascorbic acid	-	99.0%	Sigma-Aldrich
Copper(II) nitrate	Cu(NO ₃) ₂	99.99 %	Sigma Aldrich
Cerium(III) chloride	CeCl ₃	98.0 %	Sigma Aldrich
1-Octadecene	-	90.0%	Alfa Aesar
1-Octadecylamine	-	90.0%	Sigma Aldrich
Cyclohexane	-	99.0%	Sigma Aldrich
Hydrochloric acid	HCl	37.0 %	VWR Chemicals
Nitric acid	HNO ₃	69.0 %	Merck
Phosphoric acid	H ₃ PO ₄	85 wt%	Sigma Aldrich
Sodium hydroxide	NaOH	99.99 %	Sigma Aldrich
Potassium bicarbonate	KHCO ₃	99.5%	Sigma Aldrich
Formic acid	HCOOH	>95%	Sigma Aldrich
Formaldehyde	CH ₂ O	37 w% (in H ₂ O)	Merck
Carbon dioxide	CO ₂	99.995 %	Air Liquide
Hydrogen	H ₂	99.999 %	Air Liquide
Carbon monoxide	CO	99.999 %	Air Liquide
Nitrogen	N ₂	99.999 %	Air Liquide
Oxygen	O ₂	99.999 %	Air Liquide
Argon	Ar	99.999 %	Air Liquide
Helium	He	99.999 %	Air Liquide

List of abbreviations

List of abbreviations

CO ₂ RR	(Electrochemical) CO ₂ reduction reaction	CEM	Cation exchange membrane
CE	Counter electrode	(P)-XRD	(Powder) X-ray diffraction
REF	Reference electrode	Pb-UPD	Lead underpotential deposition
RHE	Reversible hydrogen electrode	ICP-OES	Inductively coupled plasma optical emission spectrometry
CA	Chronoamperometry	WE	Working electrode
DFT	Density functional theory	S/NHE	Standard/Normal hydrogen electrode
ECSA	Electrochemical active surface area	LSV	Linear sweep voltammetry
GC-plate	Glassy carbon plate	GDE / L	Gas diffusion electrode / layer
TEM	Transmission electron microscopy	MEA	Membrane electrode assembly
XPS	X-ray photoelectron spectroscopy	DL	Double layer (electrochemical)
XANES	X-ray absorption near edge spectroscopy	ORR	Oxygen reduction reaction
CPET	Concerted proton-electron transfer	PEIS	Potentiostatic electrochemical impedance spectroscopy
HPLC	High performance liquid chromatograph	XAS	X-ray absorption spectroscopy
SEM	Scanning electron microscopy	EXAFS	Extended X-ray absorption fine structure
iR	Ohmic drop	TPD	Temperature programmed desorption
GI-XRD	Grazing incidence X-ray diffraction	GC	Gas chromatograph
TGA-DSC	Thermogravimetric analysis and differential scanning calorimetry	MFC	Micro flow cell
AEM	Anion exchange membrane	RT	Room temperature
SPET	Subsequent proton-electron transfer	FE	Faradaic efficiency
HER	Hydrogen evolution reaction	OER	Oxygen evolution reaction
OHP	Outer Helmholtz plane	IHP	Inner Helmholtz plane
		HHV	Higher heating value

List of publications

Publications used as part of this thesis.

T. Möller, T. N. Thanh, X. Wang, W. Ju, Z. Jovanov and P. Strasser, The product selectivity zones in Gas Diffusion Electrodes during the electrocatalytic reduction of CO₂. *Energy & Environmental Science* **2021**, submitted and currently under review.

T. Möller, F. Scholten, T. N. Thanh, I. Sinev, J. Timoshenko, X. Wang, Z. Jovanov, M. Gliech, B. Roldan Cuenya, A. S. Varela, P. Strasser, Electrocatalytic CO₂ Reduction on CuO_x Nanocubes: Tracking the Evolution of Chemical State, Geometric Structure, and Catalytic Selectivity using Operando Spectroscopy. *Angewandte Chemie International Edition* **2020**, 59, 17974-17983, DOI: [10.1002/anie.202007136](https://doi.org/10.1002/anie.202007136).

Additional publications prepared during the PhD.

T. Möller, W. Ju, A. Bagger, X. Wang, F. Luo, T. Ngo Thanh, A. S. Varela, J. Rossmeisl, P. Strasser, Efficient CO₂ to CO electrolysis on solid Ni-N-C catalysts at industrial current densities. *Energy & Environmental Science* **2019**, 12, 640-647, DOI: 10.1039/C8EE02662A.

C. Kim, **T. Möller**, J. Schmidt, A. Thomas, P. Strasser, Suppression of Competing Reaction Channels by Pb Adatom Decoration of Catalytically Active Cu Surfaces During CO₂ Electroreduction. *ACS Catalysis* **2018**, 9, 1482-1488, DOI: 10.1021/acscatal.8b02846.

C. Kim, F. Dionigi, V. Beermann, X. Wang, **T. Möller**, P. Strasser, Alloy Nanocatalysts for the Electrochemical Oxygen Reduction (ORR) and the Direct Electrochemical Carbon Dioxide Reduction Reaction (CO₂RR). *Advanced Materials* **2019**, 31, 1805617, DOI: 10.1002/adma.201805617.

W. Ju, A. Bagger, X. Wang, Y. Tsai, F. Luo, **T. Möller**, H. Wang, J. Rossmeisl, A. S. Varela, P. Strasser, Unraveling Mechanistic Reaction Pathways of the Electrochemical CO₂ Reduction on Fe-N-C Single-Site Catalysts. *ACS Energy Letters* **2019**, 4, 1663-1671, DOI: 10.1021/acsenenergylett.9b01049.

P. Strasser, M. Gliech, S. Kuehl and **T. Moeller**, Electrochemical processes on solid shaped nanoparticles with defined facets. *Chemical Society Reviews*, **2018**, 47, 715-735, DOI: 10.1039/c7cs00759k.